Reactive Metal-Organic Interfaces Studied with Adsorption Calorimetry and Photoelectron Spectroscopy

Dissertation

zur Erlangung des
Doktorgrades der Naturwissenschaften
(Dr. rer. nat.)

dem Fachbereich Chemie
der Philipps-Universität Marburg

vorgelegt von
Han Zhou
Master of Engineering

aus Baoshan, China

Marburg an der Lahn
2018

Der praktische Teil der vorliegenden Arbeit wurde unter Leitung von Herrn Prof. Dr. J. Michael Gottfried in der Zeit von November 2011 bis Juli 2018 am Fachbereich Chemie der Philipps Universität Marburg angefertigt.

Vom Fachbereich Chemie der Philipps-Universität Marburg (Hochschulkennziffer: 1180) als Dissertation am 27.07.2018 angenommen.

Tag der Disputation:

Erstgutachter:	Prof. Dr. Michael Gottfried
Zweitgutachter:	Prof. Dr. Karl-Heinz Ernst (Universität Zürich)

Contents

Selbständigkeitserklärung

Ich erkläre, dass eine Promotion noch an keiner anderen Hochschule als der Philipps Universität Marburg, Fachbereich Chemie, von mir versucht wurde.

Ich versichere, dass ich meine vorgelegte Dissertation

Reactive Metal-Organic Interfaces Studied with

Adsorption Calorimetry and Photoelectron Spectroscopy

selbst und ohne fremde Hilfe verfasst, nicht andere als die in ihr angegebenen Quellen oder Hilfsmittel benutzt, alle vollständig oder sinngemäß übernommenen Zitate als solche gekennzeichnet sowie die Dissertation in der vorliegenden oder einer ähnlichen Form noch bei keiner anderen in- oder ausländischen Hochschule anlässlich eines Promotionsgesuches oder zu anderen Prüfungszwecken eingereicht habe.

Marburg, den

Abstract

This doctoral thesis presents investigations on the reactive interactions between Ca and oligomeric organic thin films with X-ray photoelectron spectroscopy (XPS), adsorption microcalorimetry, and scanning transmission electron microscopy (STEM).

By combining X-ray photoelectron spectroscopy (XPS) and adsorption microcalorimetry, it is concluded that Ca exhibits a rather different growth behavior on oligomeric organic thin films compared with their polymeric homologs: the diffusion of Ca atoms into the oligomeric organic thin films is generally stronger than into the comparable polymeric thin films, resulting in thicker reaction zones. These effects can be observed in the Ca/α-sexithiophene (Ca/6T) system at room temperature, where a thick reaction zone (ca. 30 nm) with a constant composition of the reacted and unreacted sulfur species is present. This finding is possibly due to steric hindrance effects in the reaction zone. Such hindrance effects are presumably the result of massive backbone structural modifications, which are introduced by ring opening reactions at the thiophene units of 6T, subsequently followed by CaS cluster formation. The initially measured adsorption enthalpy of Ca on 6T (275 kJ/mol) is discussed in the context of previous calculations and measurements on similar systems. In contrast to expectation, the initial value for the measured adsorption enthalpy remains independent of coverage up to 4 monolayers of Ca (1 monolayers corresponding to 7.4×10^{18} atoms/m^2). This indicates a continuous exposure of yet unreacted sulfur to Ca from the gas phase up to this point, resulting in the formation of an extended reaction zone. Based on literature data, one would expect that a closed metallic Ca layer would form on top of the 6T film significantly below the observed threshold of 4 monolayers, quenching the reaction between Ca and 6T at an earlier stage during the Ca deposition.

In order to improve the existing adsorption microcalorimeter setup, a reliable and multifunctional data acquisition system is built with the LabVIEW programming environment. To accommodate the pendulum style movement of the calorimeter's chopper for Ca pulse generation, synchronized timing of the desktop data acquisition program and step motor’s internal control program is realized through the calibrated compensations and the employment of pulse pair as the unit experimental step. Possible solutions for the balance between the ease of programming and runtime reliability are proposed together with the ideas for code efficiency improvement. As for the hardware development of the calorimeter, a possible transition from the PVDF film detector to the $LiTaO_3$ single crystalline detector is also proposed, with a prototype detector being designed and manufactured.

Kurzzusammenfassung

Die vorliegende Dissertation beschäftigt sich mit der Reaktion zwischen Calciumschichten und oligomerbasierten organischen Dünnfilmen. Die Systeme wurden im Rahmen der vorliegenden Arbeit mit Röntgenphotoelektronenspektroskopie (XPS), Adsorptions-Mikrokalorimetrie und Rastertransmissionselektronenmikroskopie (RTEM) systematisch untersucht.

Die Ergebnisse, welche mit Hilfe von XPS und Adsorptionsmikrokalorimetrie gewonnen wurden, erlauben folgende Schlussfolgerung: Calcium, welches auf oligomerbasierten organischen Dünnfilmen abgeschieden wird, verhält sich unterschiedlich zu Calcium auf polymeren Dünnschichten. Es zeigt sich, dass Calcium effektiver in die oligomerbasierten Filme hinein diffundieren kann und – aufgrund von Reaktionen mit dem umgebenden organischen Material – dickere Reaktionszonen ausbilden kann als in analogen polymerbasierten Systemen. Dementsprechend zeigte die Abscheidung von Ca auf α-Sexithiophen (6T), dass sich eine unerwartet breite Reaktionszone mit einer Dicke von ca. 30 nm herausbildet, innerhalb derer das Verhältnis von reagiertem und unreagiertem Schwefel nahezu konstant ist. Diese Ergebnisse werden im Zusammenhang mit möglicherweise auftretenden sterischen Reaktionsbarrieren diskutiert. Das Auftreten solcher Reaktionsbarrieren ist ausgehend von Thiophen-Ringöffnungsreaktionen und der Bildung von CaS-Clustern innerhalb der Reaktionszone denkbar. Die initiale Adsorptions- bzw. Reaktionsenthalpie von Ca auf 6T (275 kJ/mol) wird im Zusammenhang zu in der Literatur verfügbaren, theoretischen und experimentellen Ergebnissen interpretiert. Im Gegensatz zur anfänglichen Erwartung zeigte sich auch, dass die gemessenen Enthalpien im Ca/6T System, bis hin zu Monolagen von Calciummengen auf der Probe (1 Monolage, entsprechend 7.4×10^{18} Atome/m^2), konstante Werte aufwiesen. Dies lässt sich als Hinweis darauf deuten, dass bis hin zu diesen Bedeckung unreagierter Schwefel in der 6T Schicht Calciumatomen aus der Gasphase ausgesetzt ist, mit diesen reagiert und die relativ weit ausgedehnte Reaktionszone bildet. Basierend auf Literaturdaten wäre es zu erwarten gewesen, dass sich eine geschlossene, metallische Calciumschicht schon deutlich unterhalb der beobachteten Bedeckung von vier Monolagen bilden würde. In diesem Fall wären auch weitere Reaktionen zwischen Ca und Schwefel aus der 6T Schicht zu einem deutlich früheren Zeitpunkt unterblieben.

Um das bereits existierende Adsorptions-Mikrokalorimeter auch auf technischem Niveau weiterzuentwickeln, wurde ein multifunktionales Datenerfassungssystem basierend auf LabVIEW implementiert. Hierbei wurde das ein Pulspaar des choppers im Kalorimeteraufbau als kleinste experimentelle "Einheit" definiert und die Pendelbewegung des choppers mit der Datenerfassung per PC synchronisiert. Darüber hinaus werden Überlegungen zu Codeeffizienz und der Balance zwischen Codelesbarkeit und Ausführungsgeschwindigkeit diskutiert. Ebenso wurde ein neuer Detektorprototyp konzipiert und gefertigt, mit welchem ein Wechsel von den bisher eingebauten PVDF Detektorfolien zu $LiTaO_3$ Einkristallen als Detektormaterial möglich ist.

Abbreviations

Symbols

(hkl)	Crystal plane
[*hkl*]	Crystal axis
$\ldots\vert_x$	Evaluated at *x*
d	Total differential
δ	Difference
∞	Infinity
∫	Integral
∑	Sum
$^{-1}$	Inverse
′	Alternative
·	Scalar product
∝	Proportional
≡	identical
≈	Approximately
∂	Partial differential
Δ	Transition operator
∅	Diameter

Constants

π	Pi	3.1415927
c	Speed of light	$2.99792 \cdot 10^{8}$ m/s
Ag L-α	X-ray line	2984.3 eV
Mg K-α	X-ray line	1253.6 eV
Al K-α	X-ray line	1486.7 eV
e	Euler’s number	2.7182818
h	Planck constant	$6.62607 \cdot 10^{-34}$ J·s $4.13567 \cdot 10^{-15}$ eV·s
k	Boltzmann constant	$1.38065 \cdot 10^{-23}$ J/K

N_A	Avogadro constant	$6.02214085774\cdot10^{23}$ 1/mol
R	Gas constant	8.3144621 J/K·mol
Functions		
δ	Delta function	
cos	Cosine	
exp	Exponential function	
ln	Natural logarithm	
log	Common logarithm	

Variables

a	Unit cell edge length	m	
b	Unit cell edge length	m	
c	Unit cell edge length	m	
	Molar heat capacity	J/K·mol	
C	heat capacity		
	Contact sensitivity		
α	Unit cell angle	°	rad
β	Heating rate	K/s	
	Unit cell angle	°	rad
γ	Unit cell angle	°	
θ	Coverage	d.l.	ML
	Emission angle	°	
λ	Inelastic mean free path	m	
v	Pre-exponential frequency factor	1/s	
	Photon frequency	Hz	
σ	Photoionization cross section	m^2	
φ	Angular efficiency factor		
Φ	Work function	eV	
A	Area	m^2	
d	Thickness	m	
f	fraction		
D	Atomic density		

E	Energy	J	eV
F	Flux	$1/m^2 \cdot s$	
h	Molar enthalpy		
H	Enthalpy	J	
I	Intensity	a.u.	
	Current	A	
K	Calibration factor		
n	Atomic density		
	Desorption order		
p	Pressure	Pa	
P	Power	W	
q	Molar heat	J/mol	
Q	Heat	J	
R	reflectivity		
S	Sticking probability		
t	time	s	
T	Temperature	K	
	Window transmission ratio		
	Analyzer transmission function		
x	position	m	
y	Photoelectric ground state efficiency factor		
	position	m	
z	position	m	
ϱ	Density	g/cm^3	
r	Desorption rate	1/s	
Z	Acoustic impedance	$kg/m^2 \cdot s$	
	Tooling factor		

Indices

↓	Adsorbed	sam	Sample
↓↑	Reflected	m	measured
g	Gas phase	win	Window
s	Solid phase	rad	Radiation
F	Fermi	QCM	Quartz crystal microbalance
ad	Absorbed	qms	Quadrupole mass spectrometer
ads	Absorbed	nstk	non-sticking
des	Desobed	r	Reacted
diff	Diffusion	ur	Unreacted
cal	Calorimetry	refl	Reflected
cln	Clean sample	sp	Spectrometer
int	Integral	VAC	Vacuum
kin	Kinetic		
cot	Coated		

Methods

AES	Auger electron spectroscopy
AFM	Atomic force microscopy
ESCA	Electron spectroscopy for chemical analysis
EDX	Dispersive X-Ray spectroscopy
LEED	Low energy electron diffraction
NAC	Nanojoule adsorption calorimetry
NEXAFS	Near edge X-ray absorption fine structure
PES	Photoemission spectroscopy
PID	Proportional/Integral/Differential
QCM	Quartz crystal microbalance
QMS	Quadrupole mass spectrometer
TDS	Thermal desorption spectroscopy
TEM	Transmission electron microscopy
SEM	Scanning electron microscopy
TPD	Temperature programmed desorption

UPS	Ultraviolet photoelectron spectroscopy
XPS	X-ray photoelectron spectroscopy
STEM	Scanning Transmission electron microscopy
STM	Scanning tunneling microscopy

Materials

2HTPP	2H-tetraphenylporphyrin
Al	Aluminum
Au	Gold
BaF2	Barium fluoride
C	Carbon
Ca	Calcium
CaO	Calcium oxide
CO	Carbon monoxide
Cu	Copper
$LiTaO_3$	Lithium tantalate
Mg	Magnesium
MgO	Magnesium oxide
O	Oxygen
PTCDA	Perylenetetracarboxylic dianhydride
6T	α-Sexithiophene
rr-P3HT	Regioregular-Poly(3-hexylthiophene)
PVDF	Polyvinylidene fluoride

Miscellaneous

e.g.	exempli gratia
et al.	et alii
etc.	et cetera
i.e.	id est
ANSI	American National Standards Institute
DIN	Deutsches Institut für Normung

FWHM	Full width at half maximum
IMFP	Inelastic mean free path
OLED	Organic light emitting diode
OFET	Organic field effect transistor
OPV	Organic photovoltaic
PCI	Peripheral Component Interconnect
USB	Universal Serial Bus
CNC	Computer Numerical Controlling

Non SI-Units

%	Percent
Å	Ångström
a.u.	Arbitrary units
d.l.	Dimensionless
mbar	Millibar
min	Minute
ML	Substrate referenced monolayer

1 Introduction

Metal/organic interfaces occur in π-conjugated organic semiconductor devices, such as organic light emitting devices (OLEDs), organic photovoltaics (OPV) and organic field-effect transistors (OFETs),[1-3] where metals are employed as electrode materials.[4] The critical performance defining parameters, such as the charge injection rate and cross-interface charge transport, are dependent on the properties of these metal/organic interfaces. Among the various influential factors, the following three appears to be the most important: first, the charge injection barrier at the interface is determined by the energy level alignment of the molecular frontier orbitals relative to the Fermi level of the metal.[5-12] Second, The transport of the charge carrier is controlled by the wave function overlap between metal and organic semiconductor through interfacial electronic coupling.[7, 13-15] Third, the morphological properties of the interface, which depends on the film structure of organic semiconductors and the specifics of interface formation, influences charge carrier mobility and therefore the efficiency of the devices.[16-17] The properties of the interface may also play an important role in the long-term stability/reliability of the devices.[18-29] All these factors make the detailed investigation of the processes occurring during interface formation indispensable for the future improvement of organic-electronic devices.[16]

For a good design and optimization of the organic electronic devices, it is therefore important to control the properties of all the aspects mentioned above. To realize that, precise quantitative information about the electronic, geometric and morphological structure of the interfaces are required to ensure the performance and stability of devices under their operation conditions. It also requires the development of suitable techniques for the preparation of these interfaces as well as the manufacture of the applicable devices, in order to achieve the highest degree of the control over the resulting properties. In the past 40 years, numerous efforts have been devoted to the understanding of interfaces between metal and organic molecules/semiconductor. Among these efforts, surface science plays a central role because these interfaces, with thicknesses ranging from a few Ångstrøms to tens of nanometers, are ideal objectives for surface science research. Modern surface science techniques are designed to investigate the chemical and structural properties of such interfaces on the atomic level. For instance, photoelectron spectroscopy (PES) provides detailed information about the electronic structure of the interface and about the chemical state of the different species that form the interface. Scanning tunneling microscopy (STM) is able to provide the geometric information of the surface and the assembly of the adsorbates at the atomic level. In addition to that, it can also directly image the molecular orbitals at different levels. Atomic force microscopy is the best technique regarding the study of surface morphology. Scanning transmission electronic microscopy (STEM) featured with energy dispersive X-Ray spectroscopy (EDX) could provide element specific profiles of the morphology of the interfaces.[21, 30] With nanojoule calorimetry and related molecular beam techniques, energetic and kinetic parameters of the interface formation process can be determined.[31-38] Modern surface science also has powerful preparation techniques for the precise control of the interface structure as well as the tunable functionalities of the resulting devices.[39]

In this study, interactions between vapor deposited reactive metal and organic semiconductor thin films, i.e., Ca and α-Sexithiophene (6T), are studied using PES, STEM and nanojoule calorimetry. In addition, the construction of data acquisition system for the nanojoule calorimeter as well as some mechanical modifications to this calorimeter are also summarized in this thesis.

1.1 Interactions between Metal and Organic Thin Film

A metal/organic interface is formed via the contact and the resulting interactions between metal atoms and organic molecules. In many situations, especially the systems with extended π-conjugated molecules, the overlap of wave function between the metal atoms and organic molecules occurs inside the metal/organic interface. New electronic states may be developed at the interface, thus resulting in the modification of the charge injection mechanism.[13-15, 40] By choosing specific chemical species involved in the interaction, new model systems with well-defined electronic structures could be obtained. For example, with different combinations of metals (meaning different elements) attached to the two sides of a certain organic semiconductor thin film, the interfacial energy level alignment with regard to the Schottky barrier could be modified, forward bias or reverse bias are consequently introduced at the metal/organic interfaces,[39] when it refers to OFETs, this would mean two types of switching devices. Such tunability of electronic structures at metal/organic interface would provide valuable guidance to the design of new organic semiconductor devices.

Beyond the electronic coupling of metal atoms with organic molecules, stronger interactions could modify (usually irreversibly) the composition and the geometric structure of the organic molecules.[35, 41-50] Such interactions are commonly regarded as the reactive interactions. The modifications introduced by the reactive interactions are often not confined as the localized change to the electronic structure of the system. In many systems, strong chemical reactions with massive bond reorganization occur. They result in massive structural modifications to the backbone of the polymeric or oligomeric organic molecules. This is especially true when reactive low work function metals, e.g., Al or alkali earth metals, are used as electron injection electrodes.

The potential of structure modifying reactions as well as morphological change thereafter are influenced by several factors, most importantly:

1. The size and reactivity of metal atom relative to the active functional group on the organic molecule. In the fabrication of the organic semiconductor devices or the research of model system, vapor deposition of metal atoms onto organic thin film is commonly used to form metal/organic interfaces. Metal atoms from the vapor would be able to diffuse up to a certain depth into the organic phase, react, form metal clusters, or diffuse backwards out to the surface. Higher reactivity means higher probability of metal atoms to be “captured” by functional groups and thus trigger the chemical reaction. Larger metal atom would naturally encounter higher steric hindrance to effectively reach the functional group on the organic molecule.
2. Configurational and conformational properties of organic molecules and the resulting morphology of the organic film. Organic polymers with active functional groups containing hetero atoms on the main chain and non-reactive aliphatic side chains or vice versa may have fewer functional groups per unit volume than their oligomeric homologs without the side chains. An example for such a pair of materials is Regioregular-poly(3-hexylthiophene) (rr-P3HT), which has an aliphatic side chain on each thiophene ring, and α-sexithiophene (6T), a thiophene hexamer without aliphatic side chains. In such cases, the organic polymer has a lower probability of metal atoms reaching its functional groups than its oligomer counterpart. Besides that, the long chain structure and the (sometimes) broadly distributed chain lengths of polymers make it difficult for polymeric materials to crystallize during the film preparation. The amorphous regions of the polymer form random coils inside the organic film, inside these coils, the aliphatic part of

the polymer would indeed act as the protective shell to its active sites. Returning to the example of rr-P3HT vs. 6T, previous studies have shown that, when Ca is vapor deposited onto spin coated thin rr-P3HT thin films, no pronounced morphological changes to the organic phase are introduced when the Ca/rr-P3HT interface of only a few nm are formed at room temperature.[35, 46] Meanwhile, early studies has implied drastic change to the backbone of 6T after the deposition of Al at room temperature.[41] The more comprehensive study of the interaction of Ca/6T thin film will discussed in the chapter 3 and 4 of this thesis.

3. The cluster formation behavior of the metal as well as its reaction products after the reaction with organic molecule. The growth of metal films on organic substrates has been demonstrated to produce complex nano- and microstructures, including three-dimensional clusters, continuous thin films and even subsurface metal particles.[18, 21, 39, 51-52] The evolution of the metallic phase with its high cohesion energy induces morphological changes in the (much softer) organic phase. For a system with both metal/organic reactions and the formation of a pristine metal phase, multiple processes determine the chemical and morphological structure of the interface. In general, it is assumed that once a mobile metal atom adsorbed on the organic layer is captured by its own condensed phase, either cluster or consecutive thin film, the metal atom loses its ability to further react with the molecules inside the organic phase. Based on this, a system of reactive metal/organic interaction in fact has two dynamically competing processes, the attachment of the metal atoms to its own condensed phase and the metal/organic reactions with the organic phase, either on its surface or inside the bulk. Furthermore, chemical properties and the cluster formation behavior of the reaction products of metal atoms might also impose obstacles to the further reactions between metal atoms and organic molecules.[35]

1.2 Photoelectron Spectroscopy

Photoelectron spectroscopy (PES) is a versatile analytical technique based on Einstein's Nobel prize winning treatment of the photoelectrical effect. In 1905, Einstein explained experimental results that differed from the conclusion of classical electromagnetic theory. According to classical theory, photoelectron emission is the result of energy transfer from the light to the metal electron, the rate of electron emission is a function of both intensity (I) and frequency of light (ν). Therefore, a rather dim light with low I would result in a time lag between the initial impinging of light and the subsequent emission of an electrons, because the electron needs to accumulate the necessary amount of energy to overcome the work function of the material. However, the experimental observation showed the existence of a frequency threshold. Below that threshold, no electrons are emitted regardless of I or the time of exposure to the light. To bridge this gap between the classical theory and the new experimental results, Einstein proposed a quantized theory which regards light as "discrete wave packets" (later named as photon) with energy equal to hν. This theory was one the developments that led to the "quantum revolution" in the early 20th century.

The understanding of the photoelectrical effect laid the basis for the development of various spectroscopic techniques that analyze the energy and momentum of the emitted photoelectrons (PE) as a function of the energy, polarization, and angle of incidence of the incoming photons. Einstein's equation, from the perspective of PES, can be rewritten as:

$$E_{\mathrm{kin}} = \mathrm{h}\nu - E_{\mathrm{b}} - \phi_{\mathrm{sp}} \tag{1.1}$$

Where E_{kin} is the measured kinetic energy of the electrons (relative to the spectrometer), hν is the photon energy, ϕ_{sp} denotes the work function of the spectrometer and E_{b} the binding energy of the electrons to the system of their origin, referenced to the Fermi level. Because each chemical element has a unique electronic structure with discrete energy levels of the electrons, PE spectra consist of discrete lines. This make PES an extremely versatile technique for the characterization of the electronic structure and the composition of solids, liquids and gases. In a certain range of kinetic energies (see below), the methods is surface-sensitive and is therefore used for the analysis of surfaces.

Photoelectron spectrometers are typically operated under ultrahigh-vacuum (UHV) condition to eliminate energy losses arising from the collision of photoelectrons with molecules from the residual gas. The diagram in Figure 1.1 illustrates the energetics of the photoemission experiment. If the energy of the photon is in the ultraviolet regime (5-100 eV), we speak of ultraviolet photoelectron spectroscopy (UPS). Photons in the soft X-ray regime (100-2 keV) and hard X-ray regime (2 k-10 keV), give rise to soft X-ray photoelectron spectroscopy (SXPS or XPS) and hard X-ray photoelectron spectroscopy (HAXPES), respectively. UPS is used to probe the valence electronic structure, while the X-ray photoelectron spectroscopies are used to excite core levels and thereby to obtain information about the chemical composition. SXPS/XPS is surface sensitive and HAXPES can be used to access bulk materials of up to a few tens of nanometers.

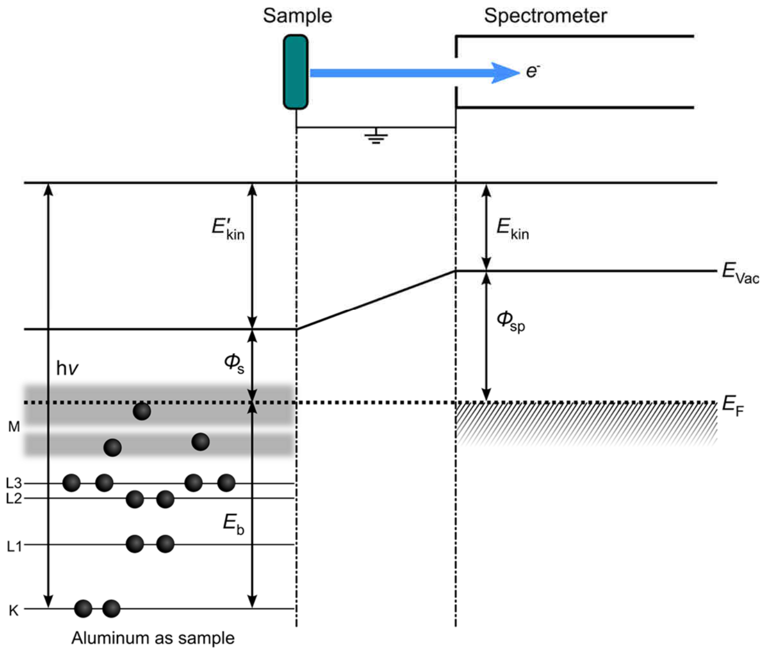

Figure 1.1: Schematic illustration to the energetics of the photoemission process. Aluminum is used as the sample material. K, L1~3, M represent the respective principal energy level of electrons. hν is the energy of the incident photons; E_b is the binding energy of the electrons, here it points to the electrons in the K shell level; ϕ_s and ϕ_{sp} denotes the work function of the sample and the spectrometer, respectively; E'_{kin} and E_{kin} denotes the kinetic energy of the emitted electron and the kinetic energy measured by the spectrometer, respectively; E_{Vac} is the energy of vacuum level; E_F is the energy of Fermi level.

After the photoelectrons are created inside the material by the photoelectrical effect, they have to travel through the material before they can leave the material's surface to enter the vacuum. On this way, the photoelectrons can undergo elastic and inelastic collisions resulting in loss of energy or change of direction. Only a fraction of the photoelectrons can enter the analyzer without having lost energy. The number of these electrons is exponentially attenuated by the material according to the Lambert-Beer Law. The electron flux intensity I as a function of travelled distance z is given by:

$$I = I_0 \exp\left(-\frac{z}{\lambda(E_{\mathrm{kin}})}\right) \tag{1.2}$$

$\lambda(E_{kin})$ is referred as the attenuation length (AL) or inelastic mean free path (IMFP) of the electrons. Equation (1.2) implies that the flux of the electrons without energy loss will decay to 1/e of its initial intensity at the distance $\lambda(E_{\mathrm{kin}})$ from surface. As many experimental results indicated, $\lambda(E_{\mathrm{kin}})$ exhibits only minor dependence on the chemical composition of the solid. Therefore, an universal curve of the IMFP versus E_{kin} is obtained combining data from various elements.[53-54]

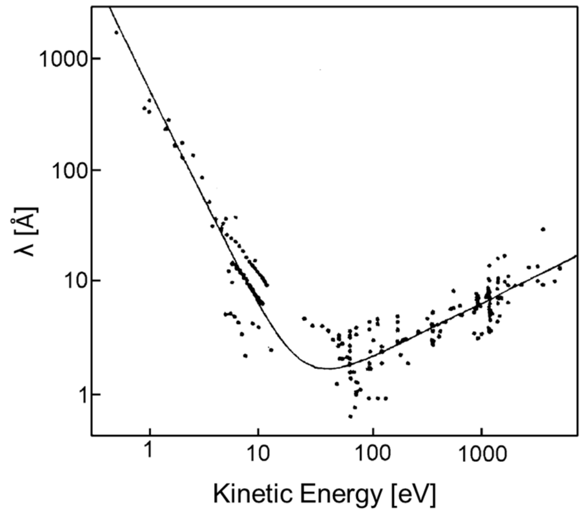

Figure 1.2: Adapted plot of IMFP vs photoelectron kinetic energy from the literature.[53-54]

1.2.1 X-ray Photoelectron Spectroscopy

X-ray photoelectron spectroscopy (XPS) can be performed with synchrotron radiation or lab X-ray sources, e.g., Al K-α (1486.7eV), Mg K-α (1253.6eV) or Ag L-α (2984.3eV) radiations. With lab sources, the kinetic energy of the photon electrons therefore typically lies in the range below 3 keV, often below 1.5 keV due to the practical need for higher photon flux and higher photoionization cross sections, where Al K-α or Mg K-α sources are advantageous. As has been shown in Figure (1.2), this kinetic energy range corresponds to an IMFP of a few nanometers. Therefore, lab XPS is surface-sensitive, i.e., it mainly probes the composition and electronic structure in the surface layers of a material.

Because each element has a unique electronic structure with discrete energies of core electrons, different elements will also emit photoelectrons with their characteristic set of kinetic energies. Figure (1.3) shows a full range XPS spectrum ("survey") of a polycrystalline Au foil using Al K-α (1486.7eV) radiation. As can be seen from the figure, all signals except those from *s*-orbitals (and Auger features) exhibit doublet patterns. This is due to the spin-orbit splitting of *p*, *d* and *f* electrons, where orbital angular momentum (*l*) and spin angular momentum (*s*) of electrons with the same principal quantum number (*n*) and non-zero *l* quantum numbers are coupled. The electron spin, either parallel or antiparallel with $s = 1/2$ or $-1/2$ respectively, sets up a magnetic field around its own axis and interact with the electron's orbital momentum vector around the nucleus. For $l > 0$ (*p*, *d*, *f* orbitals), this interaction results in two possible values for the total angular momentum $j = l + s$ and consequently to two observable binding energies in the XPS signal of non-*s* levels. In the 4*d* signal ($l = 2$) in Figure (1.3), for instance, the state with $j = 3/2$ has a lower total energy, according to Hund's rule, and therefore appears at higher binding energy in the spectra, while the peak for $j = 5/2$ appears at a lower binding energy position. These two states are expressed in a way combining information of *n, l* and *j* such as $4d_{3/2}$ or $4d_{5/2}$.

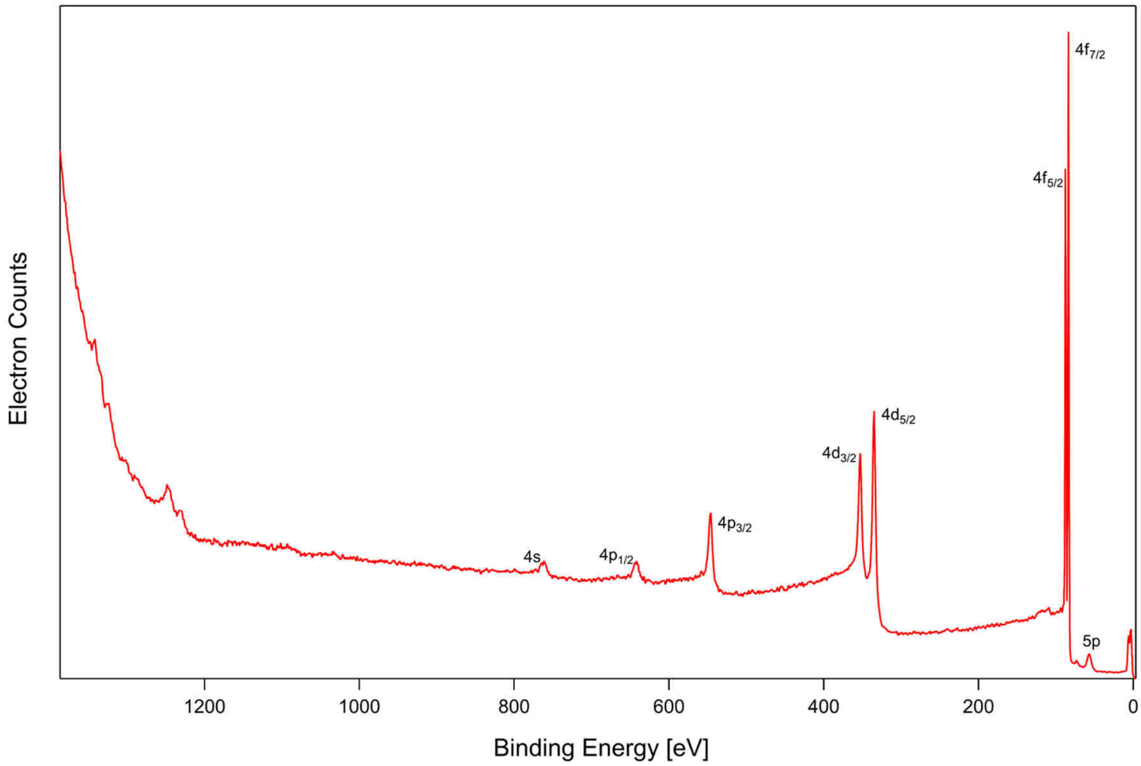

Figure 1.3: A survey spectrum of a poly-crystalline Au sample taken with Al K-α light source.

The degeneracy (g) of a state with the quantum number j is $g = 2j + 1$ and determines the relative intensities of the spin-orbit split contribution. For the $4d_{3/2}$ state, we have $g = 4$ and for the $4d_{5/2}$ state we have $g = 6$. Hence, the theoretical intensity ratio between the two lines of the $4d$ doublet is 2:3.

Based on the characteristic XPS lines of different elements, information about the chemical composition and morphology of the sample can be obtained in a quantitative manner. In particular, the stoichiometry and the oxidation states can be determined by XPS. Therefore, XPS is a very powerful tool in surface and interface science. It is sometimes referred to as electron spectroscopy for chemical analysis (ESCA). The method was mainly developed by Kai Siegbahn since the 1950s and won him the 1981 Nobel prize in physics.

1.2.2 Hard X-ray Photoemission Spectroscopy (HAXPES)

As mentioned above, photoelectron spectroscopy performed with photon energies ranging from 2 keV to 10 keV is commonly referred to as HAXPES. The HAXPES energy range lies in the rightmost region in the plot of λ vs E_{kin}, corresponding to higher IMFP of photoelectrons when compared with central energy range of soft XPS. It means that the composition and electronic structure of deeper layers of a material can be studied. By continuously varying the photon energy, the detection depth changes accordingly, which can be used for chemical depth profiling.

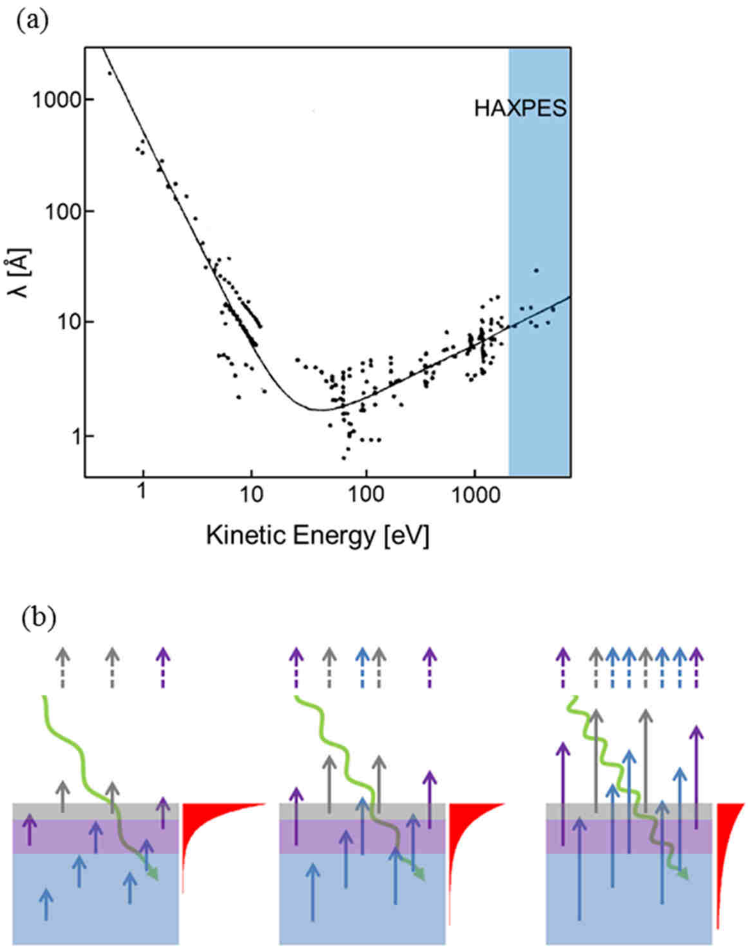

Figure 1.4: Schematic illustration of depth profiling by HAXPES. (a) Adapted plot of IMFP vs photoelectron kinetic energy, the colored region represents the kinetic energy region of HAXPES; (b) escape depth for photoelectrons with different kinetic energies. The increase of photon energy is demonstrated by the shorter wavelength of the incident light (green wave, from left to right); The probability of photoelectrons escaping from different layers (gray, purple, blue) is indicated by arrows, with their length correlated with the IMFP. The contribution of each layer, normalized to the total area, is given as a side plot in red. This scheme assumes constant photoelectron production rate (by number of arrows) and hence does not take photon flux and photon ionization cross sections into account, which normally leads to a decay of the signal intensity as the photon energy increases.[55]

The continuous variation of the photon energy is not readily possible with common lab X-ray sources. Therefore, HAXPES is usually carried out with synchrotron radiation. A synchrotron facility is mainly a storage ring for high-energy electrons under UHV condition. The electrons are accelerated to a speed very close the speed of light and trapped by electro-magnetic forces to circulate inside the ring. Due to the high velocity of electrons, even in the simple dipole deflection mode, the bending magnetic field imposed has to be rather strong so that the moving direction of the electrons could be changed correctly. This means the transverse velocity of the electrons is changed from zero to a very large value as they pass through the field, the resulting bremsstrahlung is thus much more intensive if compared with lab source of radiation. Furthermore, relativistic effects arising from the high velocity of the electrons also leads to the collimation effect of radiation in the tangent direction of their travelling circle. These two characteristics altogether result in a much higher photon flux (and brilliance) than the lab radiation sources.

1.2.3 Quantification of Layer Thickness and Reaction Depth by PES

In surface and interface science research, it is quite often that the thickness of a certain layer in the material has a large influence on a wide range of properties, such as electronic structure, distribution of the catalytic active components etc. As has been discussed before, PES provides information about the electronic structure of the material, but also about the density of a species or the chemical environment at a certain depth. On the basis of the Lambert-Beer law, the layer thickness can also be determined by PES based on proper modeling and assumptions.

In order to quantify the layer thickness, parameters representing the real photoemission process should be introduced into the equation for the photoelectron intensity. It can be given in differential form by:

$$\mathrm{d}I = n\sigma y\phi FA \cdot T \cdot \exp\left(-\frac{z}{\lambda_E \cos\theta}\right)\mathrm{d}z \tag{1.3}$$

Where n denotes the atomic density of a certain species, i.e., the number of atoms per unit volume; σ is the photoionization cross-section of the atom in the given shell under a given excitation photon energy; y is photoelectric ground state efficiency factor; ϕ is the angular efficiency factor; F is the average flux of X-rays; A is the visible area of the analyzer irradiated by X-ray; λ_E is the IMFP of electrons in a given attenuation material with a certain kinetic energy and z is the distance that photoelectrons have travelled in the attenuation layer after excitation until they enter the vacuum. A noticeable change is the inclusion of the geometry effect where θ is the photoelectrons' take-off angle from the surface. The total intensity of the PEs can be calculated by the integration of differential Equation 1.3. With different layer structure, the integral of the intensity will exhibit correspondingly different forms. First, the simplest case of a homogenous layer model is considered (Figure 1.5).

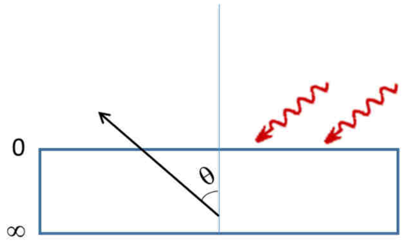

Figure 1.5: Model of photoemission from a homogenous layer with infinite thickness. 0 denotes the surface of the material; ∞ represent a point deep in the bulk which can be treated as sitting at infinite depth; θ is the photoelectrons' take-off angle from the surface.

As illustrated in Figure 1.5, the total intensity I is obtained by integration from the surface to infinite depth (∞):

$$\begin{aligned} I_{\mathrm{ho},\infty} &= \int_0^\infty n_{\mathrm{ho}}\sigma_{\mathrm{ho}} y\phi FA \cdot T_{\mathrm{ho}} \cdot \exp\left(-\frac{z}{\lambda_{E,\mathrm{ho}}\cos\theta}\right)\mathrm{d}z \\ &= k_{\mathrm{ho}} \cdot \lambda_{E,\mathrm{ho}} \cos\theta \end{aligned} \tag{1.4}$$

In this function, the subscript ho denotes that a certain parameter represents the property of this homogenous layer. k_{ho} is the total coefficient that combines all the intrinsic parameters. In the literature, Equation 1.4 is often referred to as the ideal maximum intensity of an infinite layer.

If another thin layer of different but also homogenous material with thickness *d* is adsorbed (index ad) onto this infinite homogenous layer, the infinite layer then becomes the substrate to the thin atop layer and is denoted as s. The photoelectrons from the substrate will now travel through two materials and therefore be attenuated by both layers while the photoelectrons from the adsorbed layer are attenuated only by this layer itself.

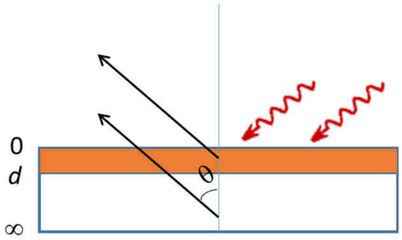

Figure 1.6: Model of photoemission from an adsorbed thin layer and an infinite substrate. 0 denotes the surface of the material; *d* is the thickness of the adsorbed thin layer and the depth of the interface below the surface; ∞ represent a point deep in the bulk which can be treated as sitting at infinite depth. θ is the photoelectrons' take-off angle from the surface.

Assuming there is a sharp (abrupt) interface between the two layers, the total intensity of a certain XPS line from the substrate and the adsorbed layer can be expressed by Equations 1.5 and 1.6, respectively. For an XPS line of the substrate, the intensity is the integral from depth *d*, the sharp interface of the two layers, to infinity in the bulk.

$$\begin{aligned} I_{\mathrm{s}} &= \int_{d}^{\infty} n_{\mathrm{s}} \sigma_{\mathrm{s}} y \phi F A \cdot T_{\mathrm{s}} \cdot \exp\left(-\frac{z-d}{\lambda_{E_{\mathrm{s}},\mathrm{s}} \cos\theta}\right) \cdot \exp\left(-\frac{d}{\lambda_{E_{\mathrm{s}},\mathrm{ad}} \cos\theta}\right) \mathrm{d}z \\ &= k_{\mathrm{s}} \cdot \lambda_{E_{\mathrm{s}},\mathrm{s}} \cos\theta \cdot \exp\left(-\frac{d}{\lambda_{E_{\mathrm{s}},\mathrm{ad}} \cos\theta}\right) \\ &= I_{\mathrm{s},\infty} \exp\left(-\frac{d}{\lambda_{E_{\mathrm{s}},\mathrm{ad}} \cos\theta}\right) \end{aligned} \tag{1.5}$$

For an XPS line of the adsorbed layer, the total intensity is the integral from 0 to its thickness *d*. which writes:

$$\begin{aligned} I_{\mathrm{ad}} &= \int_{0}^{d} n_{\mathrm{ad}} \sigma_{\mathrm{ad}} y \phi F A \cdot T_{\mathrm{ad}} \cdot \exp\left(-\frac{z}{\lambda_{E_{\mathrm{ad}},\mathrm{ad}} \cos\theta}\right) \mathrm{d}z \\ &= k_{\mathrm{ad}} \cdot \lambda_{E_{\mathrm{ad}},\mathrm{ad}} \cos\theta \cdot \left(1 - \exp\left(-\frac{d}{\lambda_{E_{\mathrm{ad}},\mathrm{ad}} \cos\theta}\right)\right) \\ &= I_{\mathrm{ad},\infty} \left(1 - \exp\left(-\frac{d}{\lambda_{E_{\mathrm{ad}},\mathrm{ad}} \cos\theta}\right)\right) \end{aligned} \tag{1.6}$$

The explicit expression of d is not available as a function of I_{ad} from Equation 1.6. In addition, the instrumental parameters such as transmission function T are sometimes not known in reality. However, some transformation is still possible in order to get the closest estimation of d. If I_{ad} and I_{s} are compared, y, ϕ, F and A are cancelled out, the fraction is expressed as:

$$\frac{I_{\mathrm{ad}}}{I_{\mathrm{s}}}=\frac{n_{\mathrm{ad}}\sigma_{\mathrm{ad}}T_{\mathrm{ad}}\cdot\lambda_{E_{\mathrm{ad}},\mathrm{ad}}\cos\theta\cdot\left(1-\exp\left(-\frac{d}{\lambda_{E_{\mathrm{ad}},\mathrm{ad}}\cos\theta}\right)\right)}{n_{\mathrm{s}}\sigma_{\mathrm{s}}T_{\mathrm{s}}\cdot\lambda_{E_{\mathrm{s}},\mathrm{s}}\cos\theta\cdot\exp\left(-\frac{d}{\lambda_{E_{\mathrm{s}},\mathrm{ad}}\cos\theta}\right)}
=\frac{I_{\mathrm{ad},\infty}\left(1-\exp\left(-\frac{d}{\lambda_{E_{\mathrm{ad}},\mathrm{ad}}\cos\theta}\right)\right)}{I_{\mathrm{s},\infty}\exp\left(-\frac{d}{\lambda_{E_{\mathrm{s}},\mathrm{ad}}\cos\theta}\right)} \tag{1.7}$$

All the material properties and experimental condition related parameters in Equation 1.7 can be combined in a calibration factor K:

$$K=\frac{k_{\mathrm{ad}}}{k_{\mathrm{s}}}=\frac{n_{\mathrm{ad}}\sigma_{\mathrm{ad}}T_{\mathrm{ad}}\cdot\lambda_{E_{\mathrm{ad}},\mathrm{ad}}}{n_{\mathrm{s}}\sigma_{\mathrm{s}}T_{\mathrm{s}}\cdot\lambda_{E_{\mathrm{s}},\mathrm{s}}} \tag{1.8}$$

In Equation 1.8, the atomic density n can be obtained from crystallographic or other morphology data of the substances; cross sections σ and IMFPs λ can be found in databases or calculated by such as the semi-empirical methods proposed by Wagner, C. D., et al. [56]; the transmission function T over a wide range of kinetic energy can either be measured for the specific spectrometer or simulated by calculations. With this definition of K, the entire fraction is now simplified as:

$$\frac{I_{\mathrm{ad}}}{I_{\mathrm{s}}}=K\cdot\frac{1-\exp\left(-\frac{d}{\lambda_{E_{\mathrm{ad}},\mathrm{ad}}\cos\theta}\right)}{\exp\left(-\frac{d}{\lambda_{E_{\mathrm{s}},\mathrm{ad}}\cos\theta}\right)} \tag{1.9}$$

If specific XPS lines of adsorbate and substrate are obtained, the value for d can be assessed by the fraction Equation 1.9 using numerical methods.

Now we go one step further by putting another homogenous layer on top of the adsorbed layer and denote them ad$_1$ and ad$_2$ from the surface to bulk, the photoemission model then becomes as shown in Figure 1.7:

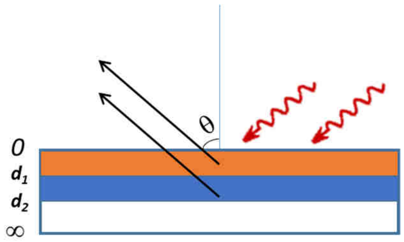

Figure 1.7: Model of photoemission from 2 adsorbed thin layers. 0 denotes the surface of the material; d_1 is the thickness of the top most adsorbed thin layer and the depth of the interface between the first and the second absorbed layer; d_2 is the depth of the interface between the second layer and substrate; ∞ represent a point deep in the bulk which can be treated as sitting at infinite depth. θ is the photoelectrons' take-off angle from the surface.

Similarly, the total intensity of an XPS signal from the $\mathrm{ad_1}$ layer is

$$\begin{aligned} I_{\mathrm{ad}_1} &= \int_0^{d_1} n_{\mathrm{ad}_1}\sigma_{\mathrm{ad}_1} y\phi FA\cdot T_{\mathrm{ad}_1}\cdot\exp\left(-\frac{z}{\lambda_{E_{\mathrm{ad}_1},\mathrm{ad}_1}\cos\theta}\right)\mathrm{d}z \\ &= k_{\mathrm{ad}_1}\cdot\lambda_{\mathrm{ad}_1}\cos\theta\cdot\left(1-\exp\left(-\frac{d_1}{\lambda_{E_{\mathrm{ad}_1},\mathrm{ad}_1}\cos\theta}\right)\right) \end{aligned} \tag{1.10}$$

While for the buried layer $\mathrm{ad_2}$, its thickness equals $d_2 - d_1$, the integral goes from d_1 to d_2, not to ∞, this changes the result as follows:

$$\begin{aligned} I_{\mathrm{ad}_2} &= \int_{d_1}^{d_2} n_{\mathrm{ad}_2}\sigma_{\mathrm{ad}_2} y\phi FA\cdot T_{\mathrm{ad}_2}\cdot\exp\left(-\frac{z-d_1}{\lambda_{E_{\mathrm{ad}_2},\mathrm{ad}_2}\cos\theta}\right)\cdot\exp\left(-\frac{d_1}{\lambda_{E_{\mathrm{ad}_2},\mathrm{ad}_1}\cos\theta}\right)\mathrm{d}z \\ &= k_{\mathrm{ad}_2}\cdot\lambda_{\mathrm{ad}_2}\cos\theta\cdot\exp\left(-\frac{d_1}{\lambda_{E_{\mathrm{ad}_2},\mathrm{ad}_1}\cos\theta}\right)\left(1-\exp\left(\frac{d_1-d_2}{\lambda_{E_{\mathrm{ad}_2},\mathrm{ad}_2}\cos\theta}\right)\right) \end{aligned} \tag{1.11}$$

Again, if the two intensities are compared, the intensity ratio is given as below. It is worth noticing that $\lambda_{E_{\mathrm{ad1}},\mathrm{ad}_1}$ and $\lambda_{E_{\mathrm{ad2}},\mathrm{ad}_1}$ should not be confused with each other.

$$\frac{I_{\mathrm{ad}_1}}{I_{\mathrm{ad}_2}} = K\cdot\frac{1-\exp\left(-\frac{d_1}{\lambda_{E_{\mathrm{ad}_1},\mathrm{ad}_1}\cos\theta}\right)}{\exp\left(-\frac{d_1}{\lambda_{E_{\mathrm{ad}_2},\mathrm{ad}_1}\cos\theta}\right)\left(1-\exp\left(\frac{d_1-d_2}{\lambda_{E_{\mathrm{ad}_2},\mathrm{ad}_2}\cos\theta}\right)\right)} \tag{1.12}$$

The Equation 1.12 shows that the thickness d_1 could be assessed if the thickness of the buried layer ($d_2 - d_1$) is already known. Practically, this is possible if the buried layer is first adsorbed onto the substrate, its thickness can be determined in advance with the signal from substrate through Equation 1.9, there it acts as the top most layer and its signal is only attenuated by the layer itself.

In many real circumstances, an interface layer is formed between the topmost layer and the buried layer, for example by a reactive interaction of deposited metals and with organic substrates. Due to the diffusion of the metal into the organic phase, the concentration of the metal atoms in the organic phase is not constant, but has a gradient. However, in order to quantify the diffusion and reaction of metal atoms, an assumed homogenous layer, in which all the possible reactive sites of the buried phase have been chemically transformed by metal atoms, is considered to be atop the pristine organic phase with no presence of metal atoms. In this model, the homogenous layer assumption is again applicable. The thickness of this assumed layer is referred to as the average reaction depth (ARD). To determine the ARD, it should be first noted that the system now has 3 adsorbed overlayers on the substrate (Figure 1.8). From surface to substrate, the latest (topmost) adsorbed adatom layer, the assumed fully reacted layer and the pristine layer stand one over the other. Photoelectrons from the reacted layer and the pristine layer are both attenuated by the topmost layer. According to the Lambert-Beer law as expressed by Equation 1.3, one extra layer of attenuating material has an impact of an exponential component to the total intensity. If the photoelectrons of the same subshell (the same XPS line as $1s$, $2p$, $3d$ etc. of an element) are chosen in the analysis for both reacted and pristine species, meanwhile the binding energy shift of the reacted and pristine signals is small enough to be neglected, the kinetic energy related parameters σ, T could all be treated as identical before and after the reaction between adatoms and pre-deposited organic molecules. The change to the attenuation caused by the topmost layer and diffused atoms into the subsurface layer are equal to the signals of pristine and reacted species. The effect on λ is therefore canceled in the fraction. In addition, all the effects of the topmost layer on the two layers beneath it can also be regarded as equal and thus omitted during the analysis.

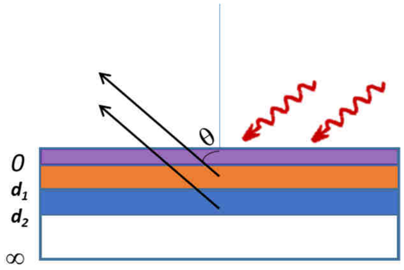

Figure 1.8: Model of a three overlayer photoemission system with an interlayer formed by reaction. from top to bottom: layer of reactive and diffusive atoms, fully reacted layer and pristine layer, inert substrate. Here 0 does not stand at the surface but at the boundary of the interlayer formed by reaction.

The assessment of the average reaction depth should be categorized into two situations. In the first situation, the thickness of the buried phase is large enough to be treated as an infinite substrate to the overlayers. Equation 1.9 is applicable in this case:

$$\frac{I_r}{I_p} = K \cdot \frac{1-\exp\left(-\frac{d_r}{\lambda_{E_r,r}\cos\theta}\right)}{\exp\left(-\frac{d_r}{\lambda_{E_p,r}\cos\theta}\right)}$$

$$K = \frac{n_r \sigma_r T_r \cdot \lambda_{E_r,r}}{n_p \sigma_p T_p \cdot \lambda_{E_p,p}} \tag{1.13}$$

The subscripts *r* and *p* here denote fully reacted layer and pristine layer, respectively. As has been reported in the literature,[35, 37, 46] for some systems the atomic density *n* of a certain species can be regarded as equal before and after the reaction. If additionally the same XPS line is chosen before and after the reaction, *K* can now be approximated by 1. Equation 1.13 is then simplified to:

$$\frac{I_\mathrm{r}}{I_\mathrm{p}} \approx \frac{1-\exp\left(-\frac{d_\mathrm{r}}{\lambda\cos\theta}\right)}{\exp\left(-\frac{d_\mathrm{r}}{\lambda\cos\theta}\right)} \tag{1.14}$$

After rearrangement, the following Equation is obtained:

$$d_\mathrm{r} = \lambda\cos\theta\ln\left[\left(\frac{I_\mathrm{r}}{I_\mathrm{p}}\right)+1\right] \tag{1.15}$$

In the second situation, the thickness of the buried pristine phase is not so large as to be treated as bulk-like substrate. This is often true in XPS studies if the buried phase is a thin film itself deposited onto another (then typically infinite) substrate. An example would be an organic compound, for which the thickness is restricted purposely to avoid charging effect due to the limited conductivity. Consequently, the Equation 1.12 should be used in this situation, which writes:

$$\frac{I_\mathrm{r}}{I_\mathrm{p}} = K \cdot \frac{1-\exp\left(-\frac{d_\mathrm{r}}{\lambda_{E_\mathrm{r},\mathrm{r}}\cos\theta}\right)}{\exp\left(-\frac{d_\mathrm{r}}{\lambda_{E_\mathrm{p},\mathrm{r}}\cos\theta}\right)\left(1-\exp\left(\frac{d_\mathrm{r}-d_\mathrm{p}}{\lambda_{E_\mathrm{p},\mathrm{p}}\cos\theta}\right)\right)} \tag{1.16}$$

It is still valid to assume that *n*, *σ*, *T* and *λ* are identical for the signals of reacted and unreacted species. Equation 1.16 is then simplified as:

$$\frac{I_\mathrm{r}}{I_\mathrm{p}} = \frac{1-\exp\left(-\frac{d_\mathrm{r}}{\lambda\cos\theta}\right)}{\exp\left(-\frac{d_\mathrm{r}}{\lambda\cos\theta}\right)\left(1-\exp\left(\frac{d_\mathrm{r}-d_\mathrm{p}}{\lambda\cos\theta}\right)\right)} \tag{1.17}$$

Furthermore, if the morphology of the previously pristine layer has not been changed prominently by the diffusion and reaction of the top layer's atoms, it is also valid to assume d_p is unchanged as what is predetermined by Equation 1.9 before the deposition of the topmost layer. The average reaction depth d_r can now be calculated by Equation 1.17.

For measurements of normal emission, the average reaction depth d_r is simplified and rearranged as:

$$\begin{aligned} d_\mathrm{r} &= \lambda \ln\left(\frac{R+1}{1+R\cdot\exp\left(\frac{-d_\mathrm{p}}{\lambda}\right)}\right) \\ R &= \frac{I_\mathrm{r}}{I_\mathrm{p}} \end{aligned} \tag{1.18}$$

1.3 Adsorption Calorimetry

In calorimetry, energy is measured in the form of heat, which can result from chemical reactions, phase transitions, or other processes. In the field of surface science, calorimetry usually focuses on the heat released by the adsorption of atoms/molecules on the surface or on surface reactions between different adsorbed chemical species. It provides direct characterization to the energetics of adsorptions, which has an important role in heterogeneous catalysis. The strength of interaction between the intermediate and the surface of the catalyst strongly influences the efficiency of the catalyst, that is, only sufficiently high adsorption energy leads to effective and sustainable catalytic cycles. Yet too high adsorption energy means the poisoning of the catalyst by the adsorbates. High-quality assessment of adsorption energies also provide valuable benchmark to the theoretical methods, i.e., density functional theory (DFT). Such benchmarks are important because DFT-based methods often struggle with the correct calculation of van der Waals contributions to the adsorbate-substrate interaction, especially in the weak bond dominated adsorption systems of large organic molecules or biomolecules.[57]

1.3.1 Enthalpy of Adsorption

Under UHV condition, the adsorptive, i.e., the vapor of atoms or molecules, is treated as an ideal gas. The procedure of adsorption is a transition from the gaseous state to the condensed state on the surface. The state function of enthalpy for both states can be given as:

$$
\begin{aligned}
H_{\text{gas}} &= U_{\text{gas}} + p_{\text{gas}} \cdot V_{\text{gas}} = U_{\text{gas}} + n \cdot R \cdot T \\
H_{\text{ads}} &= U_{\text{ads}} + [\![p_{\text{ads}} \cdot V_{\text{ads}}]\!]_{\approx 0}
\end{aligned}
\tag{1.19}
$$

Where H_{gas} is the enthalpy of the gaseous adsorptives, U_{gas} the internal energy, p_{gas} the pressure, V_{gas} the volume they occupy, n the amount of matters in moles; H_{ads}, U_{ads}, p_{ads}, V_{ads} denote the corresponding the variables in the adsorbed state. Because the volume of the adsorbate on the surface is negligibly small, $p_{\text{ads}} \cdot V_{\text{ads}}$ is then omitted. Consider as well that during the procedure of adsorption, the amount of adsorptives does not change, n_{gas} is equivalent to n_{ads}, ΔH_{ads} is now given as:

$$
\begin{aligned}
\Delta H_{\text{ads}} &= H_{\text{ads}} - H_{\text{gas}} = U_{\text{ads}} - U_{\text{gas}} - n_{\text{ads}} \cdot \mathrm{R} \cdot T \\
&= \Delta U_{\text{ads}} - n_{\text{ads}} \cdot \mathrm{R} \cdot T
\end{aligned}
\tag{1.20}
$$

ΔH_{ads} is defined to have the negative value of heat of adsorption, Q_{ads}. This correlation stems from the perspective of view over the system under investigation. Heat is conventionally regarded as the absolute change of the energy, while ΔH_{ads}, from the perspective of the system that underwent change, is negative because adsorption is an exothermic process. ΔH_{ads} may be influenced by various effects, including the energy of the surface bond, degree of freedom change of the adsorptive (atoms/molecules), interaction between the single units of the adsorbate, surface relaxation or rearrangement and perturbation of the electronic structure of the adsorbate. The latter may be used to distinguish physisorption from chemisorption. The ΔH_{ads} of physisorption stands at a few to tens of kJ/mol (very much depending on the size of a molecule),[58-60] while the ΔH_{ads} of chemisorption is usually up to hundreds of kJ/mol.[61-63] In a system forming buried interface, i.e., the adsorption of metal on organic molecules, ΔH_{ads} obtained by measurement may well contained the information of the on surface reaction between metal atoms and organic molecules.[32-33, 35, 37]

In an adsorption calorimetry experiment, U_{ads} is obtained through the measurement of Q_{cal}. Therefore, adsorption calorimetry provides a fairly straightforward method for the assessment of ΔH_{ads}. However, calorimetry is not the only thermodynamic method to characterize the energetics of adsorption at solid-gas interfaces. Other approaches in fact emerged earlier in the modern history of thermodynamics researches. For instance, at constant coverage, adsorption energy could be derived through Clausius-Clapeyron equation by observing the change of the equilibrium pressure with temperature. The strength of the adsorbate-surface bond can also be obtained through a kinetic approach known as temperature-programmed desorption (TPD). Both of the latter methods require that the adsorbate can desorb intact, which limits their applicability and leaves calorimetry as the only universal approach.

1.3.2 Kinetics of Desorption

Temperature-programmed desorption (TPD) or thermal desorption spectroscopy (TDS) measures the kinetics of desorption. First Introduced by I. Langmuir in 1916, this technique enables the correlation of desorption activation energies (E_{des}) to entropies and enthalpy of adsorption. In a modern TPD experiment, the predefined surface with a certain adsorbate coverage θ at temperature T is heated with a constant rate $\mathrm{d}T/\mathrm{d}t$, until the complete desorption of adsorbate. The temperature and coverage dependent desorption rate $\mathrm{r}(\theta, T)$ is typically determined by the transient change of the partial pressure of the studied substance in a quadrupole mass spectrometer (QMS). The desorption activation energy E_{des} is correlated with $\mathrm{r}(\theta, T)$ by Arrhenius style kinetic equation, which gives:

$$\begin{aligned} r(\theta,T) &= -\frac{d\theta(T)}{dt} \\ &= -\frac{d\theta(T)}{dT}\frac{dT}{dt} \\ &= \frac{v_n(\theta)}{\beta}\cdot(\theta(T))^n\cdot\exp\left(-\frac{E_{\text{des}}}{\mathrm{R}T}\right) \end{aligned} \tag{1.21}$$

Where β is the constant heat rate $\mathrm{d}T/\mathrm{d}t$, $\theta(T)$ is the temperature dependent coverage, t denotes the time, $v(\theta)_n$ the frequency factor of desorption, n the desorption order. Equation 1.21 is often referred to as Polanyi-Wigner equation.

In general, the desorption order n and the frequency factor $v(\theta)_n$ are unknown to a given system, and the latter are usually dependent on coverage. Yet several experimental methods were developed to work around the dependence on n and $v(\theta)_n$. Frequently used methods are "Redhead Analysis",[64] "Leading Edge Analysis",[65] "Complete Analysis".[66] With the help of theoretical methods, $v(\theta)_n$ may now be assessed independent of the TPD measurement itself.

It should be noted that TPD is founded fully on the reversible adsorption in which the complete desorption of the intact atoms/molecules will occur at higher temperature. Therefore, TPD is not suitable to study systems comprising dissociation of molecules, subsurface diffusion or irreversible chemical reaction with substrate or co-adsorbates (but note that such measurements can be useful in the form of temperature-programmed reaction spectroscopy (TPRS) to study reactive adsorbates). Meanwhile, the assessment of adsorption energy (E_{ads}) by the desorption activation energy is still difficult, since $E_{\text{des}} = -(E_{\text{act-ads}} + E_{\text{ads}})$. $E_{\text{act-ads}}$ here denotes the adsorption activation energy, which is usually difficult to measure.

The E_{des} will only approximate to the negative of E_{ads} when the activation barrier of adsorption is negligible.

1.3.3 Equilibria of Adsorption-Desorption

The isosteric heat of adsorption q_{st} at constant coverage θ is correlated to the temperature T and equilibrium pressure p via the Clausius-Clapeyron equation:

$$q_{\mathrm{st}} = -\mathrm{R}\left(\frac{d\ln(p)}{d(1/T)}\right)_{\theta} \tag{1.22}$$

This method requires the measurement of the equilibrium pressure of the adsorbate on the surface so as to obtain the change of the equilibrium pressure with T, which can be experimentally difficult. Another limitation is that, analogous to TPD measurements, this method also requires fully reversible adsorption of adsorbates. Otherwise no equilibrium of adsorption-desorption is established.

1.3.4 Direct Measurement of Heat of Adsorption

The term “heat of adsorption” is often used synonymously with “enthalpy of adsorption”. However, the measured heat Q_{cal} is conventionally regarded as the absolute change of the energy in a procedure, while the enthalpy of adsorption (ΔH_{ads}), from the perspective of the system that undergoes change, is negative because the adsorption is an exothermic process. This makes Q_{cal} correlated to $-\Delta H_{\mathrm{ads}}$.

When surface calorimetry is carried out in UHV-conditioned apparatus with constant volume, the entire system could be regarded as isochoric. The heat measured by calorimetry Q_{cal} equals the change to the internal energy of the sample (ΔU_{sam}). ΔU_{sam}, which consists of two components, represents two possibilities during the adsorption, the adsorption of adsorptive $\Delta U_{\downarrow}$, and the reflection of adsorptive $\Delta U_{\downarrow\uparrow}$,

$$Q_{\mathrm{cal}} = \Delta U_{sam} = \Delta U_{\downarrow} + \Delta U_{\downarrow\uparrow} \tag{1.23}$$

For the calorimeters employing pulsed atomic/molecular beam as the source of adsorptive. $\Delta U_{\downarrow}$ is comprised of three components: (a) the actual adsorption energy ΔU_{ads}, it is the internal energy change of the gas-surface system during the adsorption of the gas, assuming that the gas arriving at the surface has the temperature of sample (T_{sam}); (b) the energy difference between a gas flux and a gas volume at the translational temperature of the beam source with T_{bs}. Taking into account that the adsorbates is dosed with pulsed beam of evaporants but not from gas phase,[67] this component should have the form of $1/2\mathrm{R}T_{bs}$; (c) The correction of the temperature difference between T_{bs} and T_{sam}. Here the molar isochoric heat capacity of the gas (C_{v}) should be considered. $\Delta U_{\downarrow}$ is now expressed as:

$$\Delta U_{\downarrow} = -\Delta U_{\mathrm{ads}} + n_{\mathrm{ads}}\left(\frac{1}{2}\mathrm{R}\cdot T_{\mathrm{bs}} - \int_{T_{\mathrm{bs}}}^{T_{\mathrm{sam}}} C_{\mathrm{v}}^{\mathrm{g}} dT\right) \tag{1.24}$$

Where n_{ads} is the amount of adsorbed gas. It should be noted that ΔU_{ads} is with a negative sign in Equation 1.24, because the adsorption is an exothermic process, the heat is released by the gas-surface system into the adjacency, and is collected by the sample to proceed with measurement. Therefore, $\Delta U_{\text{ads}} < 0$, while $\Delta U_{\downarrow} > 0$.

Accordingly, if all reflected adsorptives adopt the sample temperature T_{sam}, the contribution of reflected adsorptive, $\Delta U_{\downarrow\uparrow}$ is expressed as:

$$\Delta U_{\downarrow\uparrow} = -n_{\text{refl}} \left(\int_{T_{\text{bs}}}^{T_{\text{sam}}} (C_{\text{v}}^{\text{g}} + \frac{1}{2}\text{R})\, dT \right) \tag{1.25}$$

with n_{refl} as the amount of reflected adsorptives. Here the term 1/2R accounts for the kinetic energy difference between the flux of adsorptives and the corresponding volume of adsorptives at rest.[7, 67]

According to Equation 1.20, ΔH_{ads}, at sample temperature T_{sam} now writes:

$$\Delta H_{\text{ads}} = \Delta U_{\text{ads}} - n_{\text{ads}} \cdot \text{R} \cdot T_{\text{sam}} \tag{1.26}$$

combining the Equations 1.23-1.25, ΔH_{ads} is expressed as:

$$-\Delta H_{\text{ads}} = Q_{\text{cal}} - K_{\text{ads}} - K_{\text{refl}} \tag{1.27}$$

which includes two temperature dependent corrections, K_{ads} and K_{refl}, which write as follows:

$$K_{\text{ads}} = n_{\text{ads}} \left(-\int_{T_{\text{bs}}}^{T_{\text{sam}}} C_{\text{v}}^{\text{g}} dT + \frac{1}{2}\text{R}T_{\text{bs}} - \text{R}T_{\text{sam}} \right) \tag{1.28}$$

$$K_{\text{refl}} = -n_{\text{refl}} \int_{T_{\text{bs}}}^{T_{\text{sam}}} C_{\text{v}}^{\text{g}} + \frac{1}{2}\text{R}dT \tag{1.29}$$

The differential adsorption enthalpy, Δh_{ads}, is expressed as:

$$-\Delta h_{\text{ads}} \equiv \frac{-\Delta H_{\text{ads}}}{n_{\text{ads}}} = \frac{1}{n_{\text{ads}}} (Q_{\text{cal}} - K_{\text{ads}} - K_{\text{refl}}) \tag{1.30}$$

-Δh_{ads} represents the molar heat of adsorption at the constant coverage. The comparison of it with standard enthalpy from literature requires conversion to standard temperature.

The integration of -Δh_{ads} over the coverage θ gives the integral heat of adsorption -$\Delta H_{\text{ads,int}}$, which is the molar heat that is released when the clean surface is covered by the adsorbate as the coverage increases up to θ'.

$$-\Delta H_{\text{ads,int}} = -\int_{0}^{\theta'} \Delta h_{\text{ads}} d\theta \tag{1.31}$$

As can be seen from the theoretical concepts presented above, adsorption calorimetry does not require reversible adsorption system or establishment of equilibrium. Especially to those systems with dissociative adsorptions or irreversible reactions with substrate, adsorption calorimetry is in fact the only method to provide the energetic information during adsorption. In addition, adsorption calorimetric measurement also does not require any pre-existing model or theoretical framework to accurately measure the heat of adsorption. Hence the adsorption calorimetry is capable of independent investigation on the adsorption systems at a specifically desired temperature.

1.3.5 Calorimeters

The development of adsorption calorimeters for well-defined surfaces (especially single crystal surfaces) is a history of improvements on the sensitivity to very small temperature changes. Because the adsorption heat is transformed into temperature change in the sample and calorimetric detector, better sensitivity to this local temperature change leads to better precision and resolution (with respect to coverage steps) of microscopic processes during adsorption.

As early as 1934, adsorption energetics of small molecules such as H_2, N_2 and O_2 were studied by J.K. Roberts using wires of refractory metals. Adsorption-induced temperature change were observed as the change to the resistance of wires.[68] P. Kisliuk later used metal ribbons instead of wires to achieve higher surface to volume ratio, thus improved the sensitivity by reducing the heat capacity per unit surface area.[69] However, due to the intrinsic properties of the polycrystalline ribbon/wire, the adsorption sites on polycrystalline metal samples were not well defined. It consequently resulted in problems of reproducibility in the results.

Adsorption calorimetry using physical vapor deposition of metal thin films was pursued by Beeck, Wedler and others.[70] O. Beeck's calorimeter consisted of a thin-walled glass cell housing evaporation wire and thin film for adsorption, with resistance thermometer attached to the outside of the cell. The core setup is mounted in a larger glass jacket for evacuation and thermostat control by cold bath of the outer glass jacket.[71] This technique was later improved by Wedler and some other groups.[70] A Wedler's calorimeter (Figure 1.9 has refined shape and feedthrough arrangement so that the entire apparatus could be submerged into cold bath to achieve better thermostat. Another improvement was the induction free twisted wiring of tungsten wires as resistance thermometer. In an experiment with the Wedler style calorimeter, a metal thin film is first deposited inside the evacuated bulb. The gas is then introduced in small pulses, while the adsorption-induced temperature changes of the glass bulb are monitored by the thermometer. With less than 1J/K heat capacity, the temperature sensitivity of this calorimeter could reach as high as 1μK or 10nJ/cm^2.[72] The resistance thermometer is also used as an electrical Joule heater to produce a precisely defined amount of heat for calibration. Adsorption of various gases, i.e., H_2, CO, CO_2 and H_2O, on transition metals such as iron, nickel and titanium were studied using this type of calorimeter.[70] Despite the improvement in sensitivity, the Wedler style calorimeter still suffers similar disadvantages as the wire/ribbon calorimeter because of the polycrystalline nature of the metal thin films and their morphological dependence on the deposition parameters. In addition, since the metal film was deposited inside the glass housing, further structural and chemical characterization of its surface is even more impractical if compared with wire/ribbon calorimeters

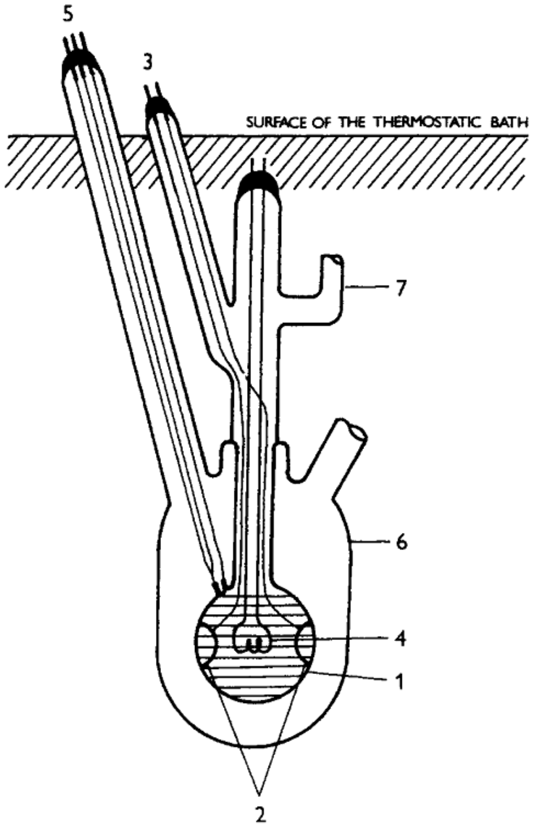

Figure 1.9: Schematic illustration of Wedler calorimeter (from[70]). (1) thin-walled glass bulb with coiled resistance thermometer; (2) platinum contact foils; (3) feedthrough of the contact foils; (4) evaporation wire; (5) feedthrough of the resistance thermometer; (6) outer glass jacket; (7) connection for evacuation.

In the UHV era of surface science, adsorption calorimetry is also incorporated to be operational with standardized UHV compatible components. This enables the construction of multifunctional instruments combining calorimetry with other contemporary surface science techniques for intensive study of surface/interface and surface processes. Černý introduced pyroelectric detector to calorimetry by employing a single-crystalline $LiTaO_3$ as the detector for very small temperature changes.[73-75] The substrate for the adsorption of molecules is a directly deposited metal thin film on a $LiTaO_3$ wafer. The molecular beam is chopped into short pulses because a pyroelectric detector is sensitive to temperature change rather than absolute temperature. The calibration is carried out by a laser beam taking exactly the same path as the molecular beam to deposit precisely known amount of heat. Since the molecular beam is pulsed for the measurement of instant temperature change before the heat is dissipated to the supporting part of the system (mostly metal parts) and the system is under constant pumping to maintain UHV condition, it is now critical to know the sticking probability of each pulse on the sample for the amount of molecules adsorbed. The King-Wells technique is employed for such purpose using a glass flag and a mass spectrometer.[76-77] The glass flag was placed in front of the sample to reflect all the flux before reaching the sample for detection by a mass spectrometer. The sticking probability on the sample was determined by subtraction of the mass spectrometer signal during the actual adsorption experiment from those obtained during non-sticking measurement with the glass flag in place. Adsorption of H_2, CO, O_2 and light hydrocarbons on lanthanides were studied by

Černý's group. The major drawbacks of this calorimeter remains the polycrystalline nature of the metal film.

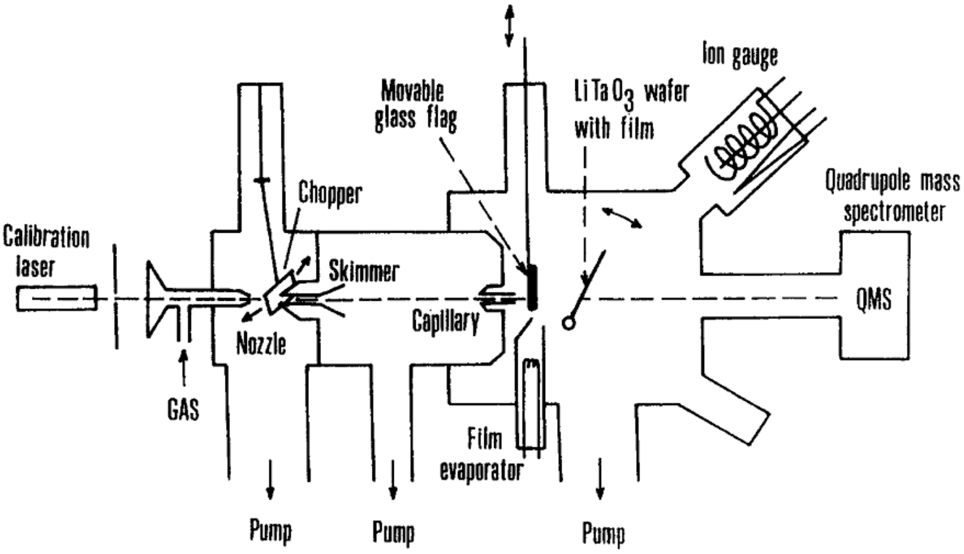

Figure 1.10: Schematic illustration of Černý calorimeter (from[70]) for polycrystalline film with pyroelectric temperature sensor, pulsed molecular beam and laser calibration.

The first attempt of adsorption calorimetry on well-defined single crystal surfaces was carried out in 1984 by Kyser and Masel.[78] Their calorimeter is equipped with a Pt(111) single crystal of 10 mm in diameter and approximately 1 mm thick. Two thermistor were mounted on quartz capillaries inside the holes drilled through the crystal (Figure 1.11 b). One thermistor acted as the detector for adsorption-induced temperature change with sensitivity in the 10^{-5} K range, while the other was used as the source of heat for calibration. The crystal is mounted in a water bath immersed UHV chamber also equipped with Auger electron spectroscopy (AES) for the check of crystal cleanliness and adsorbate coverage determination (Figure 1.11 a). The cleaning of the single crystal, which required heating in an oxygen atmosphere, usually brought about hours of thermal re-equilibration time of crystal before the next experiment could be started. This is because the typical temperature change induced by adsorption is only about 0.1-0.2 μK due to the very large heat capacity of the crystal, the thermal equilibrium is utterly important for the accuracy of the measurement. During the time of re-equilibration, the sample would typically accumulate 0.5 monolayers of CO, making it impossible to conduct adsorption of any other substances at high coverage. Another problem of thermal treatment for cleaning arise with its irreversible changes to the thermistor, the detector, which, as a consequence, had to be recalibrated for every single experiment.

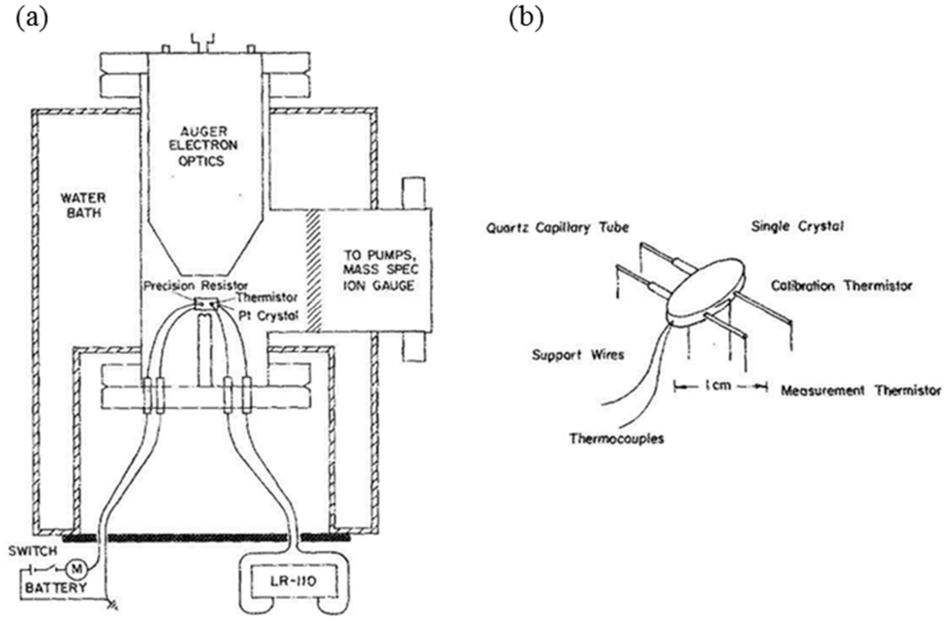

Figure 1.11: Schematic illustration of Kyser and Masel calorimeter for adsorption calorimetry on single crystal.[78] (a): Simplified assembly of the calorimeter. (b): Setup of the detector.

A major breakthrough of the adsorption calorimetry on single crystal surface was achieved by D. A. King's group in early 1990s. As can be seen with Kyser's calorimeter, the reduction of the heat capacity of the single crystal is crucial to enhance the total sensitivity of detection. King's calorimeter is equipped with single crystals of 0.2 μm thickness and approximately 1 cm^2 in surface area. The heat capacity of such sample is in order of 10^{-6} J/K.[79-82] Single crystals of these dimensions were prepared by epitaxial growth on water soluble single-crystalline substrates. The choice of substrate with specific lattice constant would result in the growth of thin film metal single crystal with desired orientation. The substrate, i.e., NaCl, is water dissolved afterwards.[83] With the application of such ultra-thin single crystal, even submonolayer adsorption of molecules could lead to temperature changes of up to 1 K, its temperature change by coverage increment of 1% monolayer amounted typically to 0.01-0.1 K.[82]

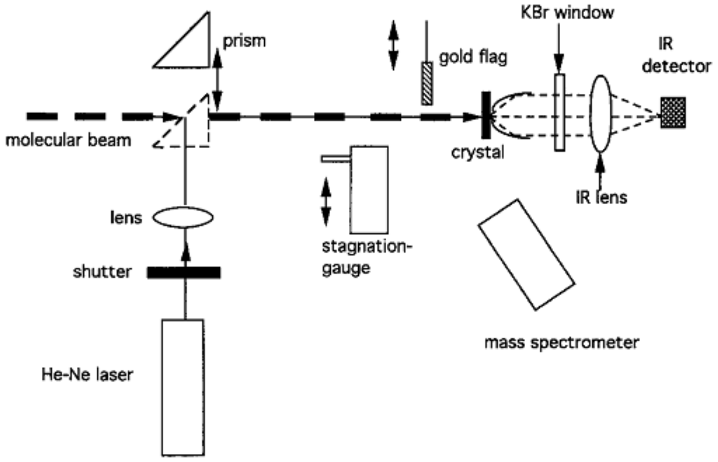

Figure 1.12: Schematic illustration of King's calorimeter for adsorption calorimetry on single crystal.[81]

Another unique characteristic of King's calorimeter is the technique for the detection of temperature changes. The intensity change of the emitted infrared radiation resulting from the adsorption-induced temperature change was detected by a broadband photoconductive mercury-cadmium-telluride (MCT) infrared unit outside the UHV chamber. The backside of the sample is covered with a thin layer of vapor deposited carbon to enhance its emissivity. Low energy electron diffraction (LEED) and AES were also equipped for surface characterization and confirmation of sample cleanliness before the experiment. Gas was dosed by a 3 stage supersonic molecular beam with a diameter of 2.09 mm. Pulsed flux, with a length of 50 ms and frequency of 0.5 s^{-1} was created by the operation of a piezoelectrical valve to maximize the temperature change of the sample. For calibration, a precisely known amount of heat was deposited with pulse laser through the same path as the molecular beam onto sample. However, the ultra-thin thickness of crystal make the precise measurement of the sample reflectivity a necessity. An alternative calibration method is to use processes with known heat of transition, for instance, the multilayer adsorption energy of the adsorbates. The flux and sticking probability of molecules in King's setup is determined via standalone measurements. First, the flux was determined with a stagnation gauge placed and throttling in front of the sample. The sticking probability was determined through an modified King-Wells method with similar concepts to Černý calorimeter.[70] The difference stands at the position of QMS relative to the sample. In King's setup, non-sticking part of the flux is directly reflected into QMS, resulting in faster and stronger response to each pulse of the molecular beam.

The major limitation of King's calorimeter is its confined temperature of application. The intensity of infrared radiation depends on the absolute temperature of sample and will reduce strongly as the decrease of temperature following the Stefan-Boltzmann law: $\Delta P_{\mathrm{rad}} \propto T^3 \cdot \Delta T$. This is a severe disadvantage, because low temperature adsorption processes (e.g., performed under cooling with liquid nitrogen), are highly favorable for the kinetic and mechanism studies of surface interactions. A solution of this problem was attempted by cold weldment of ultrathin metal single crystal to one face of a metal coated 0.3 mm thick $LiTaO_3$ wafer. Under such conditions, measurement in the temperature range of 90-410 K were carried out using the pyroelectricity of $LiTaO_3$.[80] However, permanent weldment with a $LiTaO_3$ wafer not only conflicted with the target of reducing the heat capacity of the sample, since it dragged the sensitivity down by one order of magnitude, but also encumbered the effective cleaning and annealing of the single crystal, because the suitable annealing temperature for metal single crystals may stand well above the Curie point of $LiTaO_3$, such high temperature would definitely destroy the pyroelectricity of $LiTaO_3$.

The problems mentioned above were properly resolved with the retractable pyroelectric contact detector devised by C.T. Campbell and co-workers.[84] The pioneering application of metal coated β-polyvinylidene fluoride (β-PVDF) thin film enabled the utilization of pyroelectricity while maintaining a low heat capacity of the detector. The polymer nature of PVDF also brought in design flexibility that enabled unconventional direct contact of ribbon detector with metal single crystal (Figure 1.13).[84-85] Since good thermal contact under UHV requires certain amount pressure when direct mechanical contact is used as the conduction of heat, it was necessary that the robustness of metal single crystal thin film should be increased as well. The thickness of the metal single crystal used by Campbell calorimeter were increased to 1 μm. The increase of heat capacity was counterbalanced by the high sensitivity of the PVDF together with direct contact between metal single crystal and ribbon. As small as μK temperature change was detected with this setup. A later revision to the design of detector employed 50 μm Kapton film as the supporting framework of PVDF to achieve even harder pressing onto the sample, single crystals of 100 μm in thickness were paired with such additional pressing detector.[86] Besides that, a polycrystal surface sample was also made applicable by directly using a metal coated PVDF film as sample. This was a concept similar to Černý's calorimeter, yet had much higher sensitivity because of low heat capacity, and simplicity of sample preparation.[32-33, 35, 37, 46]

Because the contact of the PVDF ribbon with the sample does not changes at low temperature, measurements below ambient temperature are possible with Campbell's design. In fact, as the thermal conductivity of metal increases with cooling. In addition to that, the enhancement of PVDF sensitivity caused by the increase of internal static dipole moment occurs when the temperature is below PVDF's glass transition point. Campbell's design is particularly suitable for low temperature measurement. The upper temperature limit for the detector stands at around 400 K, where the degradation of PVDF film starts to emerge. The pulsed beam, either supersonic for volatile small molecules or effusive for nonvolatile substances like metals, were created by continuous rotation of a metal plate with an orifice as opening, typical pulse length is 100 ms and the period of pulses is 2 s. The calibration is carried out with laser. Preciseness of sample reflectivity is also required as in King's setup. The flux of the beam is measured with a quartz crystal microbalance (QCM) positioned in front of the sample. Liquid nitrogen cooling of the QCM is employed to condense the volatile adsorptives. Similar to King's setup, modified King-Wells technique is used to determine the sticking probability of each pulse. One additional feature regarding sticking probability is the thermally heated hot plate for the complete reflection of non-volatile substances, e.g., Ca and Pb.[32-33, 35, 46]

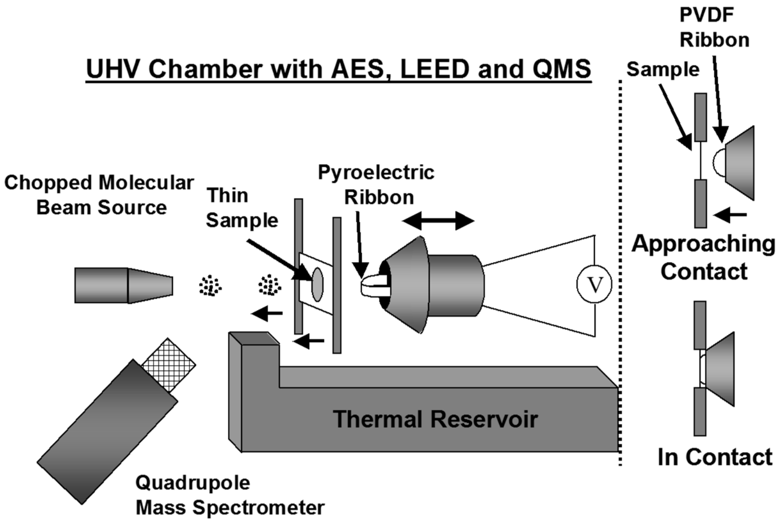

Figure 1.13: Schematic illustration of calorimeter with retractable, thin-film pyroelectric detector for back side direct attachment to thin film metal single crystal.[84]

In the experiments studying adsorption of metal atoms, because of the much elevated evaporator temperature required to produce sufficient flux, influences of thermal radiation from the evaporator weighed in as a pronounced component of the total heat deposited onto the sample.[32-33, 35, 37, 46, 63, 87] Therefore, an additional correction of radiation to the measured signal is needed. For this purpose, an IR-transmissive window (e.g., BaF_2) is placed in front of the sample to block the beam, yet let pass the radiation. After laser calibration of the transmission of the BaF_2 window, the pure contribution of radiation is obtained. However, this method relies on the assumption that the transmission of the evaporator's radiation is the same as that of the laser, regardless of their differences in wavelength. This is hardly true for the far-infrared region. Possible solutions include Au or Ag mirrors module that reflects radiation while blocking the molecular flux, or rotational velocity filters, which achieve separation of radiation and particle beam (atoms or molecules) by being only transmissive to the particle beam.[88]

Variants derived from Campbell calorimeter were developed by several other groups. Challenges facing Campbell's calorimeter were addressed using versatile techniques. For instance, Schäfer and coworkers focused on precise control of dosages by pulsed flux,[89-90] while Schauermann, Freund, and coworkers refined the laser calibration process with in-situ reflectivity measurement as well as isolation of vibration for the quenching of piezoelectric effect on signal.[91-92] For more detailed information, see the cited original publications and reviews on adsorption calorimetry.[57, 93]

2 Experimental

A brief introduction to the experimental setup used in this work is presented in this chapter. Instruments and facilities include beamlines and end stations at BESSY II as well as XPS and adsorption calorimeter at the Philipps Universität Marburg. All instruments used in this are UHV systems with base pressures in the 10^{-9} to 10^{-11} mbar range.

Organic thin films are prepared by thermal vapor deposition from a home built Knudsen cell evaporator. The cell is made of stainless steel (ANSI: 316L, DIN: 1.4404). The resistive heating of the evaporator is realized with direct current (DC) through the thin electrodes of the identical stainless steel welded onto the Knudsen cell. A K-type thermocouple is spot welded on the Knudsen cell as well to monitor the temperature during evaporation. Metal thin film are prepared by thermal vapor deposition from home built quartz Knudsen cell wrapped in a tantalum spiral. A K-type thermocouple is glued to the bottom of the quartz cell for temperature monitoring. Fluxes of evaporation are determined by QCM measurement. Cooling of the sample for desired adsorption/reaction temperature is carried out via liquid nitrogen flow.

2.1 X-ray Photoelectron Spectrometer

Conventional XPS measurements were carried out at the Philipps Universität Marburg with the instrumental setups shown in Figure 2.1. The three compartments UHV setup is comprised of a load lock/preparation chamber, a PES analysis chamber, and an STM analysis chamber. The base pressure in the chambers used for the experiments is below 2×10^{-10} mbar. PES chamber is equipped with a SPECS Phoibos 150 hemispherical electron energy analyzer using an MCD-9 detector. X-ray source is Al K-α ($h\nu = 1486.7$eV) monochromatized by a FOCUS 500 monochromator. The X-ray source is mounted on an extra manipulator for precise positioning and alignment. An as high as 0.5 eV overall resolution of energy could be reached by these setups. The PES chamber is also equipped with a gas discharge lamp for UPS measurements and a three-grid low-energy electron diffraction (LEED) optics (SPECS ErLEED-1000A) The investigations discussed in Chapter 3 are partially conducted on this apparatus using polycrystalline gold plates as substrate.

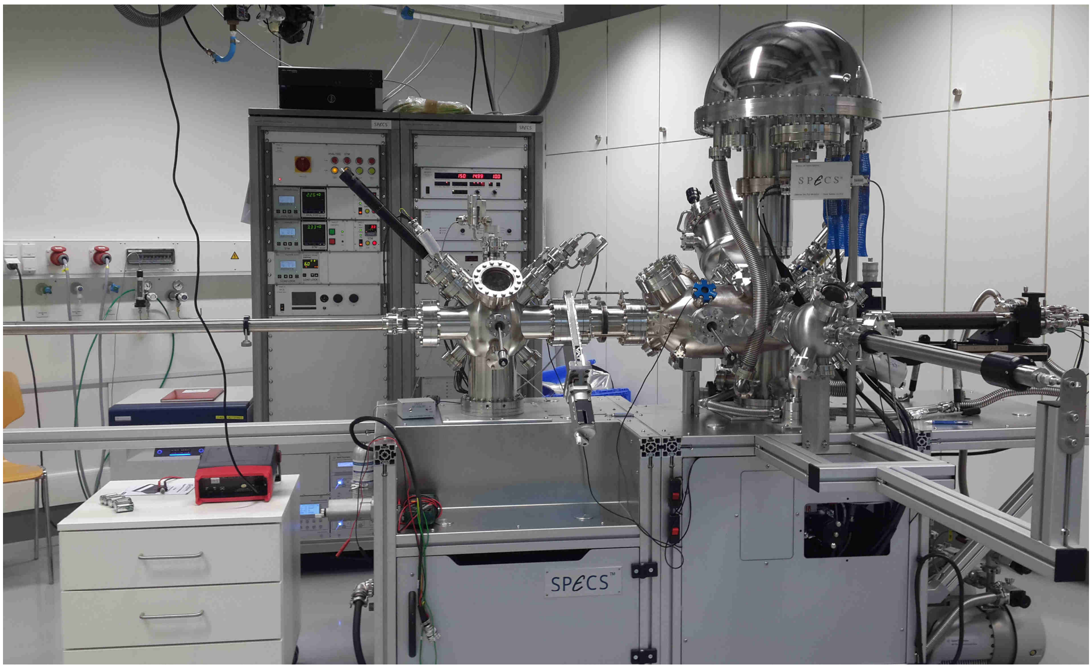

Figure 2.1: PES and STM joint apparatus at AG Gottfried, Philipps Universität Marburg. From right to left: Manipulator with four degree of freedom; PES analysis chamber with Phoibos 150 hemispheric electron energy analyzer and FOCUS 500 monochromator; STM chamber.

2.2 Synchrotron Light Source and End Stations at BESSY II

Part of the PES studies discussed in Chapter 3 are performed with synchrotron radiation at the facility BESSY II, Helmholtz-Zentrum in Berlin. Electron energy in the storage ring is up to 1.7 GeV. BESSY II can now operate under "top-up" mode, meaning constant injection of the small amount of electrons into the storage ring, which produces stable and high photon flux for the beamlines.

2.2.1 End Station SurICat at BESSY II

Near Edge X-Ray Absorption Fine Structure (NEXAFS) measurement and XPS measurements were conducted at the endstation SurICat (surface investigation and catalysis, Figure 2.2). This endstation is attached to the dipole beamline PM4, which is equipped with a plane grating monochromator to provide photon energies ranging from 20 eV to 2000 eV. The photon flux of PM4 is in the range 10^9 to 10^{10} photons/s, depending on wavelength. The entire endstation comprises four compartments: A main preparation chamber, equipped with LEED optics, QMS and Ar sputter system, stands at the center of the setup. Cleaning of sample surface was carried out by Ar+ sputtering in this chamber. Right below it is the analysis chamber with a hemisphere electron energy analyzer. A primary preparation chamber IGEL (chamber with green window flange in Figure 2.2) for the deposition of potentially more volatile molecules is connected to the main preparation chamber. Organic thin films are prepared by vapor deposition in this chamber. The other preparation chamber is connected to the main preparation chamber at the 120° direction against the IGEL preparation chamber.

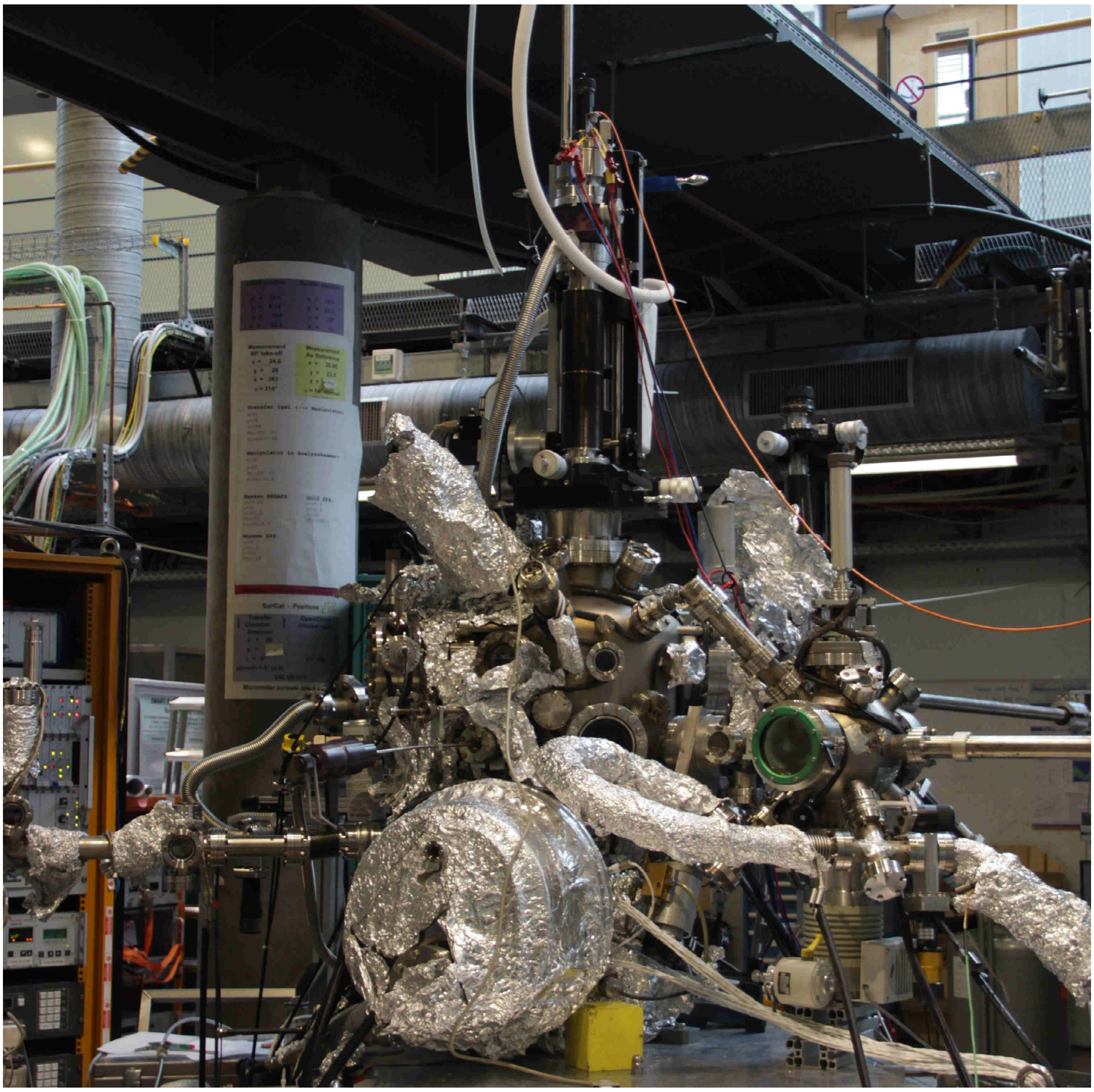

Figure 2.2: SurICat endstation at the PM4 beamline at BESSY II. From right to left: transfer rod, organic preparation chamber IGEL, main preparation chamber with a four-axes manipulator on top, hemispherical electron energy analyzer.

A Scienta SES-100 electron energy analysis system is installed for PES. A VG Helistat manipulator mounted allows for 90 K to 800 K sample temperature manipulation. Specimens are mounted on Omicron sample holders allowing 10 mm×10 mm in surface area and 3 mm in thickness.

2.2.2 End Station HIKE at BESSY II

HAXPES measurements have been performed on endstation HIKE (Figure 2.3). HIKE is located at beamline KMC-1 equipped with a double single crystal monochromator. Three single crystal pairs, optimized for different photon energy ranges, are available to provide tunable photon energy from 1.7 keV of soft X-ray to 12 keV of hard X-ray. Focused photon flux, which gives 10^{11} to 10^{12} photons/s within an area of 0.4 mm×0.6 mm, is used for HAXPES at HIKE. Since the crystal pairs for monochromatization may be changed for a certain photon energy range, given that the mechanical movement inside the monochromator is not perfect precise and reproduced every time, it is always necessary to take a certain PES line of a change-immune subshell photoemission, i.e., Au 4*f*, as photon energy reference.[94-95]

HIKE is a multifunctional endstation suitable for NEXAFS and HAXPES investigations under HV and UHV condition. It is comprised of an analysis chamber, a preparation chamber, and a sample loading system. A modified VG Scienta-manipulator is mounted inside the analysis chamber to accept Omicron type sample holders. An additional X-ray capillary focuses the beam further to a spot size of 0.1 mm×0.1 mm. A polycrystalline gold thin film is attached to the manipulator right below the sample slot for photon energy correction. The Scienta R4000 hemispherical electron energy analyzer with 200 mm radius is used for PES, giving the very best energy resolution and signal to noise ratio for kinetic energies of up to 10 keV.

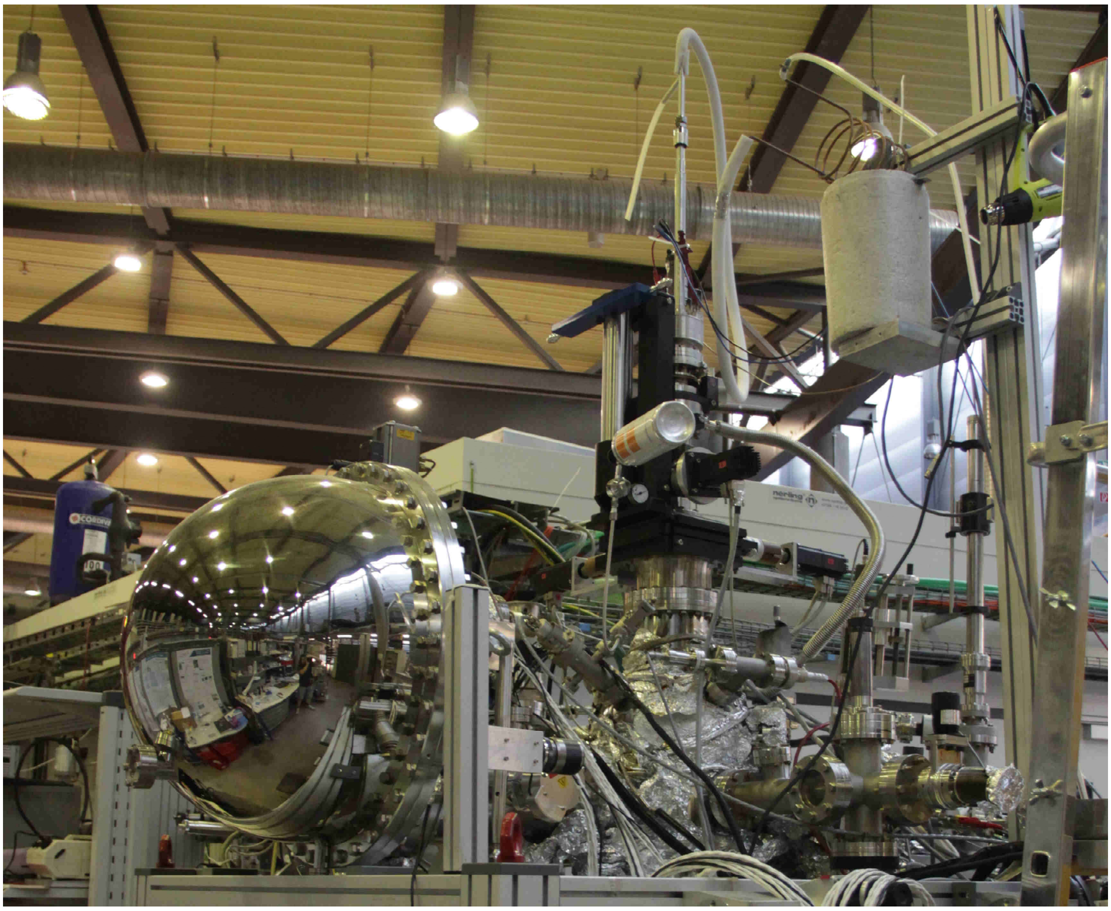

Figure 2.3: HIKE as the endstation of the KMC-1 beamline at BESSY II. From right to left: preparation chamber with fast moving load-lock; analysis chamber with VG Scienta manipulator mounted on top of it and VG Scienta R4000 hemispherical electron energy analyzer mounted perpendicular to the beamline.

Specimen dimensions of up to 10 mm×10 mm large and 3 mm thick are allowed to Omicron type sample holder. A fast moving linear motion, with unthreaded, direct magnetic locking and shifting, is mounted on top of the load-lock. It holds the sample garage on the head of its transfer rod. HAXPES studies discussed in chapter 3 of this thesis are carried out at HIKE using aluminum foil as substrate.

2.3 Nanojoule Adsorption Calorimeter

The surface adsorption calorimetric studies discussed in chapter 4 of this thesis were carried out using a home built calorimeter. It adopted the major concept of Campbell's calorimeter, using β-PVDF thin film as the pyroelectric detector for small adsorption-induced temperature changes. The author of this thesis was also intensively involved in the construction work of this calorimeter. The mechanical and electronic design as well as the data analysis module of this calorimeter was recently described in the PhD thesis by H.-J. Drescher.[96] In this chapter, measurement routine established for our calorimeter will be presented. The software module developed for apparatus control, status monitoring and data acquisition will be discussed in chapter 5. Further instrumental developments beyond the status described by Drescher[96] will be discussed in chapter 6.

2.3.1 Calibration of the Detector

Because β-PVDF is a non-single crystalline polymeric material, its properties regarding the pyroelectricity are in fact difficult to be practically assessed. Even on a single piece of commercially available PVDF sheet, materials cut from different regions may exhibit considerable deviations in properties due to the limitations of processing and manufacturing. Therefore, each PVDF thin film mounted in the sample holder as detector has to be laser calibrated for sensitivity before the adsorption calorimetry measurement.

The PVDF film used in our study is a 25 μm film coated with 40 nm copper then 15 nm nickel by vapor deposition. At this thickness of coating, it is still partially transparent to visible light, meaning that its reflectivity to our 405nm laser is unknown. However, the reflectivity of the detector to the laser is a necessity to the calibration. It has to be known before any adsorption take place. In our study, the reflectivity of the detector assembly is measured using the method described in the literature.[96]

For the calibration of the detector, the sensitivity factor, also referred as contact sensitivity, was obtained by the measurement of a clean sample's signal response to an exactly known amount of heat deposited by a laser of known intensity. The laser power was measured using a NIST calibrated photo diode power meter outside the chamber via reflection of the laser.[96] The correlation between measured signals and sensitivity factor are expressed as:

$$\begin{aligned} I_{\mathrm{cln}} &= C_{\mathrm{sen}} \cdot P_{\mathrm{sam,cln}} \cdot t \cdot (1 - R_{c\mathrm{ln}}) \\ P_{\mathrm{sam,cln}} &= P_{\mathrm{m,cln}} \cdot Z_{\mathrm{sam\text{-}m}} \end{aligned} \tag{2.1}$$

Where I_{cln} denotes the averaged intensity of the measured signal, usually of 25 pulse pairs or 50 pulses. The intensity is determined either by area, by height or by any other fitting coefficients, as long as it is based on the linear response assumption over input time. The subscript "cln" means at this stage the sample is still as clean as when its reflectivity is measured outside the UHV chamber, so that this reflectivity is applicable. C_{sen} denotes the contact sensitivity of the sample under a given temperature. $P_{\mathrm{sam,cln}}$ denotes the laser power that is deposited onto the sample, $P_{\mathrm{m,cln}}$ denotes the power measured using power meter. t denotes length of pulse time. R_{cln} denotes the reflectivity of this clean sample. $Z_{\mathrm{sam\text{-}m}}$ denotes the tooling factor of the power measured outside the chamber to the power at sample position under same laser input. It is measured through standalone processes. After the substitution of $P_{\mathrm{sam,cln}}$ and some rearrangements to equation 2.1, C_{sen}, with a unit of V/J, could be written as:

$$C_{\mathrm{sen}} = \frac{I_{\mathrm{cln}}}{P_{\mathrm{m,cln}} \cdot Z_{\mathrm{sam\text{-}m}} \cdot t \cdot (1 - R_{\mathrm{cln}})} \tag{2.2}$$

Because the sample assembly will not be disassembled during the entire procedure of calibration and calorimetry measurements, it is reasonable to assume that C_{sen} is unchanged, thus making it possible to calibrate the sample again if the reflectivity of the detector has been changed by the deposition of, i.e., an organic thin film, onto the sample surface.

2.3.2 Preparation of Organic Thin Film

To carry out the adsorption calorimetry of metal on organic surface, after the calibration to the clean detector, an organic thin film is vapor deposited inside the load lock of the calorimeter. The thickness of the thin film is determined by in-situ QCM monitoring with a predetermined geometric correction factor.

2.3.3 Calibration for the Change of Reflectivity

After the preparation of the organic thin film, another calibration for the change of the sample reflectivity has to be carried out. This step is mostly a repetition to the measurement in the first calibration of clean sample, but with the reflectivity of the coated sample being measured under UHV condition. This is critical because if reflectivity of the coated sample is measured under ambient condition, the sample surface would be contaminated by moisture and other substances in the air, thus rendering it unusable for later measurements. Since C_{sen} is calculated via equation 2.2, again, we have:

$$\begin{aligned} I_{\mathrm{cot}} &= C_{\mathrm{sen}} \cdot P_{\mathrm{sam,cot}} \cdot t \cdot (1 - R_{\mathrm{cot}}) \\ P_{\mathrm{sam,cot}} &= P_{\mathrm{m,cot}} \cdot Z_{\mathrm{sam\text{-}m}} \end{aligned} \tag{2.3}$$

Here “cot” means this sample is coated by organic thin film. In this calibration, the reflectivity after coating R_{cot} is deduced for next step, which writes:

$$R_{\mathrm{cot}} = 1 - \frac{I_{\mathrm{cot}}}{P_{\mathrm{m,cot}} \cdot Z_{\mathrm{sam\text{-}m}} \cdot t \cdot C_{\mathrm{sen}}} \tag{2.4}$$

2.3.4 Transmission of Window

To determine the contribution of the radiation to the total calorimeter signal, a BaF_2 window is placed in front of the sample to block the molecular beam. The real transmission of this window to the radiation will change over the time, since the atoms and molecule of the beam may stick to the window as contaminants. In our study, Ca is employed as metal in the beam. The transmission of the Ca thin layers that stay on the window will also change from time to time because the optical properties of these layers will be largely changed by their reactions with residual gas. As a consequence, the latest transmission coefficient of the BaF_2 window should be determined right before the measurement of radiative contribution. The transmission coefficient is determined via essentially the same process as the laser calibrations in former steps. The only difference lies in the BaF_2 window being placed in the position as they will be in the measurement of radiative contribution. Here it is assumed that the BaF_2 window exhibits the same transmission to 405nm laser as to thermal radiation from evaporator at, i.e., 900 K, although it would be better if a radiation source with no molecular flux, i.e., a hot tungsten filament, could be placed in the beam to provide the radiation at the same temperature. The correlation between transmission coefficient T_{win} and signal intensity I_{win} could be expressed as follows:

$$\begin{aligned} I_{\text{win}} &= C_{\text{sen}} \cdot P_{\text{sam,win}} \cdot t \cdot (1 - R_{\text{cot}}) \cdot T_{\text{win}} \\ P_{\text{sam,win}} &= P_{\text{m,win}} \cdot Z_{\text{sam-m}} \end{aligned} \tag{2.5}$$

R_{cot} is used because this determination of T_{win} usually closely follows the former step in which R_{cot} is determined. No change to the reflectivity of the sample should occur. T_{win} could be specifically expressed as:

$$T_{\text{win}} = \frac{I_{\text{win}}}{C_{\text{sen}} \cdot P_{\text{m,win}} \cdot Z_{\text{sam-m}} \cdot t \cdot (1 - R_{\text{cot}})} \tag{2.6}$$

2.3.5 Contribution of Radiation

In order to use T_{win} as the transmission coefficient of radiation through the BaF_2 window, it is also assumed that short time exposure of the window to flux does not impose significant change to the transmission coefficient as well. Before the measurement of radiative contribution, the evaporator of the beam is heated to and held stable at the desired temperature. With BaF_2 window being moved to shield the sample from real flux, equivalent number of pulses as the laser calibrations is dosed onto the sample. The correlation between radiative contribution q_{rad} and signal intensity I_{rad} could be expressed as:

$$I_{\text{rad}} = C_{\text{sen}} \cdot q_{\text{rad}} \cdot T_{\text{win}} \tag{2.7}$$

or

$$q_{\text{rad}} = \frac{I_{\text{rad}}}{C_{\text{sen}} \cdot T_{\text{win}}} \tag{2.8}$$

2.3.6 Measurement of Beam Flux

The flux is measured by placing a QCM in front of the sample. The QCM read out is in the form of nm/s or ML/s. For the calculation of calorimetric heat, it should be translated into the form with the unit of mol/s, the absolute dosage per pulse n_{cal} is then obtained as:

$$\begin{aligned} n_{\text{cal}} &= \frac{F_{\text{cal}} \cdot D \cdot A_{\text{sam}}}{\mathrm{N_A}} \cdot t \\ F_{\text{cal}} &= F_{\text{QCM}} \cdot Z_{\text{sam-QCM}} \end{aligned} \tag{2.9}$$

Where n_{cal} denotes the flux arrived at sample in the form of mol/s. F_{QCM} is the flux measured by QCM. $Z_{\text{sam-QCM}}$ is the geometric tooling factor between the sample position and the QCM position. D is the number of atoms per unit area of the deposited substance in each ML or nm. A_{sam} denotes the area of deposition on the sample surface. $\mathrm{N_A}$ is the Avogadro constant. In Equation 2.9, the unity sticking of the adsorbing material (e.g., Ca) on the QCM is assumed. This could be confirmed by the signal fade-out in the simultaneous QMS monitoring, in which there is always QMS signal from the non-sticking part of dosage being observed at the beginning and later converging to zero (see chapter 5 for the details of its realization).

2.3.7 Determination of Sticking Probability

Unlike on the surface of the QCM crystal, where Ca atoms eventually adsorb on bulk Ca and thus have a high sticking probability, the sticking probability of Ca on organic substrate, especially at very low coverage region, is far from unity[35, 37]. Therefore, it is always necessary to know the sticking probability of every single pulse on the sample. By employing a modified King-Wells sticking probability measurement[96], the sticking probability is given by:

$$S_{\mathrm{cal}} = 1 - \frac{I_{\mathrm{qms,cal}}}{I_{\mathrm{qms,nstk}} \cdot Z_{\mathrm{sam\text{-}nstk}}} \tag{2.10}$$

Where $I_{\mathrm{qms,cal}}$ is the QMS signal intensity of a pulse during calorimetry measurement (Figure 2.4), $I_{\mathrm{qms,nstk}}$ is the averaged intensity of QMS signal from the scattering on the hot plate (non-sticking flag). $Z_{\mathrm{sam\text{-}nstk}}$ denotes the geometric tooling factor between the sample position and the non-sticking flag.

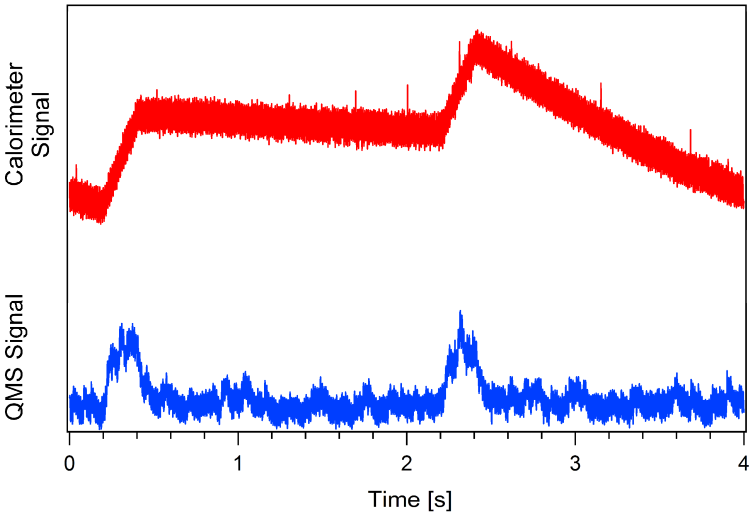

Figure 2.4: Typical raw data of a pulse pair in the adsorption calorimetry of metal on organic substrate. This figure is a pulse pair from the adsorption of Ca on a 125 nm 6T film at 310 K, with a Ca flux of 0.021 nm/s or 0.065 ML/s. Top, the calorimetric signal detected by 25 µm PVDF film detector; bottom, the corresponding QMS signal from the non-sticking fraction of the beam impinging on the sample.

2.3.8 Determination of Adsorption Energy

The calorimetric heat q_{cal} deposited by a beam pulse is determined by the following equation:

$$I_{\mathrm{cal}} = C_{\mathrm{sen}} \cdot \left(q_{\mathrm{cal}} \cdot n_{\mathrm{cal}} \cdot S_{\mathrm{cal}} + q_{\mathrm{rad}}\right) \tag{2.11}$$

The unit of the calorimetric heat should stay in line with standard, which writes kJ/mol. More specifically, q_{cal} is expressed as:

$$q_{\mathrm{cal}} = \frac{I_{\mathrm{cal}} - C_{\mathrm{sen}} \cdot q_{\mathrm{rad}}}{C_{\mathrm{sen}} \cdot n_{\mathrm{cal}} \cdot S_{\mathrm{cal}}} \tag{2.12}$$

$q_{\mathrm{ads}}=-\Delta h_{\mathrm{ads}}$ is calculated by the correction for volume work and temperature difference between the source of evaporation and the sample. Equations 1.27-1.29 are used for this purpose. It is important to point out that in equation 2.12, q_{rad} can change with coverage and therefore is not necessarily a constant over the experiment. In the adsorption of metals on organic thin films, optical properties of the metal/organic interface might change significantly with the increase of metal coverage. Two solutions are applicable to this problem. One is interrupting calorimetry with measurements of the radiative contribution. Assuming the transmission of the window does not change on a short time short time scale, the change in the strength of radiation should then be attributed to the change of reflectivity. With several data points within the coverage range of the entire calorimetry, a calibration curve for q_{rad} versus coverage will be obtained.

2.4 Materials

Chemicals employed as the subject to study the metal/organic interactions are presented below. Other materials that are used in the construction of the calorimeter are summarized in the PhD thesis of H.-J. Drescher.[96]

2.4.1 Calcium

Calcium is a highly reactive alkali earth metal with a low work function of 2.9 eV and therefore a good low-resistance cathode material for organic photovoltaics.[24-27, 97-99] It has a [Ar] $4s^2$ electron configuration and a molar mass of 40.078. The density of Ca is 1.55g/cm^3, which is 10.8% lower than its predecessor Mg in the same group. In vapor deposition, the crystal of Ca tends to grow alongside the [001] direction of the lattice. Ca used in the research of this thesis are Ca grains of 99.9% purity obtained from Sigma-Aldrich.

2.4.2 α-Sexithiophene

α-Sexithiophene (6T) is an oligomeric thiophene containing large π-conjugated system of 6 rings connected by their α positions (Figure 2.5). It has been considered to have wide range of applications in chemical sensors[100-101] or OLEDs,[102-104] and in particular, in OFET.[101, 105-106] Carrier mobilities in 6T are in the same order of magnitude as in amorphous silicon.[107] Meanwhile, the sulfur atom on the thiophene ring results in higher chemical reactivity. Compared with pure carbon based aliphatic and aromatic compound, it is easier to cleave the ring backbone at the S-C bond through a nucleophilic mechanism. This makes 6T an ideal model substance in the studies on formation of organic semiconductor devices or related topics.

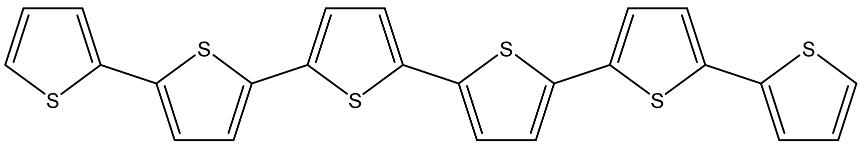

Figure 2.5: Molecular structure of α-sexithiophene (6T).

At coverages above 2 ML, vapor deposited 6T has been reported to grow alongside the long axis of the molecular plate, meaning that the molecules will “stand upright” in the multilayer[108] to form a monoclinic structure similar to its single crystal[109] (Figure 2.6). However, it has also been demonstrated that the inclination angle between 6T molecule and the long axis of unit cell might vary depending on the type of substrate on which the 6T grows.[4, 108]

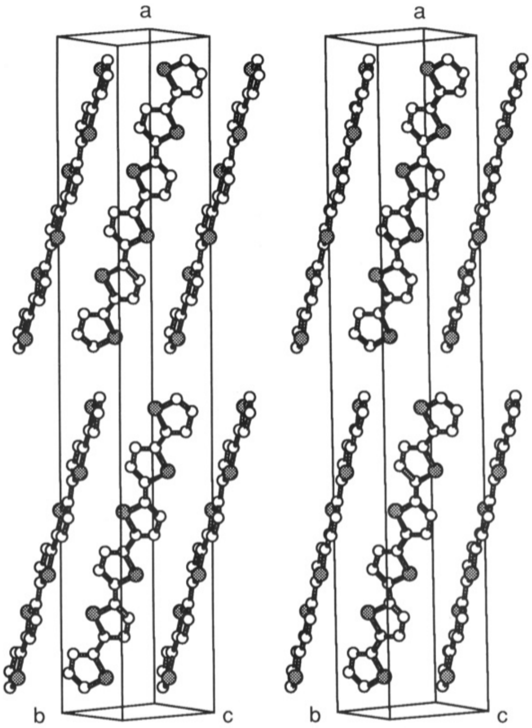

Figure 2.6: Crystal structure of α-sexithiophene (6T).[109]

3 Spectroscopic Investigations on the Interactions between Calcium and 6T

3.1 Results

3.1.1 Study of the Ca/6T Interface Using Scanning Transmission Electron Microscopy

To understand the Ca/6T interaction at the interface, it is helpful to first have an overview of the morphology of Ca/6T interphase. Scanning transmission electron microscopy (STEM) is employed to provide the direct morphological information of Ca/6T interphase formed by direct vapor deposition. The samples are prepared by sequential vapor deposition of 100 nm 6T, 82.5 nm Ca, and 320 nm Au onto a clean 30μm aluminum foil water cooled at room temperature. The dosage of each substance is monitored by the in-situ QCM measurement during depositions. The final layer of Au acted as the protective layer to the sample against air during the transportation of sample from the preparation chamber in the Group of Gottfried to the STEM in the Department of Physics, Philipps Universität Marburg.

Inside the STEM, the sheet sample first undergoes focused ion beam (FIB) cutting to form a thin tip (FIB lamella) that is suitable for transmission electron microscopy (TEM). Scanning electron microscopy (SEM) is carried out to assess the condition of the FIB lamella (Figure 3.1) before TEM measurement.

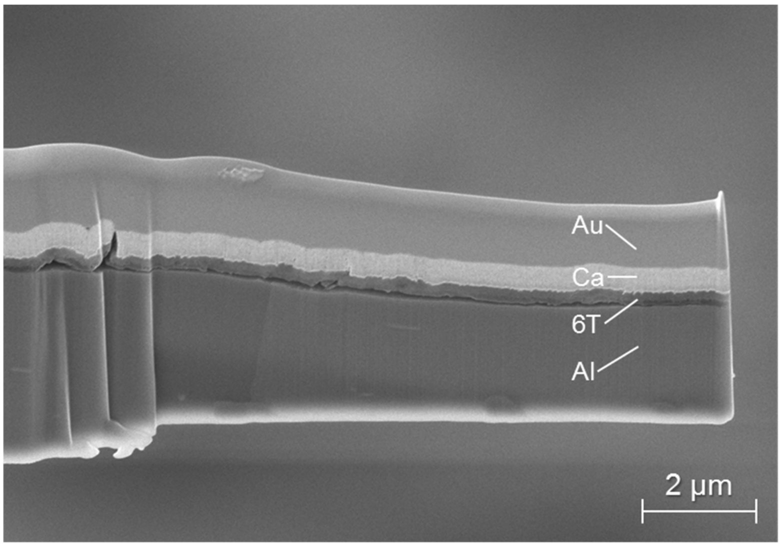

Figure 3.1: SEM image of the Ca/6T interface. The 0.16 μm sample (FIB lamella) is prepared by FIB cutting from the Au side. The Al substrate shown in the figure is the residual of a reduction from 30 μm.

Figure 3.1 shows the SEM image of the tip cut out by the FIB from the Au side of the sample. Notable deformation of the sample is observed, which might have resulted in the cracks of the absorbed layers and their detachment at the edge of the lamella. Another important phenomenon is the apparent thickness disproportion of the Ca and 6T layer. From the deposited amounts it is clear that the 6T layer should not be that much thinner than the Ca layer. These two phenomena should both be attributed to the process of FIB cutting, during which a fresh surface is created at the side of the samples. The energy of the FIB may heat up the sample, hereby the material is deformed by thermal stress. Energy from the incident ions could mobilize the atoms and small species in the surface layers to smear them over the surface. Such redistribution would create a mixture of elements on the surface layers. Therefore, in the very surface sensitive SEM image, the results is a modification by the surface redistribution rather than the objective demonstration to the structure of the layers. In Figure 3.1, the 6T layer is seen partially covered by the Ca layer, but not the other way round, because of the higher brightness difference between these two layers.

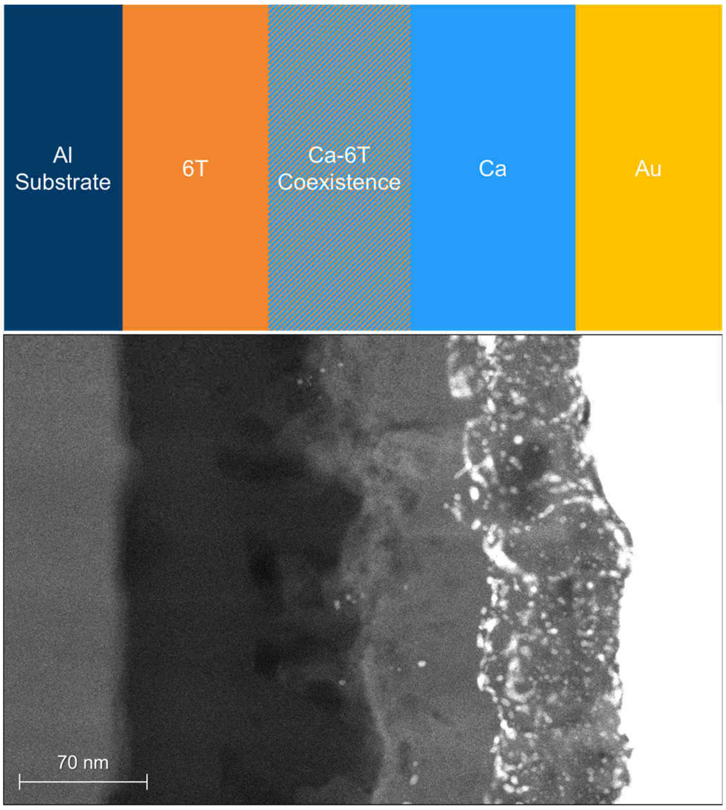

Figure 3.2: TEM image of Ca/6T interface on a 0.16 µm FIB lamella. The sample is prepared by the FIB cutting from the Au side. The nominal Ca-6T coexistence region (the blurry region) is about 40~55 nm wide. The sequence of materials is schematically shown above.

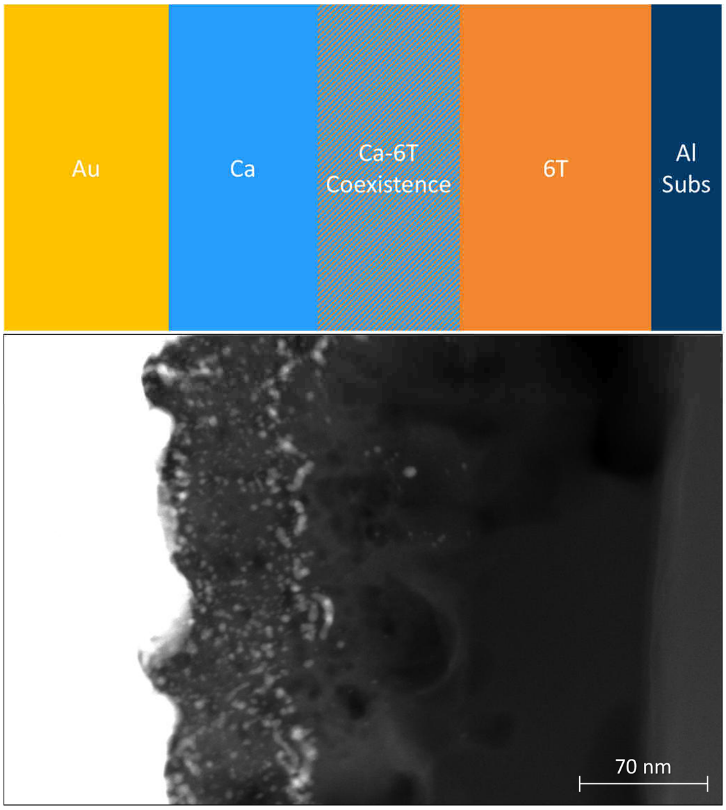

Figure 3.3: TEM image of Ca/6T interface on a 0.16 µm FIB lamella. The sample is prepared by the FIB cutting from the Al side. The nominal Ca-6T coexistence region (the blurry region) is about 40~50 nm wide. The sequence of materials is schematically shown above. Due to the varied relative position and orientation of the observation window, the observed width of Au phase, 6T phase and Al substrate are different from that is shown in Figure 3.2. The differences appearing in the image is not due to the choice of cutting-in direction.

Different from SEM, the TEM provides the aggregated signal of a three dimensional volume projected to the window of observation. Each point on the image of TEM represents not only the top most layers of atoms but also the materials inside the bulk of the lamella. In Figure 3.2, Au phase is the brightest because of its high electron scattering cross section ; the lighter metals Al and Ca exhibit similar contrast while the organic 6T layer are observed to be the darkest region. The interface between Ca and 6T is far from what has been usually assumed as a “planar layered structure”. The actual morphology of the interphase is highly uneven and rough (although it is hard to determine to which extent this is caused by the preparation of the FIB lamella). Bumps and grooves are randomly distributed alongside the interface. The irregularity of the Ca/6T interface is in good contrast to that of the 6T/Al substrate, where no strong interaction exists. The blurry area alongside the interface could originate from the simultaneous existence of Ca diffusion into the 6T and the aforementioned smearing effect caused by FIB cutting. Besides that, because the image is a projection of the whole thickness into a 2D plane, if the sample and all layers are not absolutely flat, there will be a broadening and overlap of the layers in the projection. This means the actual region of coexistence, the interface, might be smaller than the blurry region has implied. Figure 3.2 and Figure 3.3, obtained by two cutting-in direction during the TEM sample preparation respectively, exhibit similar interphase morphology, from which the effect of the cutting-in direction could be excluded. In the TEM images, Ca phase is partially covered by the bright spots, seemingly the Au, which is widely spread over the region of Ca. It is unlikely that Au atoms would diffuse so strongly into metallic Ca at room temperature. Such phenomenon should also be attributed mainly (but not only, see below) to the smearing effect of FIB cutting.

Energy dispersive X-Ray spectroscopy (EDX) is also carried out with the prepared FIB lamella. In the images shown in Figures 3.4 and 3.5, all the elements exhibit some extent of re-distribution across the volume studied in the TEM experiment. This further supports the idea that the artifacts of elementary concentration, as aforementioned in the discussion of Figure 3.1-3.3, are partially the products of the FIB cutting rather than the deposition itself. At the Ca/6T interface (Figure 3.4), geometrical overlap of Ca and S signals is observed with a pronounced density gradient of Ca in the area of overlap, as would be expected for a system of metal diffusion into the organic layers. The region of Ca/S overlap in EDX is about 40~50 nm wide, which is in accordance with that has been assessed via the TEM images. Again, the effect of the projection from the stacked regions of the different layers should be taken into consideration. The actual size of the regions with notable concentration gradient could be smaller than they appear in the EDX images.

If the signal of S and C are compared, the expected enrichment of S in the area of Ca surface is not present. Normally, S should be more affiliating to metallic Ca than hydrocarbon segment due to the chemical reactivity. By looking at the signal of O (Figure 3.5), it is known that the existence of oxides layer in the area of Ca should be attributed as the reason for the absence S affiliation. During the FIB cutting, a fresh Ca surface is created and subjected to the attack of residual gas. Therefore, the competitions between the residual gas, i.e., O_2 or H_2O, and the S from the 6T phase take place after the creation of the new surface. The Ca^0 on the surface is rapidly passivated by the more reactive O containing substances and becomes no longer attractive to S. The peculiar high intensity of S signal at the area of Au (Figure 3.4) does not represent the actual concentration of S. It is an artifact caused by the overlap of the Au M-α emission’s satellites with the S K-α emission’s main peak.

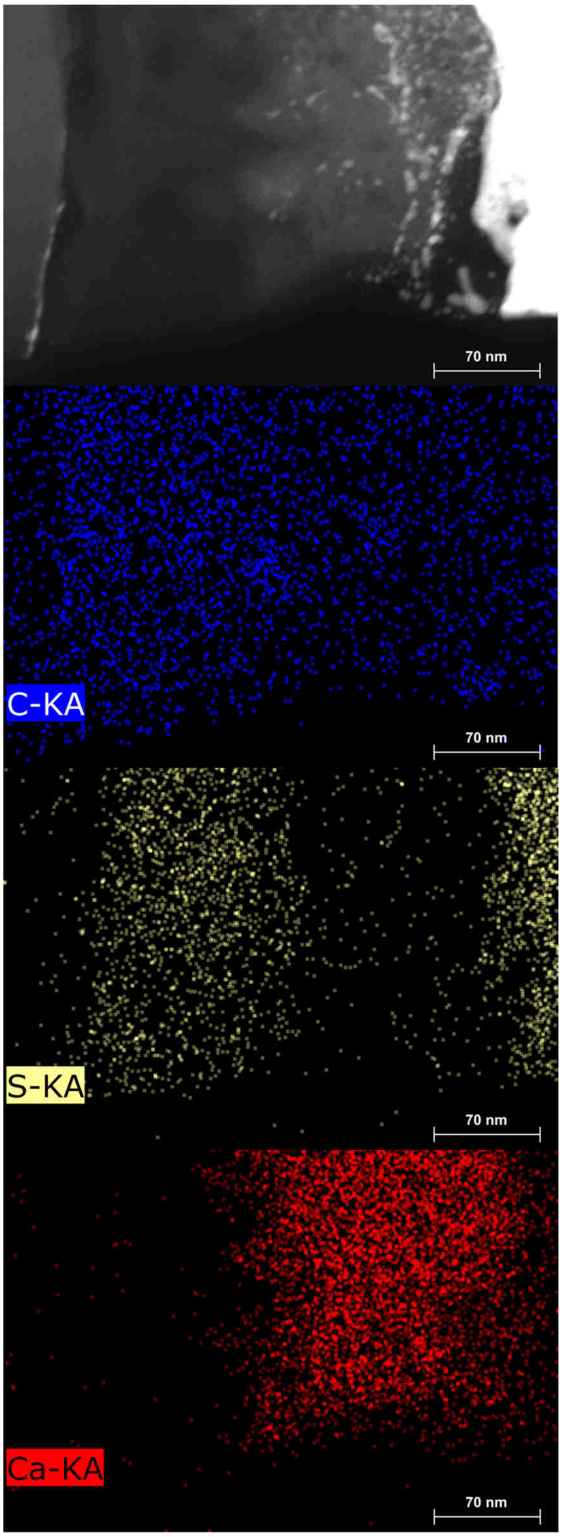

Figure 3.4: TEM and EDX image of Ca/6T interface. The top panel shows the TEM image of the sample prepared with the same method as for the Figure 3.2. Elementary densities are shown separately with the intensity of their specific X-ray emission. C-KA: carbon K-α; S-KA: sulfur K-α; Ca-KA: calcium K-α.

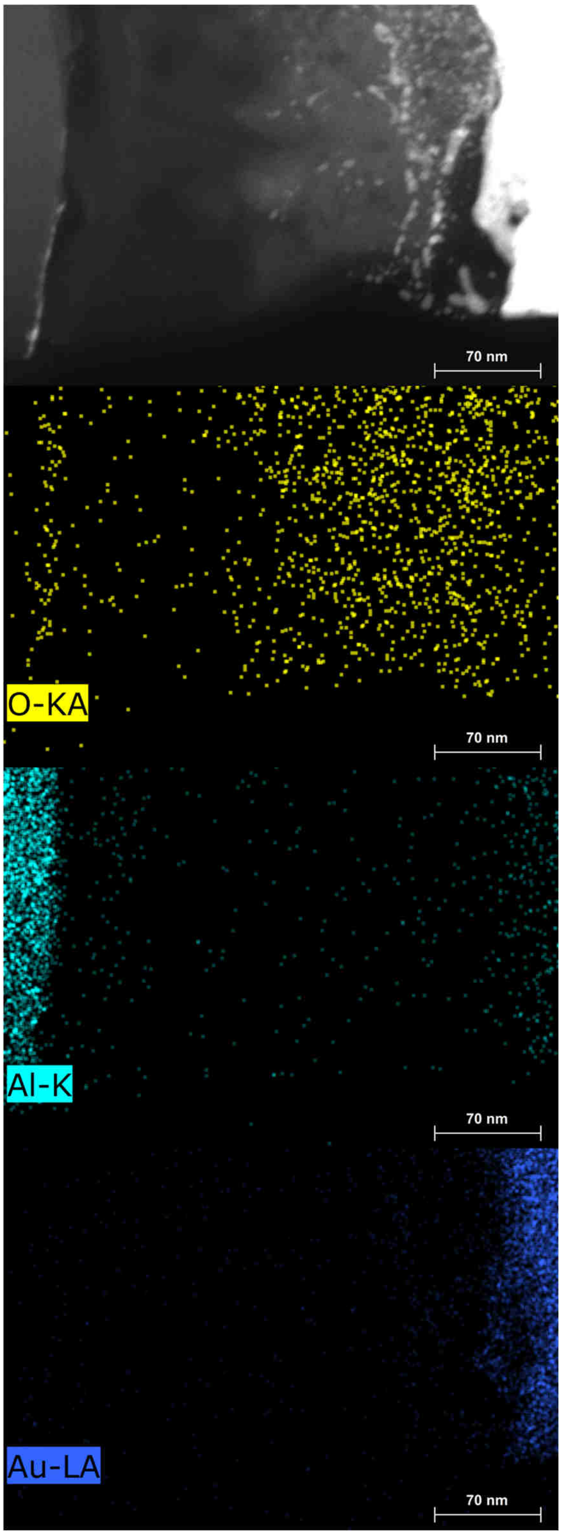

Figure 3.5: TEM and EDX image of Ca/6T interface. The top shows the TEM image identical to the one in Figure 3.4. Elementary densities of several other elements are shown separately with the intensity of their specific X-ray emission. O-KA: Oxygen K-α; Al-K: Aluminum K-α; Au-LA: Gold L-α.

3.1.2 NEXAFS investigations on the structure of vapor deposited 6T film

Because the 6T films prepared for the studies of this work are notably thicker than those thin film organic substrates previously studies for metal/organic interface and interaction,[47, 50, 110-112] the structure of the 6T thick films absorbed on the polycrystalline gold plate is largely unknown, despite that there is already a wide range of studies on the crystal structure of 6T as well as its sub-monolayer/monolayers adsorption behaviors on single crystal substrates.[4, 108-109, 113-114] A thick organic film is typically considered as a structurally an ill-defined system, since there is often no dominant orientation of the components in the film.[115] In this work, Near Edge X-Ray Absorption Fine Structure (NEXAFS) spectroscopy is employed to obtain the structural information of the pristine 6T film.

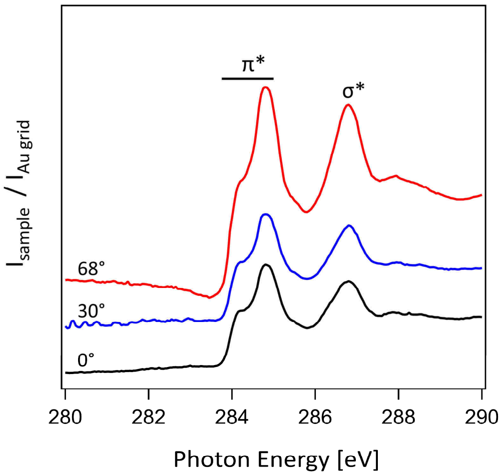

Figure 3.6: Carbon K-edge NEXFAS spectra of a 9.3 nm thick pristine 6T film absorbed on polycrystalline gold substrate. The spectra were taken with different angle of incidence using total electron yield. The electron yield was determined by comparing the current conducted through the sample with the current at the Au grid.

The total electron yield technique is used as the measurement of X-ray absorption. The experiments were carried out at the end station SurICat of BESSY II, at which the net electron yield is determined by comparing the sample current with the current at the Au grid. As is shown in Figure 3.6, the peak structure around 285 eV with low energy side shoulder is attributed to the C1s→π^* transition, whereas the single peak that appears around 287 eV represents the C1s→σ^* transition[4]. Upon the variation to the angle of incidence, no significant change of the relative peak intensities is observed. This indicates that at a film thickness as thin as 9.3 nm, the vapor deposited 6T film has already become fully disordered and isotropic, which is in good accordance with the previous studies of thick 6T films absorbed on single crystal substrates. Other vapor deposited 6T films prepared in the experiments of this work are all thicker than this one used in the NEXAFS spectroscopy, it is reasonable to assume that they are similarly disordered and isotropic as the 9.3 nm film.

3.1.3 XPS Investigations on the Interactions of Ca and 6T Thin Films as a Function of Ca coverage

With the structural information provided by TEM and EDX images and NEXAFS, a coarse model of the Ca/6T interface was established. However, TEM and EDX are unable to provide more specific chemical state of each element. To further understand the interactions between Ca and 6T during the formation of Ca/6T interphase, XPS studies are carried out in order to understand the chemical nature of the interface.

First, the growth model of Ca on the 6T substrate was studied by the stepwise incremental deposition of Ca on 6T. The sample was prepared by vapor deposition of Ca at a controlled rate onto the beforehand vapor deposited 6T film. The sample is also water cooled at room temperature to avoid that the sample is heated up by the IR radiation emitted from the hot evaporator. Core level XPS spectra of C 1s, S 2p and Ca 2p regions were taken both along the surface normal and at 70° relative to the surface normal after each deposition step of Ca. The fluxes of both 6T and Ca were monitored by QCM before and after deposition. The average of the two is used to calculate the rate of deposition. The thickness of 6T thin film was calculated through Equation 1.9 with the IMFP taken from the work of B. Lesiak et al.[116] and element photoionization cross sections from the work of C. D. Wagner et al..[56] The equation compares the intensity of C 1s signal of the pristine 6T film and the Au 4f signal from the polycrystalline gold substrate. The dosage of Ca is calculated by assuming layer-by-layer growth of Ca atom alongside the [001] direction of its crystal lattice and unity sticking of Ca atoms on the QCM crystal. With the nominal dosage calculated by the QCM recorded flux, the actual coverages are determined by proportional conversion of the nominal dosages to coverages, where the ratio of conversion is determined by comparing the highest dosage versus the highest XPS determined coverage (Equation 3.1). The Lambert-Beer law is again employed in the calculation of the highest coverage.

$$d_{\mathrm{Ca}} = \lambda_{\mathrm{Ca}} \cos\theta \ln\left[\left(\frac{I_{\mathrm{pri}}}{I_{\mathrm{n}}}\right)\right] \tag{3.1}$$

Where d_{Ca} denotes the thickness (coverage) of Ca, I_{pri} and I_{n} denote the intensity of C 1s signal of pristine 6T and after n steps of Ca deposition; λ_{Ca} is the IMFP of photoelectron with kinetic energy corresponding to C 1s level that travels in solid Ca. This IMFP is referenced from the NIST standard data base. Equation 3.1 is applicable only at high Ca coverage when most of the Ca is present in the form of metallic Ca on top of the organic phase. Under this condition, the amount of Ca atoms diffused into the organic layer is insignificant compared with those staying in the metal phase. The dampening of the substrate signal is then mainly caused by the metallic Ca phase and, therefore, the IMFP of solid Ca can be used.

Figure 3.6 shows the fitted S 2p spectra with increasing Ca coverage. Since the final product of the reaction between Ca and S is calcium sulfide,[35, 46] the fitting of the S 2p spectra in this study is conducted assuming only one new species emerges in the S 2p spectra upon deposition of Ca. Of the two doublets in the spectra, the relatively narrower doublet at the higher binding energy side is attributed to the signal of S species from pristine 6T, while the broader doublet at the lower binding energy side of the spectra represent the signal from reacted S species. The broadening of the doublet representing reacted S species may generally be attributed to two reasons. First, the complexity of the chemical environment adjacent to the reacted species. The reaction of Ca with S on the thiophene rings is not a well-defined process. Although CaS is assumed as the final product of the reaction, the composition and the structure of its organic byproducts is not yet known. The conjugation of 6T brings more possibilities to the formation of coordinated, metastable structures, the chemical environment at the reacted area is therefore more complicated than in the crystalline bulk CaS. This results in many similar species with slightly different chemical shifts in the signal of reacted S. They overlap with each other to form a broadened doublet. Second, as claimed by many researchers,[117-120] the grain size of the materials also has impact on the chemical shift of the materials. This effect is pronounced on the nanoscale particles. Because Ca is diffused into the 6T phase in our study, the grain size of the CaS product should have a size distribution in the nanoscale regime. This effect would also produce various species in the signal of the reacted S. Considering the complexity of the Ca/6T interaction, it is difficult to quantify the contribution of these two phenomena to the broadening of the signal. In addition to these two reasons, the surface core level shift should also be considered at the low coverage regime, at which the reduced coordination of the freshly formed CaS particles on the surface would significantly influence the binding energy of the reacted S species.

The intensity of the reacted species increases with the Ca coverage in both the spectra of normal emission and 70° emission. Below a Ca coverage of 4.6 ML, spectra of 70° emission exhibit a higher proportion of reacted species than its corresponding normal emission spectrum at the same Ca coverage. This difference is reduced when the Ca coverage exceeds 4.6 ML. As the coverage reaches 19.4 ML, the spectrum of 70° emission exhibit a higher relative amount of the pristine component than the normal emission spectrum. This reversal of the angular dependence of the relative signal intensities for reacted and unreacted S indicates that the actual morphology of the Ca/6T interface under high Ca coverage deviates from the thin flat layered structure, in agreement with the TEM and EDX results. Spectra from both emission angles exhibit a trend of binding energy shift to the higher binding energy direction. The amount of binding energy shift is determined by the peak position change of pristine S $2p_{3/2}$ signal relative to the pristine spectra. The shift is observable starting at the initial deposition of 0.1 ML Ca; the shifts reach values as high as 0.80 eV and 0.69 eV for spectra recorded from normal and 70° emission, respectively, at a coverage of 1.3 ML. As the Ca coverage increases further, they stay constant until 4.6 ML; then the peaks slightly move towards lower binding energy direction as the Ca coverage exceeds 4.6 ML. Such shifts are the consequences of surface/interface band alignment that occurs after the interactions of two materials with different work functions. it will be further discussed in the discussion part of this chapter.

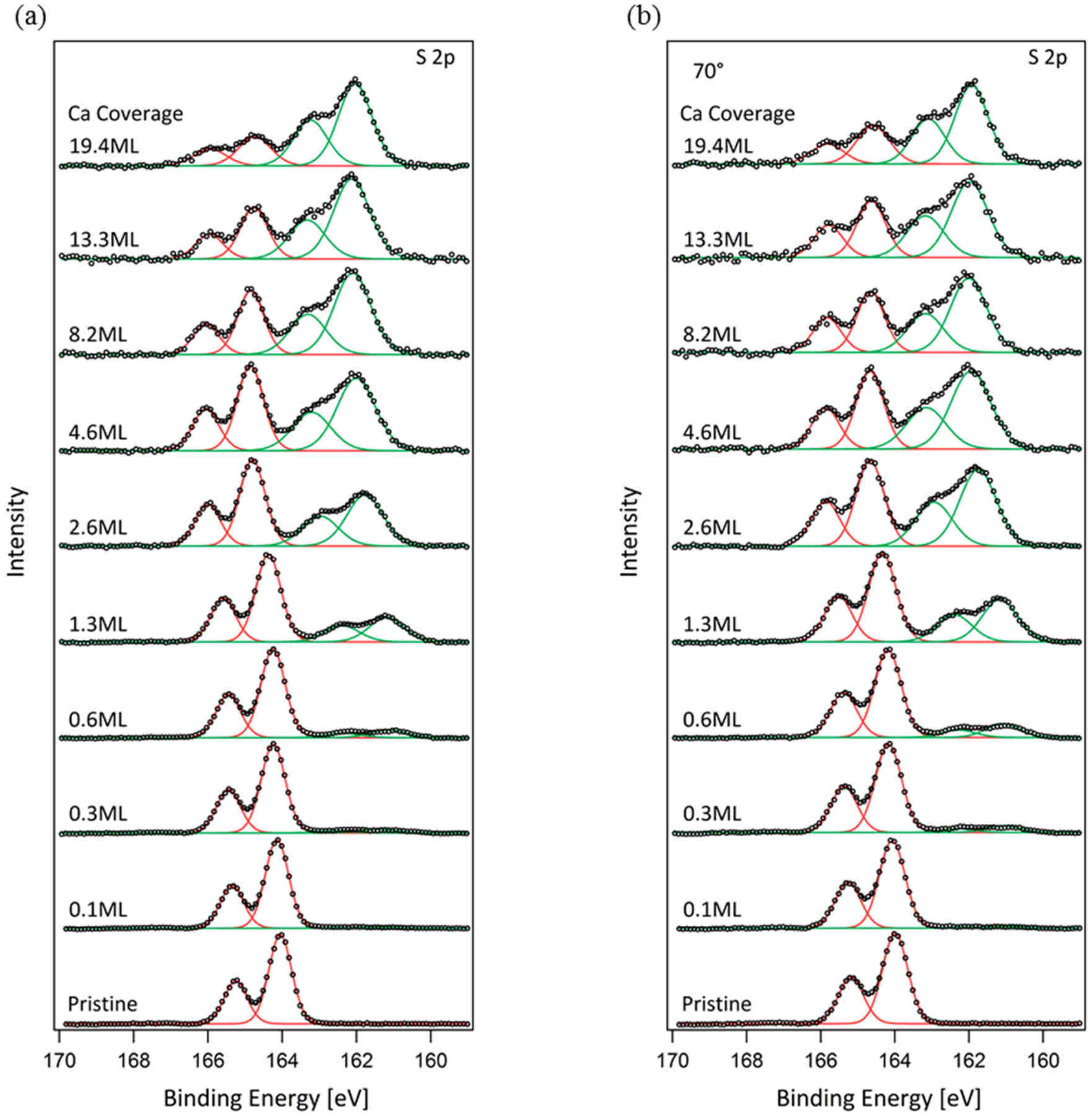

Figure 3.7: S 2p spectra (Al K-α, hν=1486.7 eV) of increasing Ca coverage on a 18.8 nm thick 6T layer. The substrate for deposition is a polycrystalline Au plate. Temperature of deposition: 298 K. (a): Spectra recorded in normal emission geometry; (b): spectra recorded at 70° emission angle relative to the surface normal. The background of the raw data is treated using Shirley background assumption. The peaks in the spectra are fitted with Gaussian-Lorentzian product (GLP) functions. All spectra are normalized to their respective amplitude of intensity (y data set).

The intensity of the reacted species increases with the Ca coverage in both the spectra of normal emission and 70° emission. Below a Ca coverage of 4.6 ML, spectra of 70° emission exhibit a higher proportion of reacted species than its corresponding normal emission spectrum at the same Ca coverage. This difference is reduced when the Ca coverage exceeds 4.6 ML. As the coverage reaches 19.4 ML, the spectrum of 70° emission exhibit a higher relative amount of the pristine component than the normal emission spectrum. This reversal of the angular dependence of the relative signal intensities for reacted and unreacted S indicates that the actual morphology of the Ca/6T interface under high Ca coverage deviates from the thin flat layered structure, in agreement with the TEM and EDX results. Spectra from both emission angles exhibit a trend of binding energy shift to the higher binding energy direction. The amount of binding energy shift is determined by the peak position change of pristine S $2p_{3/2}$ signal relative to the pristine spectra. The shift is observable starting at the initial deposition of 0.1 ML Ca; the shifts reach values as high as 0.8 eV and 0.7 eV for spectra recorded from normal and 70° emission, respectively, at a coverage of 1.3 ML. As the Ca coverage increases further, they stay constant until 4.6 ML; then the peaks slightly move towards lower binding energy direction as the Ca coverage exceeds 4.6 ML. Such shifts are the consequences of surface/interface band alignment that occurs after the interactions of two materials with different work functions. it will be further discussed in the discussion part of this chapter.

In the C 1s spectra shown in Figure 3.2, the chemical shifts introduced by Ca deposition are less pronounced (and less well-defined) than in S 2p spectra. At this stage of the investigations, it is difficult to establish a specific mechanism to explain the ring opening reaction of 6T induced by Ca. As a result, it is also not possible to attribute the C 1s spectra to certain species. However, some phenomena are clearly noticeable. First, the broadening of peak relative to the pristine spectra. In the pristine spectra, a wide plateau (FWHM of c.a. 1.4 eV) can be seen consisting of two equivalent sub components, in agreement with the literature.[3] As the Ca coverage increases, there are higher binding energy components emerging from the pristine peak. This suggests the formation of compounds with lower electron density at the C atoms as compared with the pristine 6T. Meanwhile, new features also emerge at the lower binding energy side of the pristine peak, indicating the formation of compounds with higher electron density after the cleavage of 6T rings. The coexistence of these two phenomena gives very good demonstration to the complexity of the reactions between Ca and 6T.

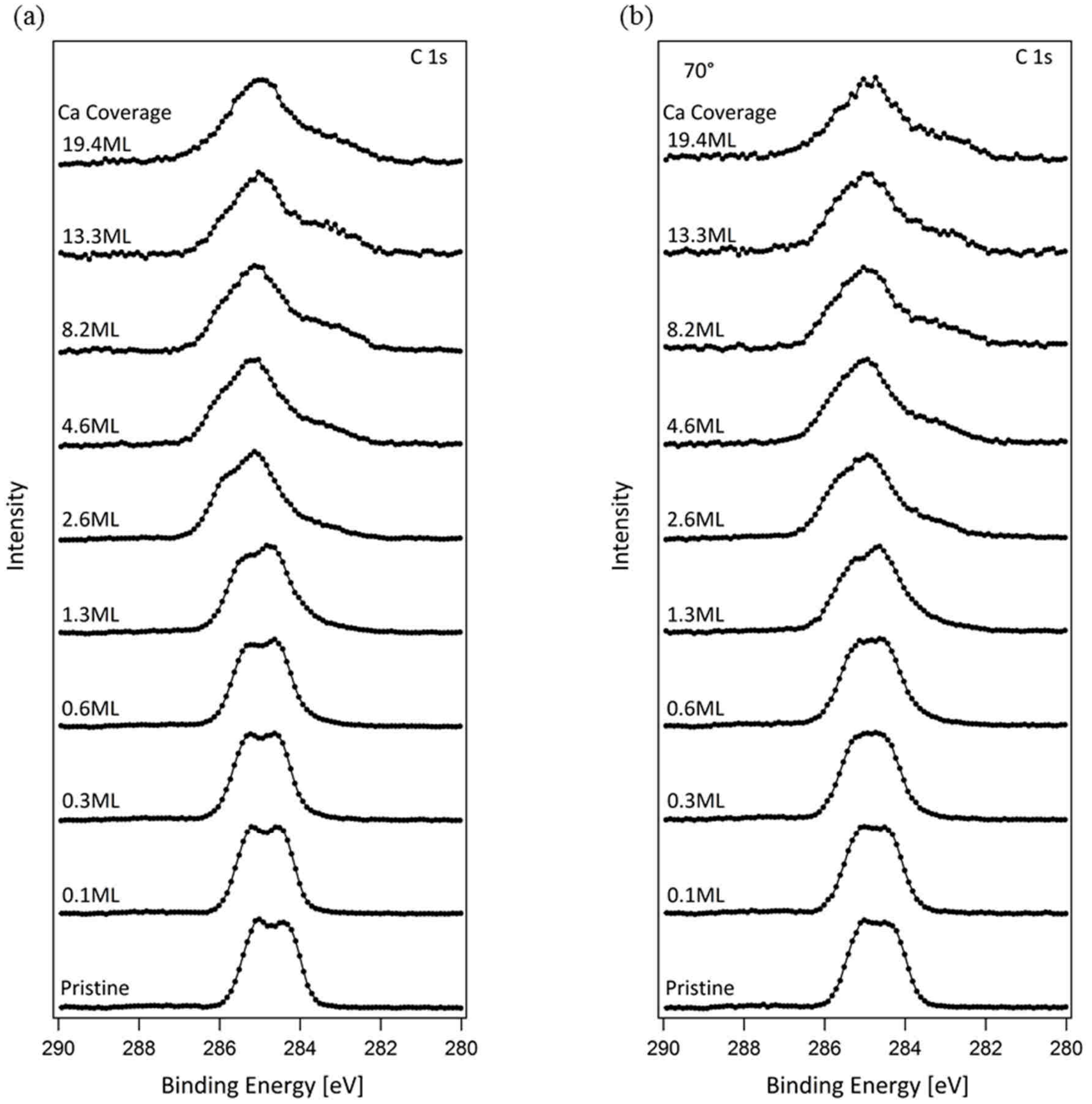

Figure 3.8: C 1s spectra (Al K-α, hν=1486.7 eV) of increasing Ca coverage on a 18.8 nm thick 6T layer. The substrate for deposition is a polycrystalline Au plate. Temperature of deposition: 298 K. (a): Spectra recorded in normal emission geometry; (b): spectra recorded at 70° emission angle relative to the surface normal. The background of the raw data is treated using Shirley background assumption. All spectra are normalized to All spectra are normalized to their respective amplitude of intensity (y data set).

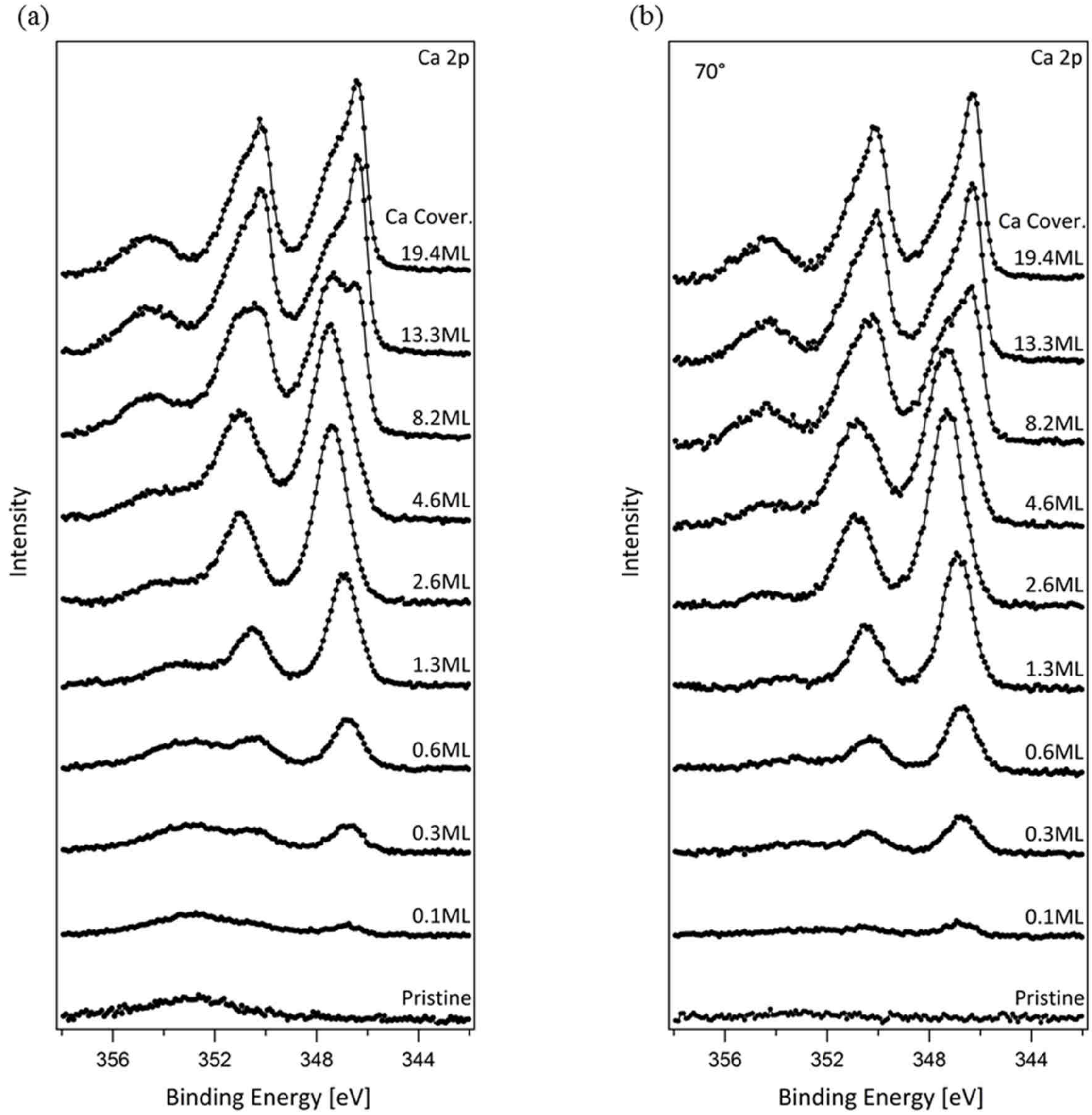

Figure 3.9: Ca 2p spectra (Al K-α, hν=1486.7 eV) of increasing Ca coverage on a 18.8 nm thick 6T layer. The substrate for deposition is a polycrystalline Au plate. Temperature of deposition: 298 K. (a) Spectra recorded in normal emission geometry; (b) spectra recorded at 70° emission relative to the surface normal. For the proper visualization of data, the background of the spectra are subtracted using a linear function, which is obtained by simply connecting the two ends of a spectrum with a line. No normalization of spectra are carried out for the Ca 2p signal.

Regarding the Ca 2p spectra, it is necessary to point out that the broad bump that appears from 348 eV to 357 eV should be attributed to Au 4d signal from the substrate. It is more pronounced in the spectra of normal emission and is almost invisible in the 70° emission spectra due to the differences of their information depth. This overlap with signals from the substrate and the steep baseline of Ca 2p raw spectra themselves make it much less valid to apply Shirley background subtraction or any other comparable background treatments. Beside that, the spin orbital split of Ca 2p signal (≈3.5 eV) is larger than the chemical shift between Ca^{II} and Ca^{0} (≈0.8 eV). This means the 2p doublet of Ca^{II} and Ca^{0} are intrinsically overlapping with each other. The surface core shifts in the Ca^{0} signal will overlap even more intensively with the Ca^{II} signal. Therefore, it is rather difficult to carry out reliable quantitative analysis to the Ca 2p spectra in our system.

In Figure 3.9, as the coverage of Ca increases, the doublet emerging at 348 eV and 351 eV with a peak separation of 3.5 eV is assigned to Ca^{II} from CaS. Starting from the Ca coverage of 1.3 ML, a wide bump appears at the 354 eV, which is attributed to the plasmon of metallic Ca^0. Simultaneously, another sharp doublet emerges closely at the lower binding energy side of Ca^{II} peak. This doublet is attributed to Ca^0. In the spectra of 70° emission, the proportion of the Ca^0 doublet is higher than its normal emission counterpart, which agrees with the assumption that a layer of metallic Ca growth on top of the reacted Ca/6T interphase. The same trend of binding energy shifts are also observable in the C 1s and Ca 2p spectra with the increase of Ca coverage as in the S 2p spectra. However, the quantification of shifts in these two series of spectra are not possible due to the absence of analytical treatment to these spectra.

3.1.4 XPS Study on the Interactions between Ca and 6T Thin Film as a Function of Temperature

Ca deposition at room temperature has been observed to have potentially resulted in the formation of highly uneven and rough interface. At this point, we started to wonder if this morphology-changing interaction could be better controlled at a reduced temperature. Two categories of attempts are carried out in this direction. Firstly, Ca is deposited on a room temperature prepared 6T thin film (38.5 nm) at an intermediately reduced temperature (218K) to see if the reaction could be quenched at that condition, after that, the sample is annealed at series of elevated temperatures up to room temperature. In each annealing step, the desired temperature is realized by the counter action of continued cooling set for 218K and adjusted electron beam heating. Sample is kept at that certain temperature for the equivalent time as the Ca deposition. The XPS measurements were conducted right after annealing after the sample was cooled again down to 218 K to avoid further reaction at the elevated temperature. The method for sample preparations as well as the calculation of film thickness and Ca coverage are the same as described above. As can be seen from Figure 3.10, right after the deposition of Ca at 218 K, the relative proportion of peaks representing reacted species is significantly lower than the spectra in Figure 3.7 with comparable Ca coverage deposited at room temperature, indicating that there is less reaction of Ca with 6T at the lower temperature. The proportion of the reacted species increases with subsequent (post-deposition) temperature increase. A considerable increase in the proportion of the reacted species occurs at temperature between 278 K and 298 K. Furthermore, even after the annealing at room temperature, the proportion of the reacted species is still significantly lower than the comparable spectra in Figure 3.7. It is a significant change from what has been presented in the previous section. Besides this major effect of temperature, other characteristics exhibited in Figure 3.10 are analogous to those we have previously discussed with Figure 3.7. A +0.9 eV of binding energy shift relative to the pristine spectra is observed after the deposition of Ca in the spectra of both emission angles. This shift stays unchanged during the three steps of annealing, indicating a constant state of band alignment.

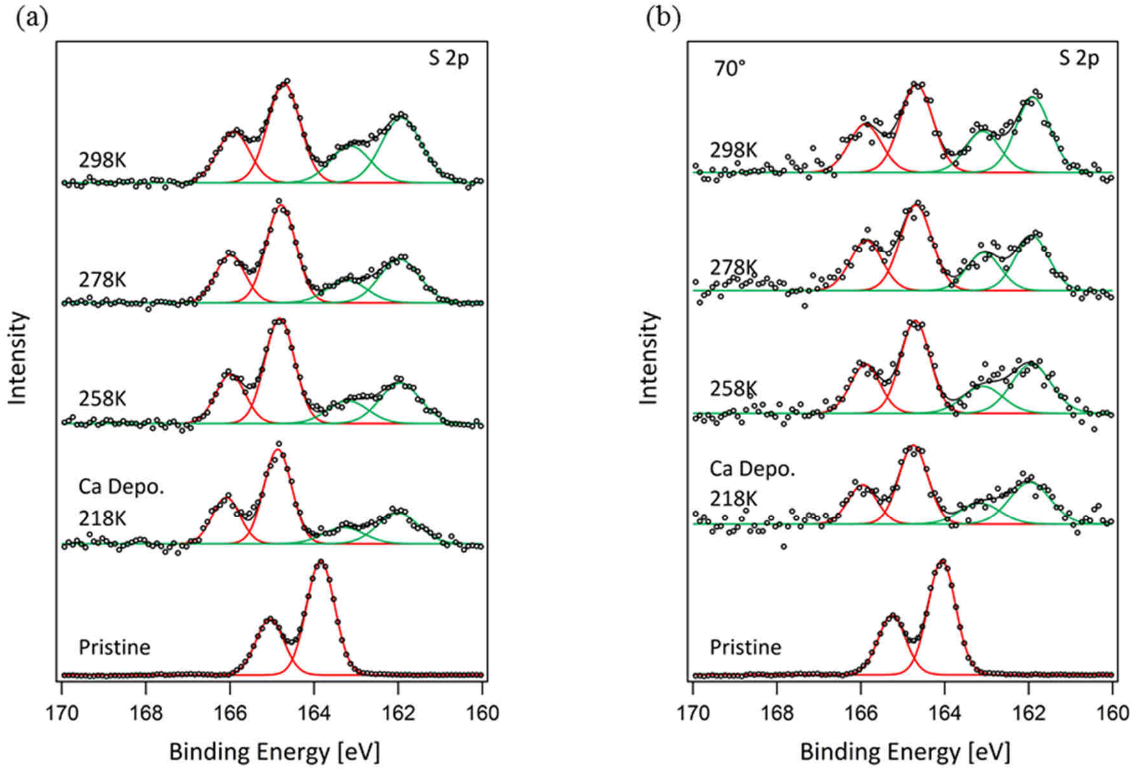

Figure 3.10: S 2p spectra (Al K-α, hν=1486.7 eV) at varied temperatures. 14.7 ML Ca is deposited onto a 38.5 nm 6T layer adsorbed on a polycrystalline Au plate. (a): spectra recorded in normal emission geometry; (b) spectra recorded at 70° emission relative to the surface normal. The background of the raw data is treated using Shirley background assumption. The peaks in the spectra are fitted with GLP functions. All spectra are normalized to their respective amplitude of intensity (y data set).

The C 1s spectra in Figures 3.11 exhibit a trend of changes in agreement with Figure 3.10; the most prominent change in the spectra comes with the Ca deposition. As the temperature of annealing increases, only slight changes are observed. The small narrow peak growing at 281 eV is attributed to C of C=O adsorbed on the surface of metallic Ca.

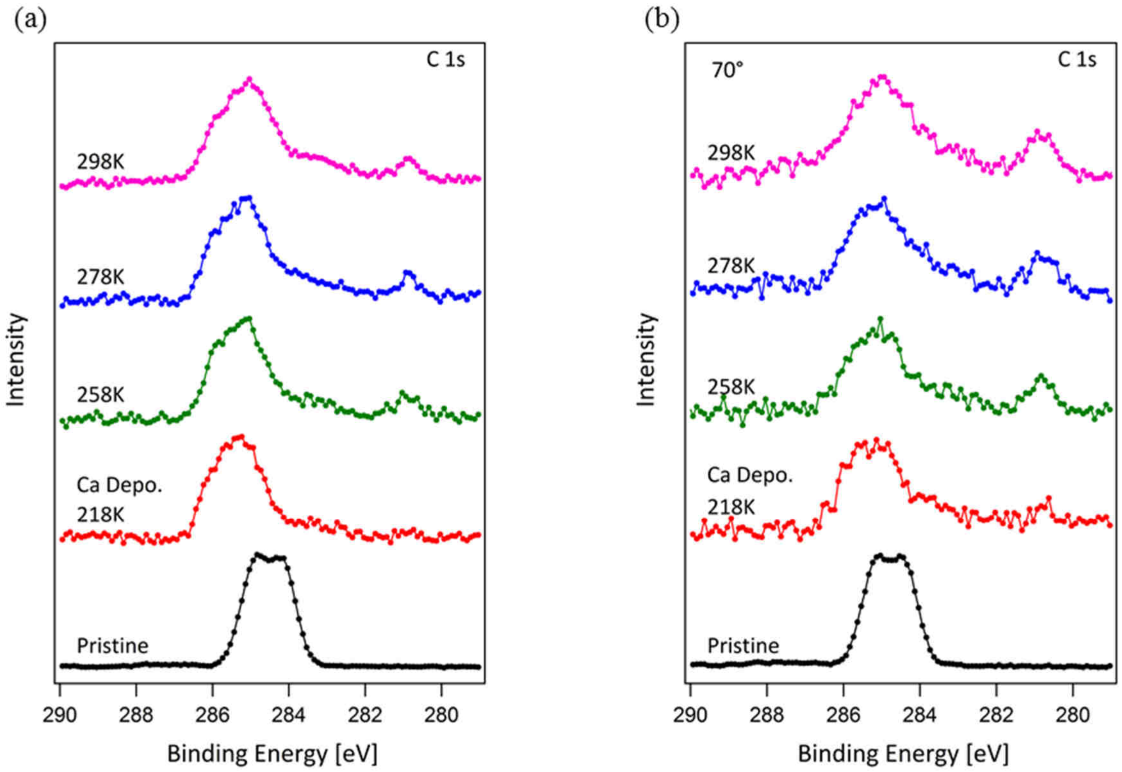

Figure 3.11: C 1 spectra (Al K-α, hν=1486.7 eV) at varied temperatures; 14.7 ML Ca is deposited onto a 38.5 nm 6T layer adsorbed on a polycrystalline Au plate. (a) Spectra recorded in normal emission geometry; (b) spectra recorded at 70° emission relative to the surface normal. The background of the raw data is treated using Shirley background assumption. All spectra are normalized to their respective amplitude of intensity (y data set).

In the related Ca 2p spectra shown in Figure 3.12, a sharp doublet at 346 eV and 350 eV as well as a plasmon at 355 eV persists through out the entire heating up process, demonstrating that the metallic Ca phase does not completely react as the reaction of Ca with S is promoted by heating up. The signal of Ca^{II} increases with heating up, the only pronounced change appears above 278 K, in accordance with what has been shown in the S 2p spectra.

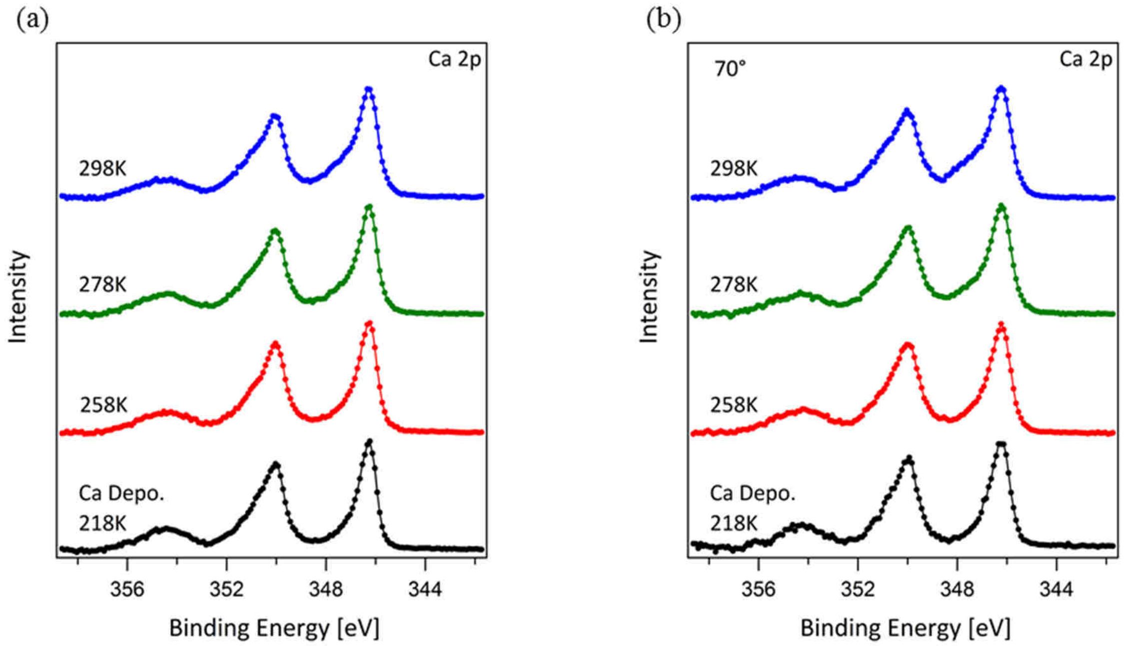

Figure 3.12: Ca 2p spectra (Al K-α, hν=1486.7 eV) at varied temperatures.14.7 ML Ca is deposited onto a 38.5 nm 6T layer adsorbed on a polycrystalline Au plate. (a) Spectra recorded in normal emission geometry; (b) spectra recorded at 70° emission angle relative to the surface normal. The background of the spectra are subtracted using a linear function, which is obtained by simply connecting the two ends of a spectrum with a line. No normalization of spectra are carried out.

As the experiments of varied annealing temperature have demonstrated, the key factor to control the amount of interfacial reaction is the temperature of the organic film during deposition rather than the temperature the metal/organic system reaches subsequently. In a second set of experiment, the temperature of the organic film was varied during Ca deposition. For this purpose, five experiments were carried out at temperatures from142 K to 298 K. The 6T thin films were prepared at room temperature in advance and their thicknesses were controlled to be within 36.4±2.5 nm. XPS measurements after Ca deposition with the same coverage were conducted at a slightly lower temperature than the deposition to prevent the undesired heating up of samples during the measurements. As has been explicitly shown by Figure 3.12, the reaction between Ca and 6T is not completely suppressed even at 142 K. This might be attributed to the high reactivity of Ca and partially to the inevitable heating up effect by the Ca evaporator. Note that we can control (and measure) only the temperature of the Au substrate that supports the organic film. The surface of the organic film may still be at a higher temperature due to the absorption of radiation from the hot Ca source. The lack of cooling to the transfer system should also be noted. However, the temperature of the samples right after the transfer is monitored to be no higher than 10 K above the target temperature. Considering what has been demonstrated in the experiments of varied annealing temperatures, the artifact introduced by the transfer of samples could be regarded as neglectable. As can be seen in Figure 3.13, the proportion of the signal from the reacted species increases with the temperature of deposition. The most pronounced change happens at temperatures above 258 K, which is comparable to the evidence shown in the section before. The ratio of I_r/I_{pri} in the 70° emission spectra is in general higher than its normal emission counterpart, the only odd point appears at spectra at 228 K, where the ratio of I_r/I_{pri} is not only smaller than that in the corresponding normal emission spectra, but also smaller than in the spectra at 178 K. Since these spectra at the meantime exhibit unrealistic high signal to noise ratio, they should be regards as faulty spectra due to unknown technical problems.

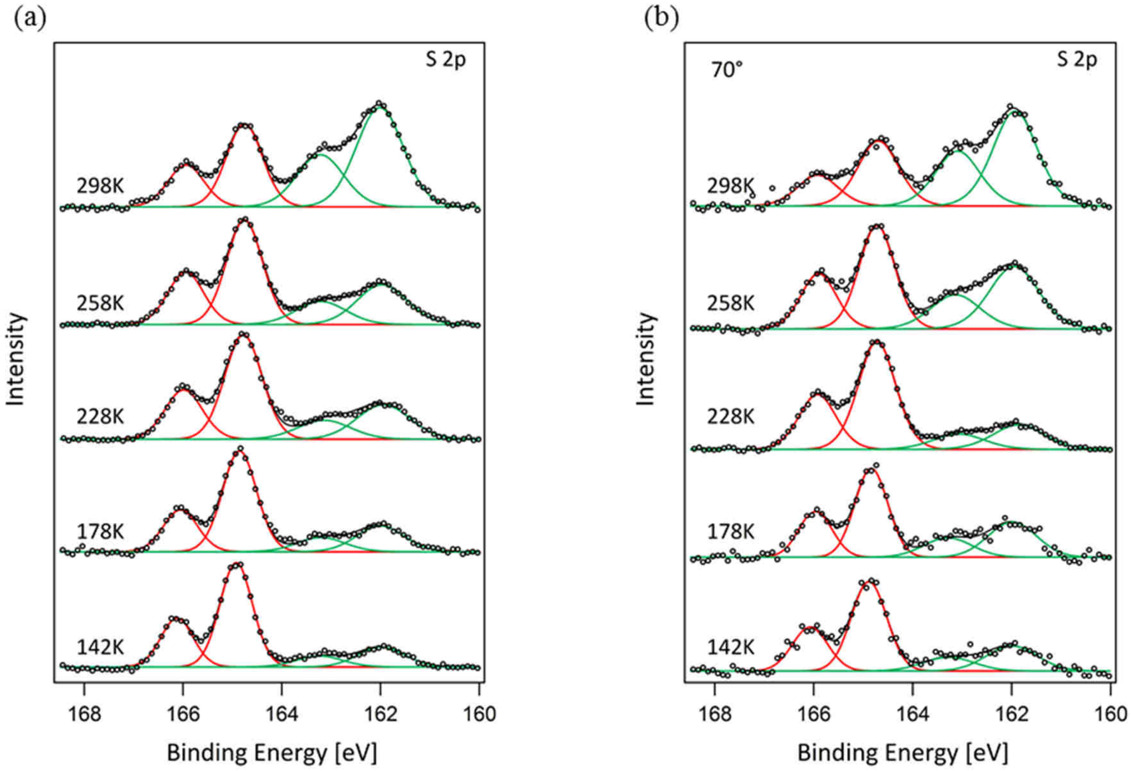

Figure 3.13: S 2p spectra (Al K-α, hν=1486.7 eV) at varied temperatures of deposition. 11.1 ML Ca is deposited onto a 6T layer adsorbed on a polycrystalline Au plate. The thicknesses of the pristine 6T films are controlled to be within 36.4±2.5 nm. (a) Spectra recorded in normal emission geometry; (b) spectra recorded at 70° emission relative to the surface normal. The background of the raw data is treated using Shirley background assumption. The peaks in the spectra are fitted with GLP functions. All spectra are normalized to their respective amplitude of intensity (y data set).

C 1s and Ca 2p spectra are not presented since they do not carry extra information about this set of experiments other than that could be deduced from Figure 3.13. Their characteristics are analogous to that of Figure 3.11 and Figure 3.12 respectively, but with less pronounced reaction related features because of the suppressed degree of reactions under further reduced temperatures.

3.1.5 HAXPES Study on the Interaction of Ca with 6T Thin Film

Hard X-ray Photoelectron Spectroscopy (HAXPES) is employed to obtain a deeper understanding of the structure of the Ca/6T interface by taking the advantage of varied information depth at different photon energies. Photon energies from 2 keV to 6 keV were used in the measurements. The samples were prepared using techniques analogous to the previous results. Thicker 6T films were prepared because the information depth is largely extended under HAXPES condition compared with the common lab source XPS. The binding energy of all spectra was corrected by the Au 4f spectra taken under the same condition from a small gold reference piece sitting next to the sample. Even after this correction, some spectra still show random shifts away from the spectra of other photon energies, these random deviations are attributed to the potential mis operations of monochromator, which, because of hysteresis, provided light with deviated photon energy. The spectra are arbitrarily shifted to lie accordingly with spectra of other photon energies.

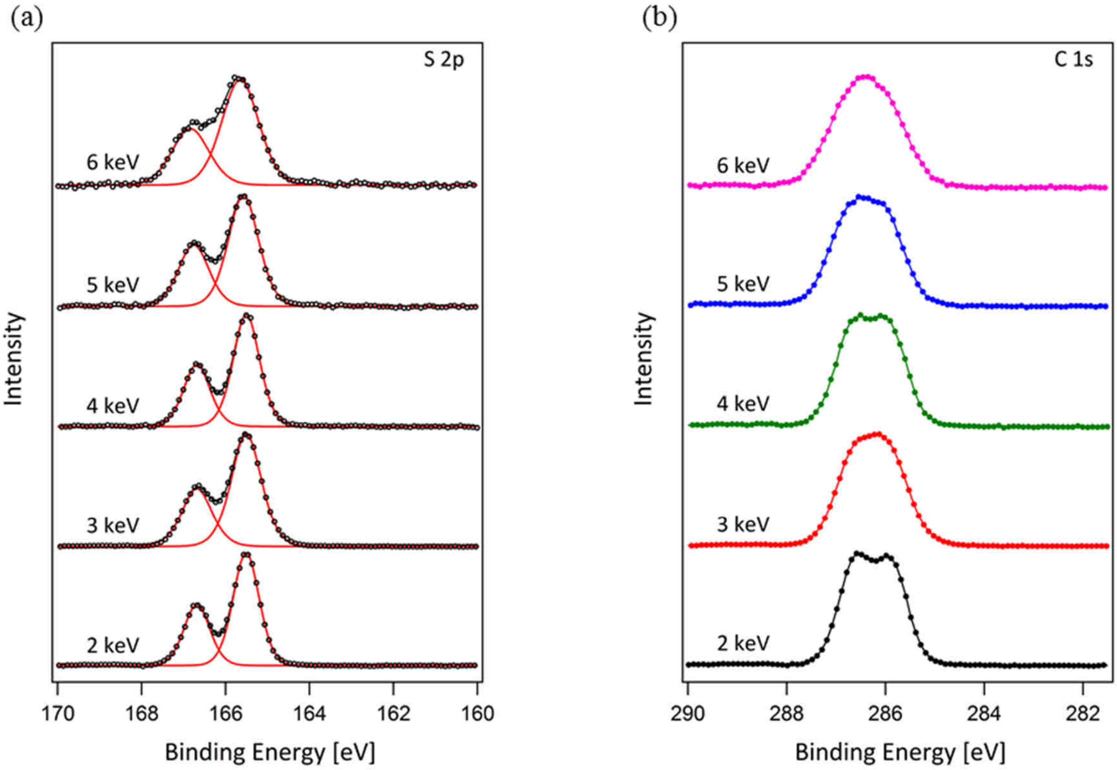

Figure 3.14: XP spectra of pristine 6T taken with different photon energies at 298K. The Spectra are from a 85.0 nm 6T film adsorbed on a polycrystalline Au plate. (a) S 2p spectra; (b) C 1s spectra. The spectra were taken in normal emission geometry. The background of the raw data is treated using Shirley background assumption. The peaks in the S 2p. spectra are fitted with GLP functions. All spectra are normalized to their respective amplitude of intensity (y data set).

The peaks at 5 keV and 6 keV are broader because of the lower monochromator resolution at higher energies. In the experiments, the Si(111) crystals was used for 2 keV and 3 keV; Si(311) was used for 4 keV and 5 keV; Si (422) was used for 6 keV. No sign of X-ray induced beam damage were observed as have been reported.[121-122]

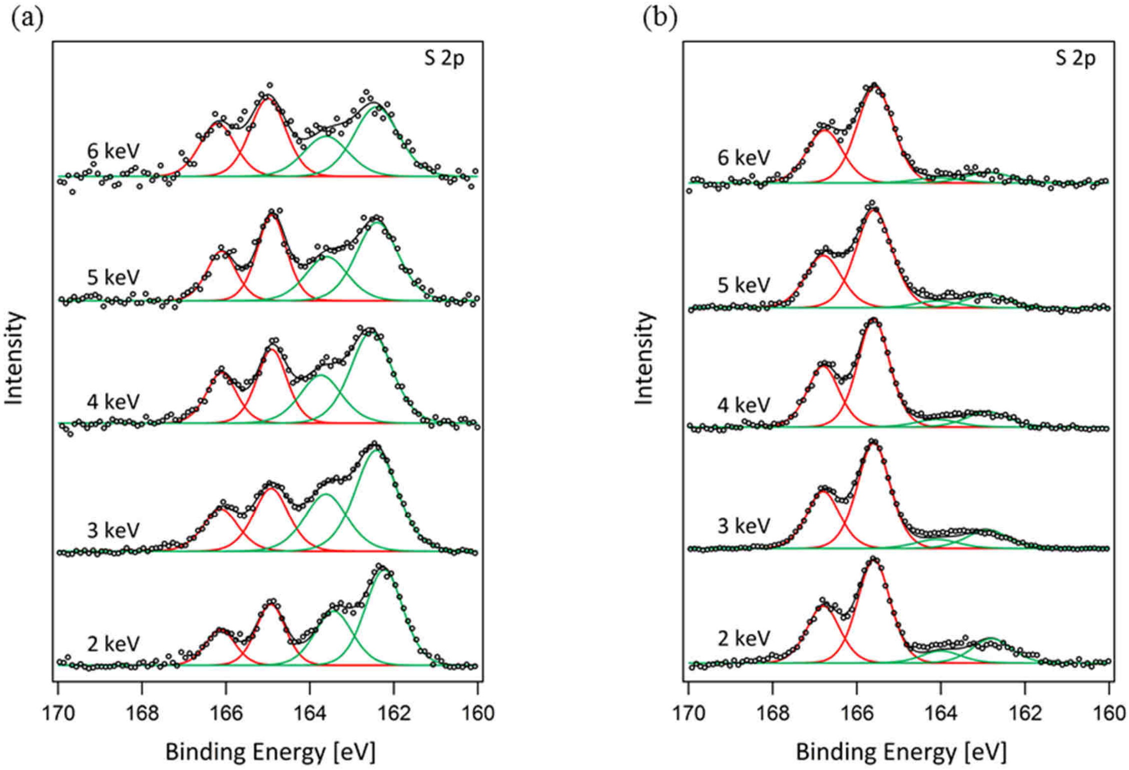

Figure 3.15: S 2p spectra of samples prepared by room temperature deposition (a) and low temperature (153 K) deposition (b) of Ca. (a) 26.1 ML Ca on 84.1 nm 6T; (b) 18.2 ML Ca on 54.2 nm 6T. The spectra are taken with different photon energies in normal emission geometry. The background of the raw data is treated using Shirley background assumption. The peaks in the spectra are fitted with GLP functions. All spectra are normalized to their respective amplitude of intensity (y data set).

In Figure 3.15, S 2p spectra of both room and low temperature experiments show that the I_r/I_{pri} ratio gets smaller with increasing photon energy. As the information depth increases with photon energy, more contributions from the unreacted species underneath the reacted layer (interphase) are observed. S 2p spectra from the deposition at 153 K exhibit much smaller proportion of reacted species than the corresponding room temperature spectra. This is in accordance with what has been demonstrated in the measurements with the lab X-ray source. The comparability of these two spectra series might be questioned since the thickness of 6T and coverage of Ca are both different in these two experiments. However, as can be seen in the Ca 2p spectra of both samples (Figure 3.16), contributions from metallic Ca^0 at around 364.5 eV are visible in both series of spectra. It confirms the existence of excessive Ca^0 above the reaction zone in both series. However, for the low temperature sample the Ca^0 component is much smaller and not proportional to its coverage if compared with what have been demonstrated in the previous section. This problem arises from the rather high residual gas pressure in the HIKE endstation, which has a base pressure around 1×10^{-8} mbar. With the sample cooled to 153 K, water condenses rapidly at the sample surface. Oxygen molecules have an even larger sticking probability on the Ca surface than at room temperature. In this way, more Ca^0 are consumed by the side reactions with residual gas at low temperature than at room temperature, provided that the time of exposure to residual gas for both samples are roughly the same during the experiment.

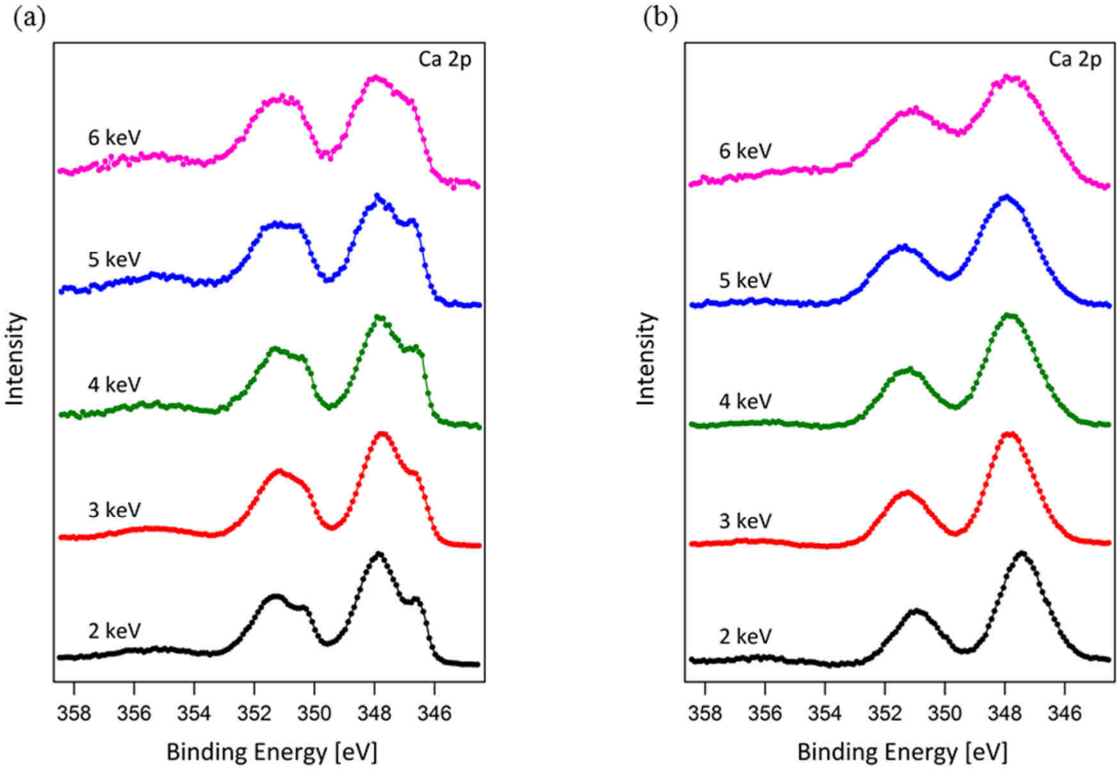

Figure 3.16: Ca 2p spectra of samples prepared by room temperature deposition (a) and low temperature (153 K) deposition (b) of Ca. (a) 26.1 ML Ca on 84.1 nm 6T; (b) 18.2 ML Ca on 54.2 nm 6T. The spectra are taken with different photon energies in normal emission geometry.

The main peak in the C 1s spectra (Figure 3.17) of the room temperature prepared sample is in general broader than its counterpart prepared by deposition at 153 K. This of course points to a higher complexity of the reacted species and more intensive reactions at room temperature than at the reduced temperature. For both deposition temperatures, the relative intensity of reacted species standing at 282-286 eV decays with the increasing photon energy. This stands in line with the trend demonstrated by the S 2p signals that relatively more signals are coming from the unreacted thiophenes as the information depth increases. It must be clarified that the C 1s spectra of the low temperature deposition from 4-6 keV are taken with the Si(111) crystal of the monochromator, making it invalid to directly compare the spectra of this three photon energies with the corresponding spectra from the room temperature experiment.

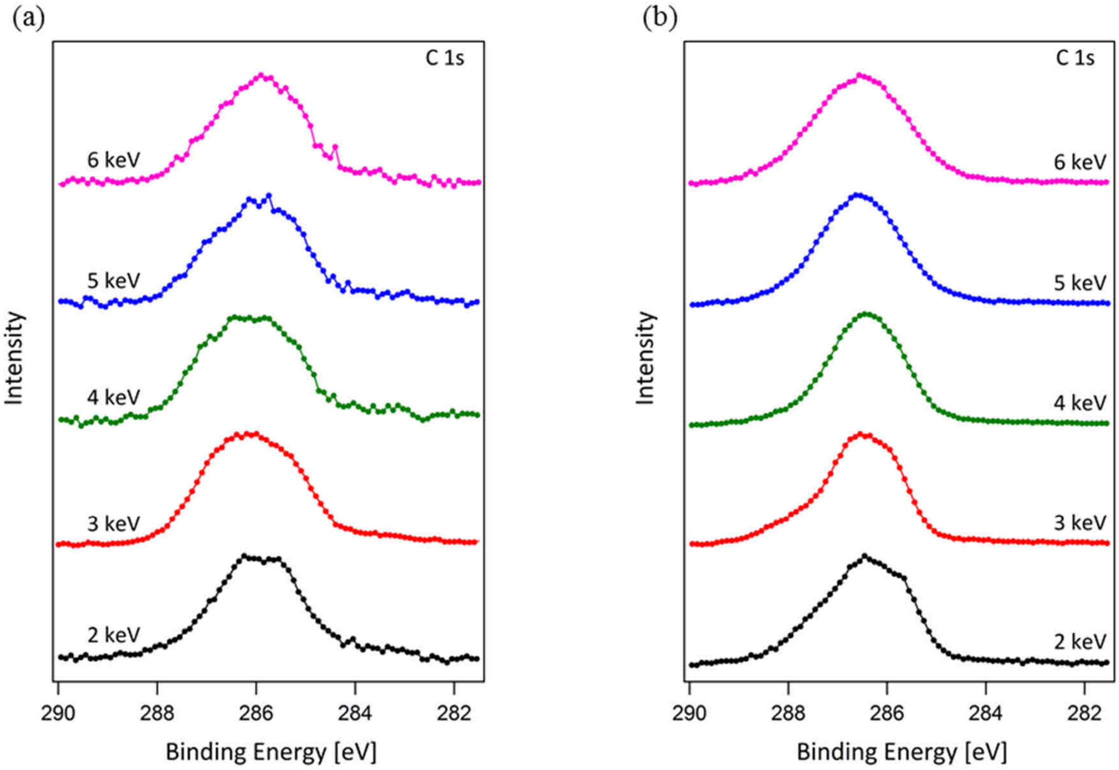

Figure 3.17: C1s spectra of samples prepared by room temperature deposition (a) and low temperature (153 K) deposition (b) of Ca. (a) 26.1 ML Ca on 84.1 nm 6T; (b) 18.2 ML Ca on 54.2 nm 6T. The spectra are taken with different photon energies in normal emission geometry. The background of the raw data is treated using Shirley background assumption. All spectra are normalized to their respective amplitude of intensity (y data set)

As has been presented by Figure 3.18, co-deposition of Ca and 6T at 298 K, with a Ca/S stoichiometry of 1:1, is carried out based on the QCM flux measurement. Because both the accurate density and acoustic impedance of 6T are not available, QCM based stoichiometry may not be realized as designed. In Figure 3.18, the two component structure of the spectra, which is demonstrated in the layer by layer deposition experiments, is no longer suitable for the interpretation of the spectra structure. Instead, a broad combination of three components structure is introduced. This indicates that, when sufficient or even excessive Ca presents, the reaction of Ca/6T might be modified as excessive metal could result in the formation of meta-stable organo-metallic complex. In the spectra, a middle doublet is fitted to represent the possible meta-stable species. The spectra of different photon energies exhibit little structural difference, which indicates that there is a “homogeneous” mixture of pristine, stable product and meta-stable product formed by co-deposition. Therefore, in contrast to the layer by layer results in the previous sections, the product of co-deposition has a depth profile indistinguishable morphology.

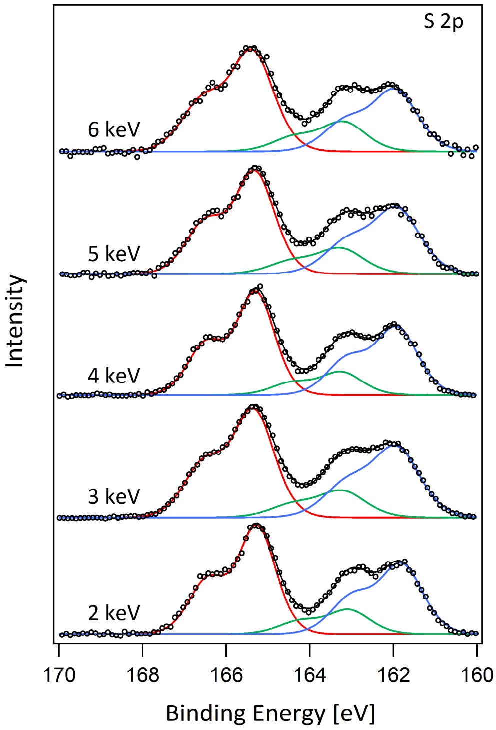

Figure 3.18: S 2p Spectra after the co-deposition of Ca and 6T on a polycrystalline Au plate at room temperature. The spectra are taken with different photon energies in normal emission geometry. The background of the raw data is treated using Shirley background assumption. The peaks in the spectra are fitted with GLP functions. All spectra are normalized to their respective amplitude of intensity (y data set).

3.2 Discussions

3.2.1 Growth of Ca on 6T at Metal-Organic Interface

When metal and organic phase with different work functions get in contact with each other, charge redistribution should occur at their interface until electrical equilibrium is reached. In another word, Fermi levels of metal and organic phases are aligned. As Ca had just started to diffuse and react with 6T, intensive charge transfer is expected to build up a interfacial dipole in the first reacted thin layer of materials. Consequently, work function of the surface layer is significantly changed. In many literature, this phenomenon is called surface/interface band alignment, which will be reflected as binding energy shifts of core level spectra.[6, 11, 123-125] This change of work function will proceed with the increase Ca coverage until the work function of Ca becomes the work function of the system, because the entire photoemission area on the surface has been covered by the first monolayer of metallic Ca.

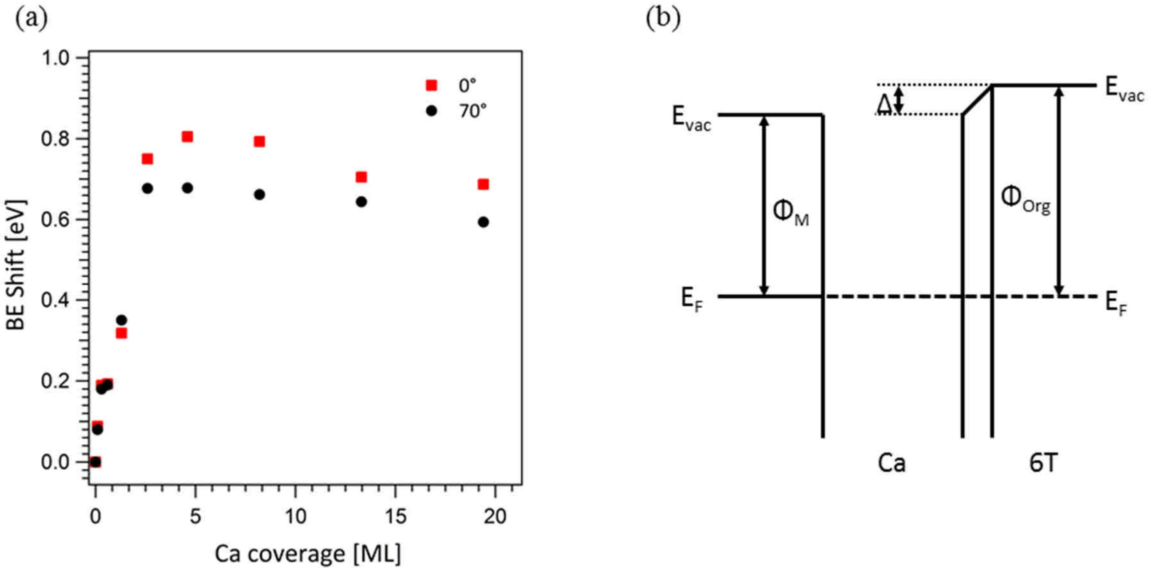

Figure 3.19: (a) Binding energy shift of normal and 70° emission as a function of Ca coverage on 18.8 nm 6T; data are extracted from the peak position of S $2p_{3/2}$ signals in Figure 3.7. The depositions are carried out at 298 K. (b) Ideal energy diagram of the Ca/6T interface; E_{vac}: Energy of vacuum level; E_F: Fermi level; Φ_M: work function of the metal, in this work it refers to the work function of Ca; Φ_{Org}: work function of the organic substrate, in this work, it refers to the work function of 6T.

Figure 3.19 shows, with the coverage of Ca increasing from 0 to 4.6 ML, the binding energy shift of the S 2p signals from the two emission angles in Figure 3.7 both peak rapidly at about 0.7~0.8 eV. As has been discussed in the results part, evidence of metallic Ca^0, the plasmon at 354 eV in the Ca 2p spectra from Figure 3.9, are clearly visible starting from a Ca coverage of 2.6 ML. In addition, the decrease of binding energy shifts after 4.6 ML could be attributed to the final state screening effect of manifested metallic Ca phase, which will in general shift the spectra to lower binding energy positions. These two evidences together indicate the existence of metallic Ca starting from the coverage of 2.6 ML. The work function of thick layer 6T, as being reported by the previous studies,[11, 125] is about 3.5–3.8 eV, while the work function of Ca is 2.9 eV. The band alignment from 6T to Ca should have a corresponding binding energy shift of 0.6~0.9 eV, which is in good accordance with the result of this study.

In the previous study on Ca/rr-P3HT system, layer-by-layer reaction of Ca with rr-P3HT was proposed.[35, 46] In this work, the polymer rr-P3HT is replaced with its oligomeric homologue 6T, which has higher density of reactive sites and better defined conformational structure. However, according to the results shown in Figure 3.20, no evidence is found to support an analogous mechanism of interphase formation and structure of metal-organic interface.

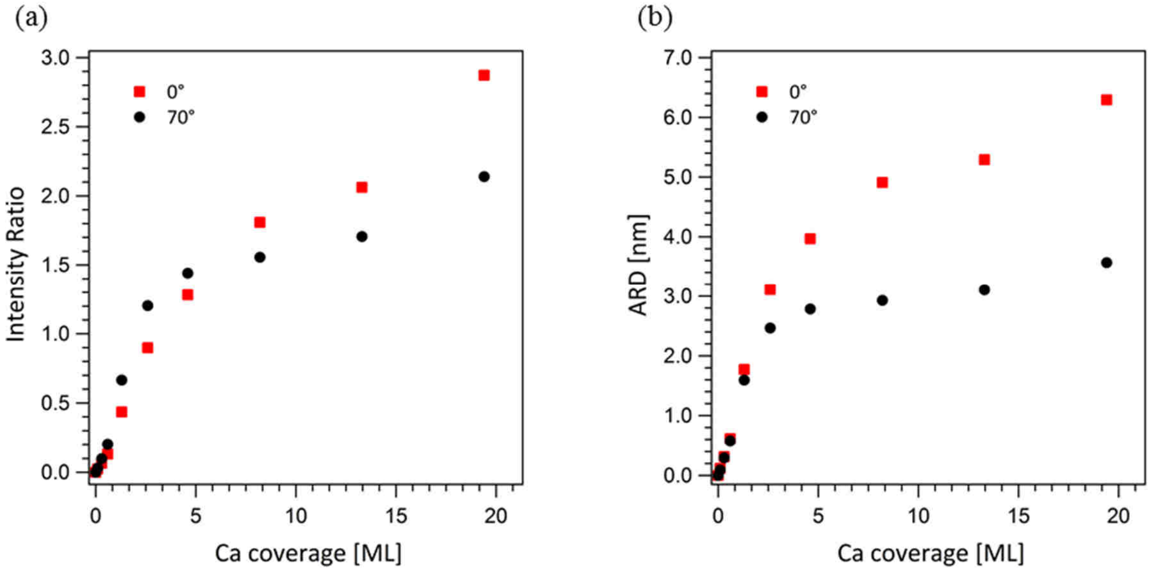

Figure 3.20: Ca coverage dependent quantities extracted from Figure 3.7: (a) Ratio between the intensities of pristine signal and the intensities of reacted species (I_r/I_{ur}) in S 2p spectra as a function of Ca coverage; (b) calculated ARD as a function of the Ca coverage; the thickness of 6T is18.8 nm; temperature of deposition is 298 K. The averaged reaction depth (ARD) is calculated using Equation 1.17. The IMFP of the photoelectrons, λ, for Equation 1.17 is taken from the literature.[126]

If the planar layered interphase and the abrupt interface are formed after Ca deposition, I_r/I_{ur} should always be higher from 70° emission than from normal emission geometry at low coverages. ARD calculated by different emission angles should not exhibit large deviation. In this study, I_r/I_{ur} of 70° emission is only slightly higher than that of normal emission geometry up to 5 ML. Thereafter, it becomes smaller than the data from normal emission geometry and increases much slower as well. As for the ARD, data match persists merely up to 1.3 ML and a rather large deviation of the data from two emission angles occurs at higher coverages. Because Equation 1.17 is based on the assumption of planar layered structure and abrupt interface, the deviation of ARDs from two emission angles implies that no such structure is present after Ca coverage exceeds 1.3 ML. Furthermore, if the I_r/I_{ur} of 70° emission becomes even smaller than the normal emission one, which means more signal from the unreacted species are observed from the grazing angle than from the surface normal, it is far beyond our initial expectation, the non-planar morphology at the interface should then be considered.

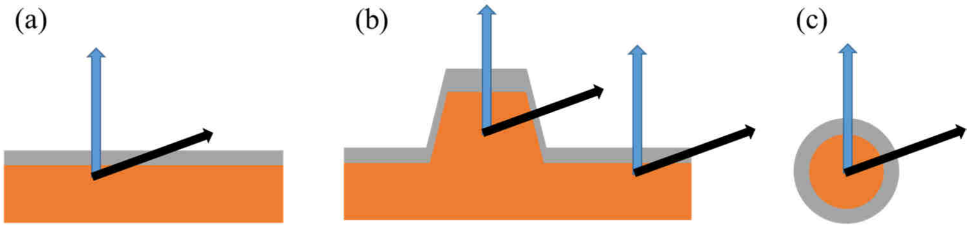

Figure 3.21: Schematic illustration to the influence of interface morphology on normal and 70° emission; (a) planar layered structure; (b) rough and uneven surface and interface; (c) core-shell type particle.

Scheme (a) in Figure 3.21 represents the ideal planar layered structure of interface, its characteristics has already been discussed. Scheme (b) represents the mixture of partially layered but rough and uneven structure at the surface and interface. In this situation, if photoelectron is emitted from the trapezoidal slope standing out of the surface, the effective reacted layer observed from 70° might be thinner than that from the surface normal, this is plausible because when the deposition of top layer is carried out from the surface normal, the projected thickness of an overlayer or interlayer on the tilted plane is intrinsically smaller. Scheme (c) represents core-shell structure of particles. In this situation, signals from all the emission angles should give exactly the same results. In this study, depositions of Ca are all carried out from the normal direction of the sample. Due to the destructive nature of the reaction between Ca and 6T as well as the tendency of clusterization that Ca bears when forming its own phase, when two factors both influence the morphology of the interphase right at the vicinity of Ca/6T interface, it is possible that starting from a certain Ca coverage (in this work above 2.6 ML), extensive roughening of the Ca/6T interface may occur as a result of intensive reactions. This hypothesis is also supported by the results of TEM and EDX (Figure 3.2, 3.3 and 3.4).

The absence of flat layered structure at the Ca/6T interface is also demonstrated by the HAXPES results. Table 3.1 presents the I_r/I_{ur} from the S 2p spectra of Figure 3.15. More relative contribution from the signal of the unreacted species are observed as the information depth increases while the calculated ARD also increases. If a thin layered structure analogous to the Ca/rr-P3HT system is formed at the Ca/6T interface, changing of information depth should give steady ARD numbers unless even the information depth under 6 keV is still not large enough to see through the entire reaction zone. However according to the dimensions of reaction zone demonstrated by TEM and EDX, the information depth under 6 keV ($3\lambda=59.3$ nm) should be enough to reach the pristine region. Therefore the only explanation to the HAXPES results at room temperature is the absence of flat layered structure and abrupt transition at the Ca/6T interface. As is presented in Table 3.2, the deposition at 153 K has significantly contained the reactions between Ca and 6T, resulting in much lower ARDs for all photon energies. However, the ARD still increases with the information depth. It means there are always some more reacted species being discovered when we look deeper into the bulk of the sample despite the overall abatement of the reactions. It implies that during the deposition of Ca at low temperature, some Ca atoms would not react instantaneously with the thiophenes in the surface layers, however would still be able to travel tens of nanometers deeper into the bulk and undergo reactions there. This phenomenon makes it necessary to further discuss the decisive factor of the Ca/6T interaction.

Table 3.1 ARD Calculated for Different Photon Energies

hv	λ [nm]	Intensity Ratio	ARD [nm]
2 keV	6.71	1.96	7.29
3 keV	10.07	1.89	10.70
4 keV	13.35	1.62	12.83
5 keV	16.57	1.29	13.60
6 keV	19.75	1.06	14.10

- Deposition of 26.2 ML Ca on 85.0 nm 6T at 298 K
- λ for photon energies from 2 keV to 6 keV are taken from the literature[126]

Table 3.2 ARD Calculated for Different Photon Energies

hv	λ [nm]	Intensity Ratio	ARD [nm]
2 keV	6.71	0.27	1.61
3 keV	10.07	0.22	1.98
4 keV	13.35	0.18	2.18
5 keV	16.57	0.16	2.39
6 keV	19.75	0.13	2.45

- Deposition of 18.2 ML Ca on 54.2 nm 6T at 153 K

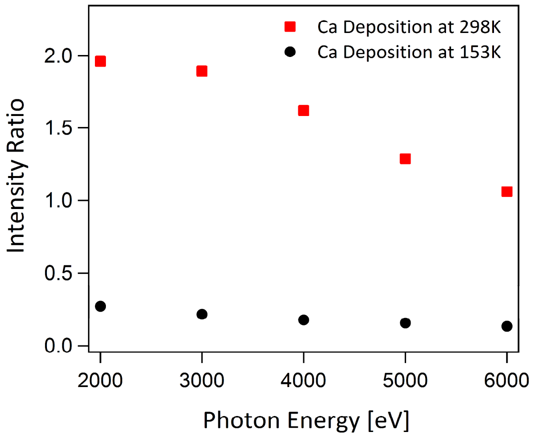

Figure 3.22: I_r/I_{ur} of the S 2p spectra from Figure 3.15. Red square: 26.2 ML Ca on 85.0 nm 6T deposited at 298 K; black disc: 18.2 ML Ca on 54.2 nm 6T deposited at 153 K.

3.2.2 Control of the Interaction Between Ca and 6T

The control of Ca/6T interaction is realized via the change of deposition temperature, albeit the complete suppression of the reactions between Ca/6T has not been achieved in our studies.

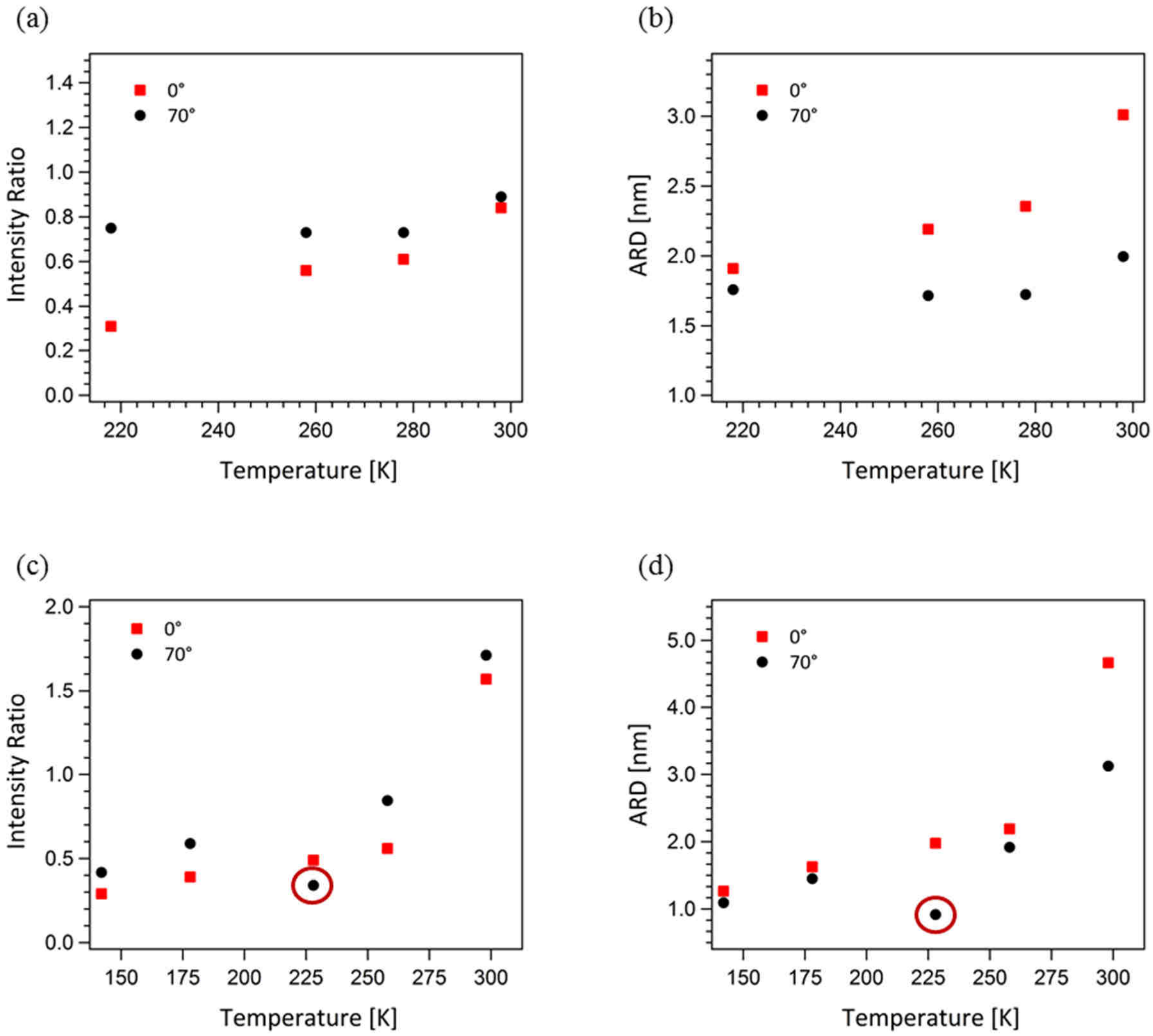

Figure 3.23: (a) (b) I_r/I_{ur} of the S 2p spectra from Figure 3.10 and the corresponding ARDs as a function of temperature. Ca deposition at 218 K, annealed at various temperatures; thickness of 6T: 38.5 nm; coverage of Ca: 13.5 ML. (c) (d) Ca deposition at various temperatures, thickness of 6T: 36.4±2.5 nm; coverage of Ca: 11.6 ML. The odd data points in the rose red circles are attributed to the technical error of the system and omitted from analysis.

Figure 3.23 shows that the temperature of the system exerts a very strong influence on the reaction between Ca and 6T. Lower Ca deposition temperatures in general result in lower I_r/I_{ur} and smaller ARD. By varying the temperature, it is possible to reduce this reaction and tune the I_r/I_{ur} at a wide range of values. By comparing the results of varied Ca deposition temperature with the results of annealing at the same temperature, it is apparent that the dominant factor is the temperature of the organic material during the deposition of the metal (c and d in Figure 3.23) rather than the temperature that the metal/organic system has after the metal deposition (a and b in Figure 3.23). When free Ca atoms arrive at the 6T surface during deposition, the reaction with 6T and diffusion into the 6T bulk are two simultaneous processes which start instantaneously. If not being captured by the surrounding thiophene units, Ca atoms may migrate deeper into the bulk.

The diffusion of the mobile atoms inside the condensed matter follows the Fick's law. For the system of Ca/6T, it can be expressed as:

$$F_{\mathrm{Ca}} = -D_{\mathrm{Ca\text{-}6T}} \frac{\partial c(x,t)}{\partial x} \tag{3.2}$$

In which F_{Ca} is the flux of incoming Ca atoms. In each experiment of this study, it is kept constant throughout the deposition. $D_{\mathrm{Ca\text{-}6T}}$ is diffusion coefficient of Ca inside 6T, $c(x,t)$ is concentration of Ca in a distance x from surface at time t. According to some previous studies,[127] the diffusion coefficient of vapor deposited metal inside an organic polymer can be expressed as follows:

$$D_{\mathrm{Ca\text{-}6T}} = D_0 \exp\left(\frac{-E_{\mathrm{diff}}}{\mathrm{k}T}\right) \tag{3.3}$$

Where D_0 is the Preexponential factor, E_{diff} is the activation energy of diffusion, k is the Boltzmann constant, T is the system temperature.

Both the reaction of Ca/6T and diffusion of Ca inside 6T can be respectively described by the Arrhenius formalism with their own Preexponential factor and activation energy. The temperature of the system dominates both processes but not equally. Because the reaction is irreversible while the diffusion is fully reversible, considering the experimental time of a few hours for each experiment, the change to the rate of diffusion rate would have much higher probability than then change of the reaction rate to influence the accumulated result observed by the experiment. Therefore, the significant drop in the extent of reactions (Figure 3.22, 3.23) at the reduced temperatures should mainly be the consequence of the sharp drop in the diffusion rate rather than the drop in the reaction rate. There could be a small proportion of the Ca atoms being "frozen" inside 6T phase as Ca^0 as the substrate temperature is reduced. Therefore, when the samples are annealed at mildly elevated temperatures, slightly more reactions between Ca and the thiophene of 6T occurs due to the increase of Ca mobility (Figure 3,23). However, if the diffusion rate the is controlling factor, one might argue that Ca should be able to react with 6T in the surface and subsurface layers even if the diffusion rate is too low for them to travel far into the bulk within the time of experiment. On the contrary, the result shows even in the longest room temperature experiment (Figure 3.7, the whole experiment took 14 hours), pristine signals are still clearly seen from the top most layers of the material (Figures 3.7 b, 70° emission) under high Ca coverages.

To address this question, we should look back to the mechanism of reaction between Ca and 6T. This reaction, though not fully understood, should always start with the cleavage of S–C bond on one of the 6 thiophenes rings.[35] Very likely, R–S–Ca (relative charge distribution unknown and not marked) meta-stable intermediates are produced.[128] Because the S–Ca bond are stronger than the R–S bond inside the meta-stable intermediates and CaS has a tendency to form cluster, upon the cleavage of CaS, R· radicals or R^+ cations may be formed depending on the chemical environment. They both exhibit very strong tendency to attack the other conjugated rings to form bicyclic compound or cross-link with neighboring molecules, thus introducing huge modification to the configuration of molecular backbone. Both intra- or intermolecular bridging would result in localized steric hindrance for Ca atoms to further contact with the still unreacted thiophenes at the vicinity. The steric barrier will strongly influence the E_{diff} of Equation 3.3 and reduce the local diffusion rate of Ca. Meanwhile, the diffusion barrier into the less reacted regions in the deeper bulk is much less affected. Furthermore, if Ca atoms diffuse at and react with the remaining thiophene inside the already chemically modified region, even higher steric hinderance is immediately added to the region. The local diffusion rate is again reduced. The diffusion barrier in the reacted region may have become so high that within the time of an experiment, the diffusion rate into the reacted region could be neglected. These chemically modified regions appear to be inert against any further reactions for a certain temperature. As a consequence, the Ca atoms arriving at the surface can only diffuse and react with the thiophenes in the less sterically hindered region in the deeper layers

3.2.3 The Structure of the Ca/6T Interphase

Since we have discussed the controlling factor and the possible mechanism of Ca/6T interactions at interface, it becomes clear that a more complete model of the Ca/6T interphase could be established. The remaining question here is the strong variation of the ARD to the information depth (Table 3.1, 3.2), The ARD is the result of applying the equation for the reaction depth, which was derived for a layer-by-layer system, in a situation where such a system is clearly not present: up to information depths of 40 nm the experimental ratio of reacted to unreacted species is practically constant for room temperature (Figure 3.22, red square). This points to a coexistence of reacted and unreacted S in the interphase region. For higher information depths, the ratio between reacted and unreacted signals decreases. This is a clear indication that the relative concentration of unreacted S increases for layers that can be measured with these higher information depths.

To better understand the actual concentration of the reacted and unreacted species at each depth from the surface, i.e., the concentration profile and its influence on the measured intensity ratio, numeric simulation based on a genetic algorithm is carried out using the method introduced in the literature.[55] This method randomly generates a large number of the test concentration profiles (up to 10^3) and calculate the intensity ratio of each profile using the following equation:

$$\frac{I_{\mathrm{r}}}{I_{\mathrm{ur}}}=\frac{\int_0^d c_{\mathrm{r(z)}}\exp\left(-\frac{z}{\lambda}\right)\mathrm{d}z}{\int_0^d (1-c_{\mathrm{r(z)}})\exp\left(-\frac{z}{\lambda}\right)\mathrm{d}z} \tag{3.4}$$

The numerator and denominator of this fraction equation are both transformed from equation 1.4, which are written as the normalized concentration of the reacted species ($c_{\mathrm{r(z)}}$) or of the unreacted species ($1-c_{\mathrm{r(z)}}$). $c_{\mathrm{r(z)}}$, the concentration of the reacted species at depth z, also represents the probability of the signal from the depth z being emitted by the reacted species. By minimizing the total deviation of the Equation 3.1 calculated ratio from the experimentally measured ratio (Figure 3.22) for various photon energies, the optimal concentration profile is sorted out over the generations of test profiles (Figure 3.25).

The concentration profile for room temperature experiments (a in Figure 3.25) exhibits constant constitution of 67% reacted and 33% unreacted species from the boundary of the organic layer to about 29 nm deeper. The concentration of the reacted species drops sharply to zero within 1.9 nm. The results of simulation for room temperature experiments also conforms with the results of EDX shown in Figure 3.4, whereby a 40~60 nm wide of signal overlap between S and Ca is observed. A sharp transition from the constant constitution indicates that 30 nm is likely the diffusion limit of Ca inside thick 6T film at room temperature.

The concentration profile for low temperature experiments exhibits a sigmoidal decay into the bulk. Such result indicates that Ca atoms may migrate into the deeper bulk without instantaneous reaction with pristine 6T molecules. Otherwise another constant concentration for this temperature should be reached. At low temperature, the reaction zone has much lower concentration of the reacted species than the reaction zone formed at room temperature. It is also considerably thinner than that of the room temperature, as the 99% of all reacted S species are found within the first 20 nm of the organic layer.

The high diffusivity of Ca inside the 6T films, especially the notable diffusion at low temperature, brings about a challenging question to the understanding of the complete interaction procedure. If we review the studies on Ca/rr-P3HT system, which has the most comparable reaction mechanism[34-35, 46] and the systems of metal/large conjugated organic molecule, i.e., Mg on PTCDA,[43] Co on 2H-tetraphenylporphyrin (2HTPP),[55] which have highly comparable molecular size and conformation.[43, 50, 129-132] High reactivity of Ca, Mg or Al means higher probability of being captured by the organic molecules. Reactions with these highly reactive metals often result in drastic modifications to the molecular backbone, which in return becomes the hinderance to the diffusion of more metal atoms, just as has been discussed in this work. However, in the previous studies, the morphology or the structure of organic layers at a relatively larger scale have not been given much attention. Most discussions try to focus on the influences of intrinsic chemical properties of the substances. As our results have suggested, structural change inside the organic film could have significant influence on the diffusivity and the growth behavior of metals on the organic film. This topic requires further and more systematic studies to address the yet unanswered questions, such as the quantification to the influence of structural factors on the diffusion coefficient and their evolvements after the reactions.

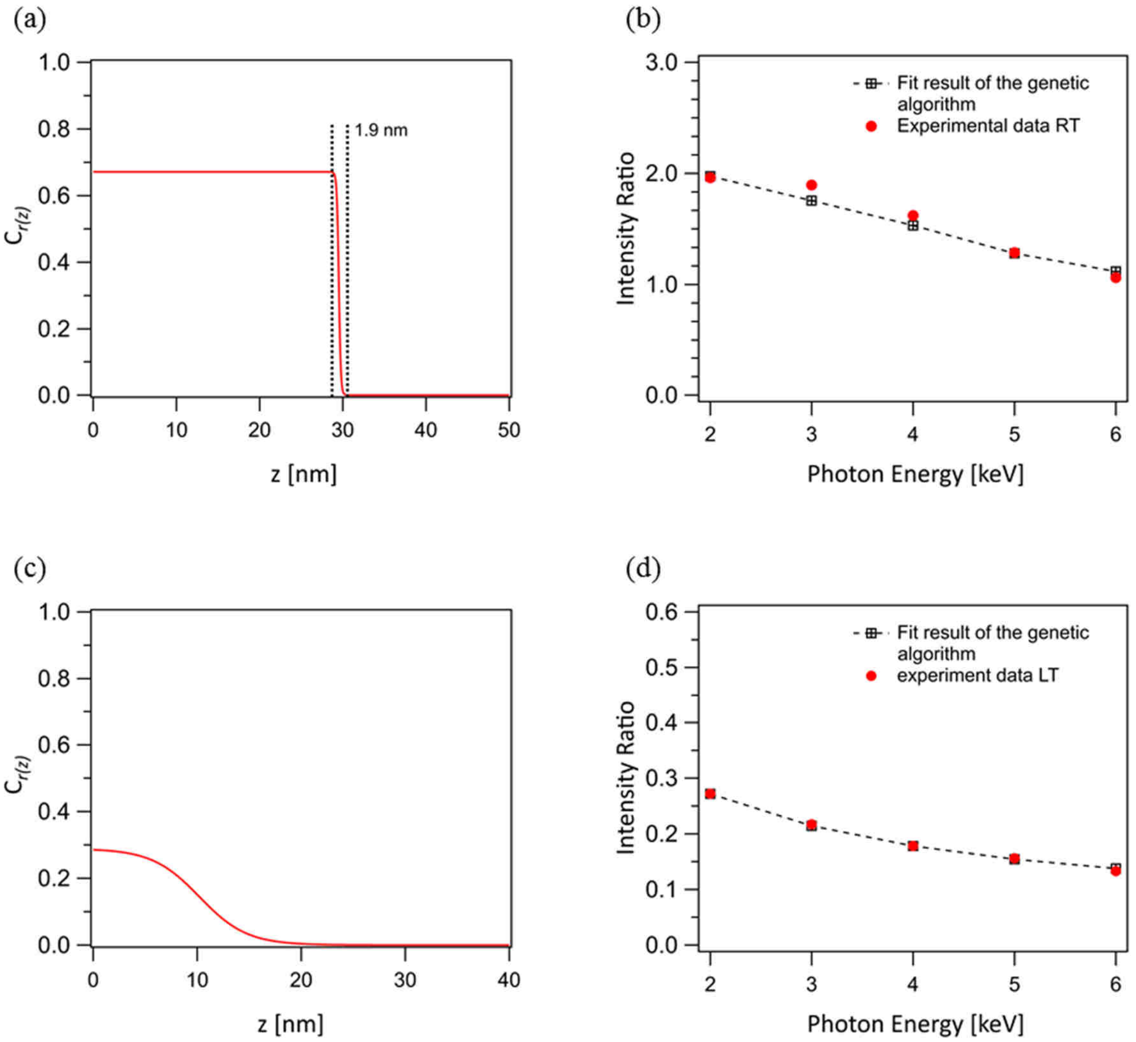

Figure 3.24: (a), (c) Simulated concentration profile for room temperature and low temperature HAXPES results; the transition region in (a) is about 1.9 nm thick. (b), (d) calculated intensities for the simulated profiles and their corresponding experimental data for various photon energies.

4 Calorimetry of Metal/Organic Interaction

4.1 Results

The adsorption of Ca on 6T has been studied with a home-built nanojoule adsorption calorimeter partly described in a previous PhD thesis.[96] For comparison, adsorption of Ca on PTCDA has also been studied by adsorption calorimetry to show the possible influences of the growth mode and the resulting interphase structure. The experiments were carried out with the organic film at room temperature (here 310 K at the position of the calorimeter) without any external manipulation of temperature. The enthalpy of adsorption as a function of Ca coverage on these two materials are obtained simultaneously with the sticking probability. The Ca coverage is expressed in units of ML; 1 ML is defined as $7.40 \cdot 10^{18}$ atoms/m^2. This is equivalent to the atomic density in the (111) crystal plane of bulk Ca.

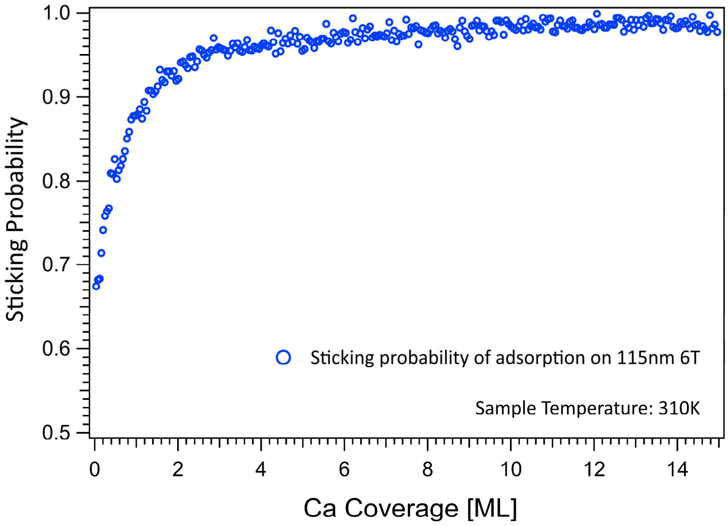

Figure 4.1: Coverage dependent sticking probability of Ca on 6T. The trace in the figure is the numerical average of three experiments under nearly identical conditions, in which thickness of 6T substrates are slightly different due to the limitation of precise vapor flux control while other conditions are kept identical.

To determine the precise amount of Ca atoms that adsorbs on 6T for calorimetry, the sticking probability of Ca must be known as a function of coverage. Figure 4.1 presents the coverage dependent sticking probability of calcium on an approximately 115 nm thick vapor deposited 6T film held at 310 K. The results shown is the numerical average of three experiments. As can be seen from Figure 4.1, two regimes can be identified. In the low coverage regime, the sticking probability sharply increases with Ca coverage from its initial value of 0.67. This is analogous to previous studies from the literature.[35, 46] The sticking probability reaches around 0.95 at 2.6 ML. Above this coverage, the sticking probability increases slowly and eventually converges to 0.98. While the lower initial sticking probability is obviously determined by the adsorption of Ca on the pristine organic film, the high-coverage range is dominated by metal-on-metal adsorption of Ca on its own bulk, for which high sticking probabilities are common.

In Figure 4.2, the differential heat of adsorption of Ca on 6T is shown. The measured heat has an initial value of about 275 kJ/mol. With increasing coverage, the heat decreases only slowly until a value of 265 kJ/mol is reached at around 3.5 ML. After this, the heat decreases faster and reaches a minimum around 10 ML, where it is approximately 25 kJ/mol below the heat of sublimation of Ca, 177.8 kJ/mol at 310 K. Above 10 ML, the heat of adsorption slowly increases until it reaches the heat of sublimation around 15 ML.

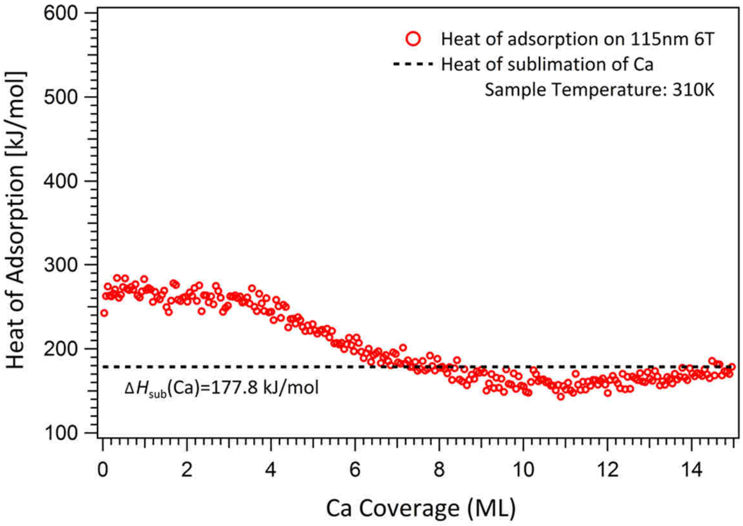

Figure 4.2: Coverage dependent heat of Ca adsorption on ~115 nm 6T. The trace in the figure is the numerical average of 3 experiments under similar conditions, in which thickness of 6T substrates are slightly different due to the limitation of precise vapor flux control while other conditions are kept identical.

In Figure 4.3, coverage dependent sticking probability of calcium on 640 nm vapor deposited PTCDA at 310 K is presented. Unlike adsorption on 6T, on PTCDA, the sticking probability of Ca starts at 0.98, already close to unity sticking. After an initial decrease with the a minimum of 0.90 around 3.5 ML, the sticking probability increases again and reaches 0.98 at 11 ML.

Figure 4.4 shows the corresponding differential heat of adsorption of Ca on 640 nm PTCDA. Different from Ca/6T system, a rapid drop of heat signal, starting from 530 kJ/mol, is observed until Ca coverage reaches 0.2 ML. No pronounced plateau of signal is found in the trace, which is principally differed from what has been shown by Figure 4.2 for Ca/6T system. The heat decreases slowly from 0.2 ML on. The minimum of 162 kJ/mol is reached at 10 ML, where the heat of adsorption is again slightly below the heat of sublimation of Ca.

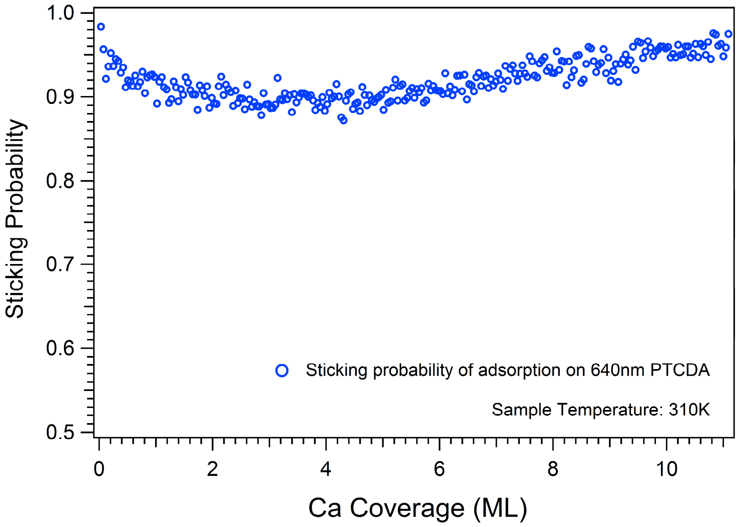

Figure 4.3: Coverage dependent heat of Ca adsorption on PTCDA. The trace in the figure is the numerical average of three experiments under similar conditions, in which thickness of 6T substrates are slightly different due to the limitation of precise vapor flux control while other conditions are kept identical.

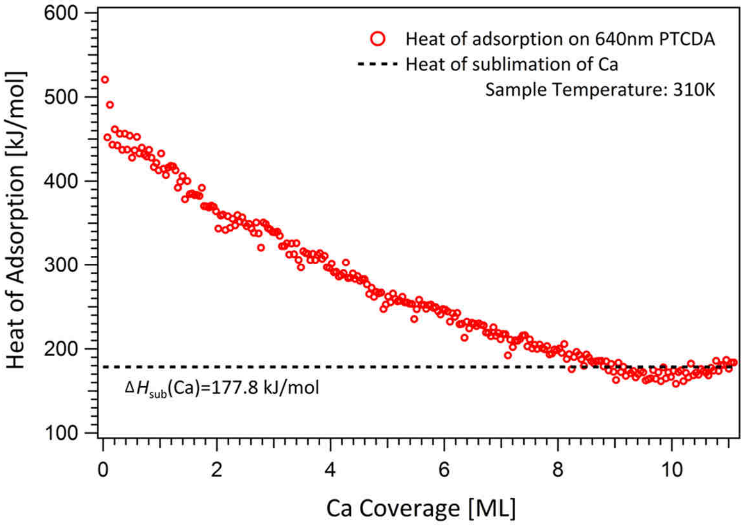

Figure 4.4: Coverage dependent heat of Ca adsorption on PTCDA. The trace in the figure is the numerical average of 3 experiments with similar conditions, in which the thickness of 6T substrates are slightly different due to the limitation of precise vapor flux control while other conditions are kept identical.

4.2 Discussions

4.2.1 Sticking Behavior Indicated Growth Model of Ca on 6T/PTCDA

From the results of the sticking probability measurements shown above, different sticking behaviors of Ca on these two organic substrates are seen. Both are dominated by the competitions among Ca bonded to Ca, Ca bonded to molecules of substrate, and desorption.[105] The intrinsic sticking probability of a metal atoms to its own bulk is usually unity or very close to it.[38, 84-85] On the other hand, the sticking probability of metal atoms to an organic substrate is highly dependent on the crystallographic structure, chemical properties of the molecules and the morphology of the organic substrate. Close to zero coverage, Ca sticks far better on PTCDA than on 6T. On PTCDA, the initial sticking probability is close to one, whereas the initial sticking probability on 6T is only 0.67. The higher initial sticking probability on PTCDA could partially be attributed to higher reactivity of the dianhydride group compared to that of the thiophene units in 6T. More specifically, the activation barrier for the reaction with the carboxyl group of PTCDA is obviously lower than the barrier with thiophene of 6T. However, this is only true for oligomeric molecules but not for polymer with comparable functional groups. Initial sticking probability of Ca on poly(methyl methacrylate) (PMMA) or rr-P3HT are reported to be both in the range of 0.4–0.5,[35, 37] because Ca sticks much poorer on aliphatic group while long aliphatic chains constitute the majority of the polymer, especially in the case of rr-P3HT.[32, 35, 37, 49]

The decrease of sticking probability on PTCDA indicates that after the occupation of unsaturation of the active sites on the surface, more Ca atoms are reflected back to the vacuum.[105] On an ideally flat surface with flawless ordered structure (Figure 4.5 a), diffusion of adatoms into the bulk of the substrate would become increasingly more difficult as the reaction progresses, because a transiently adsorbed adatom becomes less likely to reach an active substrate site deeper in the bulk. At the same time, the competing processes, i.e., desorption or formation of metal clusters, become relatively more likely. When more Ca atoms arrive at the surface, they see fewer and fewer pristine active sites in the topmost layers of PTCDA while there are not yet Ca clusters to which they can stick better. As a consequence, the sticking probability keeps decreasing until the minimum is reached, after which the sticking of Ca atoms to Ca clusters becomes the dominant process at around 3.5 ML until a consecutive metal phase is formed.[35, 37]

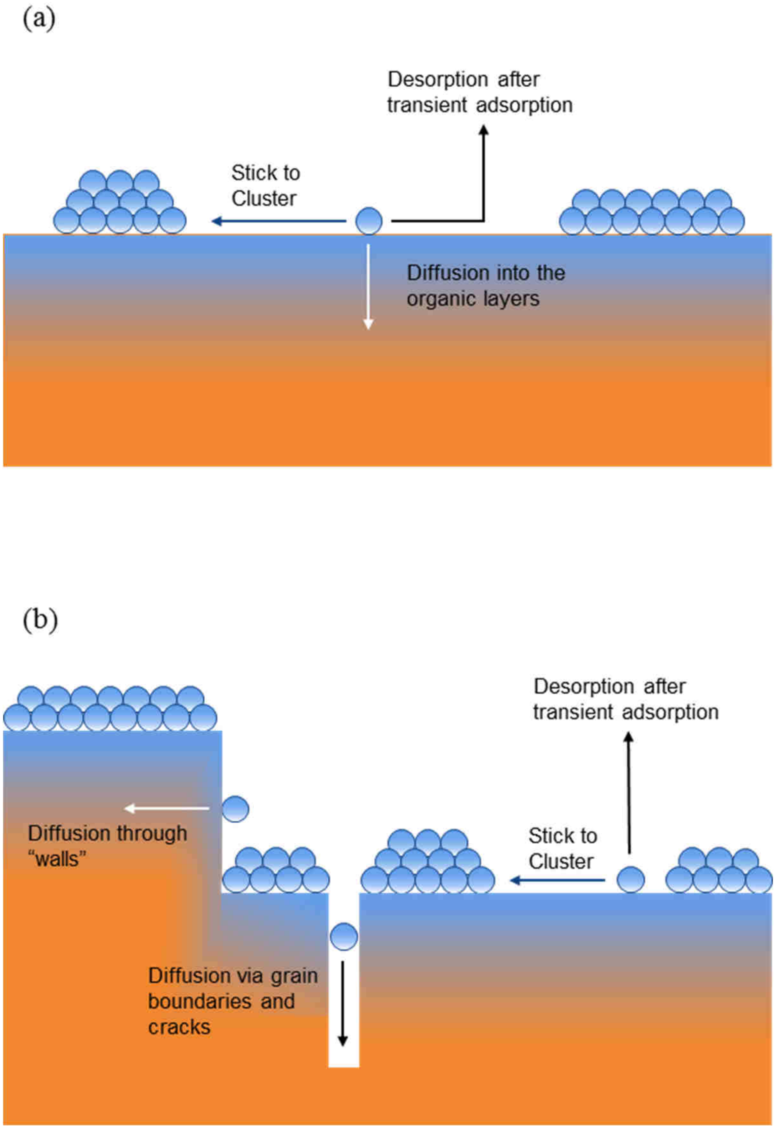

Figure 4.5: Schematic illustration to the two models of metal adsorption on organic substrate. (a) Adsorption of metal atoms on the ideally flat and defect-free substrate. (b) Adsorption of metal atoms on non-ideal surface with defects and grain boundaries.

In contrast, Ca deposition onto 6T leads to a sharp increase of the sticking probability between zero coverage and 2.6 ML (Figure 4.1). As has been argued in many studies,[35, 37-38] this increase is mainly the contribution of more Ca atoms binding to Ca clusters. The sticking probability reaches value over 0.95 when an almost fully metal covered surface has been formed. In the spectroscopic studies discussed in the previous chapter, it has been shown that the completion of band alignment appears at around 4.6 ML (Figure 3.19). Evidence for metallic Ca, i.e., the plasmon appears at 354 eV in Ca 2p spectra (Figure 3.9) are also observed since the Ca coverage of 2.6 ML. If only the data of band alignment and sticking probability are considered employing the growth model proposed by the literature,[35] the completion of band alignment would also mean the dominance of Ca sticking to 3D Ca clusters until the continuous Ca multilayer film is formed. It would be impossible for Ca to diffuse and react with more thiophenes in the bulk. However, it has also been proven that the diffusion and reaction of Ca and 6T continues even until the coverage exceeds 10 ML (Figure 3.20). This contradiction requires us to construct a new model that better reflects the nature of the Ca/6T interface system (Figure 4.5 b).

In the previous chapter, we have discussed the structure of a vapor deposited 6T film. Its supposedly rough surface and polycrystalline structure could potentially result in a situation depicted in Figure 4.5b.[133] As the Ca coverage reaches 2.6 ML, there is no exposed 6T film from the perspective of the Ca source. The surface dipole has been fully established so that the band alignment in the photoelectron spectra is completed. Yet it does not necessarily mean that the bulk like Ca layers itself is closed to stop further diffusion of Ca into the 6T bulk. As is proposed in the modified model, Ca atoms could still enter the 6T layers by the permeation through the "wall" of the bumps or diffused across the grain boundaries into the deeper bulk. Even if they back diffuse from the bulk, they have increasingly less chance to desorb from the surface because they would then be captured by the Ca clusters already sat atop the 6T phase. In this model, the increase of sticking probability is not solely contributed by the increased sticking incidences to Ca clusters. As is discussed in the previous chapter, the steric hinderance introduced by the reaction may also act as barrier to the unreacted Ca atoms or tiny Ca clusters, preventing them from back diffusion to the surface. Such deviation from the conventional model of growth will be further discussed in the following part about energetics.

4.2.2 Energetics of Adsorption of Ca on 6T/PTCDA

According to the two sites model proposed by Zhu et al.,[37] the differential heat of adsorption (ΔH_{ads}) measured by the adsorption calorimetry is the sum of two components: the heat of Ca bonding/reaction to substrate molecules ($\Delta H_{\mathrm{ads,\,R}}$) and the heat of Ca bonding to 3D Ca cluster ($\Delta H_{\mathrm{ads,Ca}}$). They represent two independent and competing processes. Their relationship is express in equation 4.1:

$$\begin{aligned}
&\Delta H_{\mathrm{ads}} = f_{\mathrm{r}} \cdot \Delta H_{\mathrm{ads,\,r}} + (1-f_{\mathrm{r}}) \cdot \Delta H_{\mathrm{ads,\,Ca}} \\
&-\Delta H_{\mathrm{ads,\,r}} = \Delta H_{\mathrm{f}}(\mathrm{OP}_{\mathrm{solid}}) + \Delta H_{\mathrm{f}}(\mathrm{CaX}) - \Delta H_{\mathrm{f}}(\mathrm{Ca}_{\mathrm{gas}}) - \Delta H_{\mathrm{f}}(\mathrm{OR}_{\mathrm{solid}}) \\
&-\Delta H_{\mathrm{ads,Ca}} = \Delta H_{\mathrm{f}}(\mathrm{Ca}_{\mathrm{gas}}) - \Delta H_{\mathrm{f}}(\mathrm{Ca}_{\mathrm{solid}}) = \Delta H_{\mathrm{sub}}(\mathrm{Ca})
\end{aligned} \tag{4.1}$$

Where f_{r} denotes the fraction of all adsorbed Ca which reacted with substrate molecules; OP denotes the organic product of the reactions of Ca with 6T or PTCDA; OR represents the organic reagent, i.e., 6T or PTCDA.

At very low coverage, it is assumed the formation of 3D Ca clusters could still be neglected,[35, 37] i.e., $f_{\mathrm{r}} \approx 1$. Therefore, the initial heat of adsorption can be regarded as the direct representation of the heat of reaction between the metal and the organic film ($\Delta H_{\mathrm{ads,r}}$ in equation 4.1). In the previous study on the adsorption calorimetry of Ca on rr-P3HT,[35] very sharp drop of adsorption heat from over 600 kJ/mol to 405 kJ/mol is observed at very low coverage range from 0 to 0.05 ML. It is attributed to a small concentration of adsorption sites on the rr-P3HT surface, which may originate from residual impurities such as chloroform or surface adsorbed water. In our study of Ca adsorption on 6T, no such sharp drop of heat signal is observed. Because rr-P3HT can only be spin coated after dissolution by solvent like chloroform and cannot be baked for degassing, it is highly likely that residual solvent or water from ambient atmosphere persists on the sample until being reacted actively with Ca. This is, however, not the situation for vapor deposited 6T, because the evaporants in the crucible have already been properly degassed before sample preparation and undergo a further purification step by sublimation before the actual deposition.

In this study, the initial heat of adsorption is 275 kJ/mol as the $\Delta H_{\mathrm{ads,r}}$ and thus much lower than the 405 kJ/mol reported for the Ca/rr-P3HT system. This deviation requires discussion, given that, in both systems, the main chemical reaction is the reaction of Ca with thiophene. As a simple model reaction, we consider the reaction between thiophene (liquid) and cyclooctatetraene (liquid) as OR and OP, respectively, in equation 4.1, which now writes:

$$-\Delta H_{\mathrm{ads,\,r}} = \frac{1}{2}\Delta H_{\mathrm{f}}(\mathrm{Cyclooctatetraene_{liquid}}) + \Delta H_{\mathrm{f}}(\mathrm{CaS_{solid}}) - \Delta H_{\mathrm{f}}(\mathrm{Ca_{gas}}) - \Delta H_{\mathrm{f}}(\mathrm{Thiophene_{liquid}}) \tag{4.2}$$

Cyclooctatetraene is the theoretical product of two butadienyl diradicals. A butadienyl diradical may be formed when the sulfur atom is removed from thiophene through a hemolytic dissociation of the carbon-sulfur bonds. It is a 10pi anti-aromatic system and therefore will avoid conjugation. The situation on polymeric thiophene after the ring opening reaction is therefore well represented. If only the standard values are used, where ΔH_{f} (Cyclooctatetraene$_{\mathrm{liquid}}$) = 254.5 kJ/mol, ΔH_{f} (CaS$_{\mathrm{solid}}$) = -473.2 kJ/mol, ΔH_{f} (Ca$_{\mathrm{gas}}$) = 177.8 kJ/mol; ΔH_{f} (Thiophene$_{\mathrm{liquid}}$) = 80.96 kJ/mol, it would give a $\Delta H_{\mathrm{ads,R}}$ = 605 kJ/mol, a value that deviates even more than the 405 kJ/mol of Ca/rr-P3HT system from the measured heat of 275 kJ/mol of this work.

There are two major factors that could contribute to the deviations between the model reaction and the calorimetric data. First, the cluster size of CaS has a very decisive influence on $\Delta H_{\mathrm{ads,r}}$. The standard formation enthalpy of CaS refers to the formation of bulk CaS solid. If the formation enthalpy of a single CaS molecule (or ion pair), 123.6 kJ/mol,[134] is employed, $\Delta H_{\mathrm{ads,R}}$ would be reduced to only 7.9 kJ/mol. This means, the CaS formed in the reaction of this study is neither in a state of single molecule (ion pair) nor bulk CaS. In the previous study of Ca/rr-P3HT system, DFT calculations were employed to demonstrate the influence of CaS cluster size (the Kelvin effect) upon the formation enthalpy. The calculation uses CaS single molecule as base point to show how the stability of the cluster evolves as the size of CaS cluster increases (negative evolution in total energy of cluster relative to the single molecule). The result shows that the cluster of $(\mathrm{CaS})_x$ is dramatically stabilized even by very small increase of cluster size. From single CaS molecule to the cluster of $\mathrm{Ca_4S_4}$, the total energy decreases by 351 kJ/mol. This trend becomes milder upon further increase of the cluster size: For the clusters $\mathrm{Ca_{32}S_{32}}$, $\mathrm{Ca_{108}S_{108}}$, and bulk CaS, the total energies relative to the CaS molecule are -471 kJ/mol, -502 kJ/mol, and -503 kJ/mol, respectively. From our experimental results, the energy deviation is about 330 kJ/mol. To justify this, even smaller average cluster size is needed. Because of the higher density of potentially reactive sites (compared with rr-P3HT) and the nature of this reaction, pronounced steric hindrance is introduced by cross linking inside the 6T phase. Such hindrance would also prevent the locally formed CaS molecules to diffuse out of this local trap and bond with other CaS molecules. Because all these happens ever since the first cleavage of S on a 6T molecules, one may assume that this steric effect took place with the start of adsorption. Therefore, a smaller average CaS cluster size in Ca/6T reaction than Ca/rr-P3HT reaction is possible. Since even very slight reduction in cluster size would result in huge increase in total energy, it is reasonable to attribute the huge deviation of $\Delta H_{\mathrm{ads,\,r}}$ from $\Delta H_{\mathrm{ads,\,model}}$ to the cluster size effect, at least partially.

The second factor should be attributed to the other product of Ca/6T reaction. Given the complexity of the reactions between Ca and 6T, the employment of cyclooctatetraene as the model product of the Ca/6T reaction should be questioned. In the study of Ca/rr-P3HT reaction,[35] the reliability of the model product is justified by the claim that no significant changes in the C 1s spectra are observed. Cyclooctatetraene as the product would cause very little change in the C 1s spectra after the reaction. However, in our spectroscopic study of the Ca/6T reaction, very pronounced features emerge on both the high and the low binding energy sides of pristine signal in the C 1s spectra (Figure 3.8). Especially the species emerging on the low binding energy side has been reported to represent the new compound with higher electron density in the metal/polythiophene interaction system.[135] It could be assumed that after the reaction, organic products with lower stability than Cyclooctatetraene are formed. As a consequence, ΔH_f (OP_{solid}) in equation 4.1 becomes larger (i.e., more positive), $\Delta H_{ads,r}$ is then reduced.

If we also refer to the DFT calculated net binding energy shift of the S 2p signal (Figure 3.7),[35] the 2.6 eV~3.0 eV shift observed in our study supports the formation of $Ca_{32}S_{32}$ clusters that produce an energy shift of 2.4 eV~3.7 eV. Formation of Ca_4S_4 or even smaller cluster would require a corresponding energy shift of 3.6 eV~3.8 eV or higher. Such large shift is never observed in the coverage dependent series of S 2p spectra (Figure 3.7). In the S 2p spectra with very low Ca coverage (<0.3 ML), the energy shift are approximately 3.0 eV. At this coverage, heat of adsorption is assumed to be contributed only by $\Delta H_{ads,r}$ (Figure 4.2). Therefore, the reaction of Ca with 6T that releases $\Delta H_{ads,r} = 275$ kJ/mol would also result in a ~3.0 eV shift in S 2p spectra. Although this agreement of the results from different techniques should not be regarded as the evidence to support the preference for a certain cluster size, it anyway further supports the existence of pronounced cluster size effect. Overall, the effect of CaS cluster size and the influence of reaction mechanism both contribute to the huge deviation of $\Delta H_{ads,r}$ from ΔH_{ads} of model, although the proportion of each part is unclear.

In the trace of adsorption heat of Ca on PTCDA (Figure 4.4), a sharp drop of adsorption heat from 550 kJ/mol to 460 kJ/mol is observed within the coverage range of 0 to 0.08 ML. This drop could be attributed to the adsorption (and reaction) on a small fraction of surface or near-subsurface defect sites. The $\Delta H_{ads,\ r}$ released by the reaction of Ca/PTCDA then stands as high as 460 kJ/mol. Although there is no direct estimation on the model reaction of Ca/PTCDA, comparable studies on similar systems have been reported. In the adsorption calorimetry of Ca on PMMA,[37] $\Delta H_{ads,\ r}$ is determined to be around 730 kJ/mol, also much higher than that of Ca on PTCDA. Formation of calcium carboxylates or a coordination model of the reaction are proposed for the Ca/PMMA system while for the reaction of Ca with PTCDA, the model with complete bond cleavage should be more applicable.[43] An XPS study on the adsorption of Mg on PTCDA has shown the elimination of C-O-C species in the O 1s spectra alongside the emerging Mg^{II} species in Mg 2p spectra with increasing Mg coverage, i.e., the complete C-O bond cleavage in the anhydride group of PTCDA and formation of MgO. Since Ca has analogous chemical properties to Mg and is even more reactive, it is reasonable to believe that, in the reaction of Ca/PTCDA, complete cleavage of C-O-C takes place and CaO is formed. The size of the formed CaO clusters are expected to have major influence on the measured $\Delta H_{ads,\ R}$. The energetic properties of the organic product formed together with CaO should also be considered. The real quantitative analysis of the total reaction heat would be possible if there are more theoretical studies available about the reaction of Ca with organic carboxylic acid anhydrides.

5 Data Acquisition Platform for the Adsorption Calorimeter

The data acquisition platform of our adsorption calorimeter is built upon the LabVIEW Professional Development Kit from National Instruments, Inc.. LabVIEW is a graphical programming environment specialized in data acquisition, instrument control, and industrial automation. It has seamless integration with data acquisition hardware produced by National Instruments. To fully utilize this advantage, the calorimetry data acquisition part of our software platform employs a slot-in Peripheral Component Interconnect (PCI) version of the National Instruments card: NI 6221. Besides that, the platform is also comprised of other subsystems for miscellaneous supporting functions. Before we step further to the software side realization of concrete functions, it is better to have an overview about the apparatus control and data acquisition system of the calorimeter (Figure 5.1). The whole system could be divided into three phases:

1. The Windows based user interface is comprised of five major applications. Among them, the main application is integrated with components needed for a complete set of measurements described in Chapter 2. The data acquisition for calorimetry is of course the key part of this application. The temperature regulation application for the beam evaporator relies on the temperature feedback from state monitoring applications, which contains two stand alone applications running as background services for the entire data acquisition platform. The global logging application, running in the background to simultaneously record all the channels of temperature and pressure under minute time resolution, is also dependent on the state monitoring applications. Unlike the LabVIEW programmed applications, the original Masssoft Professional from Hiden Analytical is still used as the controlling and monitoring software for quadrupole mass spectrometer (QMS).
2. In this phase, standardized electrical communications between main computer and other third party hardwares are realized by calling the APIs of Windows drivers system. In the LabVIEW programmed applications, this calling of APIs is carried out via the National Instruments (NI) runtime environment. It is essentially an automatic hardware communication handling system, which translates the demands of applications into specific bottom calls to the operation system hardware APIs and has to initialize with the start of operation system to function properly.
3. The third party control units and their client hardwares mounted on the calorimeter constitute this phase for raw signal collection or physical movement execution. Communications between the controllers and their client hardwares are carried out specifically with the manufacturers' protocols. Two points are worth noticing. First, the pre-amplifier is home built by the electronic workshop of the Department of Chemistry, Philipps-Universität Marburg. Second, the laser subsystem is divided into the laser generation section and the laser power meterage section. They are comprised of the hardwares from different manufacturers.

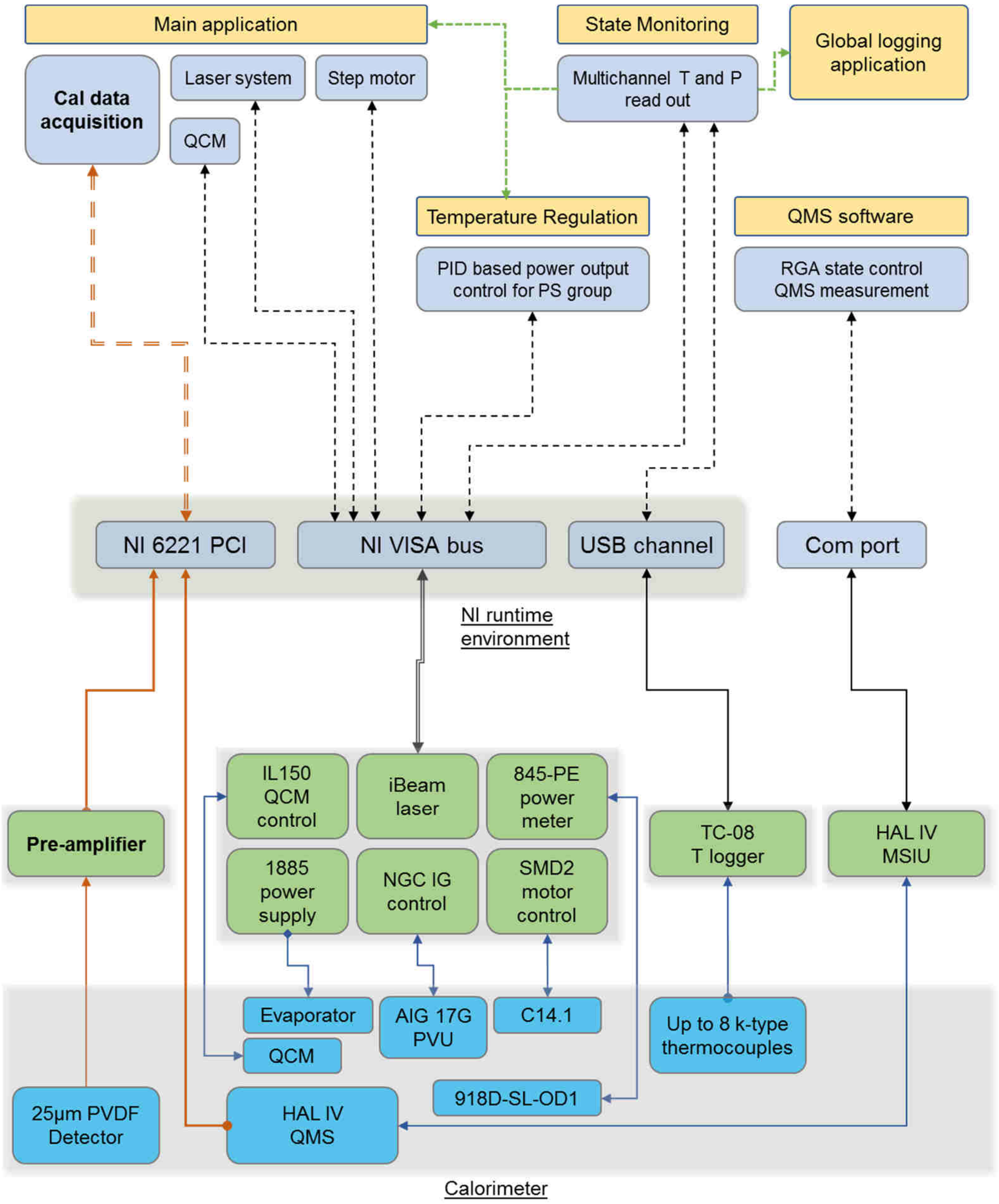

Figure 5.1: Schematic illustration to the software platform of adsorption calorimeter. Cal: calorimetry; T: temperature; P: pressure; PID: proportional–integral–derivative controlling algorithm; PS: power supply unit; RGA: residual gas analyzer; NI 6221 PCI: PCI slot-in version of National Instruments measurement card; VISA: Virtual Instrument Software Architecture of National Instruments; Com port: IBM-PC serial communication port following RS-232 protocol; IL-150: QCM controller by Intellevation Ltd.; iBeam: 405nm laser generation unit by Toptica Photonics AG; 845-PE: photo diode control and power meter by Newport Corporation; 1885: programmable DC power supply unit by PeakTech Prüf und Messtechnik GmbH; NGC IG: pressure gauge control by Arun Microelectronics Ltd; SMD2: step motor control unit by Arun Microelectronics Ltd; TC-08: USB hot plug thermocouple reader by Pico Technology Limited; HAL IV MSIU: the central control unit of HAL IV QMS by Hiden Analytical; AIG 17G and PVU: hot cathode ion gauge and pirani by Arun Microelectronics Ltd respectively; C14.1: UHV compatible step motor by Arun Microelectronics Ltd; HAL IV: QMS by Hiden Analytical; 918D-SL-OD1: wave length tunable photo diode for power meterage by Newport Corporation; 25µm PVDF detector: home designed and manufactured calorimetric detector, technical details could be referred to literature.[96]

In Figure 5.1, information flows are demonstrated as arrow headed lines. Each line represents a communication channel, either dashed for virtual data flows within the computer or solid for the physical channel that connects two hardware entities. The direction of the arrow indicate the orientation of information flows. Lines with two arrow ends represent a back and forth communication mechanism between the two sections that is connected by this channel; while single headed lines represent a passive mechanism for data collection. For instance, the voltage measurement for calorimetric signal by NI 6221 card works without any trigger or feed in signal to the pre-amplifier as well as to the detector; the information of temperature and pressure are unilaterally provided by the state monitoring applications in the common buffer, which are simultaneously referenced by three different applications at varied paces.

A very special instance here is the communications with HAL IV QMS, which has two independent parallel channels. The single headed channel fed to the NI 6221 card represent the auxiliary analogue signal that is directly read out from the QMS without processing by the MSIU. Meanwhile, the double headed one represents the built-in channel that undertakes the communications for apparatus control and data acquisition of Hiden Analytical's original Masssoft. The QMS data used for calorimetric analysis is acquired through QMS' auxiliary analogue channel and digitalized by NI 6221 card. This is because the pulsed signal of calorimetry requires sub millisecond time resolution that NI 6221 could provide. The data acquired by the built-in channel is digitalized by MSIU. Both processing speed of MSIU and communication band width of RS-232 protocol put hard limit on the time resolution of data from this channel, constraining its application to state monitoring or leak detections in this calorimeter system.

5.1 Characteristics of LabVIEW Programming and Its Execution

The development language used by LabVIEW is called G language. It is very unique combination of graphical programming and data flow driven programming. Because it is very different from the conventional text based programming language, an introduction to the characteristics of the language itself should be placed prior to the introduction of the data acquisition software. Some of its properties contributed partially to the shortage of literature coverage concerning scientific instrumental programming, despite the fact that LabVIEW has long been widely used the scientific world. As a consequence, I believe it is worth trying, though difficult, to present some structural characteristics of LabVIEW programming from the perspective of scientific instrumental programming. Because in our work, a large proportion of time has been spent on the realization of some seemingly simple functions. The extra efforts consumed stem partially from the lack of literature guidance. Special attention will be given to the hardware-timed synchronization of data acquisition and step motor movement control for pulse generation, which constitute the core of this type of adsorption calorimeter.

5.1.1 Graphical Programming

An instance of the G language programmed software is termed Virtual Instrument (VI), which has three components: a block diagram/panel for developing the code, a graphical user interfaces (GUI) termed front panel, and a connector panel, shown as an icon when placed in other VI's block diagram if it is to be called as subroutine. Creation of the GUI is integrated into the development cycle ever since the beginning. A VI does not start with declaration of variables to pre-allocate system memory. The introduction of certain types of data, i.e., integer, single/double precision floating point number, string or Boolean, is realized by placing a specific object representing this data type. The action of placing the object on the front panel/block diagram will trigger the simultaneous introduction of the object's corresponding counterpart in block diagram/front panel (Figure 5.2). The objects with front panel entity have two states: controls or indicators. These two states of an object could be freely converted at needs. Controls and indicator have programmable variable states, the data they carry is one of their built-in states. The entities in the block diagram are called state handle which transfer/accept the states to/from the program. The default state handle, which is placed on the block diagram when introducing a state variable object, is the data value state. The access to other states of an object is realized via property node, a built-in system function. All codes are put inside a loop structure with conditional stop. Such arrangement will lead to continuous running of this program if otherwise a stop is commanded by the user.

Because the code in block diagram is constituted by icons, frames or wires, the total surface area needed to fit in all the codes is largely unknown in the beginning. Stretching to enlarge the surface area of block diagram as well as realignment of icons after the introduction of new objects are constantly carried out as the development is underway. Therefore, only bottom-up strategy would work out in G language. However, bottom up strategy in a graphical language would inevitably lead to huge imperfections regarding the formalization of codes. Unlike the text based programming languages, in which the calling and dependence of the functions with sub-functions are not visually bonded. In block diagram of G language, the logic relations between a function and its sub functions/subroutine are prominently demonstrated by "wire" connections between them. Variables are "wired in" to feed into a sub function/subroutine. It may be helpful to instantly know what is actually fed as the variable by directly looking at the "wire". But when there are plenty of logical structures, especially when different blocks of codes for independent functional purposes are put together, it is in fact very difficult to show the reader the specific codes and the reason of programming so on an A4 sized sheet of paper (Figure 5.3). Therefore, neither an introduction to the basics of LabVIEW programming nor a detailed covering to the complete sets of codes will be covered in this chapter.

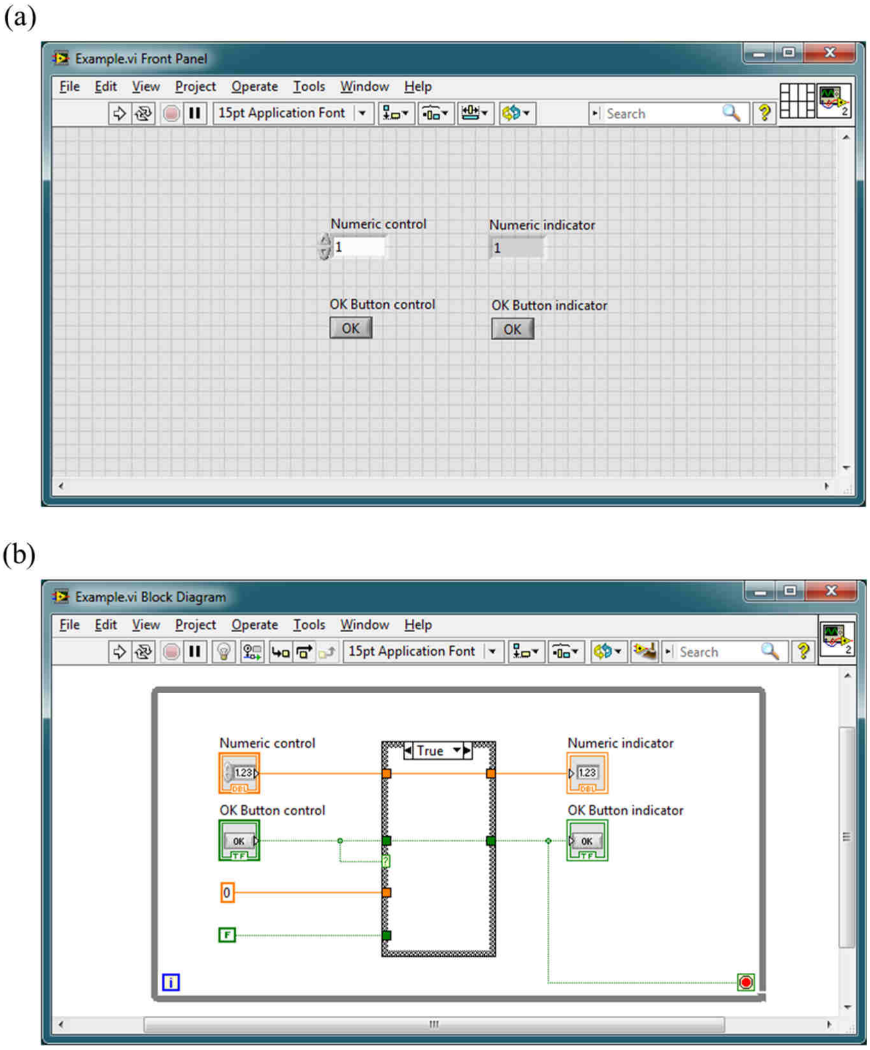

Figure 5.2: A screenshot combines both front panel (a) and block diagram (b) of a simple LabVIEW program. Objects enabling input on the front panel are controls; objects displaying information on the front panel with input from elsewhere are indicators. Constant has entity only on the block diagram.

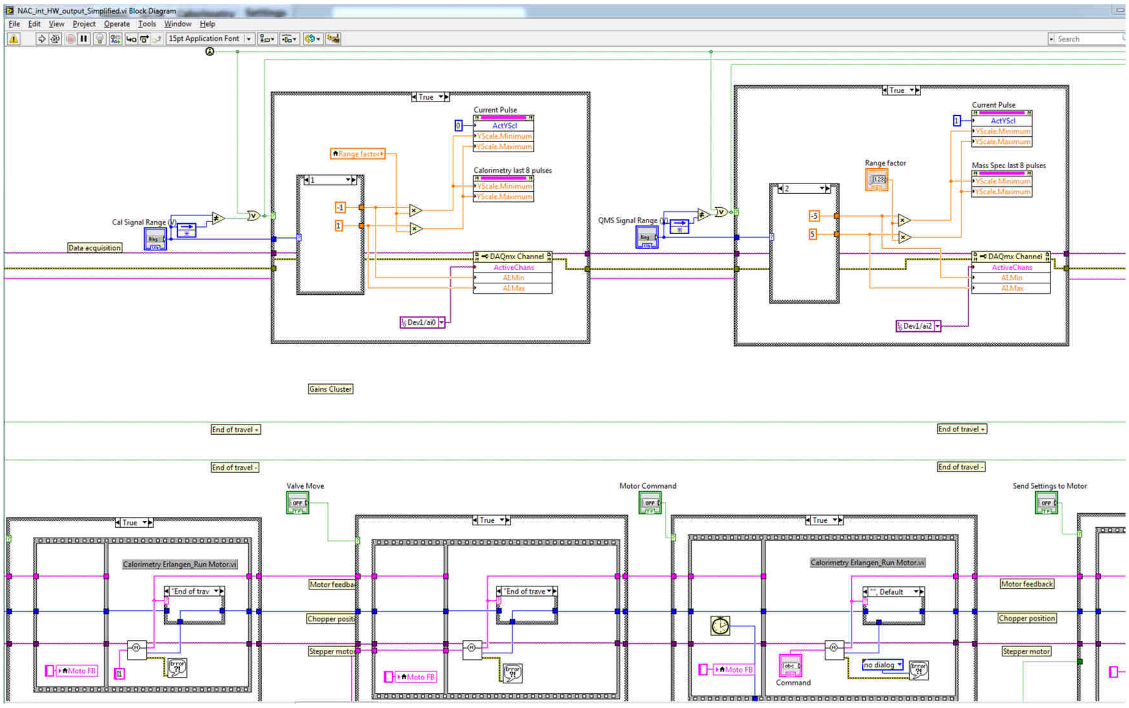

Figure 5.3: A screenshot of a section in the block panel of the main application. The upper part belongs to the data flow of the data acquisition task of NI 6221 card. In this particular block, wires are fed to control the properties of acquisition amplitude range. The lower part belongs to the miscellaneous operations that is designed for the control of the step motor. These two blocks of codes are two data flows independent to each other. The box with thick grey outer line and a combo box at the upper center is the Boolean condition structure, which means the codes shown in this figure are theoretically only half of the all. To show the full codes, another screenshot is needed by switching all the conditions to the other from what is shown in this capture. For case structure with more than two parallel options, screenshots needed for a complete demonstration will have to be multiplied by the case number accordingly. Grey frame with internal sub frames and porous upper/lower bands is the sequence structures, in which the execution of codes in the left side sub frame will always have priority over its right side neighbor.

5.1.2 Data Flow Driven Programming

Another very pronounced property of LabVIEW's G language is its data flow driven characteristic. The aforementioned wire connections among different parts are also the iconic demonstration to this characteristic, that is, the information is flown inside wires and transferred by wires (but not only by wires) to different parts. Data flow programming is a special hybrid of objective-oriented programming and imperative, procedural programming. In a data flow driven language, the logic sequence of code execution are largely defined by graphically built data flows between operations/functions, The running of data flow is resembled to a procedure, which is intrinsically designed to run only once. Data flow does not necessarily contain the restrictions for timing. An active application with GUI have to run in a loop without predefined end time. In the loop, data flows are rolled, judgements for conditional termination are repeated in every loop. As has been shown in Figure 5.3, in G language, the data flow is undertaken by wires and other logic structures. The execution of codes generally follows the order of left to right. When there are multiple independent instances of data flows, the general sequence of execution is from top left to right down. However, this sequence has nothing to do with the real thread control. In a text based language, the thread of execution is explicitly defined as line by line following well defined conditions. In G language, the real thread is assigned by its internal scheduler without documented rules. When multiple instances of data flows exist under the same logic condition (Figure 5.3), meaning there is no extra logic structure to explicitly define the priority of execution, the real thread in fact jumps among different data flows, and could easily go beyond the on screen sight focus of the debugger. This is a fundamental difference from text based languages, in which the execution of each line could always be readily grasped. Such characteristic of execution usually brings about extra difficulties when debugging a LabVIEW program that has multiple parallel data flows for multiple simultaneous tasks.

It may be argued that it is possible to always employ sequence structures to specifically define all the local sequences of execution. The very sound reason that claims simultaneous evasion of thorny thread jump when debugging and best possible formalization to the codes. However, by doing so, a lot of extra time has to be spent on squeezing the code into the sequence structure. Since top-down programming strategy does not work well in the development of a open end system using data flow driven language, fitting the all bottom up written codes into sequence structure basically means a complete rewrite to the codes. Besides that, and may be more importantly, an attempt to forcibly confine codes with sequence structure would indeed constrain all the codes to form one large single data flow rather than multiple parallel and independent ones. This would result in serious consequences, for instance the disintegration of the multi-task feature of LabVIEW, creation of artificial lags that destroy the fluency of execution as well as the time synchronization in time critical tasks. To those who are familiar with event driven languages, i.e., C++ or VB, this seems to be difficult to understand. To explain it, we need to first understand how object-oriented programming is realized in G language. As aforementioned, any objects, i.e., a button, a control for number or text, that appears in the front panel, will simultaneously place at least one state handle to join the graphical data flows in the block diagram. The operations associated with an object's behavior, i.e., click of a button, selection of an item in a drop menu, will only be incorporated into the data flow to take effect until the thread of execution reads the state information this handle transfers, i.e., the button's state of being pressed or not, the content that is placed in the input box or just empty null, the color of a label or etc.. This is another fundamental difference between data flow driven languages and event driven object-oriented languages, in which the objects associated operations are treated as events. In other event driven object-oriented languages, GUI related events are usually granted with higher priority in their scheduler for rapid system response. For example, if a data acquisition procedure is defined as a looped function that runs continuously, when a full stop is to be realized, one could introduce a button called "stop" and associate the click event of this button with operations needed for a full stop. Nothing will have to be placed in the function for acquisition, because it is easy to give click event of the stop button higher priority over acquisition function. As long as the stop button is clicked, the thread will be switched to the operations associated with a click event so that the acquisition is stopped. The user won't have to wait for a long time until the system response is observed. In G language, the function of a single click to a button is realized by the mechanism of "clutch until read", which decompose the single click into two static states: pressed and released (Figure 5.4). Because the state handle could only transfer one state upon one read to the data flow, either pressed or released will be read by the data flow at a time but not both. To simulate the instant bounce back of the button after a single click, the system will hold the button in pressed state after it has been single clicked by the user in the GUI, until the state of pressed is read by the data flow and then automatically switch the button back to the released state. If the data flow runs fast enough after the user's click, the user experience created by the "clutch until read" is not very different from those created by event driven languages. To realize the stop operation in an ongoing looped procedure like data acquisition, the state handle of a Boolean object will have to be incorporated into the data flow inside the loop of acquisition. As a consequence, it will be subject to the priority sequence assigned by the data flow as well as the internal scheduler (Figure 5.5).

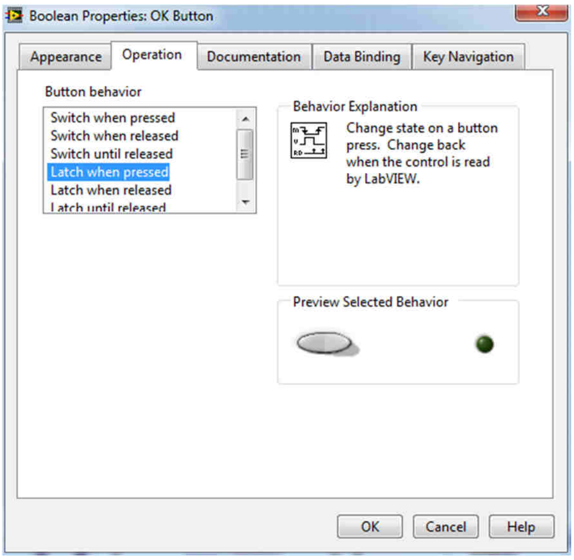

Button behavior: Latch when pressed

Behavior Explanation: Change state on a button press. Change back when the control is read by LabVIEW.

Figure 5.4: Properties dialog of Boolean object, button, in G language. The active tab describe the operation that is enabled by G language. With highlighted option in effect, the button will stay pressed until the state handle is read by the data flow, even if the intention of the user is in fact a single click with instant bounce back of button. All three options with latch behavior are constructed upon similar mechanism. Static switching behaviors are also permitted.

If we reconsider the situation that all the data flows are explicitly sorted by sequence structures, after we single-click a button, the time we have to wait to see the effect of this click, will be what is needed for the execution of all the codes stacked before the state handle of this button. To a complex system containing multiple independent yet very long data flows, a very noticeable lag is inescapable. However, smooth user experience is never the major pursuit of the software for scientific research. It is the risk of desynchronization in the time-critical procedures that really makes the perfectly explicit sequence of execution a wrong choice. To those procedures with external timing clock for loop time control, too many codes stacked in one single data flow might result in overtime of execution. This is because the external time clock is independent of the central computing system that execute the codes. The time elapsed between the two receptions of the time counting request is employed for the judgement of overtime, regardless of how much code has been executed within this period of time. The aforementioned thread transferring among data flow is designed to avoid overtime in time-critical tasks while providing strong support to multitasking. Although it does bring in difficulties to the debugger of LabVIEW program, such compromise for better reliability are still necessary. It also reminds the G language developer of the necessity to simplify the block diagram. It is always better to clean up the block diagram by putting as much code into the sub VIs as possible. The benefits of doing so are:

1. Less code in a large single block diagram will help to shrink the overall size of the block diagram. Therefore, undesired, out of sight thread jumps among data flows become less likely.

2. Sub VIs have stand-alone front panel/block diagram and thread schedule which does not interfere with the thread schedule in the mother VI. When debugging, its execution always start freshly at the top left corner on its own block diagram. Usually, a sub VI will not contain too much code, it would be much easier to catch the whole block diagram within one sight, making any thread jump in this small block diagram less unpleasant.
3. The debugger could chose not to step into a sub VI to scrutinize the procedure of execution inside this sub VI. Only the results of execution is passed on to the data flow in the mother VI. When there are problems with the codes inside the sub VI, it is also equivalently convenient to call out the block diagram of this sub VI and debug it alone.
4. Considerable amount of memory and computing power saving is achieved if a sub VI is called multiple times in the same diagram. If the same operations/calculations are carried out by duplicating the codes many times, more memory will have be occupied until the shutdown of the program, while the memory of sub VI can be released right after each incidence of calling.

An even more representative example to demonstrate the properties of the G language and its difference from other languages is the case of two mutually exclusive Boolean controls. If we have two buttons in switching mode to control two mutually exclusive function, switching of one should automatically passing the opposite value to the other and thus resulting in a state switch. In an event driven language, it is rather easy to realize. The programmer would only need to assign the opposite value to the contradictorily behaved counterpart inside the same event. Because the contradictory operations are associated to the event, only one event is allowed to occur at a time. The mutually exclusive behavior is always carried out in one direction or the other but not both. In G language however, such simple operation cannot be realized by wired value assignment. First, a user-operable object has to be a control, yet controls only give out value to wires but do not accept wire-in. To give the opposite value to the other control by the operation of one, a variable or a property node has to be used. As a consequence, a temporal mismatch between the point of assignment from the valuing object and the point of actual change in the target object is created. Second, because the mutually exclusive behavior would need mutual value assignment, any operation has to be carried out vice-versa, or one of the object would otherwise become meaningless. The real problems is, in G language the execution will sweep through all the data flows, two data flows created by the state handles of two controls are both executed. Consequently, two contradictory operations in these two data flows will put the system into chaos. It does not matter which data flow has the temporal priority. As long as the result of judgement is already generated and passed onto the data flow, depending on the size of the temporal mismatch aforementioned in the first point, the resulting symptom would either be a valuation dead loop or the execution of contradictory actions. To deal with this problem, LabVIEW provides a container-like structure in the block diagram, called “Event Structure”, to handle the purely event-driven operations. Since it is still part of the data flow, it will subject to the scheduling of the data flow. A More detailed example could be found later in introductions to the main application in this chapter.

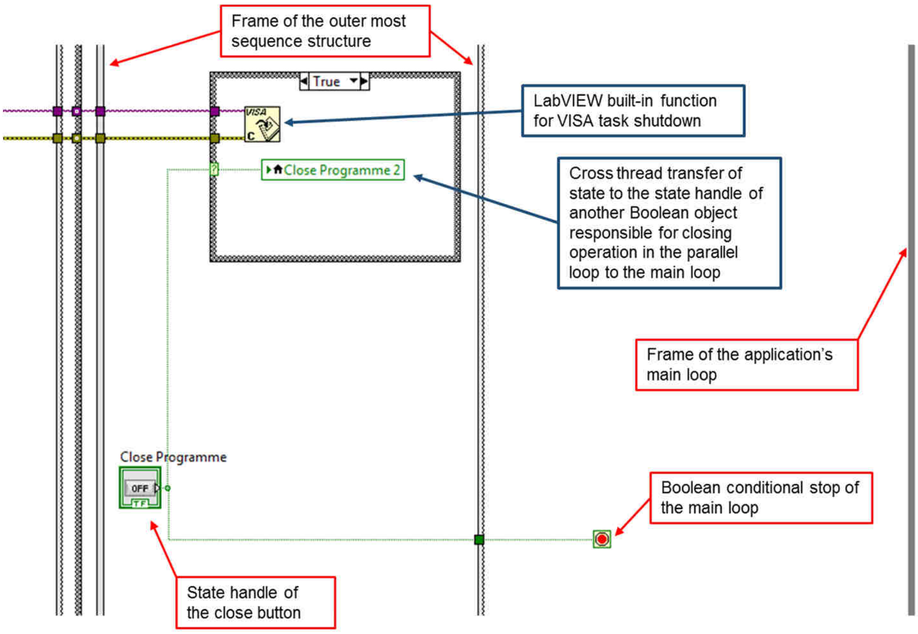

Figure 5.5: A screenshot to the end of program section in the stand-alone version of IL-150 QCM control and monitoring application. In this section, the state handle of the close button to the entire application is purposely put to the right most sub frame of the outer most sequence structure, such that its state is the last to be read by the data flow. Here, the potential lag between click and its effect is tolerated because proper settlement to the data storage and deinitialization of the involved communication channel, i.e., the shutdown of VISA task in the figure, should be accomplished before the full shutdown of the application.

5.1.3 Code Efficiency and Multithreading

Because LabVIEW is a cross platform developing environment for miscellaneous hardwares and devices, it has to be built upon the basic mechanism of virtual machine to minimize the complexity of developing LabVIEW itself, just like the more famous cross platform developing environment JAVA. This nature indicates that the optimization of code efficiency of LabVIEW itself could be limited. A less well known, yet maybe more influential challenge to the code efficiency is actually rooted on the graphical nature of G language. Because the introduction of state variable object leads to double creation of entities on both front panel and block diagram, such arrangement would automatically realize the visualization of the codes. Any data carried by the object as the state of "value" could be directly checked on the front panel via the live update of graphical appearance that shows the data. No print method or dialog of properties is needed for debugging. Unfortunately, the dynamic graphical rendering of data on the front panel seems to be rather inefficient in LabVIEW. The CPU load could easily rocket when a large amount of data in such as a 2D array is only partially presented by the object on front panel, it is unrealistic to directly plot the complete data set using graph or chart objects. In small programs, the situation is simpler because the data space could be re-dimensioned in the wired data flow without introducing larger objects to carry these data. That means that a large amount of data generated during the execution could be stored in memory by the data flow without increase to the rendering load of the front panel. However, in a more complicated program, a set of data might be needed by different sections stand "far" from each other on the block diagram. Direct wire connections between these sections are not only difficult to draw, but also a firsthand challenge to the formalization of codes since crossover of wires among data flows is almost inevitable. Under these circumstances, an object with suitable size of data space is often introduced as the carrier for data. Data is transferred to local data flows by employing Local/Global Variables or property node of the "value" state handle. No long stretching wire is needed. However, using of variables or property node would double the memory usage. Furthermore, the introduction of Global Variable in fact leads to the creation of a special sub VI with only front panel. As a consequence, the arrangement to use objects for data storage and transfer result in increases on both CPU load and memory usage. Although LabVIEW permits hiding of the objects on the front panel while still preserving full function on the block diagram, seemingly that the burden of graphical rendering load is then remitted. To my personal experience, a considerable amount of computing power is nevertheless spent on maybe checking the states of the hidden objects. As long as its state handle on the block diagram is read by the thread.

Confronted with the dilemma between practicality and efficiency, the computing power could become rather tight in some multitask systems with heavy data load. Someone may look to GPU acceleration for help. However, universal GPU computing is not supported by LabVIEW until now. CUDA of Nvidia or its descendant are partially supported only for fast Fourier transform (FFT) and Basic Linear Algebra Subprograms (BLAS) since version 2012[136]. OpenCL of AMD is merely an amateur initiative that has no official support.

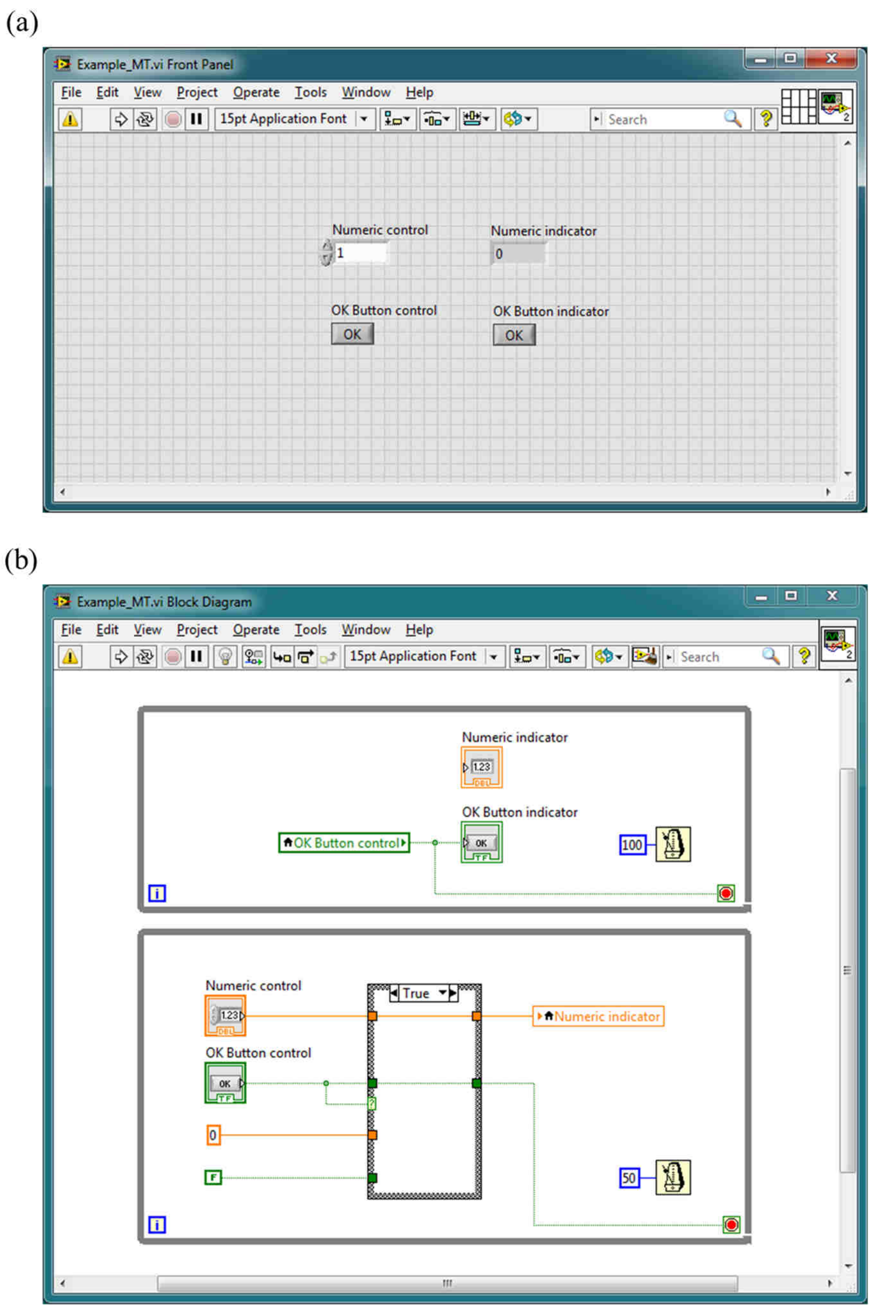

Figure 5.6: A screenshot combining both front panel and block diagram of a simple LabVIEW program structuring multithreading. (a) Front panel. its layout and results of execution are identical to what is shown in Figure 5.2, while on the block diagram (b), indicators are moved to the other thread. Data transfer is carried out by local variable without wired data flow. The “Wait until Next” function regulates the loop execution rate by commanding the rolling of the loop to wait until the milliseconds of total execution time of this thread reaches integer multiple of the input number. This timing function uses built-in millisecond resolution timer of the operation system, it does not rely on 3rd party timer. External hardware timed loop could easily be used for multithreading as well.

Indeed, computing power is never sufficient to the developers regardless of its origin. The more feasible idea is to focus on the structure of the execution arrangement. In the previous section, the mechanism of the cross data flow thread transfer has been discussed. It can be seen as a feature dedicated to the improvement of the execution structure. However, such mechanism might still be not enough to guarantee runtime reliability in some heavy loaded yet time critical procedures, especially if the total computing power of the system is rather limited. The major problem of such a mechanism is that it treats all the code in the same logic structure with equal priority. However, in multitask systems, some tasks are designed to have priority in execution. In looped diagram of G language, putting codes to the left most for earlier execution in each loop does not uplift their overall priority, because they still have to wait for the execution of all the right side codes until the next loop starts. The real solution will be a layered priority system that categorizes different parts of the codes with sorted priorities. In G language, this is realized through the dedicated structure of multithreading.

Creating a permanent multithreaded structure is relatively handier in G language than in the text-based languages. No declarations are needed for enabling multithread as feature. On the contrary, it is supported as the developing environment initializes. By placing two parallel loop structures on the block diagram, the multithread structure is instantly created. Each loop represent a single thread (Figure 5.6). The differed execution priorities for multithread could be achieved by two methods. First, putting more code into the thread assigned for lower priority while leaving less yet more critical code to the thread for higher priority. This would naturally dampen the execution in the lower priority thread, passively lifting the priority of the other thread. Second, additional timing could be imposed on each thread with different timing conditions. Take the VI in Figure 5.6 for example, this setup means the execution in the under loop would be no faster than 2 times of those in the upper loop. By increasing the difference of timing condition between the threads, larger difference on the priority of execution could be smoothly implemented without major changes to the code. This is important to real circumstances, under which the threads with dedicated higher priority are still filled with more codes/tasks than that with lower priority. The additional timing could make sure that computing power is concentrated onto the more important thread when needed. Beyond these fundamentals, a few points are worth noticing when using multithreading in G language:

1. The management of memory access is still a major issue as it would be in other languages. Although LabVIEW handles privilege to memory access very well, it does come with the price of deterioration to local code efficiency since the Local Variables or Global Variables are employed for cross thread data transfer (as shown in Figure 5.6). Because Local Variables and Global Variables duplicate the data they represent in the memory, their application will definitely have negative effects, on the memory and computing power consumption. In any LabVIEW instructions, it is recommended that good programming should avoid using these two objects but to use direct wiring as much as possible. Direct wiring is the direct assignment of access privilege to the certain data in the memory. However, because multithreading is employed to allow different threads running asynchronized, if data flows in one thread require output of data flows in another thread as input, direct assignment of access privilege to the other thread would trigger conflict between the two thread. In the least harmful scenario, the conflict would lead to forcible re-synchronization of two threads, the multithreading has therefore become meaningless. On the other hand, Local Variables and Global Variables carry duplicated data in the memory, they are not involved in the other operations/calculations of this thread. Therefore, the cross thread transfer of access privilege to these data will not trigger conflict between the threads or possible chaining of the threads.
2. Multithreads should start simultaneously to guarantee a well-defined degree of asynchronization, if data flows in one thread is dependent on the output of data flows in another thread. This is an easily neglectable aspect in G language, since in many

text-based languages multithreading has to be specifically evoked as a method. If they do share the data, most people would naturally implement multithreading at the same time. While because of the convenience of multithreading in G language, specifically arrangement of simultaneous entrances into multithreads are likely to be forgotten. Together with the cross data flows scheduling mechanism, it is possible that data flow in one thread gets either wrong or empty input, because the execution in the other thread has not produced the proper results when they are requested by the dependent thread. The problem could be solved either by using sequence structure or simply by sharing the same wired data flow input from outside.

3. In the case of using event structure for pure event-driven operations, a dedicated thread to event structure is a necessity for proper functioning. As aforementioned, the event structure would all the same rely on the data flow to take effect. When the system is large enough, the time interval between the two executions of the event structure becomes recognizably long, making it far away from the effect of real event-driven programming. Therefore, the solution to the execution lag of event structure is naturally the continuous execution of this structure. A dedicated thread to the event structure is therefore necessary.

5.1.4 The Debugging Mode and Executable Mode

The applications built by LabVIEW could run seamlessly with the NI runtime environment. The multitask features of the Windows system are well utilized by NI runtime environment. However, when the programs are still under debugging mode before being encapsulated into a stand-alone executable form, multiples instances of programs have to share the same system thread of LabVIEW. If more than one program is running, they will interfere with each other in execution. This property brings about timing problems to synchronized time critical procedures such as the pulse generation together with data acquisition. Random delays are observed in the execution of the same code that is specifically designed to produce the same time of execution. Therefore, it is better to run the applications in the form of built executable files

5.2 Applications for System State Monitoring

The system state monitoring service is the basis of the apparatus control system. It is constituted by two independent applications: the temperature reading and the pressure reading.

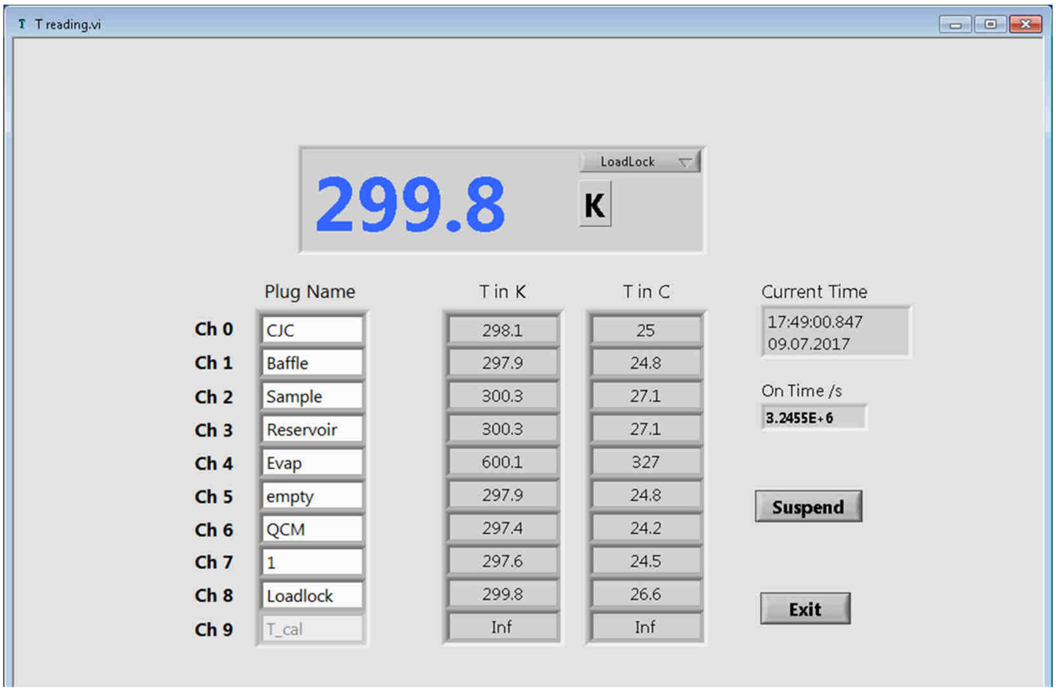

LoadLock: 299.8 K

	Plug Name	T in K	T in C
Ch 0	CJC	298.1	25
Ch 1	Baffle	297.9	24.8
Ch 2	Sample	300.3	27.1
Ch 3	Reservoir	300.3	27.1
Ch 4	Evap	600.1	327
Ch 5	empty	297.9	24.8
Ch 6	QCM	297.4	24.2
Ch 7	1	297.6	24.5
Ch 8	Loadlock	299.8	26.6
Ch 9	T_cal	Inf	Inf

Current Time: 17:49:00.847 09.07.2017

On Time /s: 3.2455E+6

Figure 5.7: A screenshot to the front panel of temperature reading application. The white background controls under the label "Plug Name" is the array of text input boxes that enables user assignment of channel names. Temperature readings are presented in both centigrade and Kelvin form. Channel 0 exhibit the electronically cold junction compensated reading of room temperature; channel 9 represents the backup temperature calculation via electrical resistance of the filament in the beam evaporator in case a simultaneous malfunction of the two thermocouples in the beam evaporator, this feature is usually deactivated.

When it runs (Figure 5.7), the temperature reading application first reads the 8 channels of temperatures collected by TC-08 temperature logger, then writes them with user defined channel names and system time stamp to a .txt file under a pace of approximately 1/s. This text file serves as the common buffer for temperature information, so that its data is refreshed rather than accumulated by the temperature reading application. During the bake out of the UHV system and other maintenance procedures, thermocouples are frequently unplugged or changed to other positions, naming of channel in this application keeps the consistency all over the entire platform. Because the temperature information are shared by several applications, especially the temperature regulation application for beam evaporator, this arrangement would help to prevent undesired mixing of temperature channel. The core part of temperature read out is shown in Figure 5.8.

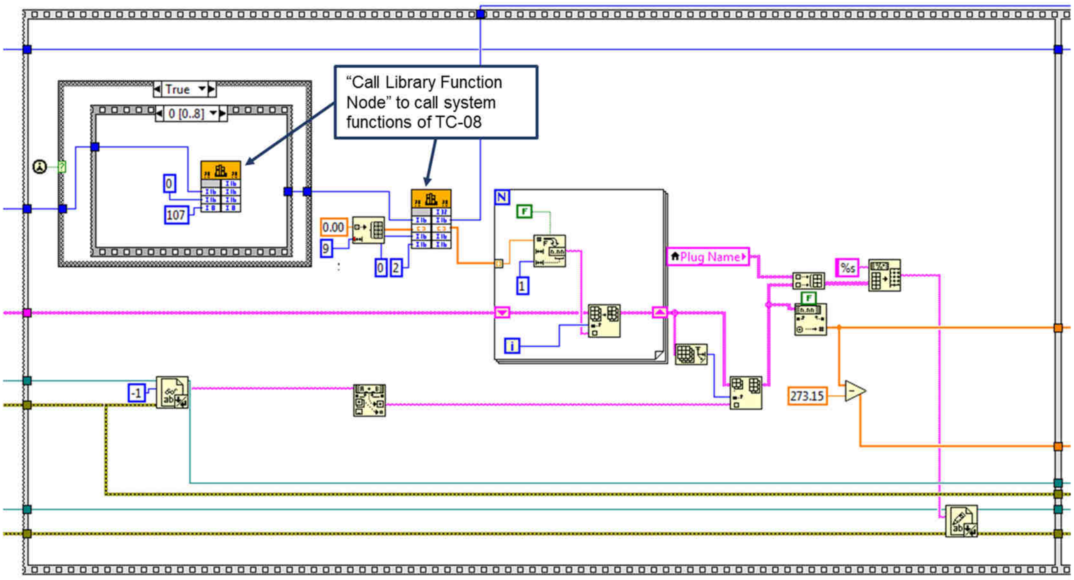

"Call Library Function Node" to call system functions of TC-08

Figure 5.8: A screenshot to a section of the block panel of temperature reading application. Windows system functions of TC-08 are called. The left calling node sets the form of temperature reading to be in centigrade or in Kelvin. The right calling node read the actual temperature. The duration of the read out depends on the number of channels requested. 8 channels plus 1 CJC channel consumes approximately 1 second.

The pressure reading application works with an AML NGC IC pirani and ion gauge control unit to read pressure information from two pirani channels and one ion gauge channel. Its front panel is shown in Figure 5.9. This application uses NI VISA to communicate with the AML NGC IC controller via com port communication under RS-232 protocol. It needs the correct choice for com port. In the figure, it is numbered com port "4". However, in the situation of hardware adjustment on a computer, a very common thing to the system under development, the com port number might be re-assigned by Windows, the selectable drop list control for com ports here is dedicated to such circumstance. The output data are also written to a .txt file as buffer. Different from the temperature reading application, the channel names for pressure are fixed because both pirani and ion gauge are normally free from re-positioning on the machine.

On the block diagram of the pressure reading application (Figure 5.10), it can be seen that the actual communication with the AML NGC IC is carried out by a sub VI dedicated for communication with the controller. The function of this VI is comparable to the evoke node for system function calling in Figure 5.8. In the development of the data acquisition platform, communications with other apparatus are realized with similar strategy. A dedicated sub VI for command translation is usually first developed, and different operations on the same device are later realized by calling of the sub VI with different inputs.

If we look further into the front panel of the sub VI for the communication with the AML NGC IC controller, a rather disorganized GUI appears (Figure 5.11). This front panel is left not cleaned up simply because it will never be shown if the pressure reading application is in the normal operational condition. If the criteria for good programming in G language are to be strictly followed as has been stressed in many video tutorials by NI staffs, the work load of the developer would be easily doubled. Here we see another example of the problems in G language. This sub VI is used as a sub function for a specialized purpose, in a text based language, no GUI would ever be developed for a sub function like this. However, since the creation of a front panel is unavoidable in G language, the developers are left with a dilemma, to either spend a lot of extra time to organize the front panel of every sub VI or to compel themselves to ignore the chaos glued on the screen when debugging. To a programmer who is conventionally trained to hold high standard over the formalization of code, this is indeed a hard choice to make.

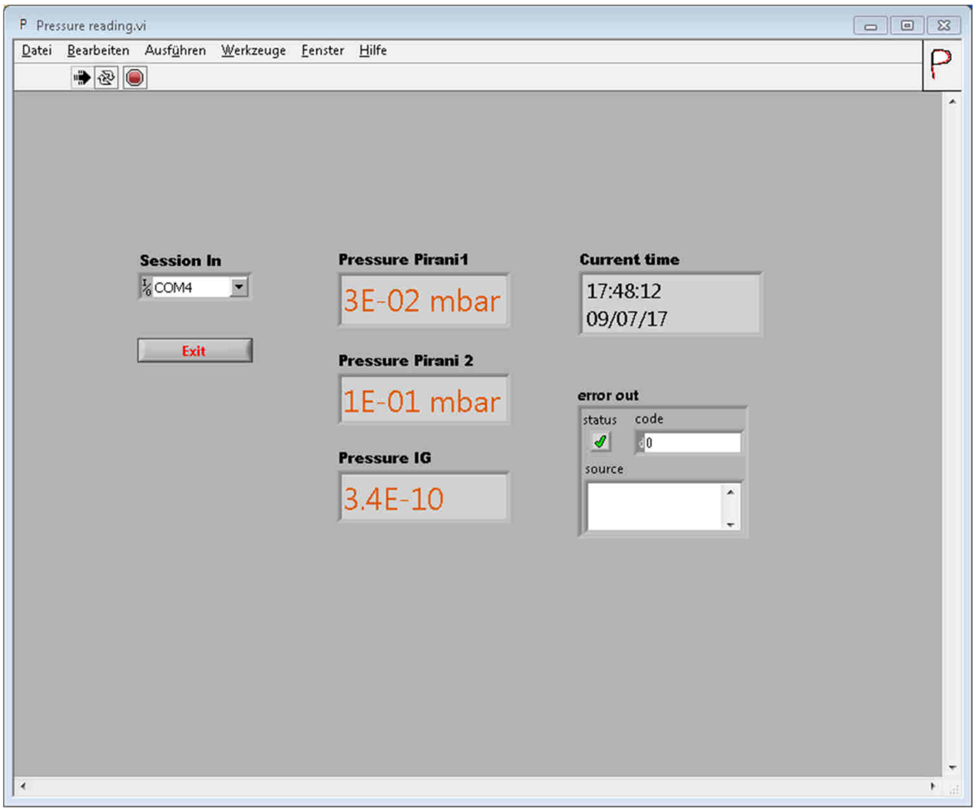

Session In: COM4

Pressure Pirani1: 3E-02 mbar

Pressure Pirani 2: 1E-01 mbar

Pressure IG: 3.4E-10

Current time: 17:48:12 09/07/17

error out
status: ✓
code: 0
source:

Figure 5.9: A screenshot to the front panel of pressure reading application. Pressure information from two pirani channels and one ion gauge channel are live read and recorded to buffer file.

In the block diagram of the sub VI for the communication with the AML NGC IC controller (lower part of Figure 5.11), codes are automatically organized (“clean up” in the term of LabVIEW) using the built-in tool of LabVIEW. It is rather clear that if a single sub VI is called several times in parallel, and input as well as output wires are squeezed from and into a large single node, the built-in clean up tool could not help to reach an easily readable state on the block diagram. It as yet has to be manually organized by the developer. Here, LabVIEW Instrument I/O Assistant is used to write the querying command to the AML NGC IC controller, it provides very powerful test-with-development environment. Here, the assistant itself is used as the data read back function because the query of all the pressure information requires very simple command, while the feed back information are relatively compressed. Information from several different parts are parsed byte by byte without tokens for separation. With the help of the Instrument I/O Assistant, fast trial and error could be easily carried out, especially the error messages are instantly seen without programming an error message handler. Although it has relatively lower code efficiency than the other dedicated functions, for light weight task such as the communication with the AML NGC IC controller, permanent employment of Instrument I/O Assistant as a sub function is still worth doing.

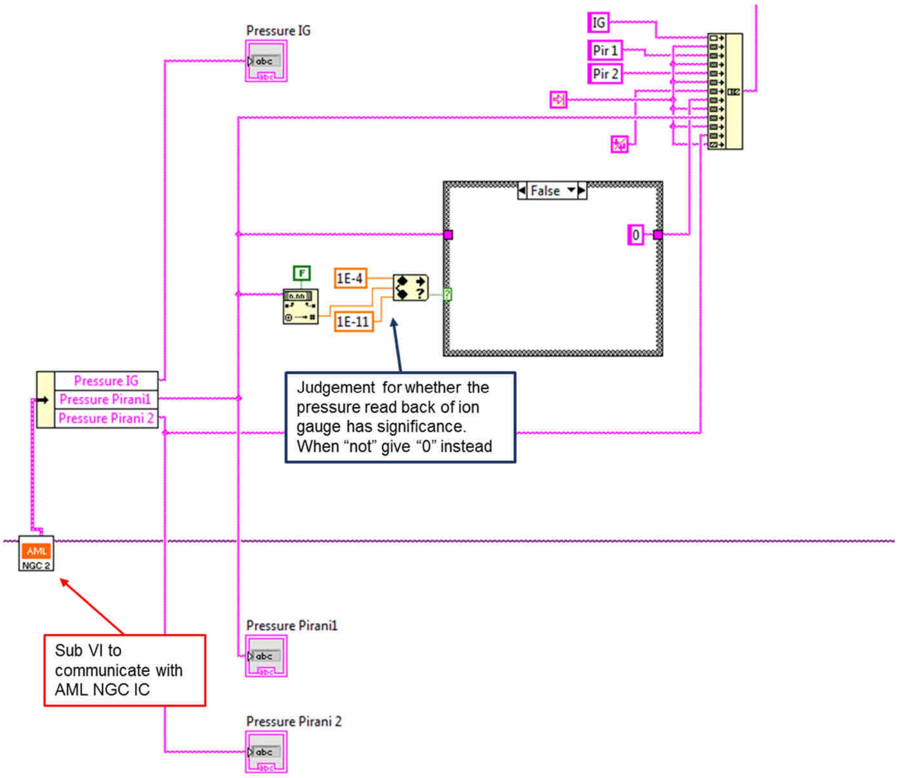

Judgement for whether the pressure read back of ion gauge has significance. When "not" give "0" instead

Sub VI to communicate with AML NGC IC

Figure 5.10: A screenshot to a section of the block diagram of pressure reading application. Pressure information is read by the sub VI pointed by the red arrow. Here, the only input is the session information for VISA communication, because the command passed to the AML NGC IG are very simple, it is embedded in the block diagram of this sub VI (see Figure 5.x). A judgement for the significance of pressure read back from ion gauge is implemented because the ion gauge may be turned off during the normal operation of our calorimeter. Under such circumstances, feedback from the controller becomes an error message like string text that is unworthy of parsing by all the applications dependent on pressure reading. Therefore, a "0" is given to specifically represent this situation.

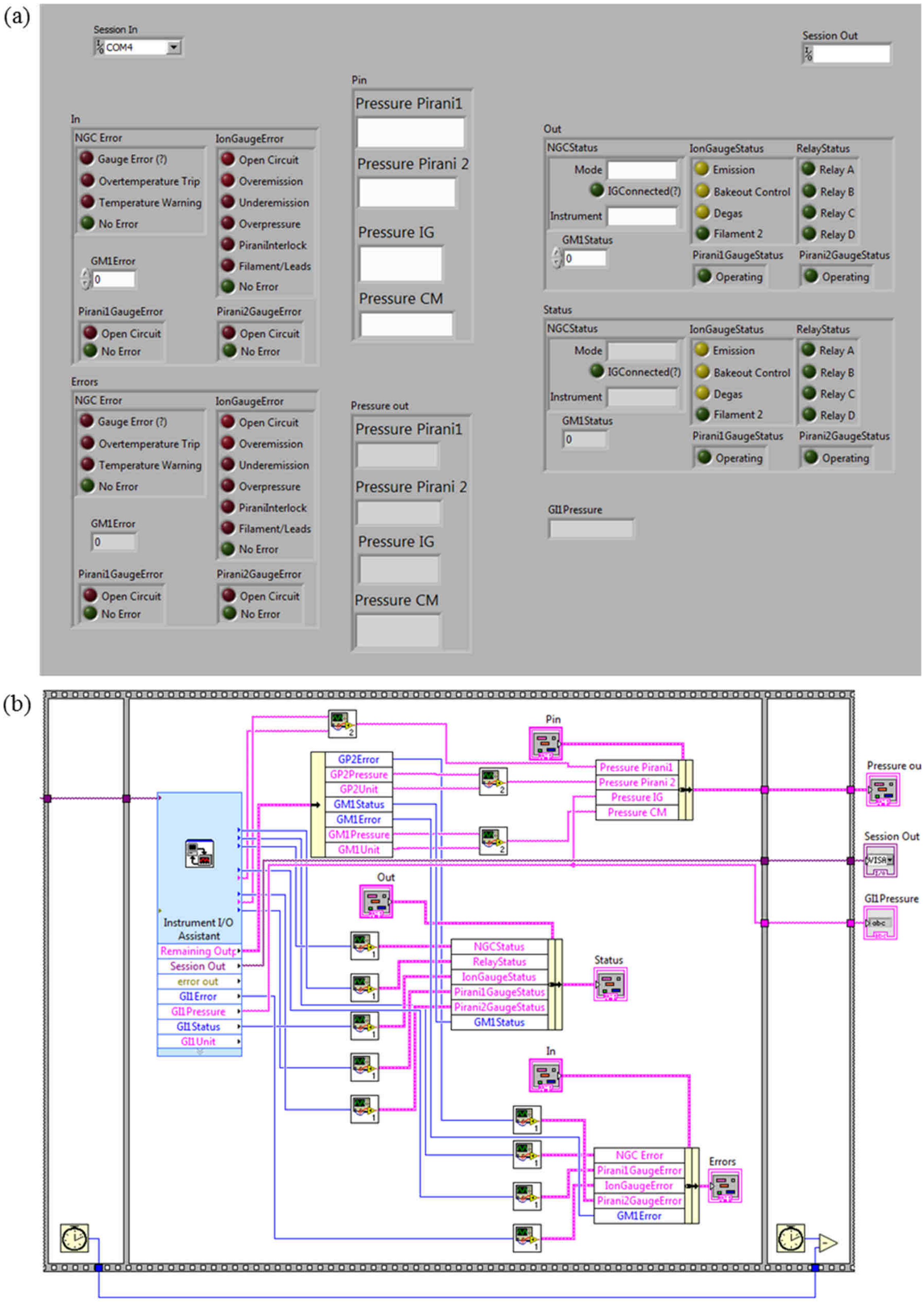

Figure 5.11: A combined screenshot for both the front panel and the block diagram of the pressure reading application. The front panel (a) shows the misalignment and size mismatch of the objects originating from the introduction of objects. The block diagram (b) is cleaned up using LabVIEW's built-in tool. Wire overlapping is not avoided. The LabVIEW Instrument I/O Assistant is used for parsing of byte data read back from the controller, see Figure 5.12 for details.

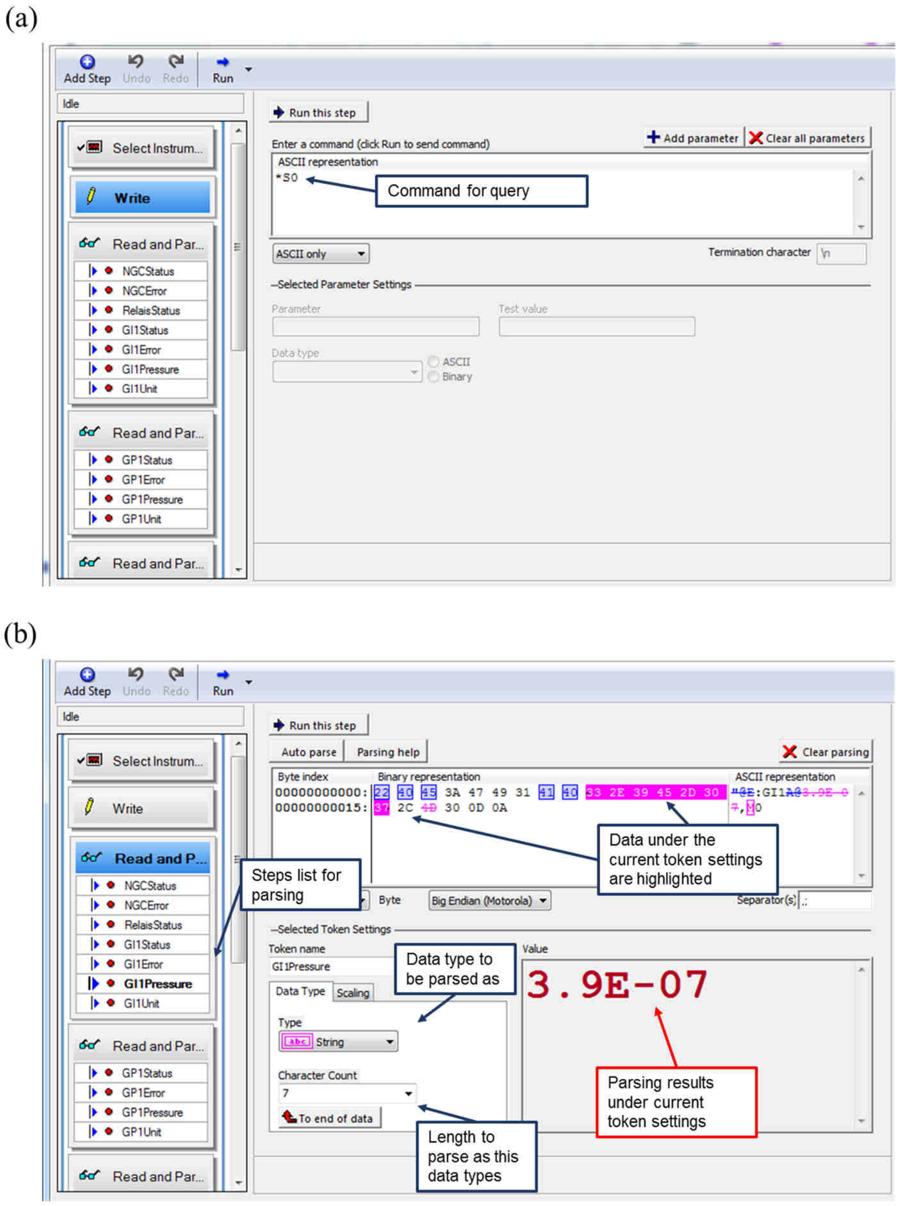

(a)

Enter a command (click Run to send command)

ASCII representation

```
*S0
```

Command for query

ASCII only

Termination character \n

(b)

```
Byte index     Binary representation                                  ASCII representation
00000000000:   22 40 45 3A 47 49 31 41 40 33 2E 39 45 2D 30           "@E:GI1A@3.9E-0
00000000015:   37 2C 4D 30 0D 0A                                      7,M0
```

Data under the current token settings are highlighted

Steps list for parsing

Byte

Big Endian (Motorola)

Separator(s) ,;

Token name: GI1Pressure

Type: String

Character Count: 7

Value: 3.9E-07

Data type to be parsed as

Length to parse as this data types

Parsing results under current token settings

Figure 5.12: Dialog of the Instrument I/O Assistant shown in Figure 5.11. (a): Dialog of “Write” tab. “*S0” is sent to the AML NGC IC controller for the query of all the pressure information. (b): Dialog of “Read and Parse”, which demonstrates the parsing assistance provided by LabVIEW. Data type and byte length is defined by the user, so that the number of steps in parsing as well as the number of separate outputs are also defined, just as can be seen in Figure 5.11. The parsing result is instantly shown on the panel for the judgement of parsing conditions.

5.3 Main Application for Calorimetry

The main application for calorimetry is the core part of the entire data acquisition platform. It combines all the measurements that is carried out for a complete set of adsorption calorimetry on the calorimeter. As a consequence, the structure of this application has the highest complexity among all the applications on the platform. It is necessary to first understand its structure before the introduction to certain functional sections (Figure 5.13)

5.3.1 Initialization of the program

As can be seen in Figure 5.13, with the start of the application, file paths for runtime parameters storage, temporary and formal data files as well as the initialized file I/O task for state monitoring buffer reading, are first passed onto the dedicated data flow. It is shown as greyed blue colored wire, which is branched into three data flows. Meanwhile, instrumental tasks are created by the corresponding methods of client hardwares. Four parallel data flows are created and passed onto the main thread. The GUI of this application, the front panel, is also initialized to the designed state with setting of states for input and control objects. The runtime structure of this application is comprised of three independent threads, two of which have synchronized start because of shared data flows for file operations as well as for instrumental tasks. When entered runtime state with three timed loops running, the timing of these three loops is dependent on the Window system timer, whose time resolution is Windows version and motherboard device dependent. Overall, it stands at 10ms regime [137].

5.3.2 Back Up Thread

The "back up thread" handles only one task, the mutual exclusive behaviors of the two machine mode buttons (Figure 5.14 and 5.15). Here, the term back up refers to the fact that the thread is essentially the open end of this application in case further improvements are going to be implemented for better user experience. The machine mode switch (Figure 5.14) by two buttons rather one is a first attempt from this perspective. In the other two threads, operations/functions for measurements, especially those time critical ones, are already properly realized. Therefore, no further codes for non-measurement purposes shall be added to the other two threads, in order that the tuned stable state of these two threads is kept intact.

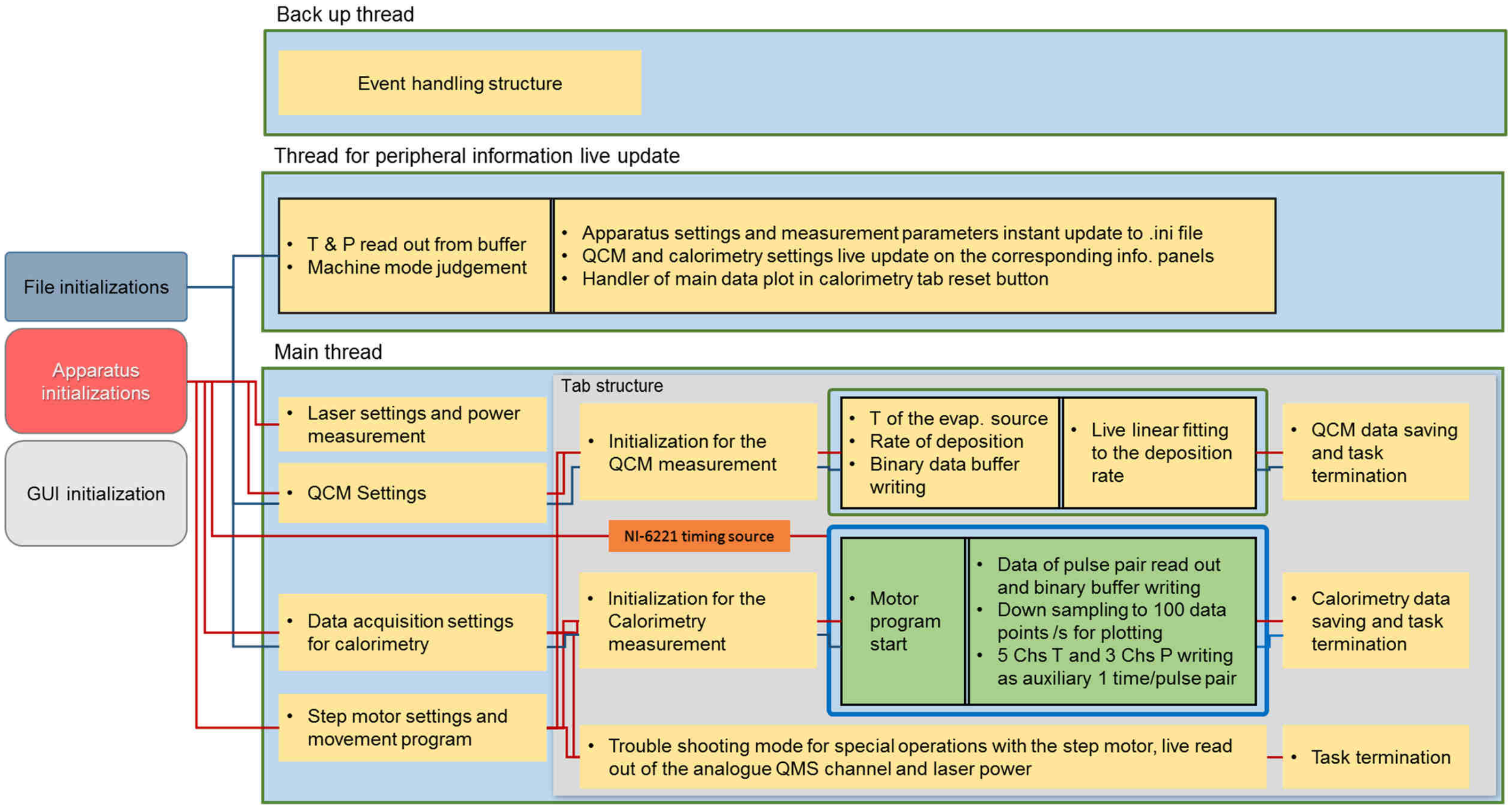

Figure 5.13: Schematic illustration to the code infrastructure of the main application. On the left, program initialization block. Grey-blue wires represent data flows that pass on the information for file operations, i.e., the file paths. Dark red wires represent the data flows that carries instrumental task for hardware communication. Light blue rectangular shapes with thick light green outlines represent timed loops using Windows system timer. A timed loop represents a thread. Inside these threads, rectangular shapes without outline represent the sections executed using native scheduling; black outlined shapes with inner vertical stroke represent the sections that are put into the sequence structures, the stroke stands for the boundary between the subframes. External hardware timed loop is outlined with thick blue line. Sections of step motor control and data acquisition for calorimetry is specially colored with light green. On the grey colored tab structure in main thread, three vertically distributed data flows are not parallel procedures but mutually exclusive to each other.

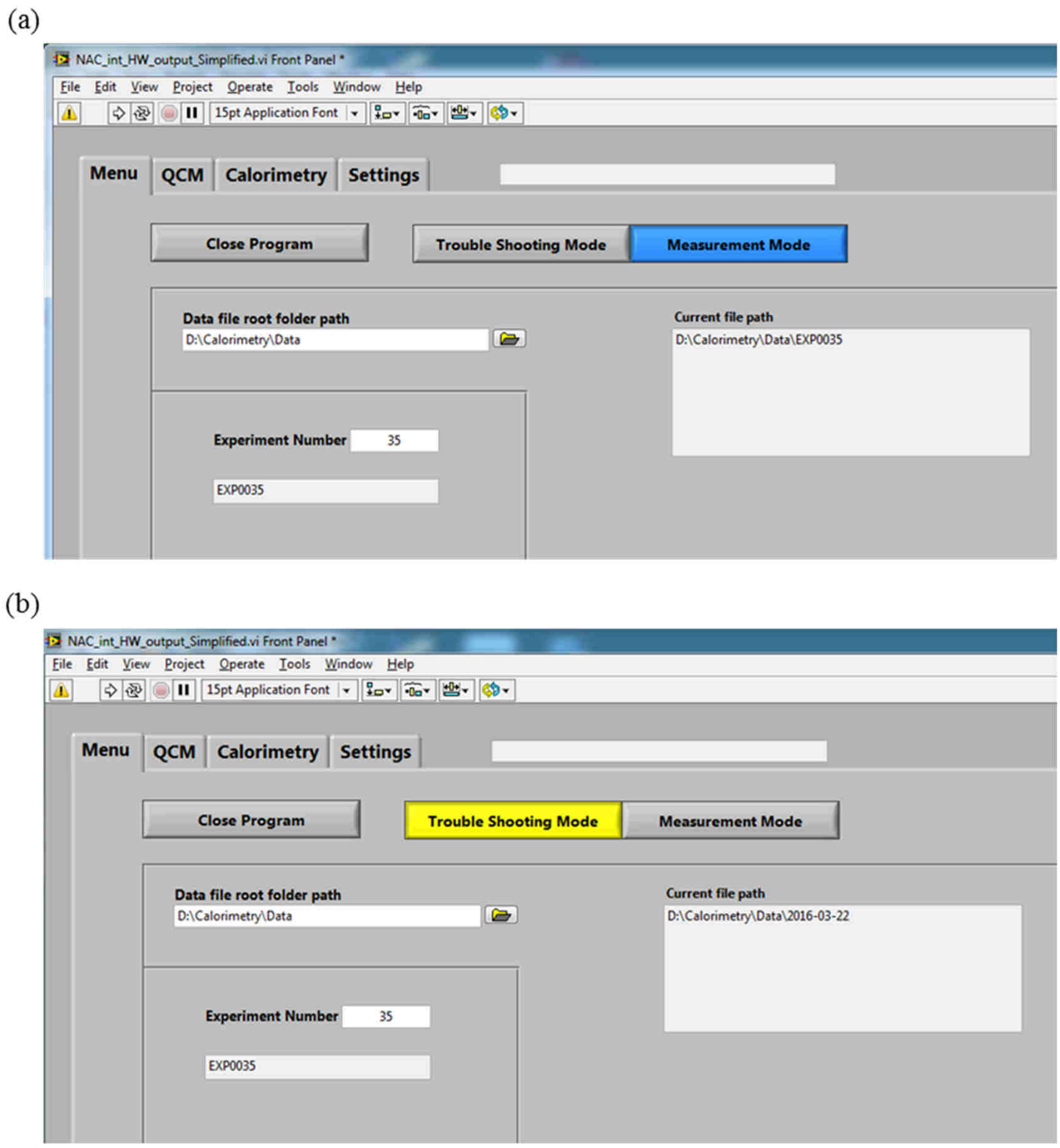

(a)

Data file root folder path: D:\Calorimetry\Data

Current file path: D:\Calorimetry\Data\EXP0035

Experiment Number: 35

EXP0035

(b)

Data file root folder path: D:\Calorimetry\Data

Current file path: D:\Calorimetry\Data\2016-03-22

Experiment Number: 35

EXP0035

Figure 5.14: Two screenshots of the “Menu” tab on the front panel of main application. (a): The situation when “Measurement Mode” is pressed, the back color of this button is changed to blue for the activated state of this mode; the button “Trouble Shooting Mode” will be automatically released. The current file path will be set as root data path + “EXP” + experiment number. (b): The situation when “Trouble Shooting Mode” is pressed; it is essentially the vice-versa of the situation when “Measurement Mode” is pressed, while with yellow button back color and current date as the folder name of the data files. Different nomenclatures for the two modes are intended to help improving the recognizability of the lab book documentations.

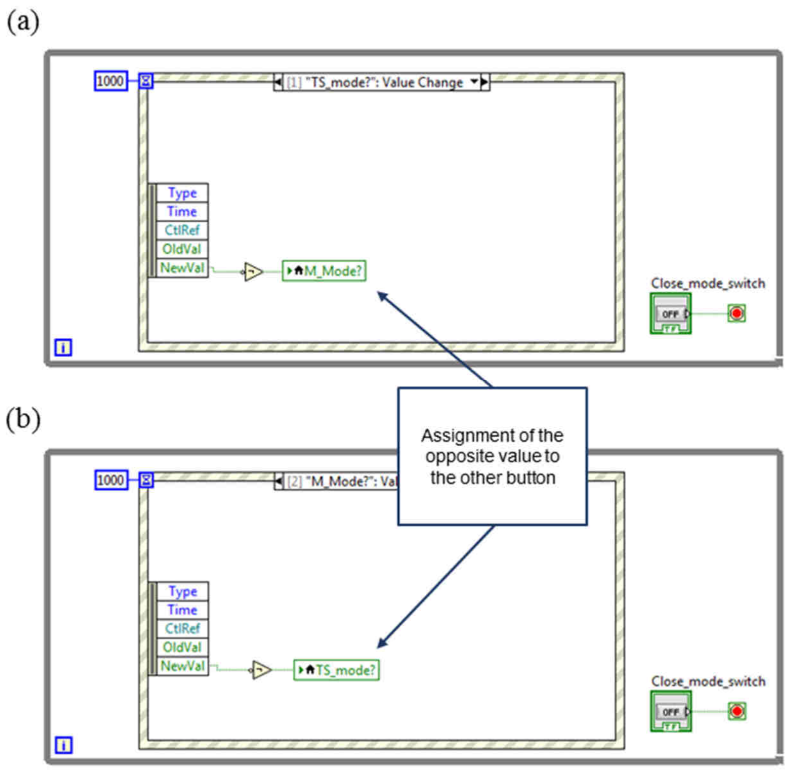

Figure 5.15: Two screenshots of the “Back up thread”. (a): The event associated with the value change of the button “Trouble Shooting Mode”. (b): The event associated with the value change of the button “Measurement Mode”. The integer number 1000 associated to the structure defines the number of milliseconds to wait for any of the included events to occur before a timeout kick in, the thread is passed to the rest of the loop. Here, it is set to 1000 because a too long time before the thread hand over to the off switch of this thread would mean the equally long delay during the shutdown process of the whole application.

5.3.3 Thread for Peripheral Information Live Update

In the “thread for peripheral information live update”, codes are fitted into a sequence structure with two subframes. In the first subframe. All eight channels of temperatures and three channels of pressures are read from the buffer and passed onto the data flow as two arrays respectively. The states handle of the two machine mode selecting buttons (Figure 5.15) are also read in their subframe to if their values have been changed, then the result of judgement as well as the value itself are passed to the next subframe for the relevant operations. In the second subframe, the confirmation of mode change from the first subframe will trigger the change of the data folder nomenclature. Any changes to the instrumental settings on the “setting” tab will trigger the saving of new settings to the runtime parameter file (RTP), a .ini file, on the hard disk. The remaining two tasks, measurement settings live update and range reset function for the main plot of the calorimetry, are in fact only relevant when the corresponding measurement is underway. They will be discussed in the later sections when the corresponding measurements are covered.

5.3.4 Main Thread

The main thread contains all the operations for the procedures of measurement and the transmission of settings to the devices as the preparation to the measurements. As has been demonstrated in Figure 5.13, there are four series of operations initiated by the wired-in data flows. The section for laser settings and laser power measurement is constituted by laser generation and laser power meter control sub blocks (Figure 5.16).

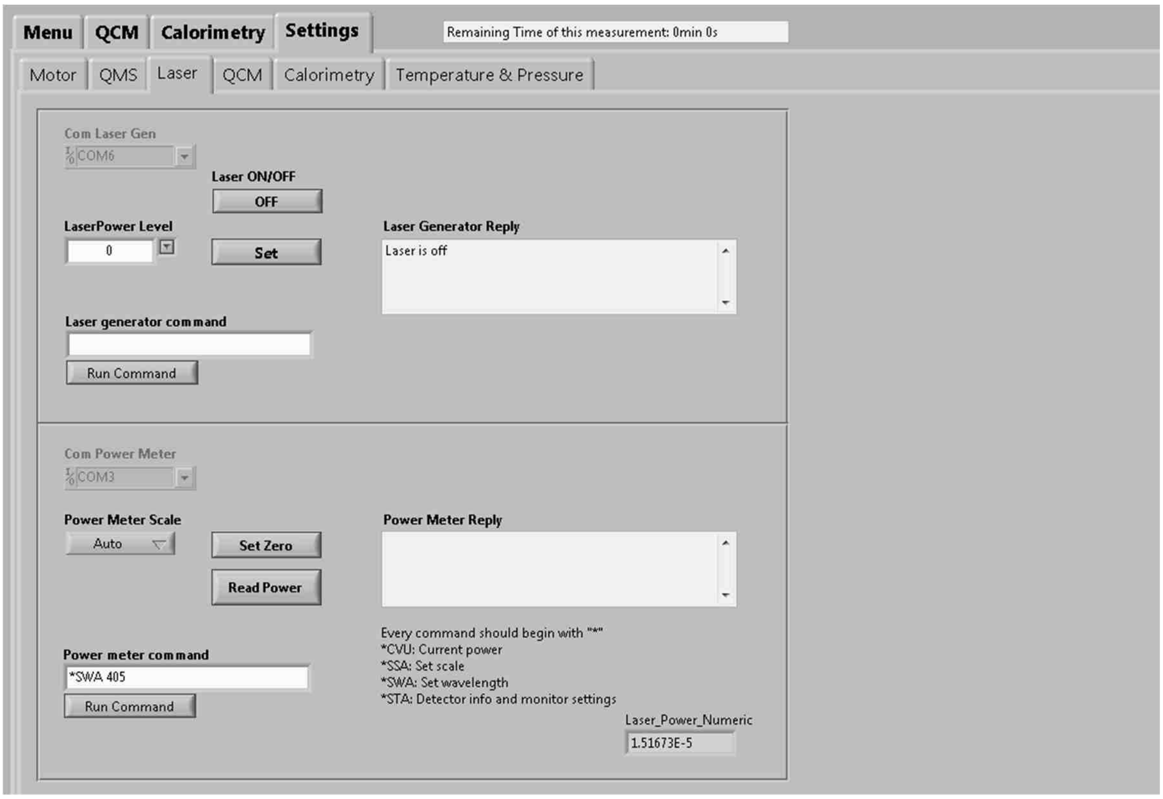

Remaining Time of this measurement: 0min 0s

Com Laser Gen: COM6

LaserPower Level: 0

Laser Generator Reply: Laser is off

Laser generator command:

Com Power Meter: COM3

Power Meter Scale: Auto

Power Meter Reply:

Power meter command: *SWA 405

Every command should begin with "*"
*CVU: Current power
*SSA: Set scale
*SWA: Set wavelength
*STA: Detector info and monitor settings

Laser_Power_Numeric: 1.51673E-5

Figure 5.16: A screenshot to the section of laser related operations on the front panel of main application. The laser part of the application sits on one of the sub tabs on tab “Settings”. It is divided into two blocks: the upper block is laser generation related, functions such as power on/off, output power level in mW and maintenance command council are included; the lower block is laser measurement related, the enabled functions are power meter sensitivity setting, reference point setting, power reading and maintenance command council. Both blocks have their own apparatus reply panel.

Both blocks communicate with the apparatus via the built-in VISA functions of LabVIEW. They have relatively higher efficiency and faster deployment when compared with the Instrument I/O Assistant discussed in the last section of this chapter. Because replies from both the iBeam laser generator and the 845-PE power meter are more natural language resembled, plus they both support multiple input commands for various functions, a common structured VISA communication sub VI is developed based on the built-in VISA functions. Concrete functions are realized by the corresponding input commands (Figure 5.17). Although as shown in Figure 5.17, the sub VI is not 100 percent modulated, communication parameters of Com port are still embedded into the VI. The plain text based structure of communication via VISA is already well established. Communications with either the 845-PE, the iBeam or any other apparatus with Com port support could be carried out with rather high flexibility over the length of input command as well as the length of reply.

As can be seen from Figure 5.18, each function shown in the lower part of Figure 5.16 is put into a subframe of the stack sequence structure. Such arrangement does not stem from the logic requirement of execution, but is because of the practical need to constrain the size of the codes and organize them in the block diagram. As the codes constructed upon bottom up strategy grow constantly more complicated with the implementation of more tasks, it becomes increasingly necessary to organize the codes in a way that each functional section could be conveniently identified. However, as has been previously discussed, constraining of data flows with sequence structure should be carefully carried out to avoid the potential timing issue. Because the laser related settings and laser power measurements are not time critical procedures, as can be seen in Figure 5.13, the codes of this section all sit directly in the outermost loop of main thread. Therefore, the implementation of the logically unnecessary sequence structures will not lead to executional problems.

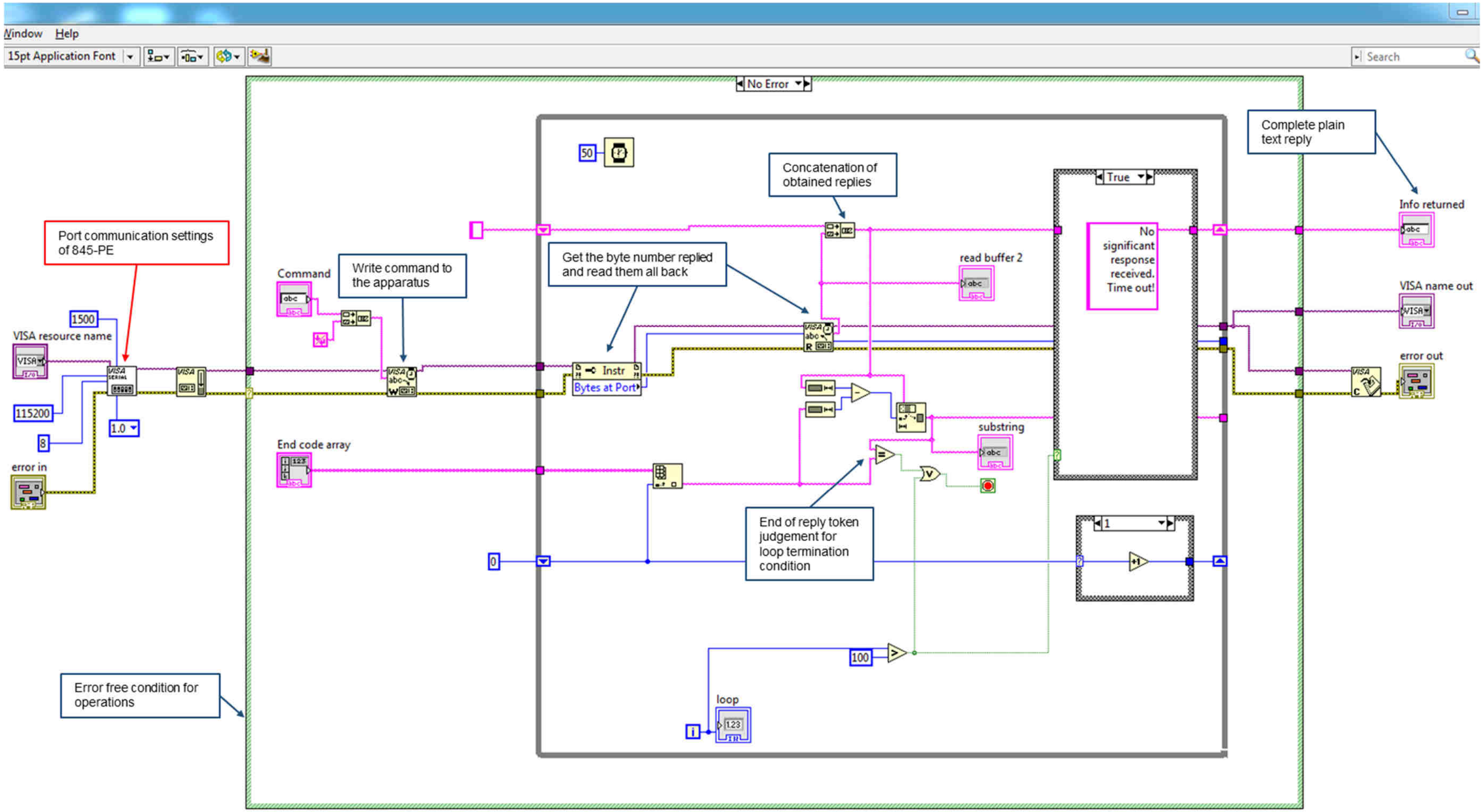

Figure 5.17: A Screenshot to the block diagram of VISA communication sub VI for the 845-PE. The Com port settings are incorporated into the block diagram. Such arrangement could avoid duplicate input nodes on the block diagram of the upper level VI, improve its orderliness. The VISA task name, error in, input command and end token of the reply are fed in as the input. This Vi is manually cleaned up and organized.

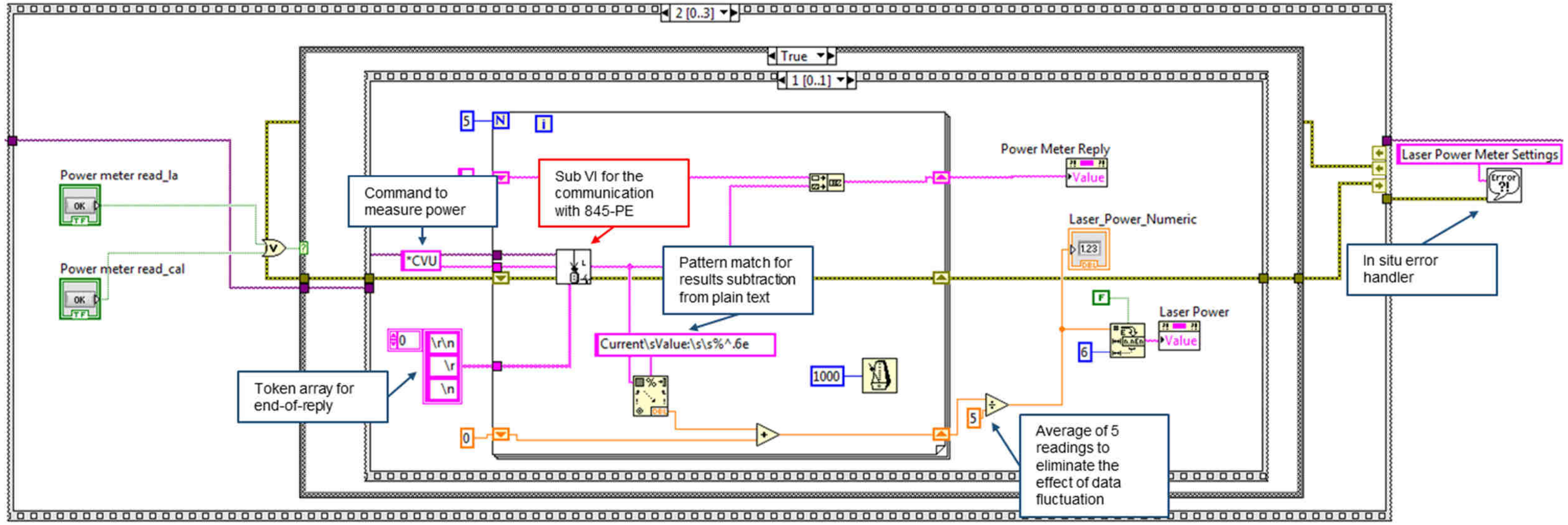

Figure 5.18: A Screenshot to the diagram for laser power measurement in main application. This section is constituted of double layer stack sequence structures. Each subframe in the outer sequence represents a function shown in the lower part of Figure 5.16. This subframe, 2nd of 3, contains the “read power” function on the front panel. In the Boolean condition box, another stack sequence structure is introduced. In this exhibited subframe of the inner sequence structure, the command for the 845-PE to measure the laser power is given to the communication sub VI. The VI is called 5 times at the interval of 1s to obtain the averaged laser power. Here, it is rather evident that embedding the Com port parameter into the communication sub VI is necessary for the cleanliness of the diagram, or the hard choice between expanding the diagram to accommodate the code and poor readability will have to be made. The in situ error handler at the end of each functional section would help the debugger to rapidly locate the problematic position. In a multitask program with huge block diagram, this trick could save a considerable amount of time.

The tab of QCM settings is shown in Figure 5.19.

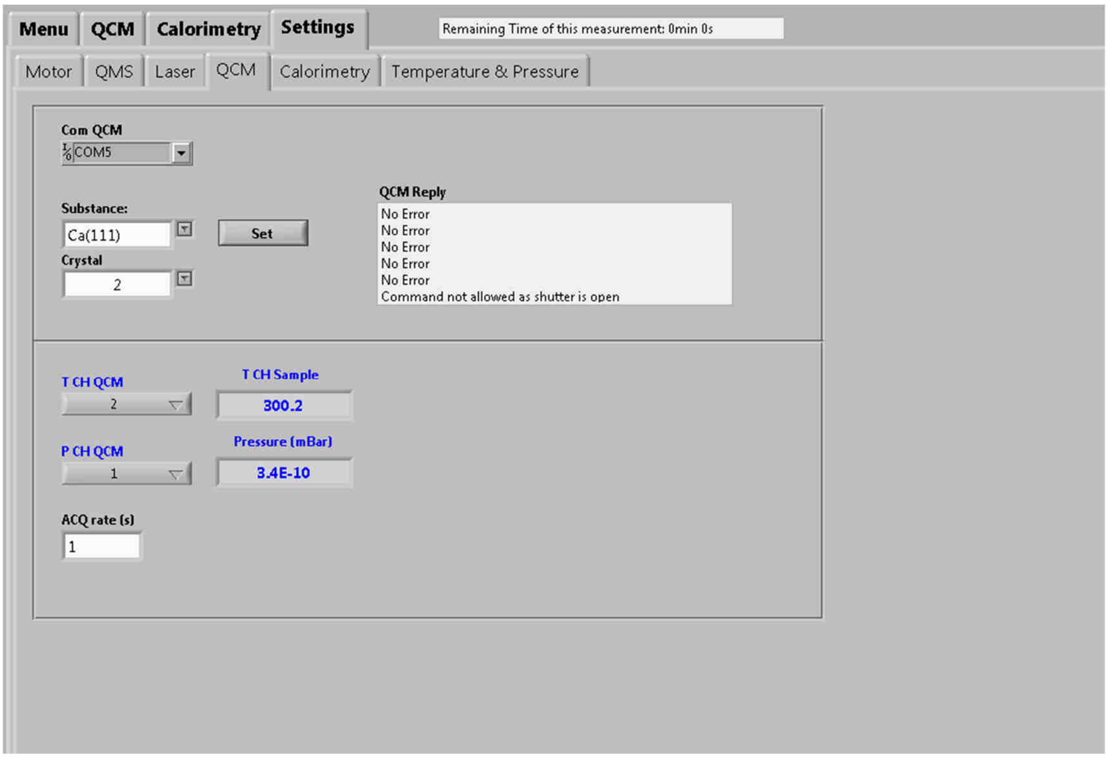

Remaining Time of this measurement: 0min 0s

Com QCM: COM5

Substance: Ca(111)

Crystal: 2

QCM Reply
No Error
No Error
No Error
No Error
No Error
Command not allowed as shutter is open

T CH QCM: 2

T CH Sample: 300.2

P CH QCM: 1

Pressure (mBar): 3.4E-10

ACQ rate (s): 1

Figure 5.19: A screenshot to the tab of QCM settings on the front panel of main application. In the upper subframe, the selection of the substance would pick the corresponding acoustic impedance and density data from the .ini file; the crystal selection between 1 and 2 defines the active electrical channel of the two that the IL150 is set to monitor. These two selection does not automatically communicate with IL150 through VISA upon the new value update, the commands are sent by the click of button “Set”. The judgment for the changes of the QCM settings in the “thread for peripheral information live update” is also associated with this button rather than the two controls for value selection. In the lower subframe, temperature channel and pressure channel selection defines from which channel, the data of temperature and pressure are to be recorded alongside the QCM data read from IL150. ACQ rate defines the time interval (s) between the two data points read from the IL150.

Settings of the QCM are sent to the IL150 QCM controller to take effect. It is realized essentially with similar Com port communication mechanism as what has been shown in the laser part, except that the reply from IL150 has relatively higher complexity than the two laser related apparatus. Same as the laser part, the setting communications of QCM are not time critical, the codes of this part also stand directly in the outermost loop of the main thread.

The tab of data acquisition settings for calorimetry is shown in Figure 5.20.

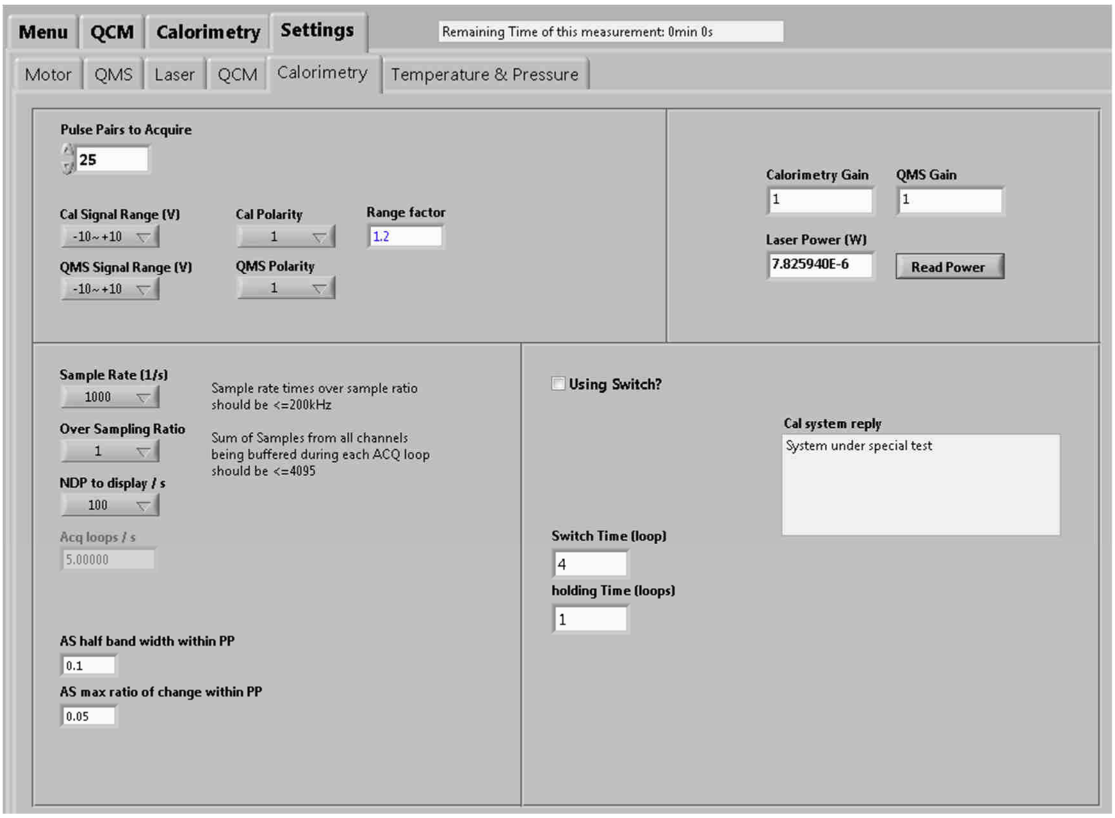

Remaining Time of this measurement: 0min 0s

Pulse Pairs to Acquire: 25

Cal Signal Range (V): -10~+10

Cal Polarity: 1

Range factor: 1.2

QMS Signal Range (V): -10~+10

QMS Polarity: 1

Calorimetry Gain: 1

QMS Gain: 1

Laser Power (W): 7.825940E-6

Sample Rate (1/s): 1000

Sample rate times over sample ratio should be <=200kHz

Over Sampling Ratio: 1

Sum of Samples from all channels being buffered during each ACQ loop should be <=4095

NDP to display / s: 100

Acq loops / s: 5.00000

AS half band width within PP: 0.1

AS max ratio of change within PP: 0.05

☐ Using Switch?

Cal system reply: System under special test

Switch Time (loop): 4

holding Time (loops): 1

Figure 5.20: A screenshot to the tab of calorimetry data acquisition settings on the front panel of main application. In the upper left subframe, the number of pulse pairs to acquire, the voltage acquisition range of calorimetry and QMS as well as their signal polarity, the range factor defines multiplying ratio of the plot pane range with respect to the voltage acquisition range. In the upper right subframe, two gain factor are reserved in case of the secondary amplification. When not, default values 1 are automatically filled and stored in the header of the data file. Another laser power reading control button is also placed here because it stands together with the gain factors in the header. The state handle of this button is placed in the diagram of the laser power measurement (Figure 5.18). In the lower left subframe, the rate of sampling for the data file, the over sampling ratio for raw data reading, and number of data points to plot for calorimetry and QMS are selected. The greyed out field "Acq loops /s" defines the number of hardware timed loops per second that will be executed or the duration of each hardware timed loop. The rest two input fields define the allowed ratio of the amplitudes change of the base line within a pulse pair if the auto start to the acquisition is going to be used.

The code diagram of "data acquisition settings for calorimetry" in Figure 5.13 are presented in Figure 5.21-5.22. The selection to the voltage acquisition range of calorimetry and QMS, the rate of sampling for data file, the over sampling ratio for raw data reading from the NI 6221 card take effect right away in this section. These three adjustments constitute the principal properties of a calorimetry data acquisition.

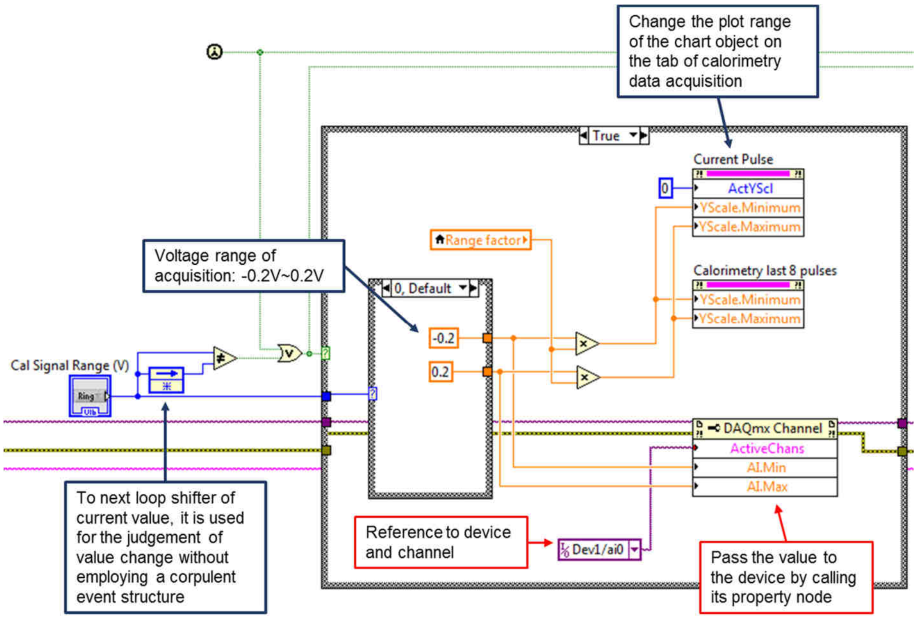

Change the plot range of the chart object on the tab of calorimetry data acquisition

Voltage range of acquisition: -0.2V~0.2V

To next loop shifter of current value, it is used for the judgement of value change without employing a corpulent event structure

Reference to device and channel

Pass the value to the device by calling its property node

Figure 5.21: A screenshot to the diagram of setting the calorimetry data acquisition range. The feedback node is used as the value shifter to the next loop. Note that the loop here refers to the outermost loop of the main thread in Figure 5.13. The judgement, for whether a change of selection take place at the front panel drop-down box “Cal Signal Range”, uses a feedback function of the same value across loops. Such arrangement exempts the use of an additional button to trigger the setting operations. The value of the drop down box is directly wired to a multi-case structure with corresponding content combinations. The settings are transferred to the NI 6221 card by calling the property node referenced to the specified channel. The setting of the QMS data acquisition range uses exactly the same method since it occupies another equivalent analog channel on the NI 6221 card.

The data acquisition range is an independent property for each input or out channel on the NI 6221 card. Therefore, it is unnecessary to put the settings for all channels in the same conditional case structure and execute all of them every time. To avoid insignificant execution of the same code, a dedicated button is usually used to trigger “true” condition for the execution of operations. However, if every single setting is bonded with a button, the cleanliness and the logical clarity on the front panel would be impaired. To deal with this problem, which is specific to data-flow driven languages, LabVIEW provides a built-in function called “feedback node”, with which the value of a state handle can be stored and shifted to the next loop, the time when this node is again read by the thread. With two values from different point-in-times, a simple comparison could be carried out for the judgement of value change. The operation, which resembles an event of data change, could then be realized with very little extra effort (Figure 5.21).

Parameters of data acquisition are critical to both the quality of the acquired data and the reliability of the synchronized operations in the hardware timed loops. Higher sampling rates are in general favorable since the least significant sampling rate should be no lower than the Nyquist rate of a signal system[138]. However, in a G language programmed system, the computing power to stably withstand the sampling and real time plotting tasks

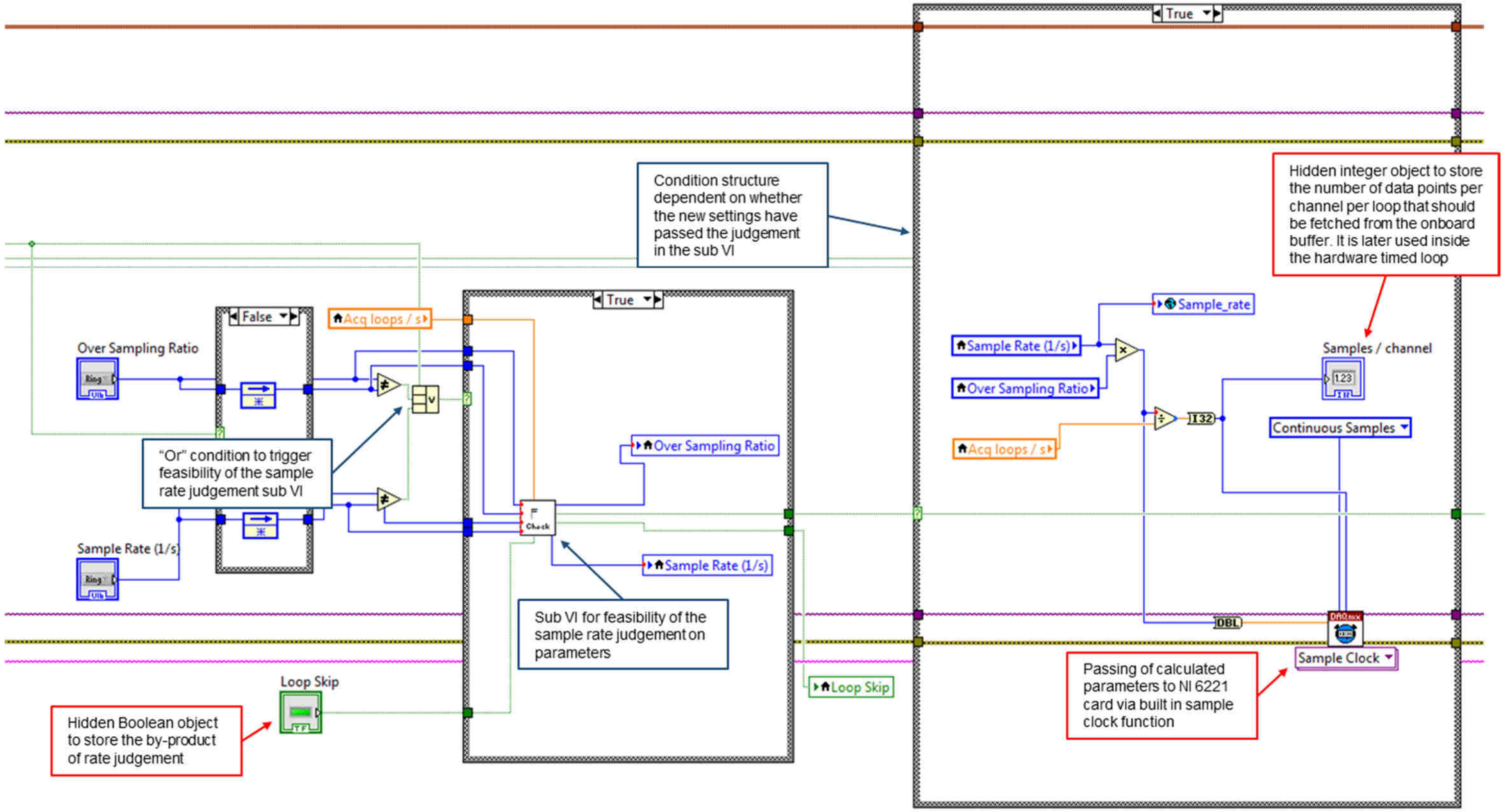

Condition structure dependent on whether the new settings have passed the judgement in the sub VI

Hidden integer object to store the number of data points per channel per loop that should be fetched from the onboard buffer. It is later used inside the hardware timed loop

“Or” condition to trigger feasibility of the sample rate judgement sub VI

Sub VI for feasibility of the sample rate judgement on parameters

Passing of calculated parameters to NI 6221 card via built in sample clock function

Hidden Boolean object to store the by-product of rate judgement

Figure 5.22: A screenshot to the diagram of setting the calorimetry data acquisition rate. Feedback node is used for the judgement of value change. Because changes to either oversampling ratio or sampling rate would lead to feasibility suspicion to the whole set of parameters, the judgement sub VI is called under “or” condition. The Boolean output from the sub VI to allow actual passing of parameter to the card and other objects will only be true if two conditions are simultaneously fulfilled: 1. the total rate of raw data read back from the card is ≤ 200 kHz. In our system, calorimetry and QMS channel have to be counted together. 2. At any time, accumulated data in the onboard buffer should be ≤ 4095. Given that 200 ms loop duration has been fixed since the initialization of the application, not all combinations of the options listed on the drop box of over sample ratio and sample ration are applicable. If the newly chosen option combination does not fulfill the two conditions simultaneously, old value before user’s change will be fed back to the controls.

could easily fall behind the demand that the NI data acquisition card is allowed to request. If such overflow of tasks occurs during the acquisition, an out-of-synchronization error always closely follows, resulting in the abrupt interruption to the ongoing data acquisition procedure. Some compromises are needed in the way to fully utilize the potential of the data acquisition card. The solution is to use a layered load assignment for different tasks.

1. The raw data conversion and sampling from analog signal is carried out by the NI 6221 card through onboard hardware algorithm, it is therefore the least computing power demanding task in the data acquisition system. The overall raw data read back rate in the card is designed to fully utilize the physical capacity of the NI 6221 card. Its total data points that all channels acquire per second, regardless of the precision, should be no more than 250 k. In our system, a 200 kHz is set as upper limit for sufficient redundancy.
2. The sampling rate for the temporary data stored as the binary file is the real sampling rate of the data file a measurement will ultimately produce. It is dependent on the data processing speed of the CPU as well as the raw writing speed of the hard disk mounted on the computer. Because the raw writing speed of binary file to the hard disk is usually the bottleneck to the overall handling speed (at least in the era of rotational magnetic hard disk), an over sampling ratio is introduced to reduce the sample rate in the binary file. That is, averaging of the raw data read from the card by the factor of this over sampling ratio. In our system, the sampling rate chosen by the user is the rate of data stored to the hard disk, while the actual setting passed to the acquisition card is the multiple of this rate with the over sample ratio. Such arrangement would help the user to focus on the real data sampling rate obtained for later analysis rather than on the settings of card parameter.
3. Because the dynamic image rendering is the most computing power consuming task in the data acquisition program, not all data stored in the binary file are plotted in real time. Another drop down box is added to select number of data points/s to be plotted. With a defined rate of plotting, a further downsample is carried out upon the data that should be stored on the hard disk.

Besides the balance between the amount of data to process and its computing load, another limitation, which also constrains the feasible parameters set to the NI 6221 card, is the size of data buffer on the card. The onboard buffer, regardless of data precision, is only 4K/4095 for all channels combined. A sustainable data acquisition procedure should be built on equal pace of analog signal conversion into the buffer as well as the fetching operation from and then the address release in the buffer, or a buffer overload would be otherwise triggered, which interrupts the data acquisition with irrecoverable error. If compared with up to 250 k/s sampling speed, the size of the buffer appears to be rather inadequate. Such mismatch raises a major issue to the design of the hardware timed loop duration. Because the data fetching function is called only once per loop for the simplicity of the code, the loop duration has to be short enough to avoid the overflow of the buffer between two calls to the data fetching function in two consecutive loops. On the other hand, other operations in each loop, especially the communication with 3rd party apparatus, writing of data to the temporary file and data plotting, will need their minimum execution time to accomplish the their related calling operations. This means although the data to process per loop decrease proportionally with the reduction of loop duration, such reduction still reaches its limit when the risk of task overflow increases significantly under the too tight time allowance for all operations. As a consequence, another balance has to be considered when defining the sample rate of acquisition. For simplicity, the loop time is first fixed in our system because it has to be defined with the creation of an external timing source. This is carried out in the initialization phase of the entire program. Therefore, as seen in Figure 5.20, the input field "Acq loops / s" is greyed out during the runtime. The change to this parameter is only allowed before the initialization of the application. Practically, the duration of the hardware timed loop is fixed at 200 ms (5 loops/s as seen in Figure 5.20). We find out that 5 times of plot update per second is already smooth enough for users, while 200 ms still enables a wide range of options for the adjustment of sample rate and oversampling ratio.

As can be seen from Figure 5.22, the Boolean object "loop skip" is used to hand over and receive values before and after the judgement sub VI. On the front panel, this object is hidden. Its function is like a local variable of the application, which can be used to store and pass on data inside this application. The "sample / channel" in the right side condition structure is used with the same method. Its value are used later inside the hardware timed loop. This method of using the hidden objects as variable is widely used in the development of our applications. When compared with the formal global variable system of LabVIEW, this non-formal method provides more possibilities of code maneuver via miscellaneous built-in properties of an object, which can be easily accessed via the built-in property node function. However, if global variables are used to enable cross VI data sharing, only default type of an object's data could be transferred through them. Properties maneuvered by local property node are not allowed to be transferred by variables. This limitation has largely confined the usage of global variables to pure data storage and transferring purposes.

The communications with the step motor controller SMD2 are carried out via Com port plain text communication, similar to that with the iBeam or the IL150. The tab of the motor settings (Figure 5.23) combines the front panel function of the codes from the section of the step motor settings and the troubleshooting mode for special operations (Figure 5.13). They are put together because the creation of troubleshooting mode started with the troubleshooting of the problem of lost relative motor position: During the construction of the adsorption calorimeter, there was once a period of time that the step motor may randomly lose its relative position against the set reference as it is in the continuous program controlled movement to generate pulse pairs. Before the real cause was found, every time we encountered this problem, a series of verification tests had to be carried out to reset the reference point of the step motor, which is "0" for the open position of the chopper to allow the full molecular beam flux to pass through. To make sure that the chopper is at the fully open position in the center of the beam, double check of maximum flux and maximum laser power is carried out every time. The verification measurements require step by step movement of chopper/motor using the maintenance console to input ±1 step commands. Impact of one step movement on the signal intensity of QMS or on laser power is observed through their chart plot. When the reference point is saved by clicking "save as open" button, "close+", "open", "close-" are used to simulate the real movement of the motor in a normal measurement and see the outcome in the QMS or laser power signal. After the verification procedure, the chopper position has to be put back to "close+", the starting point of motor program for every pulse pair period.

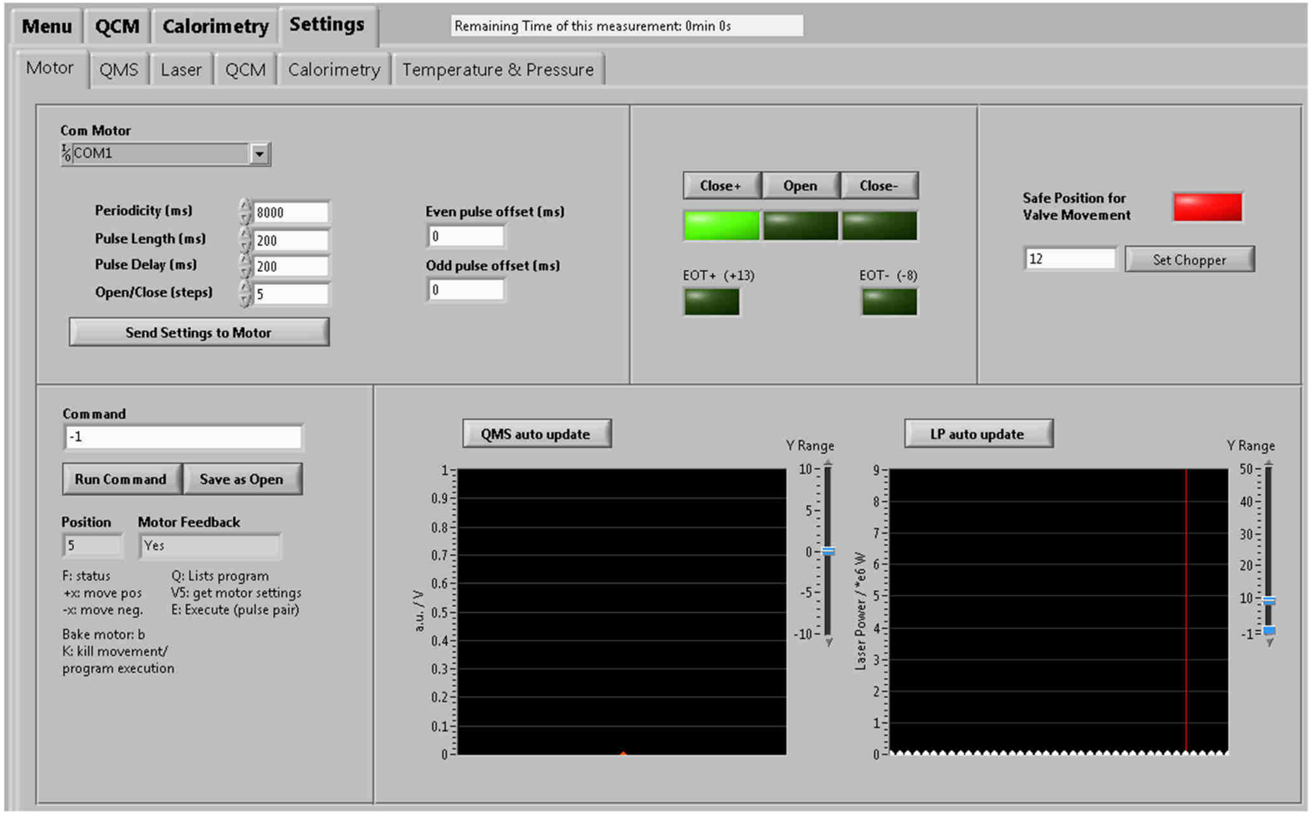

Remaining Time of this measurement: 0min 0s

Com Motor: COM1

Periodicity (ms): 8000

Pulse Length (ms): 200

Pulse Delay (ms): 200

Open/Close (steps): 5

Even pulse offset (ms): 0

Odd pulse offset (ms): 0

EOT+ (+13)

EOT- (-8)

Safe Position for Valve Movement

12

Command: -1

Position: 5

Motor Feedback: Yes

F: status
+x: move pos
-x: move neg.

Q: Lists program
V5: get motor settings
E: Execute (pulse pair)

Bake motor: b
K: kill movement/ program execution

Figure 5.23: A screenshot to the tab of motor settings and troubleshooting special operations. In the upper left subframe, input controls of the motor movement related parameters are placed. The left column stands the designed parameters for each pulse pair; the right column contain two offset correction parameters for the realization of the designed parameters. The change to the parameters will trigger disabling and greying out operation to the motor movement control buttons in the upper middle subframe as well as the buttons of the same setup in the tab of QCM and calorimetry. They will be recovered only if new settings are processed and sent to the SMD2 motor controller without triggering error. The upper middle subframe contains control buttons for the direct movement of the chopper to "close+", "open", "close-" positions. The LED indicators for these three positions and two end of travel limits on both sides of movement are also included. The upper right subframe contains the button for the direct movement of the chopper to the valve-save position, which allows the closing movement of the homemade beam/main chamber isolation valve. The lower left subframe holds the maintenance console of the SMD2 controller.

In order to achieve synchronized procedures of chopper motor movement for pulse pair generation and data acquisition, there are in general two routes to realize the synchronized and programmed motor control. Since the hardware timed loops constitute the basis of the data acquisition system for pulsed signal, both routes have to subject to the general commands of the loop timing source for start and stop.

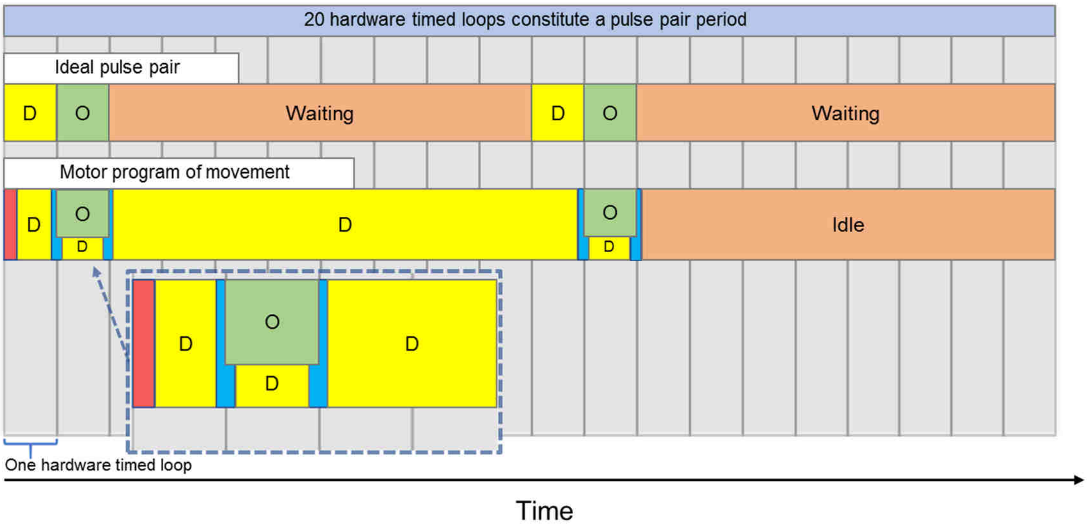

Figure 5.24: Schematic illustration of the relationship between the hardware timed loops and motor program referenced to the time of a pulse pair. Here, the period for a pulse pair is assumed to be 4s. Each hardware timed loop is assumed to last 200 ms. The time that the chopper stays in open position/ the pulse and the delay before the pulse are assumed to be both 200 ms long. D with yellow back color represents delay time, O with green back color represents chopper opening time, blue region represents chopper/motor moving time. They cross the border of the loops because the movement of the motor is not directly controlled by the hardware timed loop, but by the internal timer of the SMD2 controller. The red region in front of first delay in the motor program represents the dead time between the start of the hardware timing of each pulse pair and the start of the motor program by the SMD2 controller. The zoomed-in view to the region of the motor program start is also presented.

The more straightforward route is to directly give the movement commands via Com port communication with a planned timing sequence. Commands for different movements are transferred with different ordinal number within one iteration. The limitation of this method lies largely on its timing precision. Because the transferring of a command to the motor controller is carried out by calling the communication sub VI inside the loop, the actual time stamp for the execution of these commands may in fact sway around randomly. Although the differences in the response time of the controller to different commands may be small enough to be neglected, the dynamic computing load of the whole application or even the whole computer cannot be ensured to stay constant for all the pulse pairs. Therefore, the real time stamp of execution for each chopper/motor movement becomes runtime environment dependent. The hardware timed loop only ensures the precision on the rolling pace of loops yet the identical execution time of all operations in each loop. Take the 200 ms loop in Figure 5.24 for instance: The execution of the timed loop is underway while the other two threads are lively responsive under the asynchronized paces. Even if the user chooses to conduct no other operation to provoke codes in the other thread, there are still outside applications and Windows system services running on the same computer, Fluctuations in the CPU load would result in random delay or advancement in the execution of command transfer to SMD2. Meanwhile, all the tasks inside each 200 ms loop should still be accomplished in time while the continuous running of the measurement is not disturbed. To forcibly optimize the reproducibility of timing on the motor movement, extra tiny halts to the execution by a few milliseconds, of which the amount has to be experimentally calibrated, will have to be added before and after the command transferring. The total duration of each hardware timed loop should be compressed as much as possible to squeeze the idle time in each loop, the more the added halts constitute the total time of each loop, the higher influence is imposed by these halts on the pace of execution throughout the entire loop. However, as has been previously discussed, the loop duration is very critical to the stability of the data acquisition procedure. Improvement to the timing precision of the motor movement in exchange of system stability is a price that scientific instrumental programming could not afford. In addition to that, time resolution of the motor movement program is also constrained to be no higher than the duration of the loop since it is practically impossible to put more than one step of motor movement inside one loop.

The other route, which is the one we used in our system, requires the execution of all the motor movement program by the motor controller itself rather than by the data acquisition procedure in a step by step manner. This is of course only possible if the motor controller is equipped with its own hardware timer. In this route, the movement program for the complete pulse pair is first constructed by calculation. Before the measurement, the complete program is first sent to and stored in the controller. During the measurement, the only command transferred to the controller is the very simple execution trigger. Under such arrangement, influence of the computing load and other computer related irregularities of execution are ruled out because the data acquisition program and the motor movement program are basically two isolated parallel procedures. The runtime environment inside the motor controller is simple and stable given that there is only one task. This ensures the temporal reproducibility of the controller executed motor movement program. However, there are two major challenges to the performance of this method: 1. two separate timing sources raise issues of timing pace mismatch. Although modern electronic devices are already standardized, the actual timing paces of two devices are likely to have slight differences. This is dependent on the method of the manufacturing quality control and the working mechanism of each apparatus that employs the timing device. The internal timer of the SMD2 was found to run 0.2% faster than that of the NI 6221. To avoid the accumulation of asynchronization alongside the measurement, the motor movement program was built for only one pulse pair. An execution trigger is sent to the SMD2 in the first data acquisition loop of each pulse pair to reset the intrinsic asynchronization, In addition, calibration of the timing parameters, i.e., the wait time in the motor program, has to be carried out to correct the asynchronization caused by the unequal time speed. 2. Additional calibrations are necessary to compensate the chopper/motor moving time. The real pulse cannot start/stop abruptly, as there are always a tiny periods of time of around 16 ms when the opening of the beam is a fraction of the full opening because the chopper still covers parts of the beam passage during moving. Non-linear signal response at the beginning and the end of each pulse are inevitable. The purpose of the compensation is to make the effective pulse length/deposition time equivalent to the designed one. As has been demonstrated by Figure 5.24, the crossing of the motor moving time over the loop boundary is observed. The part that invade into the delay time of an ideal pulse represents the moving time of the chopper/motor when the chopper still fully blocks the path of the beam. According to the chopper geometry, of which the area of the blades and the width of the center groove are larger than the actual cross section of the beam, five steps of motor movement is designed to stand between the close standby position and the geometric center position. The beam starts to partially open at 2.5 steps at both sides from the geometric center position, while full open of the beam is achieved when the chopper reaches 1.5 step distance from the center.

This means as long as the chopper moves closer than 1.5 step distance from the center position, no more regulation to the beam flux is imposed by the chopper provided that it is still moving. The reason of using more than the shortest possible steps for the pendulum like open-wait-close chopper movement, as far as the control of motor is concerned, lies with the attempt to eliminate the effect of fluctuated acceleration rate and current overshot caused chopper oscillation. From stand still to full speed moving, the chopper loaded motor needs a few milliseconds to accelerate. The driving current is dynamically self-regulated to attain defined speed and adaptive to the trivial change of the electrical environment. If the chopper stands at the edge of the beam opening, any moving forward would start the opening to the beam. However, the actual settlement time between the start of acceleration and stop after damping may differ due to the fluctuation of the initial acceleration rate. This would lead to instability of the actual pulse length, even if the calibration factor is implemented. When more than two steps are given before the actual start of the beam opening, the motor would regulate itself, after two steps, to cross the boundary with the identical speed and at the identical time after the start. Therefore, the settlement time for beam opening could be kept constant. When the chopper moves close to the stop position, i.e., the concentric center of both the beam and the center groove during the beam opening process, a larger damping current is imposed on the motor to decelerate the motor faster than acceleration. Such current may overshoot to trigger tiny backward movements of the motor and the counter act oscillation of chopper until the motor stands still at the target position. But with larger groove width, when the concentric center position is reached, these subtle movements will no longer interfere with the beam flux. After the pulse, to move the chopper to the other close position, the chopper/motor will need to move another 2.5 steps until the beam is fully closed again. As a consequence, the wait time, as the chopper is standing at the center, would be considerably smaller than the designed pulse length input by the user (Figure 5.23).

The wait between the even and odd pulses is realized by another delay in the motor movement program. Technically it only has a different length as compared with that for the pulse delay or pulse itself. The program for the odd pulse/second pulse is a complete reversal to that of the even pulse/first pulse. After that, the program itself has ended, the motor control is put to idle until the next trigger of execution is sent by the data acquisition program.

Because the ten step movement of the motor for every pulse would cost as much as 80 ms time, pulse lengths shorter than 100 ms are in principle not allowed when designing the pulse pair program. Above this threshold, up to minutes of pulse length or pulse pair time are possible if needed[96]. The real limit is in fact the memory size of the SMD2 because for each delay command, the maximum wait time is 60 s. Longer wait would require more lines of consecutive delay commands, until the maximum length of the program is reached.

The even and odd pulse offsets (shown in Figure 5.23) are two individual temporal corrections to the delay time before each pulse. The introduction of these parameters originates from the needs to correct the timing mismatch after the small changes of chopper's relative position with regard to the beam center. Maintenance work to the chopper-motor assembly or the re-defining of concentric open position will lead to the change of the chopper's relative position. Because the re-positioning of the chopper will not change the kinetic characteristic of the motor, the calibration of the motor is still valid. The offset only fix the obsolete compensation time for the correct start time of the pulses. They could be easily obtained after one test measurement.

The initialization section of the QCM or calorimetry measurement does not contain further transmissions of parameter to the devices. Instead, these so-called initialization procedures are filled with operations that put applications into the runtime state of the corresponding measurement. A major task of such procedures is changing the state of the objects on the front panel to fit the runtime requirements to those objects, i.e., disabling them during measurement. Figure 5.25 shows part of the codes that assign value of states to the objects.

As can be seen in Figure 5.25, the states of some objects on the QCM or Settings tab are changed by the initialization of calorimetry measurement. This operation is aimed to prevent unnecessary operations being carried out unintentionally. Special consideration is given to the motor control objects because a wrong position of the chopper would significantly increase the risk of contamination of the laser reflection mirror or the sample. Actually, the data flows involving objects for the other measurements or operations will not be executed when this measurement, here the calorimetry, is underway. The user operations on those controls will anyhow not influence the ongoing measurement. However, because, for instance, the state of a button will stay unchanged after the user click until its data flow is executed, accidental user click or false data assignment triggered by the buggy chained operations during the ongoing measurement might take effect after this measurement is terminated. The disabling operations are designed to provide some foolproof redundancy.

In G language, value assignment through the referenced property node is rather inconvenient to use as compared with the property value assignment operations in the text-based languages. In those languages, hints on object name and its properties are usually very easy to obtain alongside typing. Some modern programming languages are equipped with the intelligent autofill function, which considerably accelerates the repeated value assignment to the same property of different objects. Even without these advanced functions, as long as a language is text based, copying and pasting the names of an object or its properties is always possible. However, in G language, these conveniences do not exist at all. When assigning a value to a property node, the programmer has to manually pick the property node from the function box and place it onto the block diagram, then right click on this node, browser through the name list tree of all the objects that is allowed to be referenced in this application, click on the name of the target object to link this property node to this object (Figure 5.25). Next, the programmer has to browse again through the list of all the properties this object carries and link the node to the right property. Finally, the complete reference to a property of an object for value assignment is established. During the whole process, neither hint nor autofill is provided. Although copying of property nodes is possible, the programmer would still have to either go through the list of properties to link the correct property or go through the list of object names to link the correct object with a predefined property.

The three major data flows of the main thread: QCM, calorimetry and trouble shooting special operations, are exclusive to each other because they are logically separated by the tab-case structure (Figure 5.13) on the block diagram. It should be pointed out that placing an object on a tab does not necessarily combine block diagram codes of the object with this tab. In fact, a front panel tab structure may act only as a container to visually categorize the objects and meanwhile has no block diagram cases bonded to it at all. This is the reason why the settings of different devices are placed on several sub tabs of tab “Settings”, yet their corresponding codes are put directly in the outermost loop of the main thread without exclusive arrangement against each other. On the other hand, QCM measurement or calorimetry could not proceed simultaneously. They have to be logically exclusive to each other. Therefore, their codes are separated by the main tab bonded case structure. The data acquisition for QCM measurement and calorimetry are carried out in their respective subsidiary loops. During the measurement, the thread will be kept inside these loops. Other sections of the main thread will not be swept by the thread.

The front panel of the QCM tab is shown in Figure 5.26. Because the QCM measurement requires continuous deposition rather than pulse flux, the opening/closing of the beam is controlled manually by the user. “Close+”, “open”, “close-” button as well as the position indicating LEDs, which have the same function as those on the motor setting tab, are also placed on this tab for chopper position control during the measurement. A relatively special feature on this tab is the chart plot for analog QMS signal monitoring. It originates from the need to observe the sticking behavior of the adsorptive on the quartz crystal. In many studies in the literature, when a QCM is used to determine the flux of a metal adsorptive, it is generally assumed that the unity sticking of this metal on the metal coated quartz crystal surface is achieved as the data is taken. However, this assumption might not be true if there is no in-situ observation to the non-sticking part of the flux. In the adsorption calorimeter, we have such in-situ observation through QMS. It is found out that the highly reactive metals, i.e., Mg or Ca, do not reach unity sticking even after the several minutes of direct deposition on the quartz crystal. The time needed to reach unity sticking is of course dependent on the condition of the QCM surface prior to deposition. To determine the flux for the later data analysis of calorimetry, the acquisition of significant data will not start until the corresponding QMS signal of the adsorptive disappears in the chart. For convenience, a live chart of analog channel signal read out is placed aside the total thickness chart of QCM (Figure 5.26). The data acquisition of the QMS signal is carried out by the NI 6221 card through the same channel as that of calorimetry, but with very different apparatus settings from those used for calorimetry data acquisition.

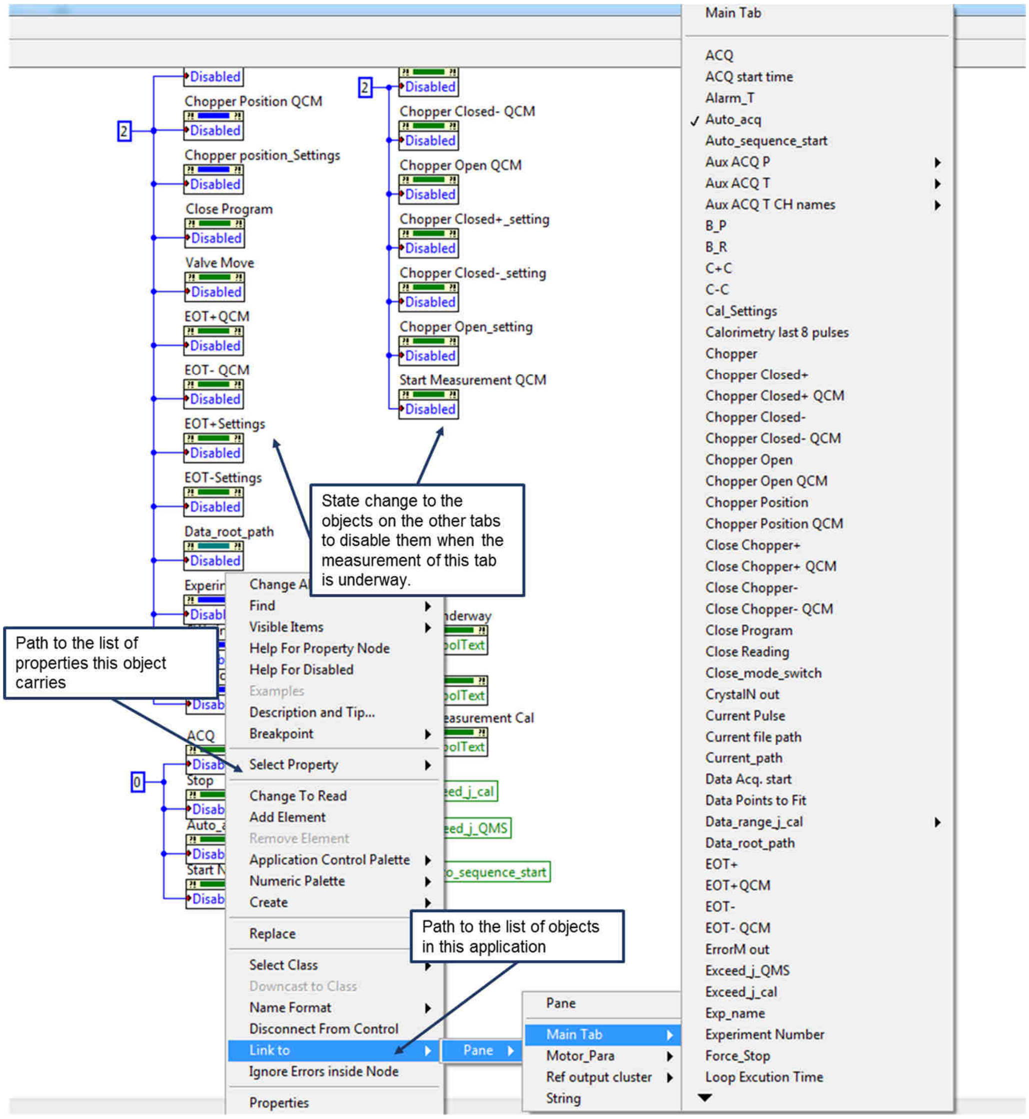

State change to the objects on the other tabs to disable them when the measurement of this tab is underway.

Path to the list of properties this object carries

Path to the list of objects in this application

Figure 5.25: A screenshot of the diagram of the initialization section of calorimetry measurement. The value are given to the property nodes, a special state handle referencing function built-in in LabVIEW. “2” means greyed and disabled at the same time when setting the “disabled” property of an object. “0” means to enable the certain properties. This section is placed right before the loop structure of data acquisition. Here the right-click menu is opened to show how the reference to a property of an object is realized.

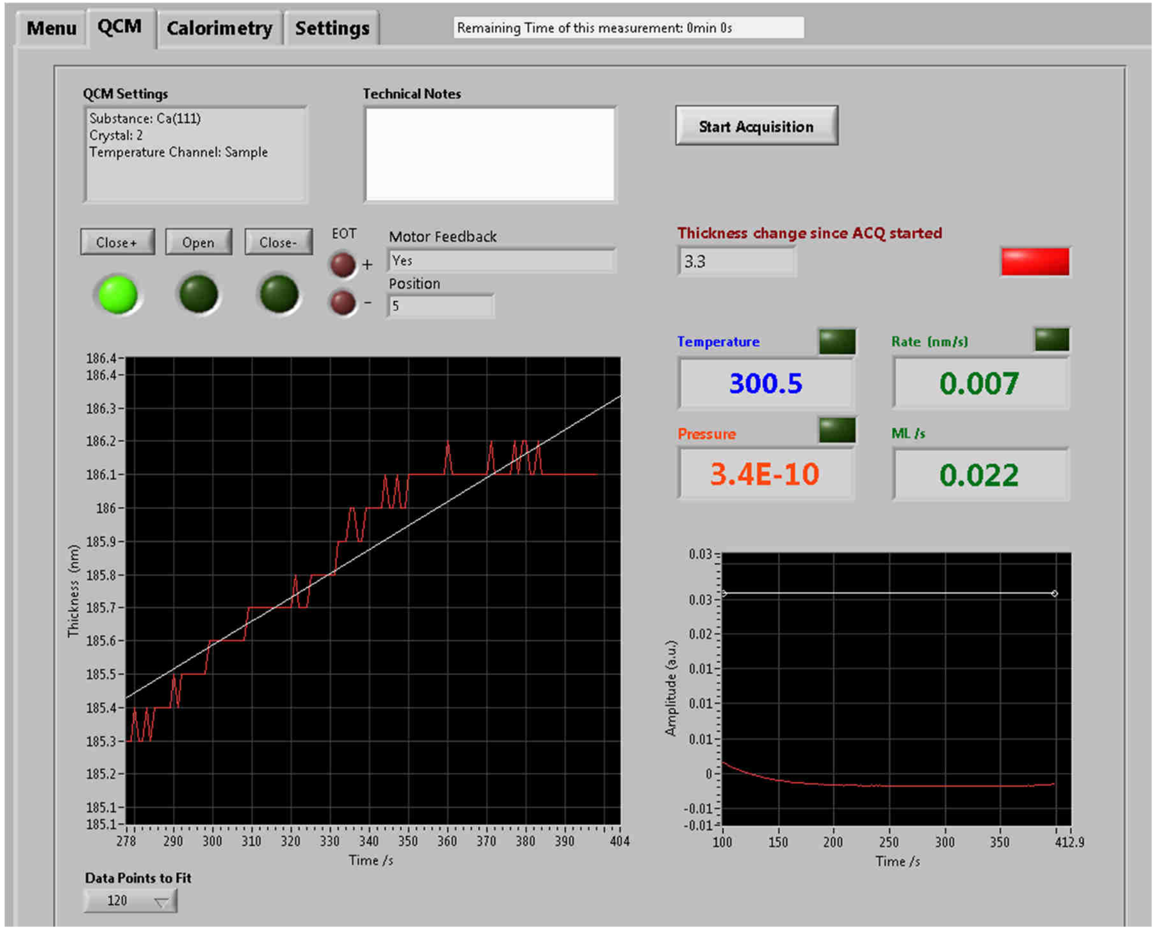

Remaining Time of this measurement: 0min 0s

QCM Settings

Substance: Ca(111)
Crystal: 2
Temperature Channel: Sample

Technical Notes

Motor Feedback: Yes

Position: 5

Thickness change since ACQ started: 3.3

Temperature: 300.5

Rate (nm/s): 0.007

Pressure: 3.4E-10

ML /s: 0.022

Data Points to Fit: 120

Figure 5.26: A screenshot to the front panel tab of the QCM data acquisition. The parameters chosen on its setting tab are displayed in the upper left message box. Motor control buttons as well as LED position and state feedback indicators, which have identical functions as those on the motor setting tab, are also placed here because the QCM measurement requires manual opening of the beam. One channel of temperature, the evaporator temperature, and ion gauge pressure reading are displayed. The left side chart plot displays the real time data of the total thickness readback from the recent 120 s. Below it stands the drop down box to choose the number of the latest points to fit for the deposition rate in two forms. The right side smaller chart plot display the real time QMS read out at the mass of the deposited substance.

The QCM measurement is conducted in a loop timed by the system timer of Windows. Unlike the pulsed calorimetry measurement, the QCM measurement is not as much time critical. The flux is extracted by the fitting from the data over a period of several minutes. Meanwhile, the communication mechanism with the IL150 for the QCM data acquisition is identical to that of the apparatus parameter setting procedure. Baud rate of the RS-232 Com port communication and the command processing speed of the IL150 has constrained the refreshing rate of the QCM data acquisition to be no more than approximately 2 Hz. Therefore, although possible, it does not make sense to use hardware timing for this procedure.

Figures 5.27-5.29 show the codes that are built for the QCM data read back and temporary data storage in a data acquisition loop. These three consecutive figures contain only a fraction of the codes in a complete loop. Plotting and fitting part are not yet included give that already three pages are used for Figures 5.27-5.29. This is a very symbolic example of the difficulty to present the G language codes in printed form. However, the code structure of multitask data acquisition could already be seen from the three figures. One task of QCM data read back from IL150 via Com port communication and the other task of QMS data read back from NI 6221 card are placed in two independent and parallel data flows. Their resulting data are combined together with temperature and pressure information to form a row/line in the data stored in the binary temporary file. In this simplest example of a multitask data acquisition system, the execution priority of the each task is not specifically defined because this acquisition procedure does not rely on strict synchronization of the tasks. In reality, the loop is often running at 1Hz, thus making the potential Windows timer caused ±10 ms asynchronization of the two data read back operations neglectable.

As can be seen from Figure 5.29, the raw data from the NI 6221 card contain both calorimetry and QMS channels while the calorimetry part is later abandoned. Such arrangements stem from the task structure initialized at the beginning of the entire application. For convenience, the device task of two channels acquisition for calorimetry is directly fed into the QCM data acquisition provided that only the QMS channel is needed. If a specifically defined device task is to be used, the previously initialized two channel task would have to be terminated to free the QMS channel. Another task would also have to be initialized inside the application and terminated again once its operation is finished, plus the re-initialization

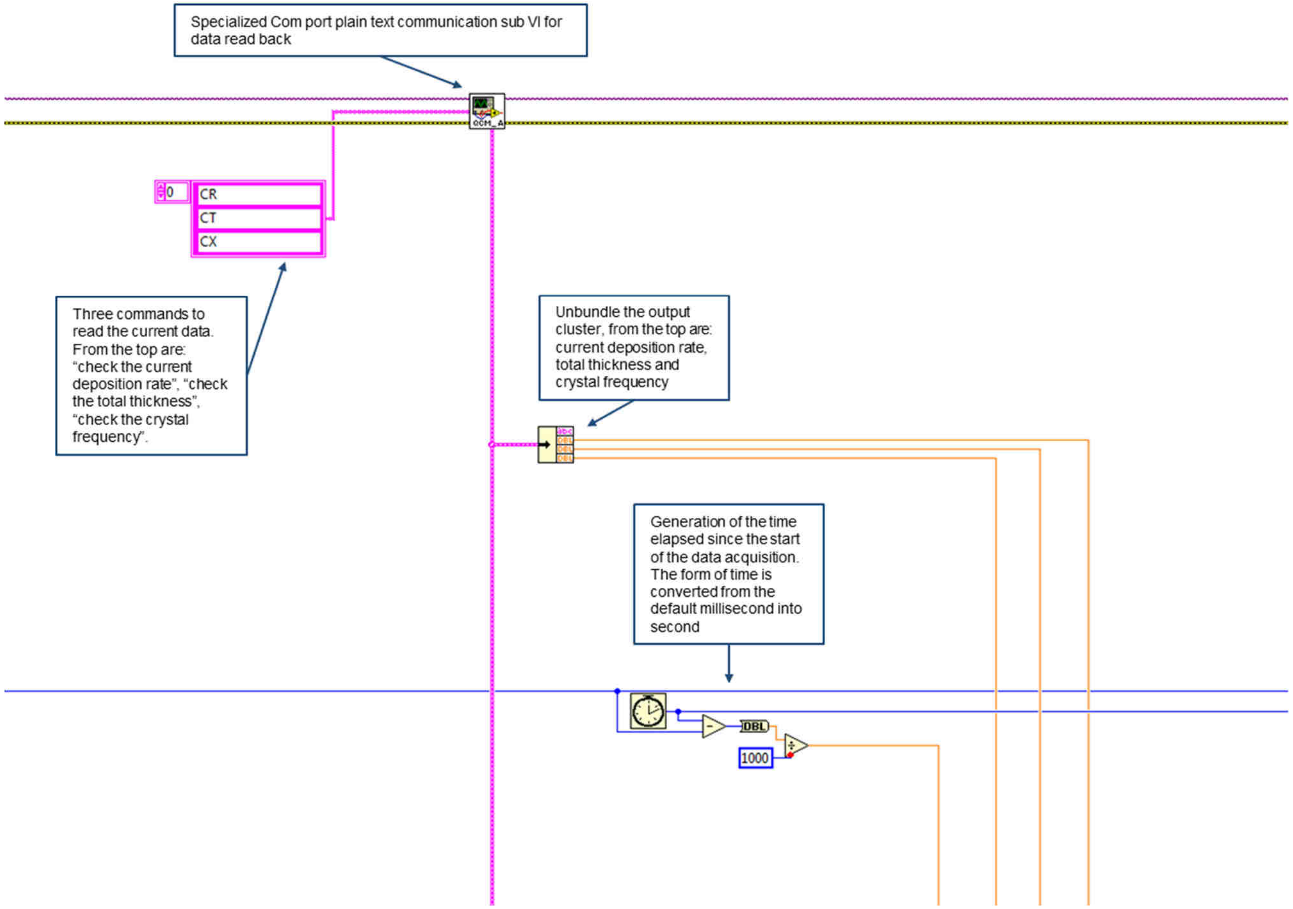

Specialized Com port plain text communication sub VI for data read back

Three commands to read the current data. From the top are: "check the current deposition rate", "check the total thickness", "check the crystal frequency".

Unbundle the output cluster, from the top are: current deposition rate, total thickness and crystal frequency

Generation of the time elapsed since the start of the data acquisition. The form of time is converted from the default millisecond into second

Figure 5.27: A screenshot to a section of the QCM data acquisition block diagram. The sub VI for data read back is a specialized Com port plain text communication subroutine which is dedicated to IL150 controller. Its format of output is fixed to the need of QCM data acquisition in the main application. Therefore, its output is bundled into a cluster that can be directly unbundled and feed into the following part. This helps to keep the diagram clean and simple. The timer of the system gives absolute time reading in milliseconds, it is transformed into second for plotting and storage. In each data acquisition loop, there is only one point of data of various category being read back and recorded, because the requirement for the time resolution of QCM data acquisition is rather low.

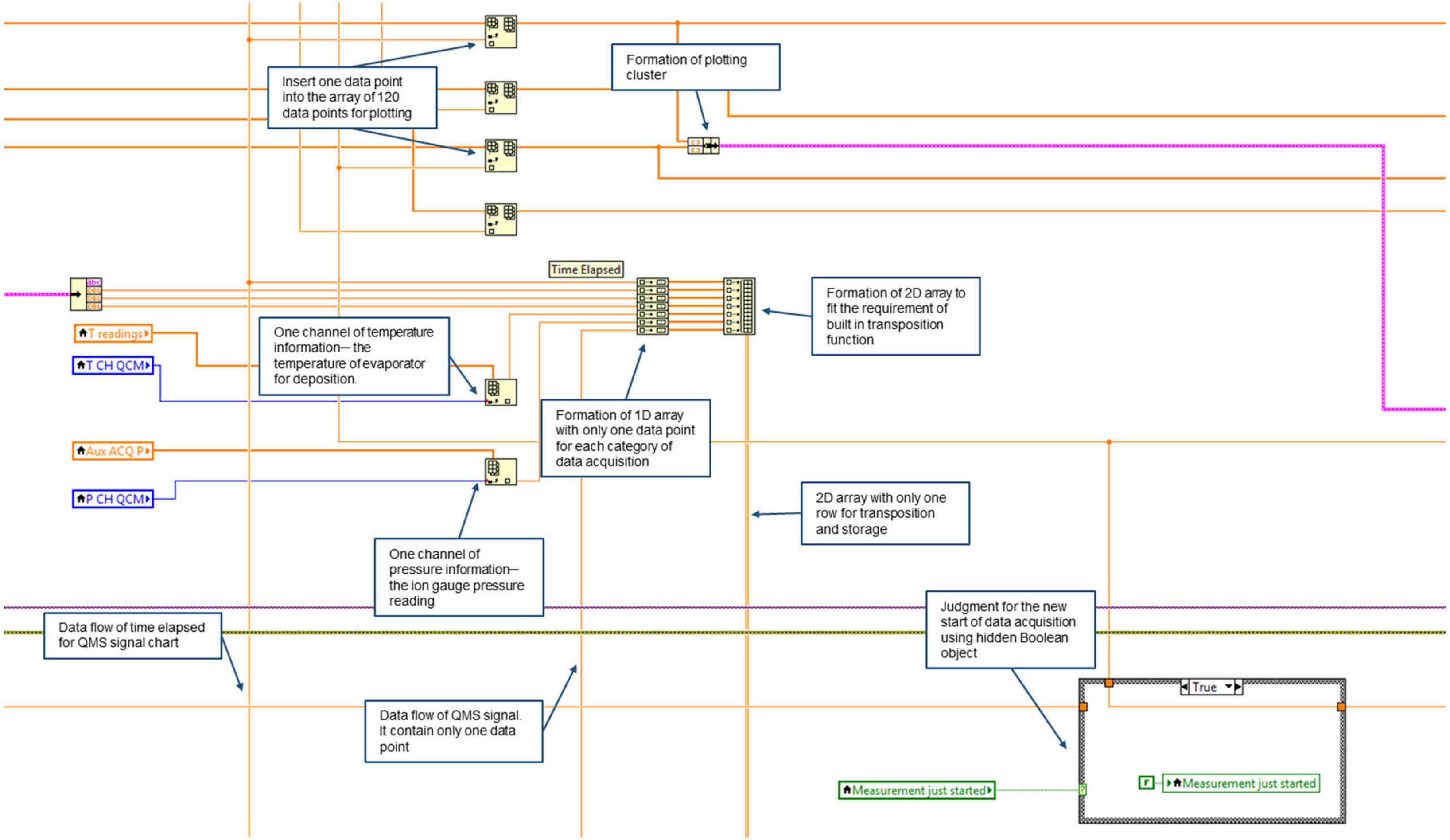

Insert one data point into the array of 120 data points for plotting

Formation of plotting cluster

Formation of 2D array to fit the requirement of built in transposition function

One channel of temperature information– the temperature of evaporator for deposition.

Formation of 1D array with only one data point for each category of data acquisition

2D array with only one row for transposition and storage

One channel of pressure information– the ion gauge pressure reading

Data flow of time elapsed for QMS signal chart

Judgment for the new start of data acquisition using hidden Boolean object

Data flow of QMS signal. It contain only one data point

Figure 5.28: A screenshot to a section of the QCM data acquisition block diagram. The total film thickness on the quartz crystal is chosen for real time plotting. However, current deposition rate and crystal frequency are also prepared as arrays in case temporary monitoring is needed. The total amount of the plotting data is limited to 120 data points. In the figure, the latest point is inserted into the array. The one data point of various categories for storage are put into a 2D array of only one row for further processing. The Boolean condition structure will reset the counting reference at the beginning of each data acquisition procedure for the count of thickness change in the ongoing procedure.

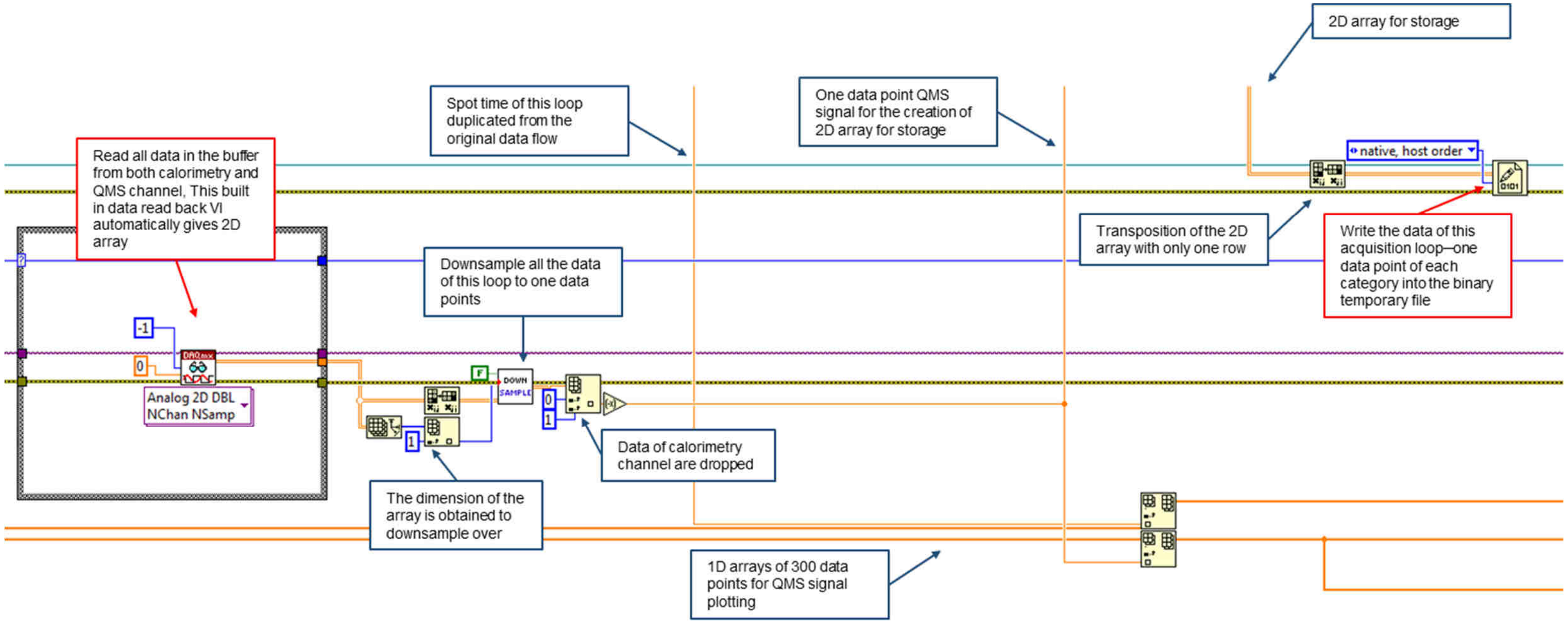

2D array for storage

Spot time of this loop duplicated from the original data flow

One data point QMS signal for the creation of 2D array for storage

Read all data in the buffer from both calorimetry and QMS channel, This built in data read back VI automatically gives 2D array

Transposition of the 2D array with only one row

Write the data of this acquisition loop—one data point of each category into the binary temporary file

Downsample all the data of this loop to one data points

Data of calorimetry channel are dropped

The dimension of the array is obtained to downsample over

1D arrays of 300 data points for QMS signal plotting

Figure 5.29: A screenshot to a section of the QCM data acquisition block diagram. This section contains the QMS data read back from the NI 6221 card and writing of data into binary temporary file. The data of the calorimetry channel is fetched by the read back VI but dropped without processing (mostly for the onboard buffer refreshment). The downsample sub VI is home built to work flexibly with various circumstances of averaging. Downsampling over its own dimension means the calculation of numerical average of this data set. The plot of the QMS signal contains the data of 300 points/loops since the confirmation of unity sticking requires longer time of observation than that is needed for the stable flux from the deposition thickness reading of QCM.

of the two channel task. It will therefore largely complicate the code structure on the block diagram. On the other hand, data reading back from the NI 6221 card consumes very limited computing power, one redundant channel does not impose much burden to the system, especially in a non-time-critical procedure. In additional to that, duplication of codes with different parameters in G language does not work out as simple as those in a text based language, stretching and connecting of data flows would have to be manually carried out with the mouse pointer. Therefore, the direct adoption of the two channel device task becomes the most practical solution to the QMS signal read back in the QCM data acquisition procedure.

Because in each loop, only one data point of total thickness, current deposition rate and crystal frequency are acquired from IL150 controller, the out numbered QMS data read back from NI 6221 card have to be averaged to one point as well. Here, the downsample sub VI is employed as the averaging function (Figure 5.29). It is designed to handle the data of 2D array under a given downsampling ratio. When the ratio is the dimension of the data itself, this VI then works as the function for the numeric average.

As for the storage of temporary data, the binary format is chosen because it has the highest writing speed while consuming the least computing power. The instantly built and transpositioned 2D array with one row is written into the temporary file once every loop calling the built-in binary write function. Because all the binary information of the temporary data will be preserved in the file, when the 2D array is directly fed to the binary file, its structural information, the array format is preserved as well. Some bytes of space will be occupied before and after each row of the data to represent the array structure. As a consequence, the binary file written in such manner could not be properly recovered by other data processing software, i.e., Igor Pro, unless specifically programmed to do so. Because the other software does not know how to interpret the additional bytes besides the real data. Format error will occur if an attempt to directly import the binary file into the other software is made. The benefit of using the 2D array to contain the data does not only lie with the convenience of using the built-in transposition function (This function only supports manipulation on 2D array), but also with the ease of data conversion from the 2D array to spread sheet plain text using another built-in function when it comes to the final phase of data saving to the readable text file. If the data are first converted to concatenated text before stored in the binary file, as has been seen in many simple data acquisition programs, much more efforts will have to be spent on the parsing of binary text structure when the temporary file is recovered and converted in the final phase. This data storage method demonstrated in Figures 5.27-5.29 is also employed in calorimetry data acquisition.

The tab of calorimetry is the core functional part of the entire application (Figure 5.30). Since the application is built upon bottom-up strategy, the code of this tab is first programmed and preliminarily tested for data acquisition. The large chart plot shows the data of the current pulse pair being acquired. Calorimetry and QMS signals are plotted in the left and right axis, respectively. The two charts below show the stacked data of the past eight pulse pairs for calorimetry and QMS separately. The stacked data would help the user to instantly see the recent trend of signal change. A major difference between the data acquisition of calorimetry and that of QCM is that the existence of the data readback only mode in the calorimetry data acquisition. In the routine of measurements described in Chapter 2, the QCM measurement will take place before the real adsorption calorimetry because the flux has to be first determined as suitable for calorimetry. The duration of this confirmation process is usually unclear, because both the unity sticking from QMS signal and stable flux in the thickness reading need to be achieved. Meanwhile, any signal change that is seen on the total thickness plot of the QCM data would mean that something is already adsorbed on the surface of quartz crystal. It is therefore worth recording every data point to the hard disk ever since the beginning of data read back. On the contrary, some part of the system's readiness for calorimetry measurement, i.e., the stability of flux or laser power, should be already confirmed before the corresponding measurement is carried out. But the baseline stability of calorimetry signal might still be not good enough for data acquisition due to the yet unstable sample temperature or the random physical shock (i.e., vibration from the heavy door closing in the neighboring rooms or from upstairs due to the falling of heavy things) transferred from outside the chamber which exhibit strong impact through the piezoelectricity of the sample. The eventual readiness of the system could only be confirmed after the stable baseline is observed on the chart plot after the data read back from the NI 6221 card is started. If the data acquisition is started together with the data read back from the NI 6221, there could be random amounts of waste data sitting at the beginning of a data file that has to be manually trimmed before the analysis of data. The split of data acquisition and data read back would easily solve this problem by letting the user to decide the starting point of the real acquisition. Then, of course more data acquisition related functional buttons are needed on the tab of calorimetry. As is shown in Figure 5.30, besides the button “start reading”, there are also “stop”, “acquisition”, “chopper”, buttons on the front panel. The split of data acquisition and data readback requires both the button of “start reading” and “stop” to work under latch mode rather than that of single button on the QCM tab working under switch mode. That is, the clicking of “start reading” would trigger condition change in a Boolean condition structure which contains the entire hardware timed loop structure. When the condition is switched to the case of the hardware timed loop, the data flow will step into the loop and start data readback together with other tasks. However, the condition for the termination of this timed loop does not rely on the value/state of the “start reading” button since it is already switched back to “false” state after the read of its value by the data flow. The loop will terminate if the “stop” button is clicked and latched. When the data readback is underway continuously, the buttons “acquisition” and “chopper” are working under switch mode, because the data acquisition for storage and the execution of the motor program are made into two independent procedures built upon the data readback task. The three extra buttons, “start now”, “auto start” “force stop”, are "lazy user" features. The former two allow the automatic execution of the calorimetry data acquisition routine that produces the data file with flat baseline at the beginning and the end[96]. The “force stop”, as its name implies, will trigger the fastest possible termination of the current loop while the normal “stop” will terminate the loop until the current pulse pair is completely executed.

Remaining Time of this measurement: 0min 0s

Motor Feedback
Yes

Position
5

Calorimetry Settings

Pulse Length: 200
Pulse Delay: 200
Calorimetry Gain: 1
QMS Gain: 1
Laser Power: 7.825940E-6

Baffle: 297.4 : 3.4E-10
Sample: 300.2
Source: 600.0
Reservoir: 300.1
empty: 297.9

Pulse Pair Time: 8000
Remaining Time of this measurement: 0min 0s

Figure 5.30: A screenshot to the front panel tab of calorimetry data acquisition. The figure shows that the system is at standby state after the data acquisition. No error is encountered during the latest data acquisition.

The motor control module on this tab is comprised of the button combination which is identical to the one on the “motor” sub tab of the “settings” main tab. It will be fully disabled following the click of “start reading” (the initialization section of data acquisition described in Figure 5.25) if the application is running under measurement mode, or left enabled under troubleshooting mode.

The hardware timed loop structure of the calorimetry data acquisition contains the most complicated codes and is the largest single diagram structure of this application. Therefore, it is not realistic to properly present its full codes in an A4 printed manner. What should be emphasized, however, is the strictly sequenced execution of the motor program triggering, raw data readback and data storage into temporary file, because they are the most critical parts of a pulsed calorimetry measurement. Because the three tasks are from three data flows, especially the VISA communication task of the motor control has no mutual dependence on the other two, to assure a strictly sequenced execution of first the motor program, second the data read back and third the data storage, a sequence structure is necessary here to restrict the order (Figure 5.31). The second subframe for the raw data read back function alone is a redundancy for code readability. The execution privilege of data read back over data storage operation is already realized by its role as input provider to the data processing sub VI and the built in data writing function. Here, the two data flows are merged together (Figure 5.32).

From Figure 5.31, it can be seen that the operations for both the termination of data read back/acquisition and the triggering of chopper program are contained inside a Boolean condition structure. The unshown operations provide the judgement on whether the current loop count is the last of, i.e., 20 for a 4 s pulse pair period. This means the operations for termination or motor program triggering will only be executed at the end of a pulse pair period. The triggering of the motor program is always set for the next pulse pair period. In case the termination is triggered, either by the pressing of the “stop” button or the fulfillment of pulse pairs to acquire, the operations for termination will be executed prior to the possible triggering of motor program. The “chopper” button for motor program triggering will be first set to false before its value is read by the thread in each loop. The termination by “stop” button leads to additional judgement on whether the data acquisition is underway. If the continuous data acquisition is to be interrupted by the pressing of the “stop” button, still a “false” is passed onto the data flow as the condition for loop termination judgement. This means the ongoing data acquisition will still proceed for another pulse pair period. Meanwhile, the current pulse pair count (not the loop number count within a pulse pair period) is passed to an invisible object for storage. At the end of the next pulse pair period, when this block is again executed, the “current pulse pair count” stored just now would match the real current pulse pair count by +1. A “true” is then passed to the loop termination condition through wire connection, which will terminate the timed loop structure at the end of the current loop. Such delay on the termination of the ongoing data acquisition for yet another pulse pair period is designed to fulfill the requirement of tail flat baseline in the data for proper analysis[96]. On the other hand, manually pressing of “stop” button without ongoing data acquisition will directly pass “true” to the loop termination condition to terminate the loop structure.

The multichannel analog data read back function, as has been previously discussed in the QCM part of this chapter, is employed to simultaneously read back the calorimetry signal and the QMS signal. Different from its application in the non-time critical QCM data acquisition, in calorimetry, this built-in function is configured with precise number of samples to read back per calling. Theoretically, in a hardware-timed loop, the number of samples configured to read and those accumulated in the on-board buffer during the time of one loop should match with each other. Therefore, each time when the data read back function is called, there should be already enough buffered data waiting to be fetched. In reality, it is found out that if the wait time is set to 0, random errors of insufficient data are encountered. A seemingly handy solution would be to command the function to wait until the configured number of samples are available in the on-board buffer. However, since the temporal mismatch occurs only randomly, the wait-until method would introduce timing fluctuation to the system. This is the situation that should be avoided in a synchronized time-critical procedure, even if the actual fluctuation turns out to be rather trivial. The best solution to this problem is setting a fixed and small enough wait time to ensure the completion of data read back within this wait time. This wait time should also be not too large to erode the time of execution for the rest of the tasks inside the loop. As is shown in Figure 5.31-32, a 2 ms wait time is employed in our application. It is proved to be the shortest possible wait time that could ensure both the completion of data read back at any time and the overall stability of execution.

As is stated in Figure 5.13, the data acquisition procedure also records five channels of temperature and three channels of pressure as auxiliary information. The auxiliary information are formatted and stored in a binary temporary file during the data acquisition. It will be converted into a readable plain text file together with the calorimetry data at the file saving phase. The auxiliary information is formatted as a cluster comprised of a 2D double precision array and a string. A cluster defined in the global variable panel is used as the template for the data formatting. As is shown in Figure 5.33, the cluster is directly written into the binary file. Such convenience is another advantage of using a binary temporary file over plain text, because for data of mixed type, plain text conversion would require more complex code as well as more computing power.

According to Figure 5.31 and 5.33, the operations for motor program triggering and auxiliary information acquisition are only executed in the last loop during a pulse pair period. This arrangement would of course result in some extent of load imbalance between the last loop and the other loops, consequently impairing the stability of execution. Theoretically it is true. However, since the most computing power demanding tasks during the data acquisition are dynamic image rendering and temporary data writing, after the downsample of plotting to hundreds data points per second regime and the employment of binary temporary file format, the few bytes sent via VISA communication and written to the auxiliary binary file do not really stretch the system into instability.

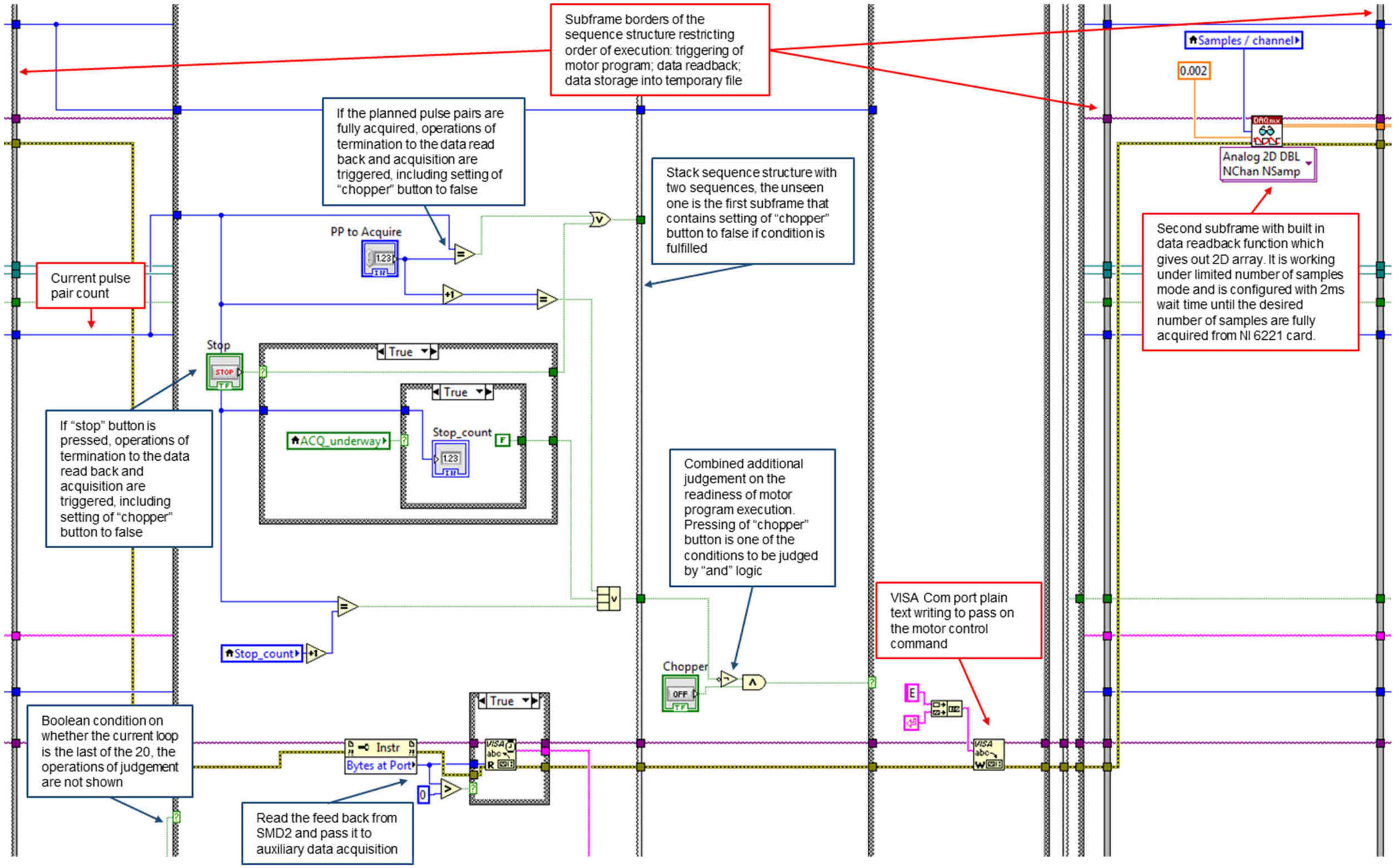

Subframe borders of the sequence structure restricting order of execution: triggering of motor program; data readback; data storage into temporary file

If the planned pulse pairs are fully acquired, operations of termination to the data read back and acquisition are triggered, including setting of "chopper" button to false

Stack sequence structure with two sequences, the unseen one is the first subframe that contains setting of "chopper" button to false if condition is fulfilled

Current pulse pair count

If "stop" button is pressed, operations of termination to the data read back and acquisition are triggered, including setting of "chopper" button to false

Combined additional judgement on the readiness of motor program execution. Pressing of "chopper" button is one of the conditions to be judged by "and" logic

VISA Com port plain text writing to pass on the motor control command

Second subframe with built in data readback function which gives out 2D array. It is working under limited number of samples mode and is configured with 2ms wait time until the desired number of samples are fully acquired from NI 6221 card.

Boolean condition on whether the current loop is the last of the 20, the operations of judgement are not shown

Read the feed back from SMD2 and pass it to auxiliary data acquisition

Figure 5.31: A screenshot to a section of the block diagram for calorimetry data acquisition. The figure shows the first and second subframe of the outmost sequence structure inside the hardware timed loop structure. This sequence structure restricts the order of execution as: motor program triggering, raw data read back, temporary data storage onto hard disk.

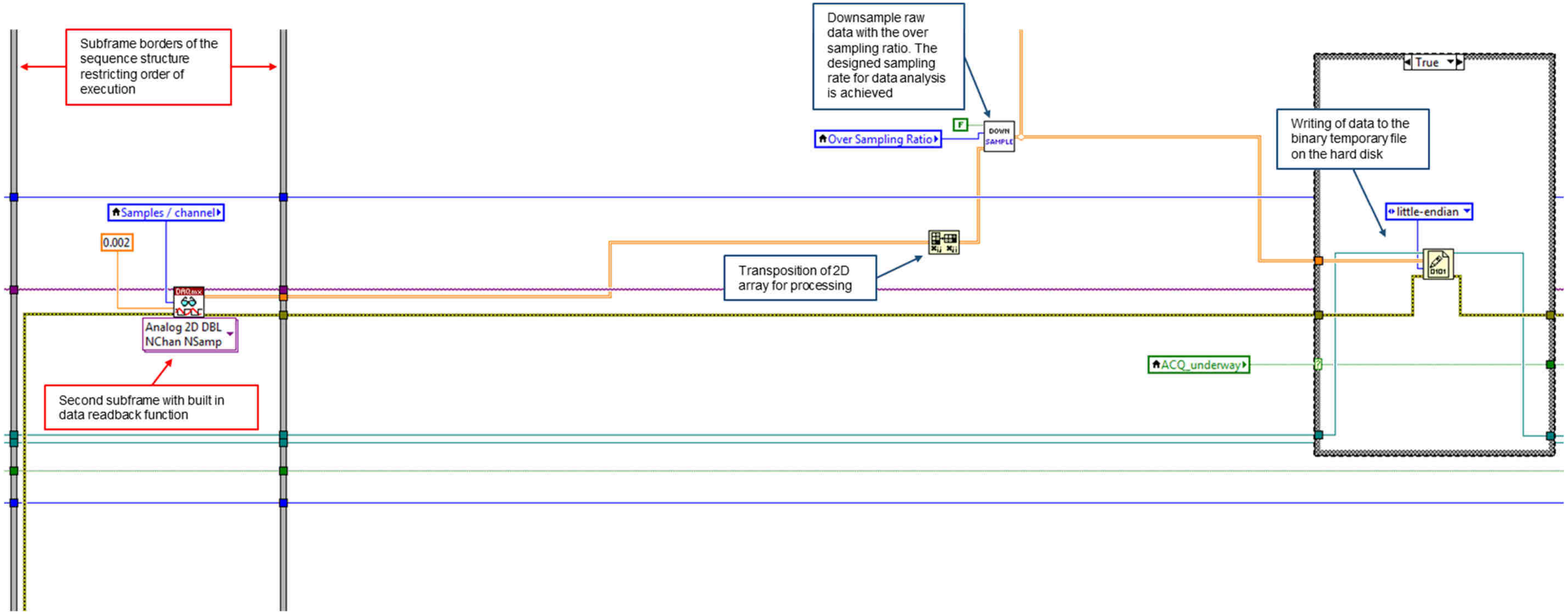

Figure 5.32: A screenshot to a section of the block diagram (overlapping with Figure 5.31 from the right) for calorimetry data acquisition. In the second subframe of the sequence structure, the data read back built-in function is configured with 0.002 s (2m s) wait time to read back the number of samples defined by “samples/channel”. The data transposition, downsampling and storage to the binary temporary file are carried out with the same method as is discussed in the QCM part

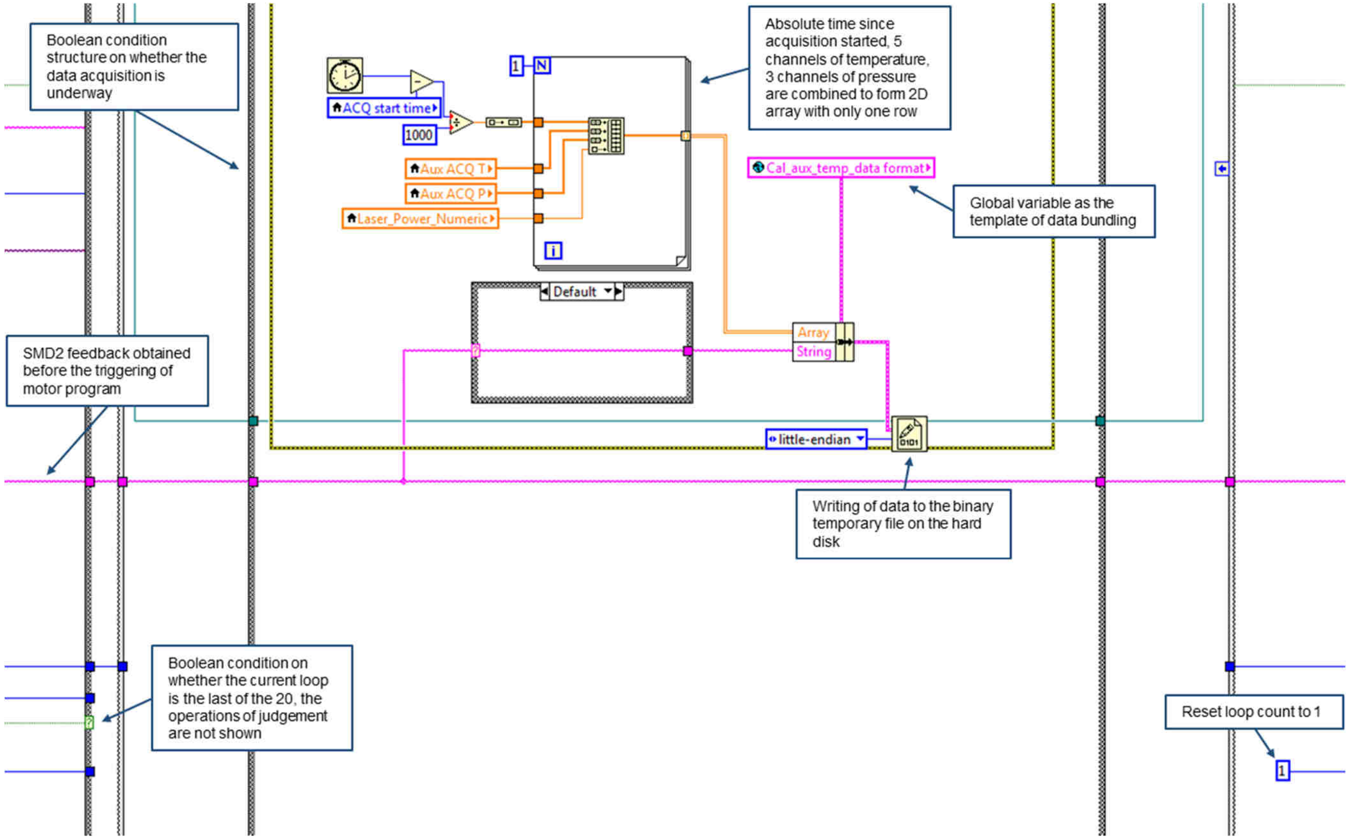

Boolean condition structure on whether the data acquisition is underway

Absolute time since acquisition started, 5 channels of temperature, 3 channels of pressure are combined to form 2D array with only one row

Global variable as the template of data bundling

SMD2 feedback obtained before the triggering of motor program

Writing of data to the binary temporary file on the hard disk

Boolean condition on whether the current loop is the last of the 20, the operations of judgement are not shown

Reset loop count to 1

Figure 5.33: A screenshot to a section of the block diagram for calorimetry data acquisition. The outer Boolean condition structure shares the same condition on the last loop judgement with that for task termination and motor program triggering. The SMD2 feedback in magenta wire represents the plain text obtained from the VISA Com port communication exhibited in Figure 5.31. The numerical auxiliary data are combined to build a 1D array inside a “for loop” with only one iteration, then directly converted to a 2D array by the for loop structure. Here, the build array function inside the for loop structure is working under “concatenate input” mode, which will put all the elements of every 1D array together into a new 1D array without the expansion of array dimension as that is seen in Figure 5.28. Therefore, no array transposition is needed when building a 2D array with this method. The global variable employed in this block does not pass on any value to the data flow but the format of data bundle with a 2D numerical array and a plain text string. The code shown in this figure is always executed after the storage of calorimetry data into the binary file to confirm the completion of a pulse pair period.

The file saving procedure is the last step of a complete data acquisition cycle. For both QCM and calorimetry, it is realized by their respective dedicated sub VIs. Inside the file saving sub VI, a popup dialog is first shown to the user to record the user's note for the preceding measurement. Then, a typical Windows style file dialog is shown for the file name and suffix choosing. After that, the binary temporary files are opened, the preliminary file header, which contain the technical information of the measurements, is read out using format template to match the suitable binary data inside the temporary file. These string data are combined with the user notes just taken and the number of complete pulse pair acquired to form the complete file header for the plain text data file (Figure 5.34). The calorimetry and its auxiliary data are recovered from the binary file using their corresponding data format as template. As can be seen from Figure 5.34, a -1 is configured to the binary read function, this means to scan through the whole file and automatically match the data type with the template given. This is a very powerful feature in G language that frees the programmer from the usually complicated job of address searching and starting point defining. The binary read function outputs a 1D array of clusters, each elementary cluster contains the data that was written by one time calling of the binary write function, which was done iteratively inside the timed loop of data acquisition (Figure 5.29, 5.32, 5.33). Because the writings of calorimetry data and auxiliary information to binary files are asynchronized inside the timed loop, the resulting output arrays from the binary read function have different dimensions. Their dimension difference is exactly by a factor of loop numbers per pulse pair period. In our common setup, this factor is 20. As a consequence, the two "for loop" structures are iterated for different times to convert the corresponding data to plain text and write them into the text files. In Figure 5.34, it is also seen that the "for loop" for calorimetry data conversion is fed with two different iteration conditions. One is the normal array-driven iteration condition, which, in the meantime, takes out each element of the array for data conversion. The other is the calculated total number of loops contained by the completed pulse pair period. To a normal data acquisition procedure, the two conditions should be identical since the binary write function is called once per loop; each time of calling creates one element in the binary readout array. However, when the measurement is interrupted by the external or internal incidents, i.e., the power failure or the blue screen shutdown of Windows, termination by the error of execution, etc., the recorded binary data of calorimetry may contain a tail part that is incomplete for a pulse pair. According to the data analysis software developed by Drescher, the incomplete data for a pulse pair may trigger error in the pulse pair based analysis procedure[96]. Therefore, it is necessary to equip the data acquisition application with a data trimming function. This would help to recover the maybe useful data from an interrupted measurement as much as possible. Because the completion of a pulse pair period is confirmed by the auxiliary data acquisition, the dimension of the output array from the auxiliary binary file should tell the number of completed pulse pair periods during the acquisition. This number multiplied by the pulse pair period (in seconds) and the loop frequency would give the total number of loops that should be recovered. When this number is smaller than the actual dimension of the output array from the binary read function, the "for loop" structure will be terminated as its iteration count reaches this smaller number. The rest of the data in the output array, if there are any, is then abandoned. Or in other words, the entire set of the calorimetry data is trimmed.

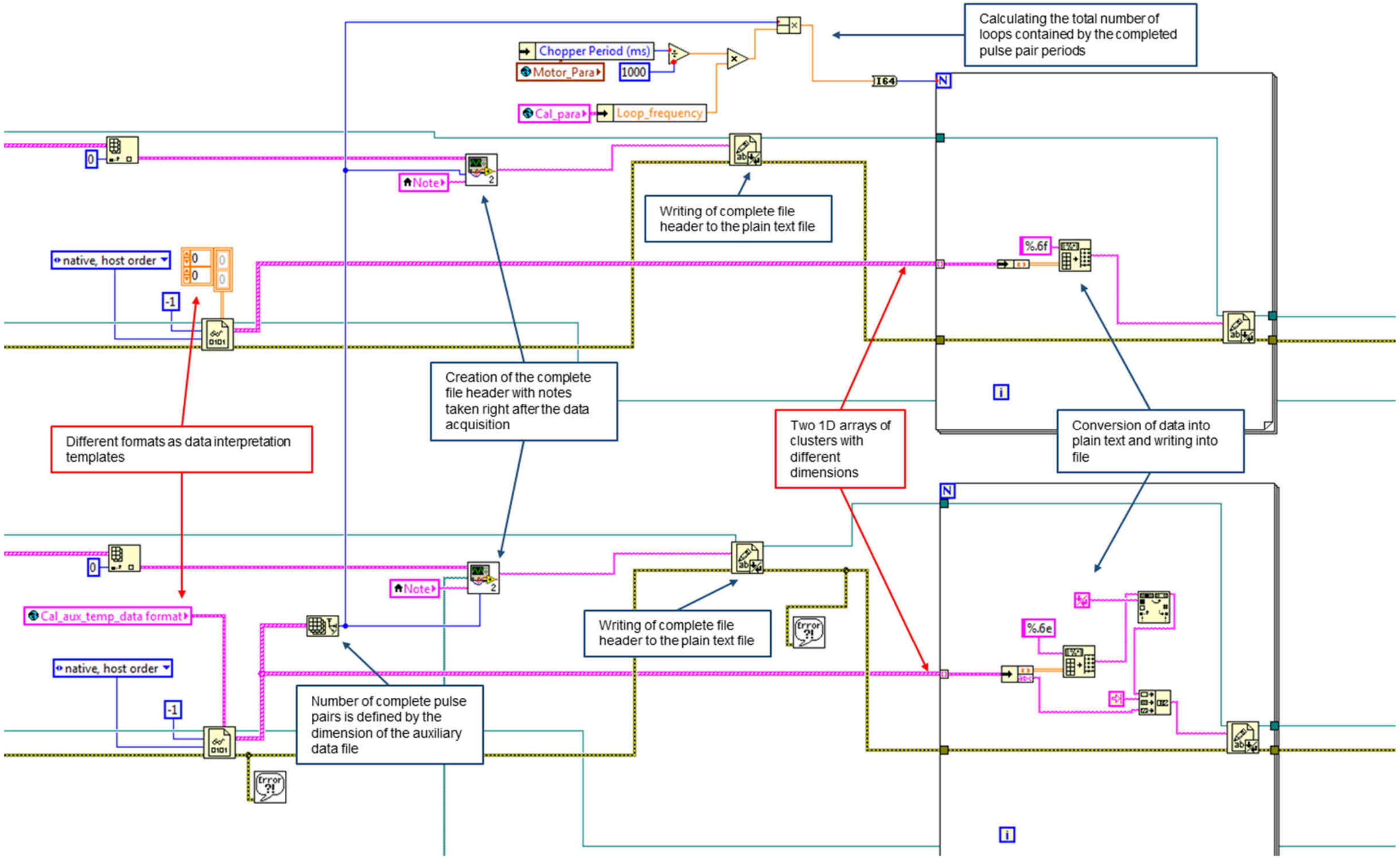

Calculating the total number of loops contained by the completed pulse pair periods

Writing of complete file header to the plain text file

Creation of the complete file header with notes taken right after the data acquisition

Different formats as data interpretation templates

Two 1D arrays of clusters with different dimensions

Conversion of data into plain text and writing into file

Writing of complete file header to the plain text file

Number of complete pulse pairs is defined by the dimension of the auxiliary data file

Figure 5.34: A screenshot to a section of the block diagram for calorimetry data file saving. The upper data flow is for the calorimetry data and the lower is for the auxiliary information. Different formats are used as the data type to recover the data from the respective binary file, the template for the auxiliary file is the same global variable that is previously used for binary data writing. A -1 configured to the binary file read function means to read the entire file. Because the data structural difference, for the auxiliary data file, there are more steps to concatenate the text inside the "for loop" structure.

5.4 Temperature Regulation for Beam Evaporator

The temperature regulation application is a single thread program that is built upon the modified version of the LabVIEW APIs provided for the PeakTech 1885/1890 DC power supply. To avoid thread interference with the application of calorimetry, it is also working as a published executable file of Windows like the applications for state monitoring. Its front panel is shown in Figure 5.35. The upper left frame contains the controls for the Com port selection, communication protocol selection, slider for the number of power supplies to team up, the power supply address shift. Like the other tasks relying on the VISA Com port communication, the user must define the Com port number assigned by Windows. In addition to that, the user must also define the communication protocol for the PeakTech 1885/1890 because they support both protocols. Under the RS-232 mode, one Com port can only control one device while under RS-485 mode, up to 32 devices could be controlled through one Com port with internal address allocations. This application is built for up to four power supplies forming a series, thus the default working mode is set to RS-485. The slider chooses the number of supplies to be controlled by this application. In Figure 5.35 for instance, the selection is two, there are two PeakTech 1885 being chained as the powerhouse to heat the beam evaporator of the calorimeter. On the left side of the upper center frame stand the selection of the temperature channel to regulate against, the target temperature input, and its commanding buttons. Below them are the controls for bridge mode on/off, voltage and current set button, button for power supply panel setting inquiry, and central power output switch under bridge mode. The upper center indicator shows the spot temperature of the channel to regulate against. Its past trend of up to half an hour is also shown. Below the temperature chart, the chart of the total current output shows the trend of current within the same temporal range as that of the temperature chart. The spot total current is shown by “PID I”, while the total power output, together with the grouping mode of the power supplies, is shown below the spot temperature. When the evaporator is heated up, it is also very useful to monitor the pressure of the system as a safety precaution besides the temperature. The three channel pressure information is displayed at the upper right corner of the front panel.

This application employs a modified LabVIEW PID self-regulating module to control the power output from the power supplies. Under the auto control mode, the voltage allowance on the power supplies is constantly set to the physical maximum, while the output current, which is more critical the heating power, is regulated by the PID. All the power supplies are given the same settings to achieve the simplest possible regulation mechanism. Therefore, the power supplies are working under current constant mode. The modifications to the original PID module focuses on the security issues, such as the range of output and, often neglected, the current changing gradient. Because the evaporator contains approximately 9 meters of tantalum wire filament [96], which is much longer than a common Knudsen cell evaporator would use, the thermal stress accumulated during the heating cycles of the measurements would have rather pronounced impact to the durability of the filament. After several times of re-constructions of the beam evaporator, it is found out that a limit on the current changing gradient is very helpful to maximize the lifetime of the evaporator. The heating gradient would mostly take effect at the beginning of a heating cycle and the moment a set of measurements are completed, at which the target temperatures are notably changed. The original PID algorithm would respond with huge changes to the output in the corresponding directions. Even after constraining the output range for heating devices, with which the negative and too large output values are filtered, the very rapid output change to the current may still be too large for the health of the filament.

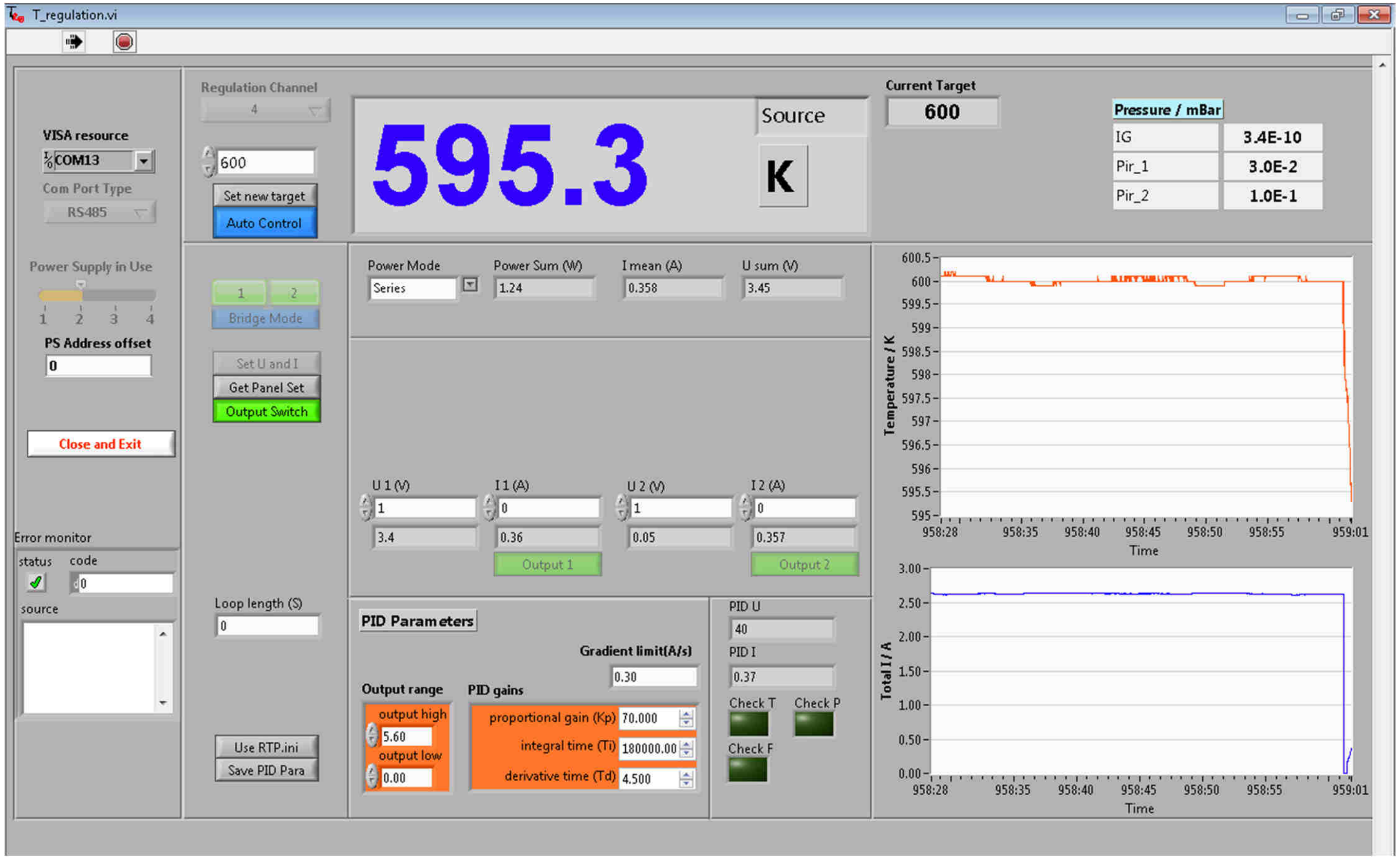

VISA resource: COM13

Com Port Type: RS485

Power Supply in Use: 1 2 3 4

PS Address offset: 0

Regulation Channel: 4

600

595.3

Source: K

Current Target: 600

Pressure / mBar	
IG	3.4E-10
Pir_1	3.0E-2
Pir_2	1.0E-1

Power Mode: Series

Power Sum (W): 1.24

I mean (A): 0.358

U sum (V): 3.45

U 1 (V)	I 1 (A)	U 2 (V)	I 2 (A)
1	0	1	0
3.4	0.36	0.05	0.357

Error monitor

status ✓ code 0

source

Loop length (S): 0

Gradient limit(A/s): 0.30

Output range
output high: 5.60
output low: 0.00

PID gains
proportional gain (Kp): 70.000
integral time (Ti): 180000.00
derivative time (Td): 4.500

PID U: 40

PID I: 0.37

Figure 5.35: A screenshot to the front panel of the evaporator temperature regulation application. The figure indicates that the system is under temperature regulation mode. “Regulation channel”, “bridge mode”, “set U and I” as well as the power supply’s own output switches are disabled and greyed out, while the central output switch is still operative. Com port protocol selection and number of power supplies to use are greyed out since the start of the application. The value of the slide indicate that two power supplies should be in use, therefore at the center of the front panel there are only two groups of objects visible, representing power supplies No.1 and 2.

Because only the temperature stability is decisive to the performance of this temperature regulation, the power output response lag, resulted in by an extra constrain on the gradient of current change (upon PID current output), does not have negative effect on the performance of this temperature regulation. Because the crucible of the evaporator is a long thick-walled stainless steel tube, its heat capacity is large and its thermal conductance is quite limited. The practical integral time of the PID parameter has to be rather large to avoid huge overshoot and achieve fastest possible temperature regulation. Meanwhile, the derivative time of the PID parameter has to be small enough to avoid regulatory oscillation (Figure 5.35).

The button “use RTP.ini” represents the function that allows further integration between the applications on the data acquisition platform. When this button is pressed, the temperature regulation application will read the target temperature that is written into the runtime parameter configuration file by other applications with the configuration file access function. The automatic temperature regulation will then be activated without any user operation on the front panel of this application. This function is intended to allow users to focus only on the measurement related operations if necessary.

Figure 5.36 demonstrates the very typical communication operations with the PeakTech 1885/1890 power supplies. Inside the "for loop" structure, there are two sub VIs to undertake the VISA Com port communications. The upper one read back the voltage and current settings on the front panel of a power supply. The regulations, either manual or automated, are realized via the program changes to the settings on the power supply’s control panel─the upper limit of the corresponding item. Therefore, it is always necessary to know if the settings from the last iteration of loops are correctly realized. The lower sub VI read back the actual voltage and current a power supply is providing to the heating circuit. With the number of power supplies to group and the address offset, it is easy to quest the information from each power supply iteratively. The results from the quest could be conveniently put into the data flow of array just initiated on the left side of the loop structure. However, when the corresponding information of each power supply is going to be displayed to the user, the developer of G language will have to face the really thorny situation of passing the information to the corresponding object that represents each power supply. As is shown in Figure 5.36, only for the display of actual voltages and currents, there are already eight indicators placed on the block diagram as well as eight times of array indexing and wiring. The number of the objects being placed by the programmer will multiply with the number of power supplies supported by this application. One may argue that it is possible to bundle the objects into a cluster container or even define a user object that already contains the objects needed for certain functions. This would only help a little to accelerate the placement on the block diagram, yet the data passing will still cost as much work. If this object cluster/user object is further placed into an array container, the iterative data transferring operation is enabled but at the cost of freedom of the front panel design, because LabVIEW only allows 1D array of one row or one column, objects array will have to stand in a line. Unlike the other text based languages, in LabVIEW, user-define class is possible through the building of so called X control, through which the array of user defined objects could be organized freely on the front panel. However, to my experience, the construction of such controls costs much more time and energy than simply placing the single objects and wiring them. The complexity of the programming work on the block diagram is the real reason that the application supports up to 4 power supplies while the communication mechanism of the PeakTech 1885/1890 is designed to support up to 32 power supplies.

To enable the simultaneous running of the multiple instances of temperature regulation, modification to the stock version of the communication VIs are necessary. Iterative Com port configurations are introduced to compete for the port access privilege (Figure 5.36). A 50 ms timeout is set to let the built-in VI run repeatedly in short time. As long as the configuration gives success feedback, the access privilege is proved to be held by this instance. Thus the "for loop" structure can be terminated to allow the following communication operations. Accordingly, a release of port occupation is also introduced after this group of operations (Figure 5.35). An error condition structure for execution condition judgement is also implemented for the security of execution.

Unlike the Com port communications sub VIs introduced in Figure 5.17-18, the commands for certain operations are embedded in a specific VI rather than the employment of a common communications VI. This arrangement would require one VI for a specific function because both the commands and the corresponding interpretation of feedback message have to be incorporated into VI. For the situations that require high cleanliness on the block diagram of the upper level VI, such arrangement could avoid prior- and post-operations outside the communication VI, as is shown in Figure 5.17-18. Inside the error condition structure, after the writing of command, a 80 ms wait time is placed between the write function and read function. It is critical that this wait time is incorporated into the data flow of the series operations. Here, a one-frame sequence structure is used to catch the data flow. As has been discussed at the beginning of this chapter, the internal scheduler of thread does not locally follow the relative positions of the objects to decide their priorities of execution. Placing of an object between the others without logic bonding to the data flow will not ensure the sequence of execution. In the situation shown by Figure 5.36, without this sequence structure, which itself commands no sequence but acts as a container, the 80 ms wait time may be executed sometime before the whole condition structure is finished, yet the byte query function will be executed too soon after the writing of commands. It is very likely that there are not enough bytes available at the buffer, therefore no read operation will be executed. The entire VI has then failed on its functions.

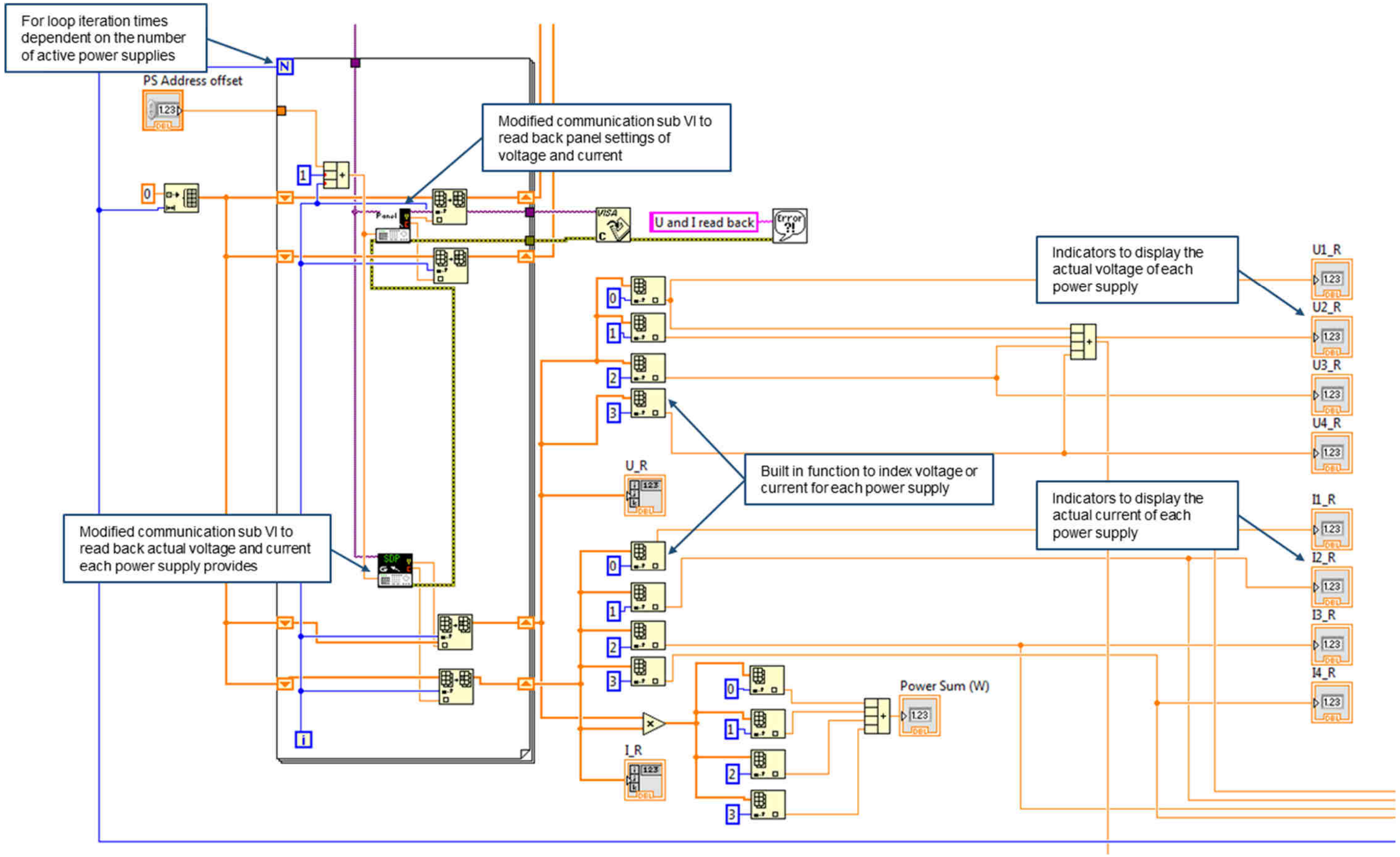

For loop iteration times dependent on the number of active power supplies

Modified communication sub VI to read back panel settings of voltage and current

Indicators to display the actual voltage of each power supply

Built in function to index voltage or current for each power supply

Indicators to display the actual current of each power supply

Modified communication sub VI to read back actual voltage and current each power supply provides

Figure 5.36: A screenshot to a section of the block diagram for evaporator temperature regulation. According to the system status shown in Figure 5.35, objects for power supply 3 and 4 are hidden from the user. Indicators array “U_R” for actual voltages and “I_R” for actual currents are hidden by default, the information they carry are used in the other blocks elsewhere.

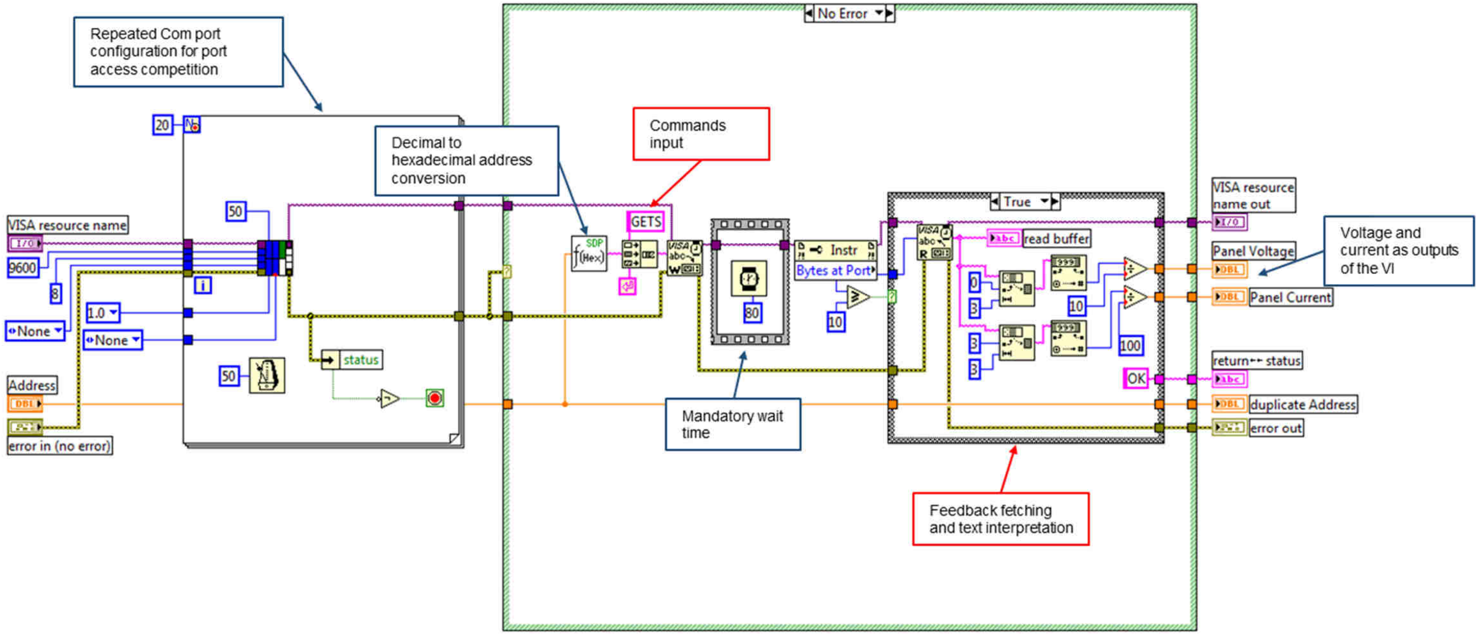

Figure 5.37: A screenshot to the block diagram of the sub VI for voltage and current settings on the panel of the PeakTech 1885/1890 power supply. The codes are modified from the manufacturer API version of the VIs.

5.5 Global Logging Application

The global logging application is a service like program which runs mostly in the background on the data acquisition computer. It relies on the system state monitoring applications to provide the eight channels of temperature and the three channels of pressure information as well as their time stamps. Because the system state monitoring applications put emphasis on stable and rapid data updating, they are not designed with logging function. However, for a data acquisition platform that runs non-stop all year long, it is necessary to equip it with a logging program that records instrument related information of the whole platform.

As can be seen from Figure 5.37, the numeric information tab uses enlarged fonts to allow effective reading from meters away, this feature is very useful when manually adjusting heating power, valve opening and etc., in which the operation of the user must carried out on the calorimeter but not by the desk of the computer. Especially in the troubleshooting procedure, when sometimes quick reverse of operation is needed. Good visibility of information would help the user to see the change in the information as soon as possible. Considering the size of the font and the front panel, four of eight channels of the temperature information are displayed numerically at this tab. To our experience, it is more than enough for most of the occasions. During the calorimetry measurements, no more than two channels of temperatures are regulated, with one or two extra monitoring on the hot molecular reflection plate and QCM crystal. It also meets the needs for instrumental maintenance such as the bake out, in which three or four channels of temperatures are usually watched for security.

For a logging program, the mechanism of data obtaining should be fully passive. There are two time intervals available for adjustments. The sampling rate defines the time interval between the two readings of the on-disk buffer file carried out by this application; it does not influence the updating frequencies of the system state monitoring applications. The acquisition rate defines the time interval between two series of data/data points that are written into the log file. This interval is usually one or two minutes. The three LEDs to indicate system faults represent the operations that check the time stamp in the corresponding state monitoring files. If the time stamp has not been updated for more than 5 seconds, the light will turn red and hold on, indicating that the state monitoring is not working properly as it should. The voltage and current warning will only be effective if the temperature regulation application is set to use RTP file (Figure 5.35).

The six plots on the tab “Plots” share the same data with the data acquisition function of this application; they will update at the same rate as is defined in the tab “Miscellaneous”. The width of the plot stands for a window of 24 hours. To have a better overview of the relative longer time range, the logged data from one day before are also plotted for all the sorts with dimmer color. This function would be rather useful during the unmanned process of instrument bake out, which may last for two days or even longer. A clear trend of the temperature and pressure evolution could be drawn from the stack plot of two day’s data.

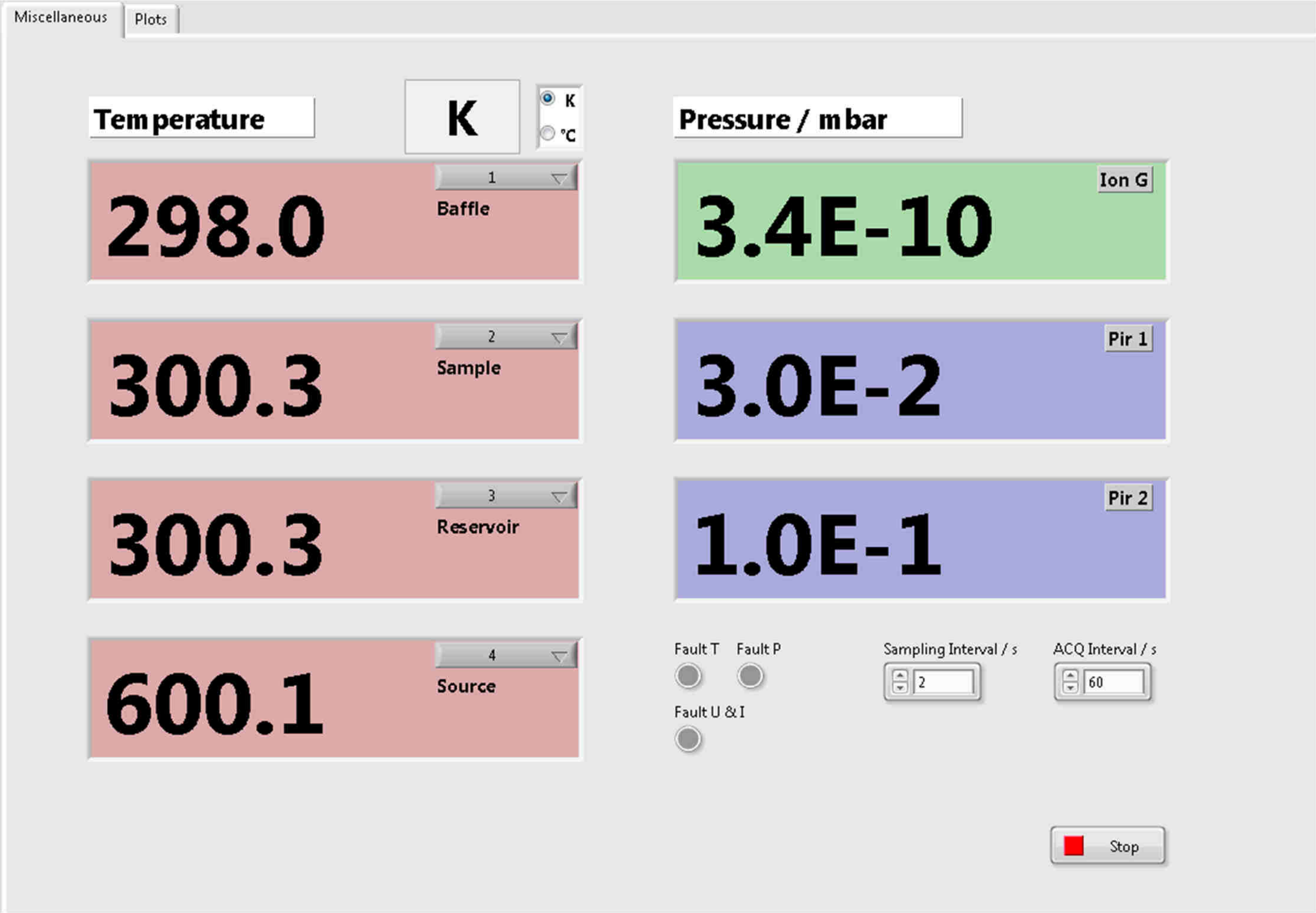

Temperature

K

● K
○ °C

1 Baffle 298.0

2 Sample 300.3

3 Reservoir 300.3

4 Source 600.1

Pressure / mbar

Ion G 3.4E-10

Pir 1 3.0E-2

Pir 2 1.0E-1

Fault T ●

Fault P ●

Fault U & I ●

Sampling Interval / s: 2

ACQ Interval / s: 60

Figure 5.38: A screenshot to the front panel of the global logging application. This tab shows the numeric form of the information, the fonts size is enlarged for meters away visibility. Users could chose four of eight channels to look over. All three channels of pressure information are shown. The data sampling speed and acquisition speed could be set in a form of time interval in second. Three red warning lights on temperature, pressure and the heating power of beam evaporator will be on if the time stamp of their corresponding source data is not updated for more than 5 s.

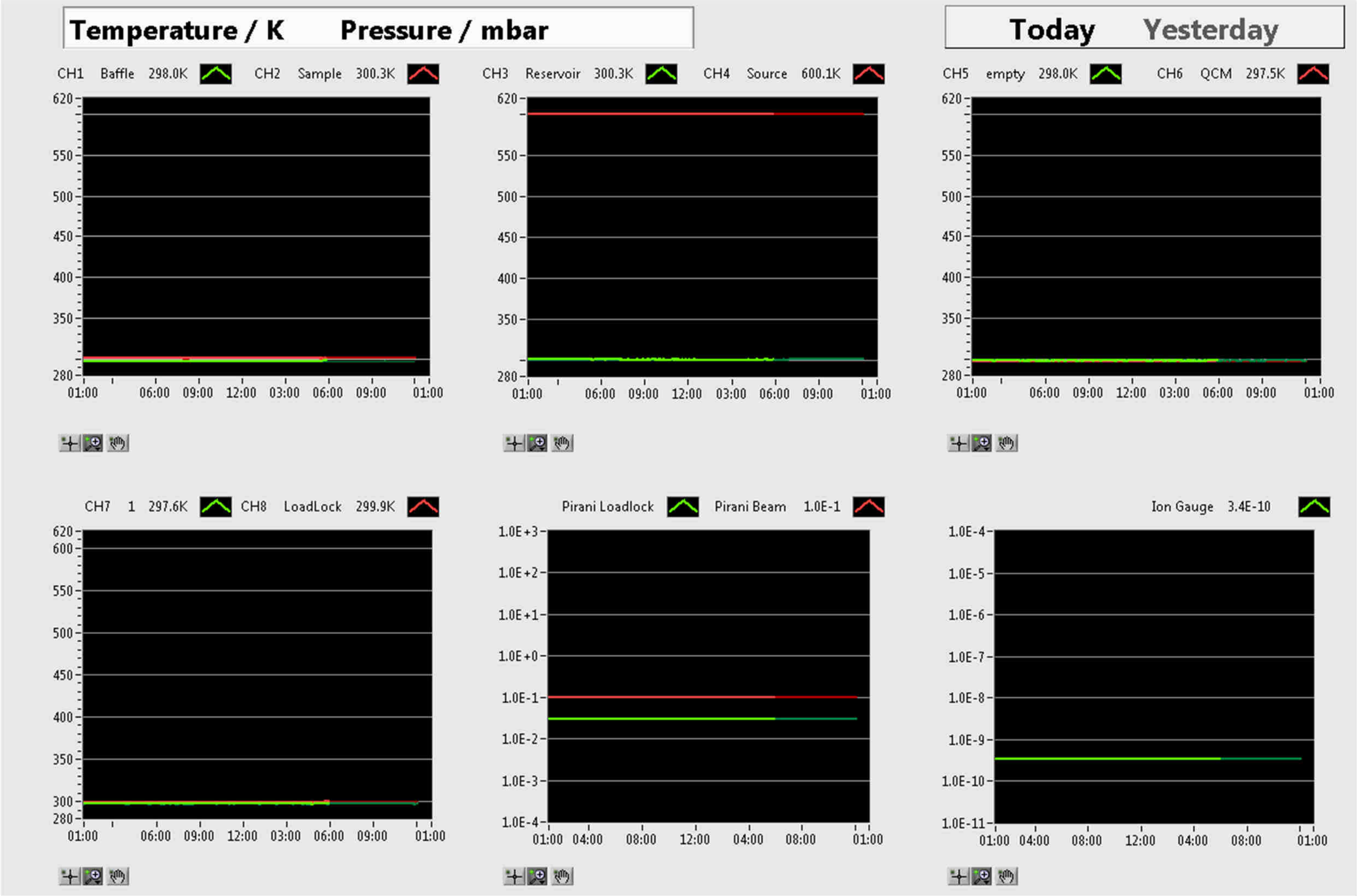

Figure 5.39: A screenshot of the tab "plot" on the front panel of the global logging application. The data for today and yesterday are plotted in colors of different brightness. The lower right plot is for the ion gauge pressure alone.

The code side realization of the logging and plotting has a very pronounced characteristic if compared with the calorimetry measurements applications: the absence of time criticality. As a consequence, no measures for higher code efficiency or faster processing, i.e., the binary file or data downsampling, are needed in this application. All the data are directly converted into strings and then written into the final version of the data file inside the main loop (Figure 5.39). The additional step data recovery from binary file is exempted. In fact, because the logging should be able to provide the last information before the running of the system being interrupted by an incidence, e.g., a sudden power failure, the direct plain text recording is a better choice than binary file writing regardless of the code efficiency or computing load. If the failure coincide with data writing operation, the probability of file corruption is significantly higher with the binary file of LabVIEW than with plain text. Normally, the writing of plain text file would simply stop at the address where the pointer is in, while the LabVIEW binary file, as has been previously discussed, would corrupt if the additional data structure information has not been correctly written. A corrupted file may either be impossible or rather difficult to recover, resulting in the loss of the most critical logging information this application is designed to provide.

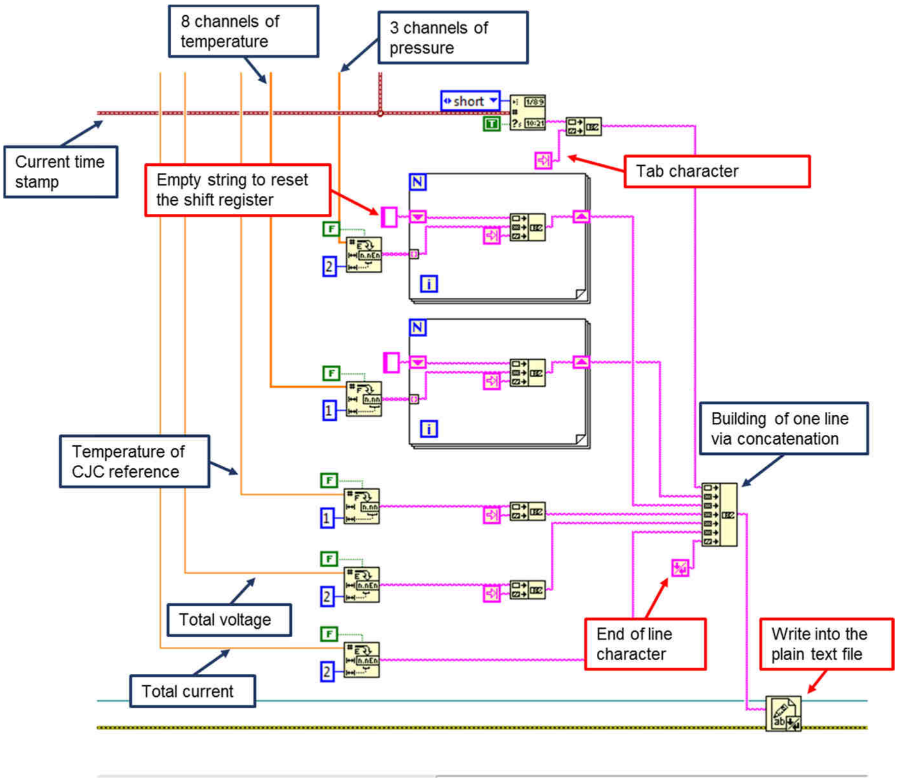

Figure 5.40: A screenshot of a section of the block diagram for plain text writing. The time stamp generated elsewhere is wired into this block and formatted into string. The arrays of numeric data are directly converted into arrays of string, thus could command the "for loop" to concatenate the strings. The array of data are therefore fitted into one line. Several sorts of data are concatenated together to form a line in the data file.

6 Mechanical Designs

The mechanical designs included in this thesis are not for the standalone projects, but for the improvements to the existing systems that the author have worked with during his PhD study. There are two types of improvements realized after the design by the author and the manufacturing by the department's mechanical workshop: the improvements for adsorption calorimeter and a mobile sample manipulator with cooling capability.

6.1 Improvements to the Adsorption Calorimeter

Two major improvements are introduced upon the system described in the literature[96]. The first and the more substantial one is the modification of the laser transmission system. The second is the re-design to the encapsulated pyroelectrical sample holder for thin $LiTaO_3$ detector.

6.1.1 Modification to the Laser Transmission System

As has been described by the PhD thesis of Dr. Drescher [96], the 405 nm laser beam coming out of the iBeam monochrome laser generator is focused and conducted into the optical fiber based laser transmission system with a "laser dock" for beam introduction into the fiber and a "laser out" for beam exportation. It later turned out that the alignment of laser inside the transmission system may easily subject to pronounced changes by ambient temperature change or quality of components mounting. Therefore, it was decided that a more conventional yet robust system for the introduction of the laser beam has to be built. The basic idea is that more reliable and easier adjustable mirror reflection system will replace the delicate optical fiber based system. Upon this idea, mounting stages were designed to clamp the iBeam and a reflection mirror firmly to the main frame of the NAC. Two existing laser system apparatuses, a three-axes adjustable mirror holder mounted on an micro linear motion from OWIS and a height adjustable mounting table from MELLES GRIOT were also employed to construct the new system.

As is shown in Figure 6.1, the iBeam laser generator, the grey box with black wavy heat dissipater, is mounted to a 7.0 mm thick aluminum adapter piece. The assembly is later mounted to the MELLES GRIOT mounting table together with a 38 mm diameter cooling fan (**a** and **e** in Figure 6.1). This assembly sits on the homemade aluminum mounting stage which clamps the assembly to the main steel frame of the NAC. The outcoming laser beam from iBeam is turned 90° by a mirror mounted on the OWIS Trans 60L mirror holder before it reaches the port window for laser incidence. The mirror assembly also sits on another homemade aluminum mounting stage (**f** in Figure 6.1) that clamps to the main frame.

To align the laser beam to the port window for incidence, coarse alignment is first carried out with horizontal shifting of the mounting stage **f** to roughly align the center vertical axis of the mirror assembly to the port window. Next, the height of the laser generator assembly is adjusted by the up-liftable mounting table **e** to match the height of the laser path with the port window center. The standing height and the distance of the mirror assembly with regard to the main frame were also adjusted to preliminarily match the mirror center to the laser beam. These two adjustments were enabled by making mounting grooves rather than mounting holes on the base piece (**f1** in Figure 6.3) and the lower half of the clamp (**f2** in Figure 6.3). Fine tuning of alignment starts with adjusting the three fine micrometer on the OWIS TRANS 60 L mirror holder (**b1** in Figure 6.3). By changing the direction of reflection, the laser should be able to reach the sample position inside the main chamber. The height of the mounting table **e** is then again finely adjusted back and forth together with those three micrometer screws on the mirror holder as well as micrometer screws on the linear motion on which the mirror is mounted, until the maximum laser intensity is obtained at the sample position.

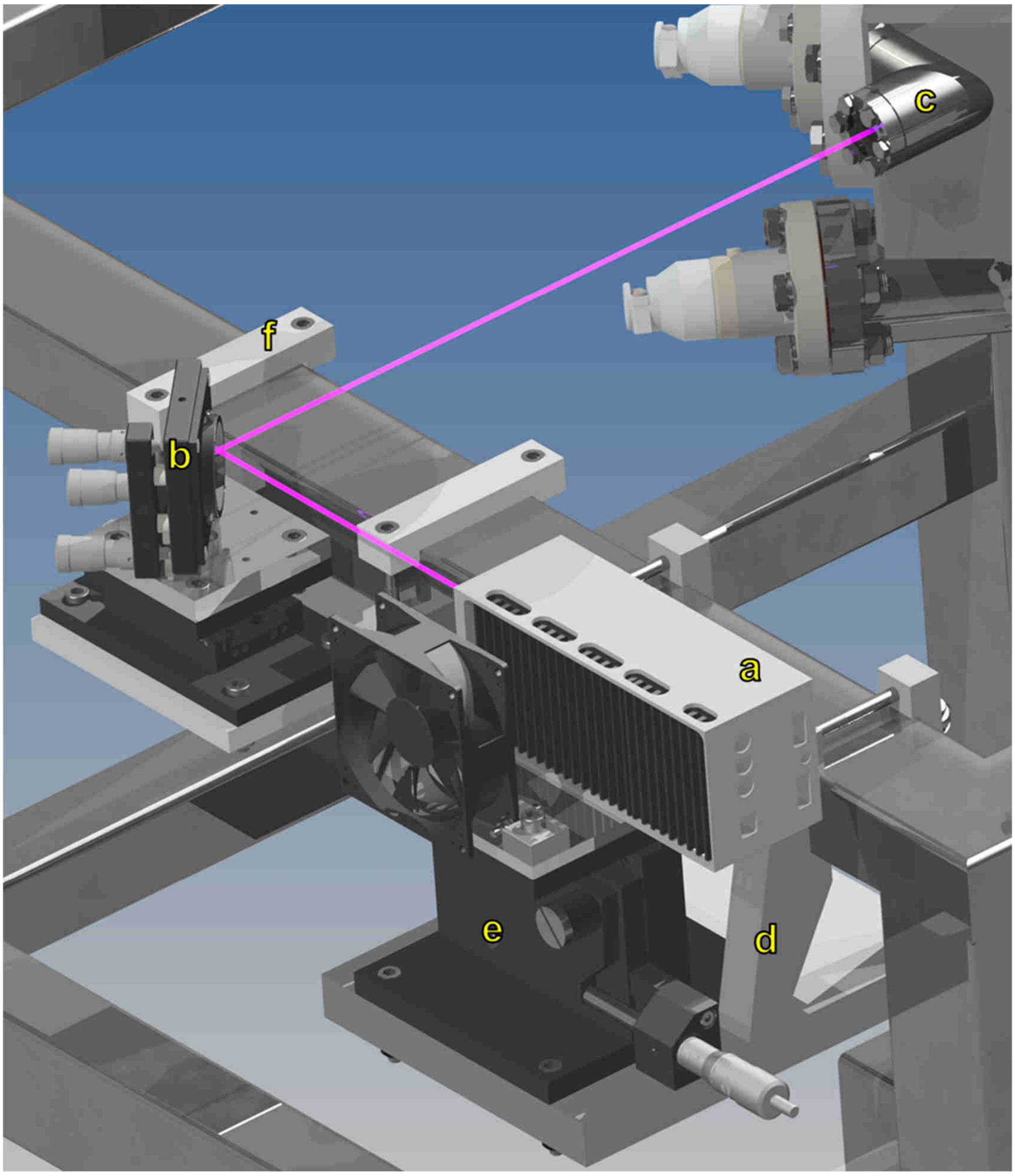

Figure 6.1: 3D model of the mirror reflection based laser system for the NAC. The thick purple beam represent the actual path of the laser beam. (However, in the real world, the laser is invisible from this perspective.) All the cables and hoses connected to the NAC system are not shown for image simplicity. a: iBeam 405 nm laser generator from TOPTICA; b: modified OWIS mirror reflection module with TRANS 60L mirror holder, aluminum adaption inter piece mounted on a linear motion; c: port of laser incidence on the molecular beam block of the NAC; d: homemade mounting stage for laser generator and its table; e: MELLES GRIOT mounting table (module number unknown); f: homemade mounting stage for the mirror reflection module.

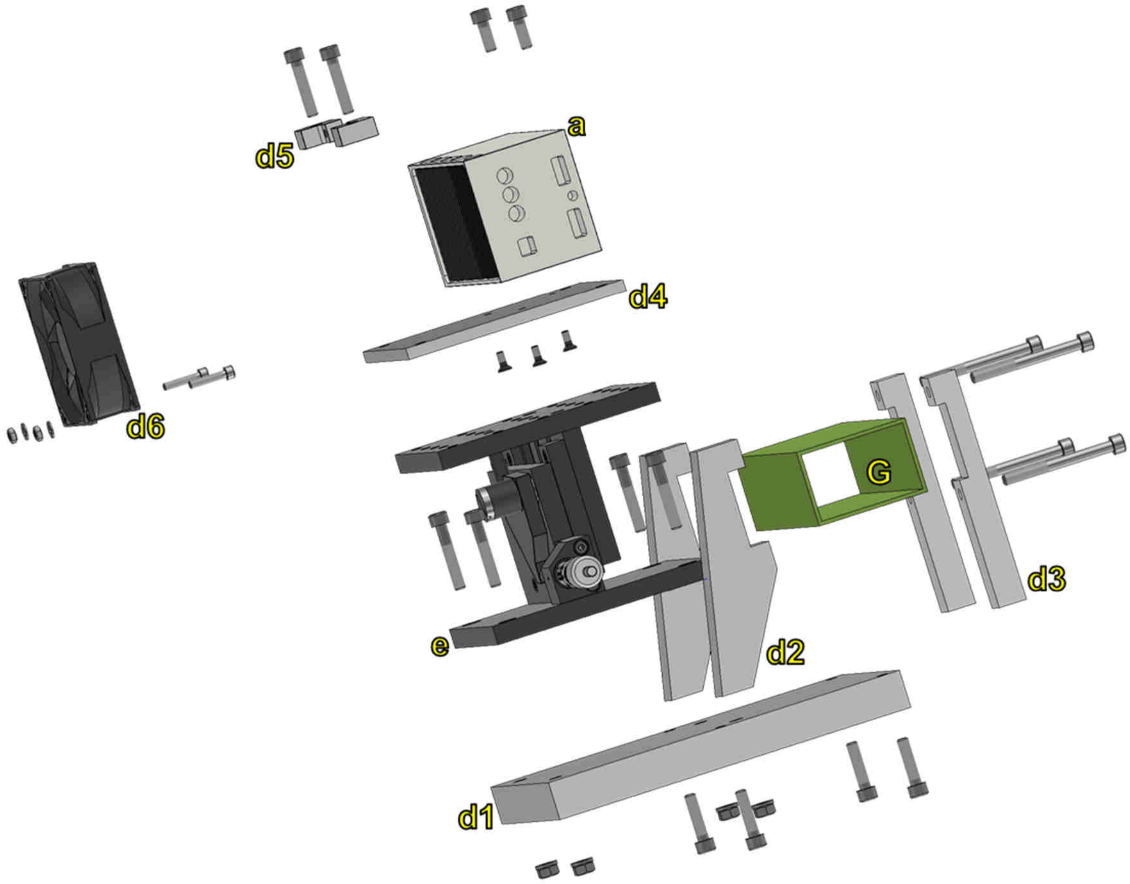

Figure 6.2: Expanded 3D presentation of the laser generation assembly. G: the cross section of the main frame of the NAC on which the assembly is clamped; a: iBeam 405 nm laser generator; d1: base piece of the mounting stage; d2: outer arm of the clamp that (relative to the NAC main chamber); d3: inner arm of the clamp; d4: adapter piece on which the laser generator is directly mounted; d5: adaptor piece on which the cooling fan is directly mounted; d6: Ø 80 mm cooling fan; e: MELLES GRIOT height adjustable mounting table for laser system. Tightening pieces are of the DIN norm and are therefore not specified. The MELLES GRIOT table is not further expanded because it is used as received.

As is demonstrated in Figure 6.2, the iBeam laser generator **a** is first screwed to aluminum adaptor piece **d4**, then together with cooling fan **d6** and its adaptor piece **d5**, they are all mounted to the MELLES GRIOT table **e** by screws. The upper deck of the mounting table is natively built with a matrix of threaded holes. As for the mounting stage, arms of the clamp, **d2** and **d3**, are firstly screwed together onto the main frame **G**. Followed by the mounting of the base piece **d1** from bottom to form the firm base for the whole laser generation assembly. Next, the table with laser generator atop is mounted to the main frame clamped stage.

Figure 6.3 demonstrates the packing of the laser reflection assembly. Different from the laser generation assembly, through holes are replaced by grooves whose width are same as the diameter of holes for mounting.

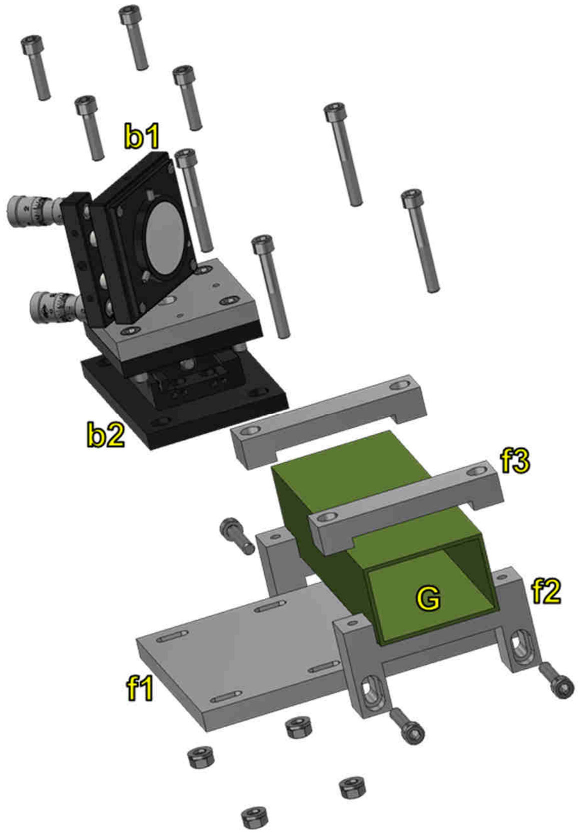

Figure 6.3: Expanded 3D presentation of the mirror assembly and its mounting stage. G: the cross section of the main frame of the NAC on which the laser reflection system is clamped; b1: OWIS TRANS 60L mirror holder and Ø35 mm mirror; b2: OWIS micro linear motion (module number unknown); f1: base piece of the mounting stage with grooves that enables horizontal movement of the mirror assembly when adjusting; f2: lower part of the clamp with grooves that enables vertical movement of the base piece when adjusting; f3: upper part of the clamp that withstand the weight of the entire assembly. Tightening pieces are of the DIN norm and are therefore not specified. The mirror assembly is not further expanded because it is used as received.

The design of the clamp in this assembly focuses on maintaining the precise distance between the two mounting points on each side the base piece **f1**. Therefore, the two grooves on **f2** are rigidly bonded with a strong arm. The precision of this distance is critical to the adjustment of the screws' hanging position when aligning the laser system. If the two grooves on **f2** were to be separated on two different arms as those in the laser generation assembly (Figure 6.2), tiny deviations of tightening between the upper and lower screws would result in vertical misalignment of the two arms. This means the two grooves on the same side would be non-parallel. Since the adjustment to the mounting height of the mirror assembly are purely manual, non-parallel grooves would make it more likely that the base piece **f1** is locked up during the movement, thus seriously obstructing the progress of alignment. Making the cross-section of the grooves wider would not help the whole process because wider grooves would definitely diminish the chance of lock-up, it however also make it more difficult to keep the base piece **f1** in strictly horizontal orientation. Under such circumstances, each of the four screws that binds the base piece with the lower arm of the clamp would have two more dimensional freedoms to move inside its groove, the alignment work is therefore becoming more complicated rather than simplified.

6.1.2 Modification to the Encapsulated Sample Holder

To take the advantage of good thermal stability and pyroelectricity of $LiTaO_3$ single crystals, the encapsulated sample holder designed for PVDF film detector[96] were modified to house a Ø10 mm, 0.1 mm thick $LiTaO_3$ single crystal (Figure 6.4).

Figure 6.4: A 200 nm Au coated Ø10 mm, 0.1 mm thick $LiTaO_3$ single crystal. ~20 nm Cr is first deposited as the intermediate layer for the adhesion of Au layer. The $LiTaO_3$ single crystal was obtained from SurfaceNet GmbH.

Because the PVDF film is a comparatively thin (25 µm or 9 µm in our study) and flexible polymeric material, to maintain a good electrical contact under UHV, the sample holder for PVDF is designed to have a rigid and strong back electrode and a flexible aluminum shield as front electrode to push the PVDF film against the back electrode. However, given that the manufacturing and positioning errors of the sample holder components as well as the inevitable inhomogeneity of polymer film and its coating, this design seldom produces two samples with identical electrical properties. This effect is corrected by the calibration of every single sample before the real calorimetric measurement. On the contrary, the $LiTaO_3$ single crystal is a highly regular yet extremely brittle material. Its properties are much more predictable compared with the PVDF film, while its housing into the sample holder of our NAC requires a more delicate handling. To maintain a good electrical contact without imposing excessive physical stress that breaks the 0.1 mm thick $LiTaO_3$ single crystal, the front electrode is changed into the ground piece to be pushed against. It is redesigned as a milled 1.5 mm thick stainless steel (1.4404 of DIN norm or 316L of ANSI norm) round plate (**a** in Figure 6.5). The increased thickness and employment of harder material assure sufficient stiffness or, in other words, limited deformation when it holds the $LiTaO_3$ single crystal. Limited deformation means the inevitable stress on the single crystal could be as evenly distributed over the contact area as possible. It also has a central socket to sink the crystal right at its center without drifting. Based on this, relatively higher pushing forces could be imposed by the other electrode for better and more stable electrical contact. In the modified design, the back electrode was changed into a pressing bracket with three elastic arms (**c** in Figure 6.5). It is a Computer Numerical Controlling (CNC) milled metal sheet molded by the home designed and also CNC milled aluminum mold (**a1**,**a2** in Figure 6.6). After a series of tests, a 0.05 mm Ta sheet was finally chosen as the material for the bracket **c** because of its excellent thermal and chemical stability, especially of its good elasticity in the thin sheet form. The three under curved arms of the bracket reply mostly on the Ta sheet's elasticity to impose sufficient yet mild pressure onto the $LiTaO_3$ crystal.

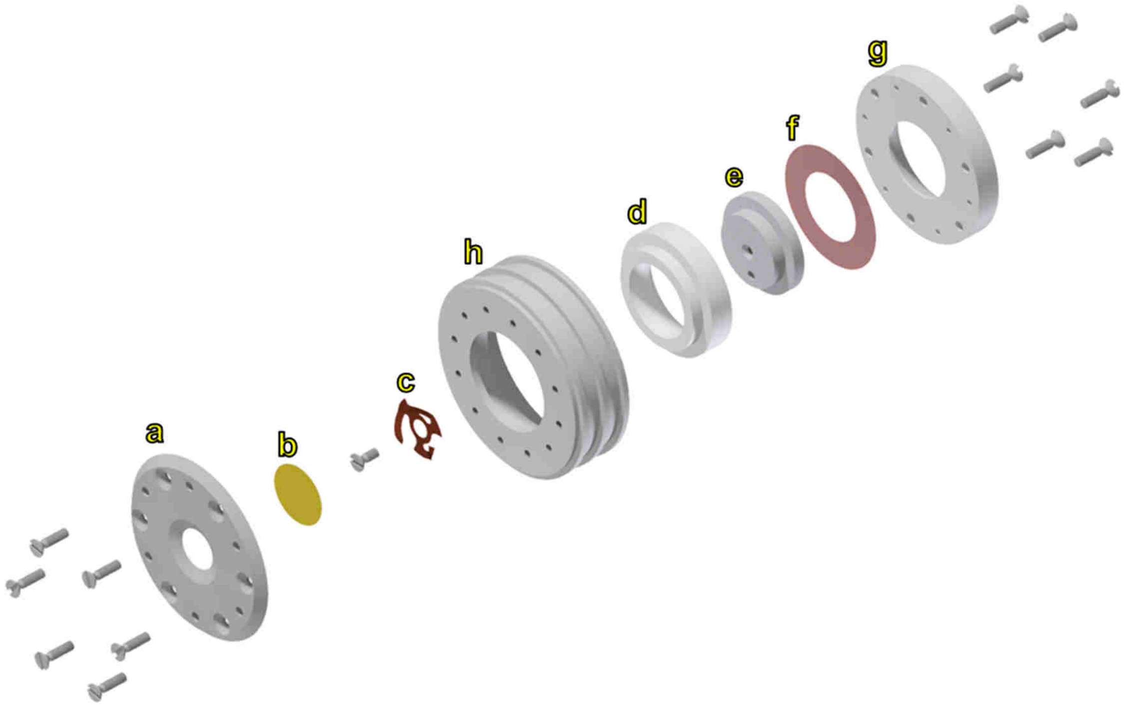

Figure 6.5: Expanded 3D presentation of the modified sample holder for $LiTaO_3$ single crystal. a: stainless steel front cap/electrode; b: gold coated Ø10 mm, 0.1 mm thick $LiTaO_3$ single crystal; c: CNC milled and molded pressing bracket as back electrode; d: Macor ceramic isolation bush; e: aluminum mounting piece for the pressing bracket; f: Kapton polyimide isolation washer; g: aluminum back pressing piece mounted on the outer shell; h: grooved aluminum outer shell as the backbone of the sample holder. Tightening pieces are of the DIN norm and are therefore not specified.

The mold shown in Figure 6.6 would also find its applications in various circumstances where a structure of delicate electrical contact is needed, i.e., QCM or mounting of thin metal single crystals.

Figure 6.6: Home designed mold and molded brackets of different materials. a1,a2: the male and female mold respectively; b: 0.05 mm Ta film bracket; c: 0.4 mm Cu sheet bracket; d1,d2: 0.2 mm Al sheet bracket.

6.2 Portable manipulator with cooling capability

A portable manipulator with cooling capability was developed from a commercial VG Scienta manipulator with 50 mm axial stroke for in/out maneuver. Its allowance of planar movement parallel to the base plane of the holding flange is 25 mm × 25 mm (Figure 6.7).

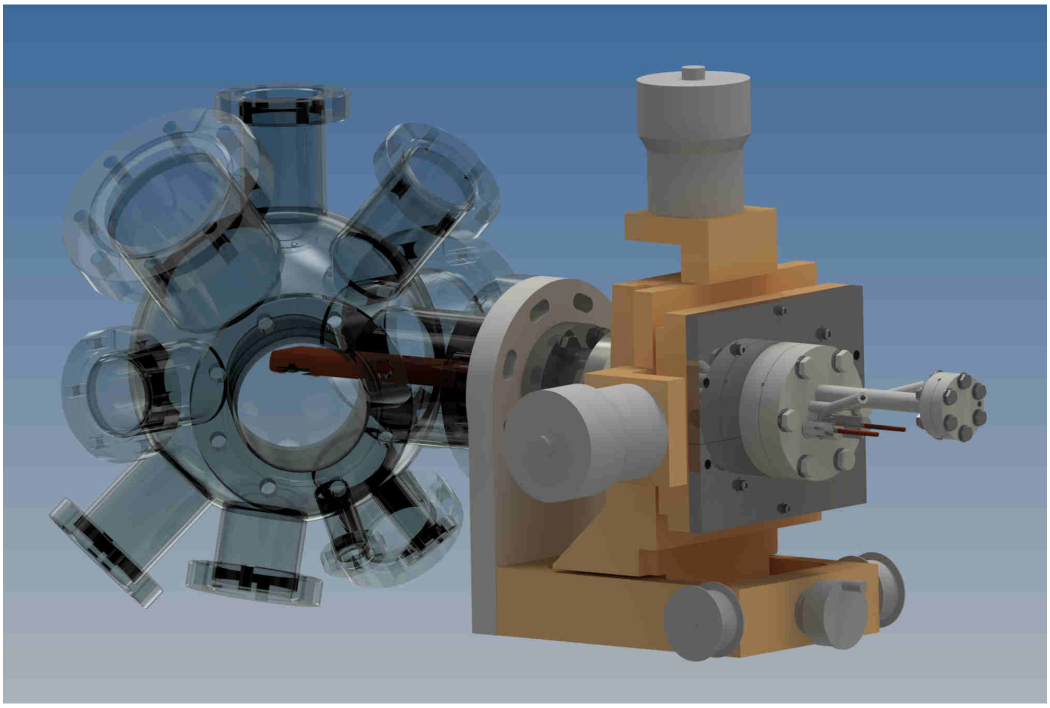

Figure 6.6: 3D model of the modified manipulator. The assembly is coupled to a CF 63 flange on a transparent virtual chamber to demonstrate the general size of the assembly. The sample holder on the reservoir stands at the center of the spherical chamber.

The ground flange (**a** in Figure 6.8) of the whole manipulator assembly is changed from the original CF-40 to CF-63 norm. This is due to our experience that a block of this size and weight would usually be arranged with a CF-63 flange for sample preparation and other tasks. However, the cross section of the X-Y stage for planar movement only allows CF-40 bellow to be fitted, the ground flange is therefore made into an CF-63 to CF-40 adaptor as well. The dimensional restriction of a CF-40 flange means the room for planar maneuver parallel to the flange would theoretically be rather confined. The internal structure built on the CF-40 flange must have a cross section that is significantly smaller than the Ø38 mm CF-40 bellow. The existing coolable evaporator designed by Dr. Drescher[96] is employed for convenience and cost reasons. In its design, robust stainless steel tubes are fed through the base flange and welded to a hollow stage. Its backbone frame for parts mounting and cooling pipeline are merged together to save space while maintaining the strength to withstand additional parts such as a Cu thermal shield. However, since it was initially designed for a thermal evaporator, the heat exchange rate of this design is relatively limited by its small contact area available for mounting. To compensate this limit, a chunky Cu block was used as the thermal reservoir and the holding stage to accommodate the sample (**f** in Figure 6.8).

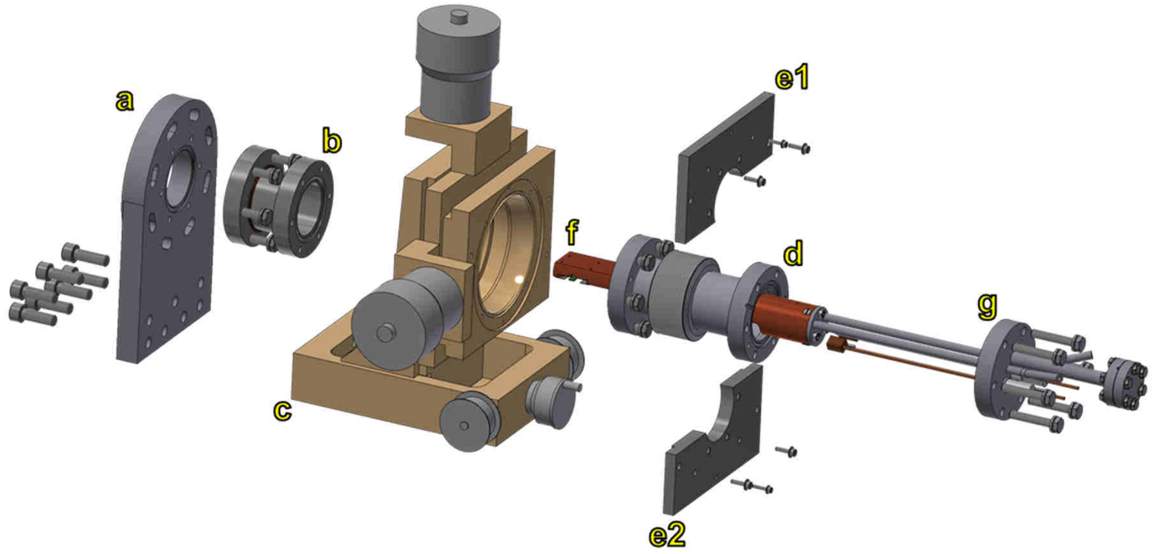

Figure 6.7: Expanded 3D presentation of the portable manipulator assembly. a: ground flange; b: home made CF-40 extension tube; c: three dimensional linear motion; d: Bellow with 50 mm axial stroke from Vakuum-Anlagenbau GmbH; e1, e2: two piece plate to mount the base flange g and bellow d; f: Cu reservoir; g: CF-40 base flange of the installment. Tightening pieces are of the DIN norm and are therefore not specified.

The original manipulator is equipped with a CF-40 rotational feedthrough at the center for the azimuthal adjustment of the sample. However, it is not suitable to hold heavy parts such as a Cu block, separate flanges will be need to build a setup with cooling and etc.. For a portable manipulator, 360° azimuthal adjustment is not the core necessity that always has to be realized, yet simple adjustment when mounting the manipulator are still needed to ensure proper sample transfer. Therefore, a compromise is made on the ground flange **a**. The original through holes for M8 screws are widened for ±5° to form a groove. It allows azimuthal adjustment by rotating the entire manipulator as a single block during the mounting process. This 10° allowance is enough to bridge the gap of misalignment in most occasions.

The sample stage on the Cu reservoir (**f0** in Figure 6.9) and its pressing bracket was designed to accommodate the SPECS style samples. More specifically, this manipulator was used for the sample preparations in the XPS studies discussed in the Chapter 3 of this work.

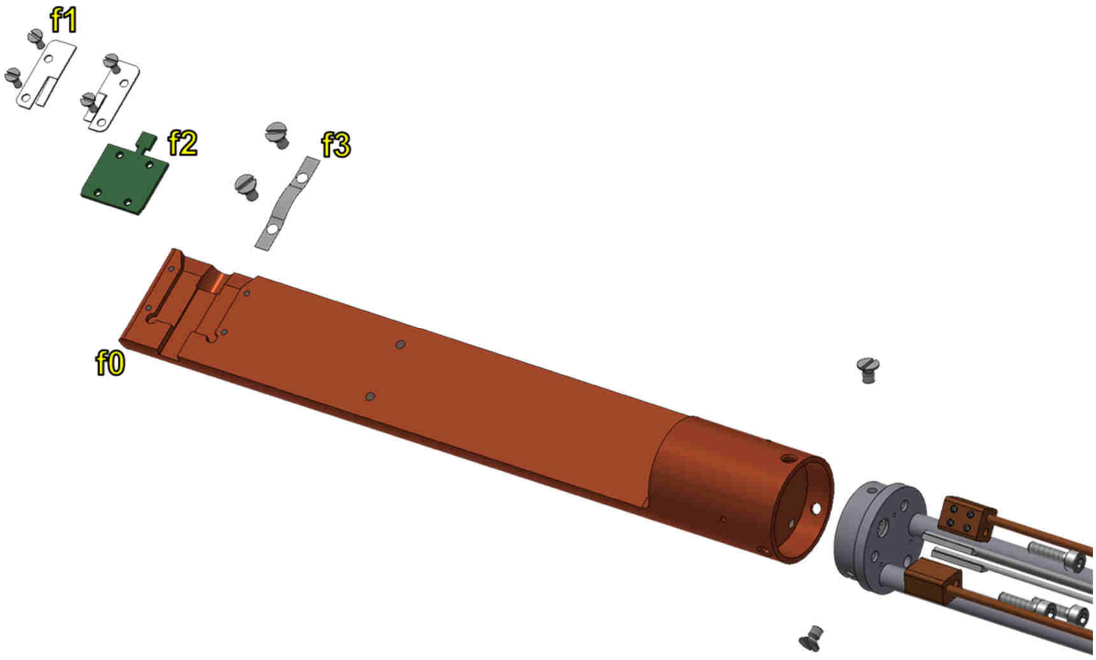

Figure 6.8: Zoomed view to the expanded 3D presentation of the reservoir assembly. f0: sample stage milled on the Cu reservoir; f1: pressing bracket for the sample; f2: sample of SPECS style; f3: pressing strip for the thermocouple wire. The thermocouple wire is not shown in the figure. Tightening pieces are not specified.

7 Summary

In this thesis, the structure of interfaces/interphases between Ca and organic thin films has been investigated and characterized by soft X-ray photoelectron spectroscopy (XPS) and hard X-ray photoelectron spectroscopy (HAXPES), scanning transmission electronic microscopy (STEM), and nanojoule adsorption calorimetry. The growth behaviors of Ca on different organic substrates are discussed.

The data acquisition system as well as the mechanical instrumental development for the home built adsorption calorimeter are also presented in this work.

Because the surface science investigations and instrumental constructions belong to two very different categories of work, the summary of this work will be divided into two independent parts.

7.1 Investigations on the Ca/Organic Interactions

7.1.1 Adsorption and Reaction of Ca on Organic Thin Films

Coverage controlled studies on the growth Ca on 6T thin films at room temperature are carried out with conventional XPS as well as adsorption calorimetry. These methods show that no simple layer by layer sequence (reacted layer with a sharp interface to an unreacted layer) emerges from the diffusion and reaction processes that occur in the Ca/6T system. Intensive chemical modifications to the backbone of 6T molecules upon the reactions with Ca are indicated by significant changes in the C 1s spectra with increasing Ca coverage. A metallic Ca layer starts to emerge at a coverage of 2.6 ML, while the surface of the organic film is fully covered by metallic Ca at around 4.0–4.5 ML. This is simultaneously confirmed by the full band alignment of ~0.8 eV to metal Ca in the XPS results and the downward reflection point in the trace of adsorption heat at this coverage.

By changing the substrate temperature during the Ca deposition, the interactions between Ca and 6T thin film have been accordingly confirmed (by XPS). However, even at reduced temperatures (142 K and 153 K), a considerable amount of the thiophen sulfur still reacts with Ca. Beside the high reactivity of Ca, a possible influence of the thermal radiation of the Ca source should also be concerned. Increasing the sample temperature has a limited effect on the extent of reaction between Ca and 6T. In a series of temperature dependent studies, it was found that the temperature dependence of the Ca diffusion rate in 6T films is the controlling factor to the interaction between Ca and 6T. Meanwhile, the reactions between Ca and 6T introduce significant steric hindrance to the diffusion of Ca. This phenomenon has intensively influenced the growth behavior of Ca on 6T thin films.

Growth of Ca on Perylenetetracarboxylic dianhydride (PTCDA) is also studied by adsorption calorimetry at room temperature. The sticking behavior and adsorption heat indicated growth model of this system is more analogous to the diffusion and reaction of Ca on polymers, creating a layer-by-layer structure.

7.1.2 The Structure of the Ca/6T Interphase

The structure of the Ca/6T interphase formed at room temperature is studied by HAXPES and STEM. The high diffusivity of Ca in 6T resulted in a reaction zone of ca. 30 nm. By employing the genetic algorithm based simulation on the data of HAXPES, a concentration profile of the reacted S species is established. The profile indicates a constant 67% reacted S species in the 30 nm reaction zone followed by a 1.9 nm wide abrupt transition to fully unreacted species. The structure of the Ca/6T interphase formed at reduced temperature (153 K) is also studied by HAXPES and simulated by the genetic algorithm. The result shows that low-temperature preparation leads to a concentration profile that decays sigmoidally from the boundary of the organic phase to ~20 nm in the bulk.

7.2 Development for the Adsorption Calorimeter

The data acquisition system for the home built adsorption calorimeter is developed with the LabVIEW graphic programming environment. LabVIEW is a very powerful developing tool for quick start of device test, automated instrumental control, and data acquisition with intrinsically integrated graphical user interface. The characteristics of the LabVIEW programming language are briefly discussed. Possible challenges, stemming from these characteristics when dealing with the requirements of multitask, time critical procedures, are discussed with examples from the constructed system of this work.

The original fiber based laser system for adsorption calorimeter is replaced by the more conventional and robust mirror reflection system with home built mounting setups to accommodate the commercially obtained components.

To take the advantages of $LiTaO_3$'s thermal and electrical stabilities. A new encapsulation for the $LiTaO_3$ single crystal is designed and manufactured. It emphasizes the rigidity of the ground piece and the gentle but also stable contact of the pressing electrode.

List of Figures

List of Tables

Bibliography

[1] Siegrist, T.; Fleming, R. M.; Haddon, R. C.; Laudise, R. A.; Lovinger, A. J.; Katz, H. E.; Bridenbaugh, P.; Davis, D. D., The Crystal Structure of the High-Temperature Polymorph of A–Hexathienyl (A–6t/Ht). *Journal of Materials Research* **1995**, *10*, 2170-2173.

[2] Sengupta, S. K.; Ahn, H.; Whitten, J. E., Adsorption of Thiophene on Al(111) and Deposition of Aluminum on Condensed Thiophene. *Surface Science* **2002**, *520*, 207-216.

[3] Schwieger, T.; Liu, X.; Peisert, H.; Adolphi, B.; Kiriy, N.; Knupfer, M., Electronic Properties of Interfaces between Different Sexithiophenes and Gold. *Journal of Applied Physics* **2005**, *97*, 123712.

[4] Oehzelt, M.; Berkebile, S.; Koller, G.; Ivanco, J.; Surnev, S.; Ramsey, M. G., A-Sexithiophene on Cu(110) and Cu(110)–(2x1)O: An Stm and Nexafs Study. *Surface Science* **2009**, *603*, 412-418.

[5] Seki, K.; Tani, T.; Ishii, H., Electronic Structures of Organic-Inorganic Interfaces Studied by Uv Photoemission. *Thin Solid Films* **1996**, *273*, 20-26.

[6] Seki, K.; Ito, E.; Ishii, H., Energy Level Alignment at Organic/Metal Interfaces Studied by Uv Photoemission. *Synthetic Metals* **1997**, *91*, 137-142.

[7] Zhu, X. Y., Electronic Structure and Electron Dynamics at Molecule–Metal Interfaces: Implications for Molecule-Based Electronics. *Surface Science Reports* **2004**, *56*, 1-83.

[8] Koch, N.; Duhm, S.; Rabe, J. P.; Vollmer, A.; Johnson, R. L., Optimized Hole Injection with Strong Electron Acceptors at Organic-Metal Interfaces. *Physical Review Letters* **2005**, *95*, 237601

[9] Witte, G.; Lukas, S.; Bagus, P. S.; Woll, C., Vacuum Level Alignment at Organic/Metal Junctions: "Cushion" Effect and the Interface Dipole. *Applied Physics Letters* **2005**, *87*, 3.

[10] Ge, Y.; Whitten, J. E., Energy Level Alignment between Sexithiophene and Buckminsterfullerene Films. *Chemical Physics Letters* **2007**, *448*, 65-69.

[11] Grobosch, M.; Knupfer, M., Energy Level Alignment and Interface States at A-Sexithiophene/Ag Interfaces. *Organic Electronics* **2007**, *8*, 625-630.

[12] Hwang, J.; Wan, A.; Kahn, A., Energetics of Metal–Organic Interfaces: New Experiments and Assessment of the Field. *Materials Science and Engineering: R: Reports* **2009**, *64*, 1-31.

[13] Schwalb, C. H.; Sachs, S.; Marks, M.; Schöll, A.; Reinert, F.; Umbach, E.; Höfer, U., Electron Lifetime in a Shockley-Type Metal-Organic Interface State. *Physical Review Letters* **2008**, *101*, 146801.

[14] Sachs, S.; Schwalb, C.; Marks, M.; Schöll, A.; Reinert, F.; Umbach, E.; Höfer, U., Electronic Structure at the Perylene-Tetracarboxylic Acid Dianhydride/Ag(111) Interface Studied with Two-Photon Photoelectron Spectroscopy. *Physical Review Letters* **2009**; *131*, 144701.

[15] Marks, M.; Zaitsev, N.; Schmidt, B.; Schwalb, C.; Schöll, A.; Nechaev, I.; M. Echenique, P.; V. Chulkov, E.; Höfer, U., Energy Shift and Wavefunction Overlap of Metal-Organic Interface-States. *Physical Review B* **2011**; *84*, 081301

[16] Gottfried, J. M., Quantitative Model Studies for Interfaces in Organic Electronic Devices. *New Journal of Physics* **2016**, *18*. 111002

[17] Hwang, J.; Wan, A.; Kahn, A., Energetics of Metal–Organic Interfaces: New Experiments and Assessment of the Field. *Materials Science and Engineering: R: Reports* **2009**, *64*, 1-31.

[18] Strunskus, T.; Zaporojtchenko, V.; Behnke, K.; von Bechtolsheim, C.; Faupel, F., Tailoring the Morphology of Metal/Polymer Interfaces. *Advanced Engineering Materials* **2000**, *2*, 489-492.

[19] Zaporojtchenko, V.; Strunskus, T.; Behnke, K.; Von Bechtolsheim, C.; Kiene, M.; Faupel, F., Metal/Polymer Interfaces with Designed Morphologies. *Journal of Adhesion Science and Technology* **2000**, *14*, 467-490.

[20] Prakash, J.; Pivin, J. C.; Swart, H. C., Noble Metal Nanoparticles Embedding into Polymeric Materials: From Fundamentals to Applications. *Advances in Colloid and Interface Science* **2015**, *226*, 187-202.

[21] Strunskus, T.; Kiene, M.; Willecke, R.; Thran, A.; von Bechtolsheim, C.; Faupel, F., Chemistry, Diffusion and Cluster Formation at Metal-Polymer Interfaces. *Materials and Corrosion-Werkstoffe Und Korrosion* **1998**, *49*, 180-188.

[22] Halls, J. J. M.; Arias, A. C.; MacKenzie, J. D.; Wu, W. S.; Inbasekaran, M.; Woo, E. P.; Friend, R. H., Photodiodes Based on Polyfluorene Composites: Influence of Morphology. *Advanced Materials* **2000**, *12*, 498.

[23] Krebs, F. C.; Spanggaard, H., Significant Improvement of Polymer Solar Cell Stability. *Chemistry of Materials* **2005**, *17*, 5235-5237.

[24] Reese, M. O.; Morfa, A. J.; White, M. S.; Kopidakis, N.; Shaheen, S. E.; Rumbles, G.; Ginley, D. S., Pathways for the Degradation of Organic Photovoltaic P3ht:Pcbm Based Devices. *Solar Energy Materials and Solar Cells* **2008**, *92*, 746-752.

[25] Reese, M. O.; White, M. S.; Rumbles, G.; Ginley, D. S.; Shaheen, S. E., Optimal Negative Electrodes for Poly(3-Hexylthiophene): [6,6]-Phenyl C61-Butyric Acid Methyl Ester Bulk Heterojunction Photovoltaic Devices. *Applied Physics Letters* **2008**, *92*, 053307.

[26] Grossiord, N.; Kroon, J. M.; Andriessen, R.; Blom, P. W. M., Degradation Mechanisms in Organic Photovoltaic Devices. *Organic Electronics* **2012**, *13*, 432-456.

[27] Watters, D. C.; Kingsley, J.; Yi, H.; Wang, T.; Iraqi, A.; Lidzey, D., Optimising the Efficiency of Carbazole Co-Polymer Solar-Cells by Control over the Metal Cathode Electrode. *Organic Electronics* **2012**, *13*, 1401-1408.

[28] Ahmad, J.; Bazaka, K.; Anderson, L. J.; White, R. D.; Jacob, M. V., Materials and Methods for Encapsulation of Opv: A Review. *Renewable and Sustainable Energy Reviews* **2013**, *27*, 104-117.

[29] Yu, D.; Yang, Y.-Q.; Chen, Z.; Tao, Y.; Liu, Y.-F., Recent Progress on Thin-Film Encapsulation Technologies for Organic Electronic Devices. *Optics Communications* **2016**, *362*, 43-49.

[30] Fladischer, S.; Neuhold, A.; Kraker, E.; Haber, T.; Lamprecht, B.; Salzmann, I.; Resel, R.; Grogger, W., Diffusion of Ag into Organic Semiconducting Materials: A Combined Analytical Study Using Transmission Electron Microscopy and X-Ray Reflectivity. *Acs Applied Materials & Interfaces* **2012**, *4*, 5608-5612.

[31] Gottfried, J. M.; Schuster, R., Surface Microcalorimetry. In *Surface and Interface Science*, Wiley-VCH Verlag GmbH & Co. KGaA: **2016**; 73-126.

[32] Sharp, J. C., et al., Calcium Thin Film Growth on Polyfluorenes: Interface Structure and Energetics. *The Journal of Physical Chemistry C* **2014**, *118*, 2953-2962.

[33] Sharp, J. C.; Bebensee, F.; Baricuatro, J. H.; Steinrück, H. P.; Gottfried, J. M.; Campbell, C. T., Calcium Thin Film Growth on a Cyano-Substituted Poly(P-Phenylene Vinylene): Interface Structure and Energetics. *Journal of Physical Chemistry C* **2013**, *117*, 23781-23789.

[34] Bebensee, F.; Zhu, J. F.; Baricuatro, J. H.; Farmer, J. A.; Bai, Y.; Steinrück, H. P.; Campbell, C. T.; Gottfried, J. M., Interface Formation between Calcium and Electron-Irradiated Poly(3-Hexylthiophene). *Langmuir* **2010**, *26*, 9632-9639.

[35] Zhu, J. F.; Bebensee, F.; Hieringer, W.; Zhao, W.; Baricuatro, J. H.; Farmer, J. A.; Bai, Y.; Steinrück, H. P.; Gottfried, J. M.; Campbell, C. T., Formation of the Calcium/Poly(3-Hexylthiophene) Interface: Structure and Energetics. *Journal of the American Chemical Society* **2009**, *131*, 13498-13507.

[36] Farmer, J. A.; Campbell, C. T.; Xu, L.; Henkelman, G., Defect Sites and Their Distributions on Mgo(100) by Li and Ca Adsorption Calorimetry. *Journal of the American Chemical Society* **2009**, *131*, 3098-3103.

[37] Zhu, J. F.; Goetsch, P.; Ruzycki, N.; Campbell, C. T., Adsorption Energy, Growth Mode, and Sticking Probability of Ca on Poly(Methyl Methacrylate) Surfaces with and without Electron Damage. *Journal of the American Chemical Society* **2007**, *129*, 6432-6441.

[38] Murdey, R.; Stuckless, J. T., Calorimetry of Polymer Metallization: Copper, Calcium, and Chromium on Pmda-Oda Polyimide. *Journal of the American Chemical Society* **2003**, *125*, 3995-3998.

[39] Strunskus, T.; Grunze, M.; Kochendoerfer, G.; Wöll, C., Identification of Physical and Chemical Interaction Mechanisms for the Metals Gold, Silver, Copper, Palladium, Chromium, and Potassium with Polyimide Surfaces. *Langmuir* **1996**, *12*, 2712-2725.

[40] Schwalb, C.; Marks, M.; Sachs, S.; Schöll, A.; Reinert, F.; Umbach, E.; Höfer, U., *Time-Resolved Measurements of Electron Transfer Processes at the Ptcda/Ag(111) Interface*, **2010**; *75*, p 22.

[41] Dannetun, P.; Boman, M.; Stafstrom, S.; Salaneck, W. R.; Lazzaroni, R.; Fredriksson, C.; Bredas, J. L.; Zamboni, R.; Taliani, C., The Chemical and Electronic Structure of the Interface between Aluminum and Polythiophene Semiconductors. *The Journal of Chemical Physics* **1993**, *99*, 664-672.

[42] Gottfried, J. M.; Flechtner, K.; Kretschmann, A.; Lukasczyk, T.; Steinrück, H. P., Direct Synthesis of a Metalloporphyrin Complex on a Surface. *Journal of the American Chemical Society* **2006**, *128*, 5644-5645.

[43] Gavrila, G.; Zahn, D. R. T.; Braun, W., High Resolution Photoemission Spectroscopy: Evidence for Strong Chemical Interaction between Mg and 3,4,9,10-Perylene-Tetracarboxylic Dianhydride. *Applied Physics Letters* **2006**, *89*, 162102-162103.

[44] Shubina, T. E.; Marbach, H.; Flechtner, K.; Kretschmann, A.; Jux, N.; Buchner, F.; Steinrück, H. P.; Clark, T.; Gottfried, J. M., Principle and Mechanism of Direct Porphyrin Metalation: Joint Experimental and Theoretical Investigation. *Journal of the American Chemical Society* **2007**, *129*, 9476-9483.

[45] Kretschmann, A.; Walz, M. M.; Flechtner, K.; Steinrück, H. P.; Gottfried, J. M., Tetraphenylporphyrin Picks up Zinc Atoms from a Silver Surface. *Chemical Communications* **2007**, 568-570.

[46] Bebensee, F.; Schmid, M.; Steinrück, H. P.; Campbell, C. T.; Gottfried, J. M., Toward Well-Defined Metal-Polymer Interfaces: Temperature-Controlled Suppression of Subsurface Diffusion and Reaction at the Calcium/Poly(3-Hexylthiophene) Interface. *Journal of the American Chemical Society* **2010**, *132*, 12163-12165.

[47] Chen, M.; Feng, X. F.; Zhang, L.; Ju, H. X.; Xu, Q.; Zhu, J. F.; Gottfried, J. M.; Ibrahim, K.; Qian, H. J.; Wang, J. O., Direct Synthesis of Nickel(II) Tetraphenylporphyrin and Its Interaction with a Au(111) Surface: A Comprehensive Study. *Journal of Physical Chemistry C* **2010**, *114*, 9908-9916.

[48] Fan, Q. T.; Wang, C. C.; Han, Y.; Zhu, J. F.; Hieringer, W.; Kuttner, J.; Hilt, G.; Gottfried, J. M., Surface-Assisted Organic Synthesis of Hyperbenzene Nanotroughs. *Angewandte Chemie-International Edition* **2013**, *52*, 4668-4672.

[49] Sharp, J. C.; Bebensee, F.; Baricuatro, J. H.; Steinrueck, H. P.; Gottfried, J. M.; Campbell, C. T., Calcium Thin Film Growth on a Cyano-Substituted Poly(P-Phenylene Vinylene): Interface Structure and Energetics. *Journal of Physical Chemistry C* **2013**, *117*, 23781-23789.

[50] Chen, M.; Zhou, H.; Klein, B. P.; Zugermeier, M.; Krug, C. K.; Drescher, H. J.; Gorgoi, M.; Schmid, M.; Gottfried, J. M., Formation of an Interphase Layer During Deposition of Cobalt onto Tetraphenylporphyrin: A Hard X-Ray Photoelectron Spectroscopy (Haxpes) Study. *Phys Chem Chem Phys* **2016**, *18*, 30643-30651.

[51] Comstock, M. J., *Metallization of Polymers*; American Chemical Society: Washintong, DC, **1990**; Vol. 440.

[52] Sacher, E., *Metallization of Polymers Ii*; Springer, Boston, MA: New York, **2002**, 208.

[53] Seah, M. P.; Dench, W. A., Quantitative Electron Spectroscopy of Surfaces: A Standard Data Base for Electron Inelastic Mean Free Paths in Solids. *Surface and Interface Analysis* **1979**, *1*, 2-11.

[54] Westphal, C., The Study of the Local Atomic Structure by Means of X-Ray Photoelectron Diffraction. *Surface Science Reports* **2003**, *50*, 1-106.

[55] Chen, M.; Zhou, H.; Klein, B. P.; Zugermeier, M.; Krug, C. K.; Drescher, H.-J.; Gorgoi, M.; Schmid, M.; Gottfried, J. M., Formation of an Interphase Layer During Deposition of Cobalt onto Tetraphenylporphyrin: A Hard X-Ray Photoelectron Spectroscopy (Haxpes) Study. *Physical Chemistry Chemical Physics* **2016**, *18*, 30643-30651.

[56] Wagner, C. D.; Davis, L. E.; Zeller, M. V.; Taylor, J. A.; Raymond, R. H.; Gale, L. H., Empirical Atomic Sensitivity Factors for Quantitative Analysis by Electron Spectroscopy for Chemical Analysis. *Surface and Interface Analysis* **1981**, *3*, 211-225.

[57] Gottfried, J. M.; Schuster, R., Surface Microcalorimetry. In *Surface and Interface Science: Solid-Gas Interfaces I*, First Edition ed.; Wandelt, K., Ed. Wiley-VCH Verlag GmbH & Co. KGaA: **2015**; *1.*

[58] Gottfried, J. M.; Vestergaard, E. K.; Bera, P.; Campbell, C. T., Heat of Adsorption of Naphthalene on Pt(111) Measured by Adsorption Calorimetry. *Journal of Physical Chemistry B* **2006**, *110*, 17539-17545.

[59] Lytken, O.; Lew, W.; Harris, J. J.; Vestergaard, E. K.; Gottfried, J. M.; Campbell, C. T., Energetics of Cyclohexene Adsorption and Reaction on Pt(111) by Low-Temperature Microcalorimetry. *Journal of the American Chemical Society* **2008**, *130*, 10247-10257.

[60] Lew, W. D.; Crowe, M. C.; Karp, E.; Campbell, C. T., Energy of Molecularly Adsorbed Water on Clean Pt(111) and Pt(111) with Coadsorbed Oxygen by Calorimetry. *Journal of Physical Chemistry C* **2011**, *115*, 9164-9170.

[61] Larsen, J. H.; Ranney, J. T.; Starr, D. E.; Musgrove, J. E.; Campbell, C. T., Adsorption Energetics of Ag on MgO(100). *Physical Review B* **2001**, *63*. 195410

[62] Campbell, C. T.; Starr, D. E., Metal Adsorption and Adhesion Energies on Mgo(100). *Journal of the American Chemical Society* **2002**, *124*, 9212-9218.

[63] Zhu, J. F.; Diaz, S. F.; Heeb, L. R.; Campbell, C. T., Adsorption of Pb on Nial(110): Energetics and Structure. *Surface Science* **2005**, *574*, 34-42.

[64] Redhead, P. A., Thermal Desorption of Gases. *Vacuum* **1962**, *12*, 203-211.

[65] Habenschaden, E.; Küppers, J., Evaluation of Flash Desorption Spectra. *Surface Science* **1984**, *138*, 147-150.

[66] King, D. A., Thermal Desorption from Metal Surfaces: A Review. *Surface Science* **1975**, *47*, 384-402.

[67] Comsa, G.; David, R., Dynamical Parameters of Desorbing Molecules. *Surface Science Reports* **1985**, *5*, 145-198.

[68] Roberts, J. K., The Adsorption of Hydrogen on Tungsten. *Mathematical Proceedings of the Cambridge Philosophical Society* **1934**, *30*, 74-79.

[69] Kisliuk, P., Calorimetric Heat of Adsorption—Nitrogen on Tungsten. *The Journal of Chemical Physics* **1959**, *31*, 1605-1611.

[70] Černý, S., Adsorption Microcalorimetry in Surface Science Studies Sixty Years of Its Development into a Modern Powerful Method. *Surface Science Reports* **1996**, *26*, 1-59.

[71] Beeck, O.; Cole, W. A.; Wheeler, A., Determination of Heats of Adsorption Using Metal Films. *Discussions of the Faraday Society* **1950**, *8*, 314-321.

[72] Wedler, G.; Ganzmann, I.; Borgmann, D., Calorimetric Investigations of Processes at the Solid/Gas Interphase. *Berichte der Bunsengesellschaft für physikalische Chemie* **1993**, *97*, 293-297.

[73] Černý, S.; Smutek, M.; Buzek, F., Calorimetric Studies of Hydrocarbon Adsorption on Metal Films. *Journal of Catalysis* **1977**, *47*, 166-177.

[74] Smutek, M.; Černý, S., Calorimetric Studies of Hydrocarbon Adsorption on Metal Films. *Journal of Catalysis* **1977**, *47*, 178-189.

[75] Pálfi, S.; Lisowski, W.; Smutek, M.; Černý, S., Calorimetric Studies of Hydrocarbon Adsorption on Metal Films. *Journal of Catalysis* **1984**, *88*, 300-312.

[76] King, D. A.; Wells, M. G., Molecular-Beam Investigation of Adsorption Kinetics on Bulk Metal Targets - Nitrogen on Tungsten. *Surface Science* **1972**, *29*, 454.

[77] King, D. A.; Wells, M. G., Reaction Mechanism in Chemisorption Kinetics: Nitrogen on the {100} Plane of Tungsten. *Proceedings of the Royal Society of London. A. Mathematical and Physical Sciences* **1974**, *339*, 245-269.

[78] Kyser, D. A.; Masel, R. I., Design of a Calorimeter Capable of Measuring Heats of Adsorption on Single-Crystal Surfaces. *Review of Scientific Instruments* **1987**, *58*, 2141-2144.

[79] Borroni-Bird, C. E.; Al-Sarraf, N.; Andersoon, S.; King, D. A., Single Crystal Adsorption Microcalorimetry. *Chemical Physics Letters* **1991**, *183*, 516-520.

[80] Dixon-Warren, S. J.; Kovar, M.; Wartnaby, C. E.; King, D. A., Pyroelectric Single Crystal Adsorption Microcalorimetry at Low Temperatures: Oxygen on Ni{100}. *Surface Science* **1994**, *307*, 16-22.

[81] Stuck, A.; Wartnaby, C. E.; Yeo, Y. Y.; Stuckless, J. T.; Al-Sarraf, N.; King, D. A., An Improved Single Crystal Adsorption Calorimeter. *Surface Science* **1996**, *349*, 229-240.

[82] Brown, W. A.; Kose, R.; King, D. A., Femtomole Adsorption Calorimetry on Single-Crystal Surfaces. *Chemical Reviews* **1998**, *98*, 797-832.

[83] Stensgaard, I.; Jakobsen, F., Adsorption-Site Location by Transmission Channeling: Deuterium on Ni(100). *Physical Review Letters* **1985**, *54*, 711-713.

[84] Stuckless, J. T.; Frei, N. A.; Campbell, C. T., A Novel Single-Crystal Adsorption Calorimeter and Additions for Determining Metal Adsorption and Adhesion Energies. *Review of Scientific Instruments* **1998**, *69*, 2427-2438.

[85] Stuckless, J. T.; Frei, N. A.; Campbell, C. T., Pyroelectric Detector for Single-Crystal Adsorption Microcalorimetry: Analysis of Pulse Shape and Intensity. *Sensors and Actuators B: Chemical* **2000**, *62*, 13-22.

[86] Diaz, S. F.; Zhu, J. F.; Shamir, N.; Campbell, C. T., Pyroelectric Heat Detector for Measuring Adsorption Energies on Thicker Single Crystals. *Sensors and Actuators B: Chemical* **2005**, *107*, 454-460.

[87] Zhu, J. F.; Diaz, S. F.; Heeb, L. R.; Campbell, C. T., Microcalorimetric Studies of Adsorption Energies on Thicker Single Crystals: Pb on Nial(110). *Abstracts of Papers of the American Chemical Society* **2005**, *229*, U741-U741.

[88] Murdey, R.; Liang, S. J. S.; Stuckless, J. T., An Atom-Transparent Photon Block for Metal-Atom Deposition from High-Temperature Ovens. *Review of Scientific Instruments* **2005**, *76*, 023911.

[89] Schießer, A.; Schäfer, R., Versatile Piezoelectric Pulsed Molecular Beam Source for Gaseous Compounds and Organic Molecules with Femtomole Accuracy for Uhv and Surface Science Applications. *Review of Scientific Instruments* **2009**, *80*, 086103.

[90] Schießer, A.; Hörtz, P.; Schäfer, R., Thermodynamics and Kinetics of Co and Benzene Adsorption on Pt(111) Studied with Pulsed Molecular Beams and Microcalorimetry. *Surface Science* **2010**, *604*, 2098-2105.

[91] Fischer-Wolfarth, J. H.; Farmer, J. A.; Flores-Camacho, J. M.; Genest, A.; Yudanov, I. V.; Rosch, N.; Campbell, C. T.; Schauermann, S.; Freund, H. J., Particle-Size Dependent Heats of Adsorption of Co on Supported Pd Nanoparticles as Measured with a Single-Crystal Microcalorimeter. *Physical Review B* **2010**, *81*.

[92] Fischer-Wolfarth, J. H.; Hartmann, J.; Farmer, J. A.; Flores-Camacho, J. M.; Campbell, C. T.; Schauermann, S.; Freund, H. J., An Improved Single Crystal Adsorption Calorimeter for Determining Gas Adsorption and Reaction Energies on Complex Model Catalysts. *Review of Scientific Instruments* **2011**, *82*.

[93] Crowe, M. C.; Campbell, C. T., Adsorption Microcalorimetry: Recent Advances in Instrumentation and Application. *Annual Review of Analytical Chemistry, Vol 4* **2011**, *4*, 41-58.

[94] Gorgoi, M., et al., The High Kinetic Energy Photoelectron Spectroscopy Facility at Bessy Progress and First Results. *Nuclear Instruments and Methods in Physics Research Section A: Accelerators, Spectrometers, Detectors and Associated Equipment* **2009**, *601*, 48-53.

[95] Schaefers, F.; Mertin, M.; Gorgoi, M., Kmc-1: A High Resolution and High Flux Soft X-Ray Beamline at Bessy. *Review of Scientific Instruments* **2007**, *78*.

[96] Drescher, H.-j. Nanojoule Adsorption Calorimetry Design, Construction, Novel Evaluation Approach, Software Development, Characterization, and Exemplary Measurements. Philipps-Universität Marburg, Marburg, **2016**.

[97] Chen, L.-M.; Xu, Z.; Hong, Z.; Yang, Y., Interface Investigation and Engineering - Achieving High Performance Polymer Photovoltaic Devices. *Journal of Materials Chemistry* **2010**, *20*, 2575-2598.

[98] Jiang, C. Y.; Sun, X. W.; Zhao, D. W.; Kyaw, A. K. K.; Li, Y. N., Low Work Function Metal Modified Ito as Cathode for Inverted Polymer Solar Cells. *Solar Energy Materials and Solar Cells* **2010**, *94*, 1618-1621.

[99] Tseng, W.-H.; Chen, M.-H.; Wang, J.-Y.; Tseng, C.-T.; Lo, H.; Wang, P.-S.; Wu, C.-I., Investigations of Efficiency Improvements in Poly(3-Hexylthiophene) Based Organic Solar Cells Using Calcium Cathodes. *Solar Energy Materials and Solar Cells* **2011**, *95*, 3424-3427.

[100] Kendrick, C.; Semancik, S., Doping Effects and Reversibility Studies on Gas-Exposed A-Sexithiophene Thin Films. *Journal of Vacuum Science & Technology A* **1998**, *16*, 3068-3075.

[101] Krause, B. Growth and Structure of the Organic Molecule. Universität Stuttgart, Stuttgart, **2002**.

[102] Uchiyama, K.; Akimichi, H.; Hotta, S.; Noge, H.; Sakaki, H., Light-Emitting Diodes Using Semiconducting Oligothiophenes. *MRS Online Proceedings Library Archive* **1993**, *328*, 389.

[103] Horowitz, G., et al., Two-Layer Light-Emitting Diodes Based on Sexithiophene and Derivatives. *Advanced Materials* **1994**, *6*, 752-755.

[104] Geiger, F.; Stoldt, M.; Schweizer, H.; Bäuerle, P.; Umbach, E., Electroluminescence from Oligothiophene-Based Light-Emitting Devices. *Advanced Materials* **1993**, *5*, 922-925.

[105] Kisliuk, P., The Sticking Probabilities of Gases Chemisorbed on the Surfaces of Solids. *Journal of Physics and Chemistry of Solids* **1957**, *3*, 95-101.

[106] Cheney, W.; Kincaid, D., Numerical Mathematics and Computing. 6th ed.; Bob Pirtle Thomson Brooks/Cole: Belmont, **2008**.

[107] Garnier, F.; Horowitz, G.; Peng, X.; Fichou, D., An All-Organic "Soft" Thin Film Transistor with Very High Carrier Mobility. *Advanced Materials* **1990**, *2*, 592-594.

[108] Loi, M. A.; da Como, E.; Dinelli, F.; Murgia, M.; Zamboni, R.; Biscarini, F.; Muccini, M., Supramolecular Organization in Ultra-Thin Films of [Alpha]-Sexithiophene on Silicon Dioxide. *Nature Materials* **2005**, *4*, 81-85.

[109] Horowitz, G.; Bachet, B.; Yassar, A.; Lang, P.; Demanze, F.; Fave, J. L.; Garnier, F., Growth and Characterization of Sexithiophene Single-Crystals. *Chemistry of Materials* **1995**, *7*, 1337-1341.

[110] Gottfried, J. M.; Flechtner, K.; Kretschmann, A.; Lukasczyk, T.; Steinrück, H. P., Direct Synthesis of a Metalloporphyrin Complex on a Surface. *Journal of the American Chemical Society* **2006**, *128*, 5644-5645.

[111] Bai, Y.; Buchner, F.; Wendahl, M. T.; Kellner, I.; Bayer, A.; Steinrück, H. P.; Marbach, H.; Gottfried, J. M., Direct Metalation of a Phthalocyanine Monolayer on Ag(111) with Coadsorbed Iron Atoms. *Journal of Physical Chemistry C* **2008**, *112*, 6087-6092.

[112] Bai, Y.; Buchner, F.; Kellner, I.; Schmid, M.; Vollnhals, F.; Steinrück, H. P.; Marbach, H.; Gottfried, J. M., Adsorption of Cobalt (Ii) Octaethylporphyrin and 2h-Octaethylporphyrin on Ag(111): New Insight into the Surface Coordinative Bond. *New Journal of Physics* **2009**, *11*, 125004.

[113] Taliani, C.; Blinov, L. M., The Electronic Structure of Solid A-Sexithiophene. *Advanced Materials* **1996**, *8*, 353-359.

[114] Milligan, P.; McNamarra, J.; Murphy, B.; Cowie, B. C. C.; Lennon, D.; Kadodwala, M., A Nixsw and Nexafs Investigation of Thiophene on Cu(111). *Surface Science* **1998**, *412–413*, 166-173.

[115] Ivanco, J.; Krenn, J. R.; Ramsey, M. G.; Netzer, F. P.; Haber, T.; Resel, R.; Haase, A.; Stadlober, B.; Jakopic, G., Sexithiophene Films on Clean and Oxidized Si(111) Surfaces: Growth and Electronic Structure. *Journal of Applied Physics* **2004**, *96*, 2716-2724.

[116] Lesiak, B.; Kosinski, A.; Jablonski, A.; Kover, L.; Toth, J.; Varga, D.; Cserny, I.; Zagorska, M.; Kulszewicz-Bajer, I.; Gergely, G., Determination of the Inelastic Mean Free Path of Electrons in Polythiophenes Using Elastic Peak Electron Spectroscopy Method. *Applied Surface Science* **2001**, *174*, 70-85.

[117] Mason, M. G., Electronic Structure of Supported Small Metal Clusters. *Physical Review B* **1983**, *27*, 748-762.

[118] Lopez-Salido, I.; Lim, D. C.; Dietsche, R.; Bertram, N.; Kim, Y. D., Electronic and Geometric Properties of Au Nanoparticles on Highly Ordered Pyrolytic Graphite (Hopg) Studied Using X-Ray Photoelectron Spectroscopy (Xps) and Scanning Tunneling Microscopy (Stm). *Journal of Physical Chemistry B* **2006**, *110*, 1128-1136.

[119] Kruse, N.; Chenakin, S., Xps Characterization of Au/Tio2 Catalysts: Binding Energy Assessment and Irradiation Effects. *Applied Catalysis a-General* **2011**, *391*, 367-376.

[120] Peters, S.; Peredkov, S.; Al-Hada, M.; Neeb, M.; Eberhardt, W., Positive Xps Binding Energy Shift of Supported Cun-Clusters Governed by Initial State Effects. *Journal of Electron Spectroscopy and Related Phenomena* **2014**, *192*, 52-54.

[121] Heister, K.; Zharnikov, M.; Grunze, M.; Johansson, L. S. O.; Ulman, A., Characterization of X-Ray Induced Damage in Alkanethiolate Monolayers by High-Resolution Photoelectron Spectroscopy. *Langmuir* **2001**, *17*, 8-11.

[122] Frey, S.; Rong, H. T.; Heister, K.; Yang, Y. J.; Buck, M.; Zharnikov, M., Response of Biphenyl-Substituted Alkanethiol Self-Assembled Monolayers to Electron Irradiation: Damage Suppression and Odd-Even Effects. *Langmuir* **2002**, *18*, 3142-3150.

[123] Ishii, H.; Sugiyama, K.; Ito, E.; Seki, K., Energy Level Alignment and Interfacial Electronic Structures at Organic Metal and Organic Organic Interfaces. *Advanced Materials* **1999**, *11*, 605-625.

[124] Xiao, J., The Study of Molecular Band Offsets at the Heteromolecular Interface. The University of Nebraska - Lincoln, Ann Arbor **2009**.

[125] Grobosch, M.; Knupfer, M., Electronic Properties of the Interface between the Organic Semiconductor A-Sexithiophene and Polycrystalline Palladium. *Organic Electronics* **2008**, *9*, 767-774.

[126] Lesiak, B.; Kosinski, A.; Jablonski, A.; Kövér, L.; Tóth, J.; Varga, D.; Cserny, I.; Zagorska, M.; Kulszewicz-Bajer, I.; Gergely, G., Determination of the Inelastic Mean Free Path of Electrons in Polythiophenes Using Elastic Peak Electron Spectroscopy Method. *Applied Surface Science* **2001**, *174*, 70-85.

[127] Faupel, F.; Willecke, R.; Thran, A., Diffusion of Metals in Polymers. *Materials Science and Engineering: R: Reports* **1998**, *22*, 1-55.

[128] Wiegand, B. C.; Friend, C. M., Model Studies of the Desulfurization Reactions on Metal Surfaces and in Organometallic Complexes. *Chemical Reviews* **1992**, *92*, 491-504.

[129] Hirose, Y.; Kahn, A.; Aristov, V.; Soukiassian, P.; Bulovic, V.; Forrest, S. R., Chemistry and Electronic Properties of Metal-Organic Semiconductor Interfaces: Al, Ti, in, Sn, Ag, and Au on Ptcda. *Physical Review B* **1996**, *54*, 13748-13758.

[130] Salvan, G.; Paez, B. A.; Silaghi, S.; Zahn, D. R. T., Deposition of Silver, Indium, and Magnesium onto Organic Semiconductor Layers: Reactivity, Indiffusion and Metal Morphology. *Microelectronic Engineering* **2005**, *82*, 228-235.

[131] Braun, W.; Gavrila, G.; Gorgoi, M.; Zahn, D. R. T., Influence of the Molecular Structure on the Interface Formation between Magnesium and Organic Semiconductors. *Radiation Physics and Chemistry* **2006**, *75*, 1869-1871.

[132] Hirose, Y.; Kahn, A.; Aristov, V.; Soukiassian, P., Chemistry, Diffusion, and Electronic Properties of a Metal/Organic Semiconductor Contact: In/Perylenetetracarboxylic Dianhydride. *Applied Physics Letters* **1996**, *68*, 217-219.

[133] Ivanco, J.; Haber, T.; Krenn, J. R.; Netzer, F. P.; Resel, R.; Ramsey, M. G., Sexithiophene Films on Ordered and Disordered TiO_2(110) Surfaces: Electronic, Structural and Morphological Properties. *Surface Science* **2007**, *601*, 178-187.

[134] Chase, M. W.; National Institute of, S.; Technology, *Nist-Janaf Thermochemical Tables*; American Chemical Society ; American Institute of Physics for the National Institute of Standards and Technology: [Washington, D.C.]; Woodbury, N.Y., **1998**.

[135] Iucci, G.; Polzonetti, G.; Altamura, P.; Paolucci, G.; Goldoni, A.; Russo, M. V., X-Ray Photoelectron Spectroscopy Studies of Novel Π-Conjugated Ethynyl Thiophene Containing Pd(Ii) Complexes and of Their Interaction with Chromium. *Journal of Vacuum Science & Technology A* **2000**, *18*, 248-256.

[136] National Instruments, L. Labview 2012 Gpu Analysis Toolkit Readme. http://digital.ni.com/public.nsf/websearch/2E5B336298C0B32786257A1600647C56?OpenDocument#overview.

[137] Microsoft Acquiring High-Resolution Time Stamps. https://msdn.microsoft.com/en-us/library/windows/desktop/dn553408(v=vs.85).aspx.

[138] Shannon, C. E., Communication in the Presence of Noise. *Proceedings of the IRE* **1949**, *37*, 10-21.

Acknowledgement

First and foremost I wish to express my gratitude to Prof. Dr. J. Michael Gottfried, for providing me the opportunity to conduct this doctorate within their research groups. His inspirational mentorship and philosophy of scientific research has greatly influenced me in the past six years. I would also like to thank him for the continuous support and guidance in my research work.

I am especially grateful to my coworkers, in particular Dr. Hans-Jörg Drescher, for introducing me to the world of UHV systems and unreserved help both in office and in daily life; Dr Martin Schmidt, for the many fruitful discussions in the work and help to the improvement of scientific writing; Dr. Min Chen, Malte Zugermeier, Benedikt Klein, Claudio Krug and many others who have participated in the research work of AG Gottfried, your commitment and enthusiasm to the research work have always been a promotion to me.

I would like to express my sincere gratitude to Marco Hill, for the many helps in the work, especially those because of my limited german language skills. To members of the mechanical workshop and electronic workshop, Fachbereich Chemie, Philipps Universität Marburg, your excellent works of craftsmanship have provided definitive support to overcome the challenges in my work.

I would also like to give my special thanks to Prof. Dr. Rainer Fink of Friedrich-Alexander-Universität Erlangen-Nürnberg, for the crucial introduction of me to Prof. Dr. J. Michael Gottfried, which made everything thereafter possible.

Financial support by the China Scholarship Council for the doctor fellowship is gratefully acknowledged.

Finally, I would like to tell my family how utterly grateful I am for the support in all the past years, in particular, my wife Yunjie Zong, for the unlimited love that had propped me up all the time.

Appendix

Technical Drawings

All the drawings are resized to fit into the A4 pages. The absolute size of a drawing on the page bears no significance any more as they would normally do in a DIN norm technical drawing.

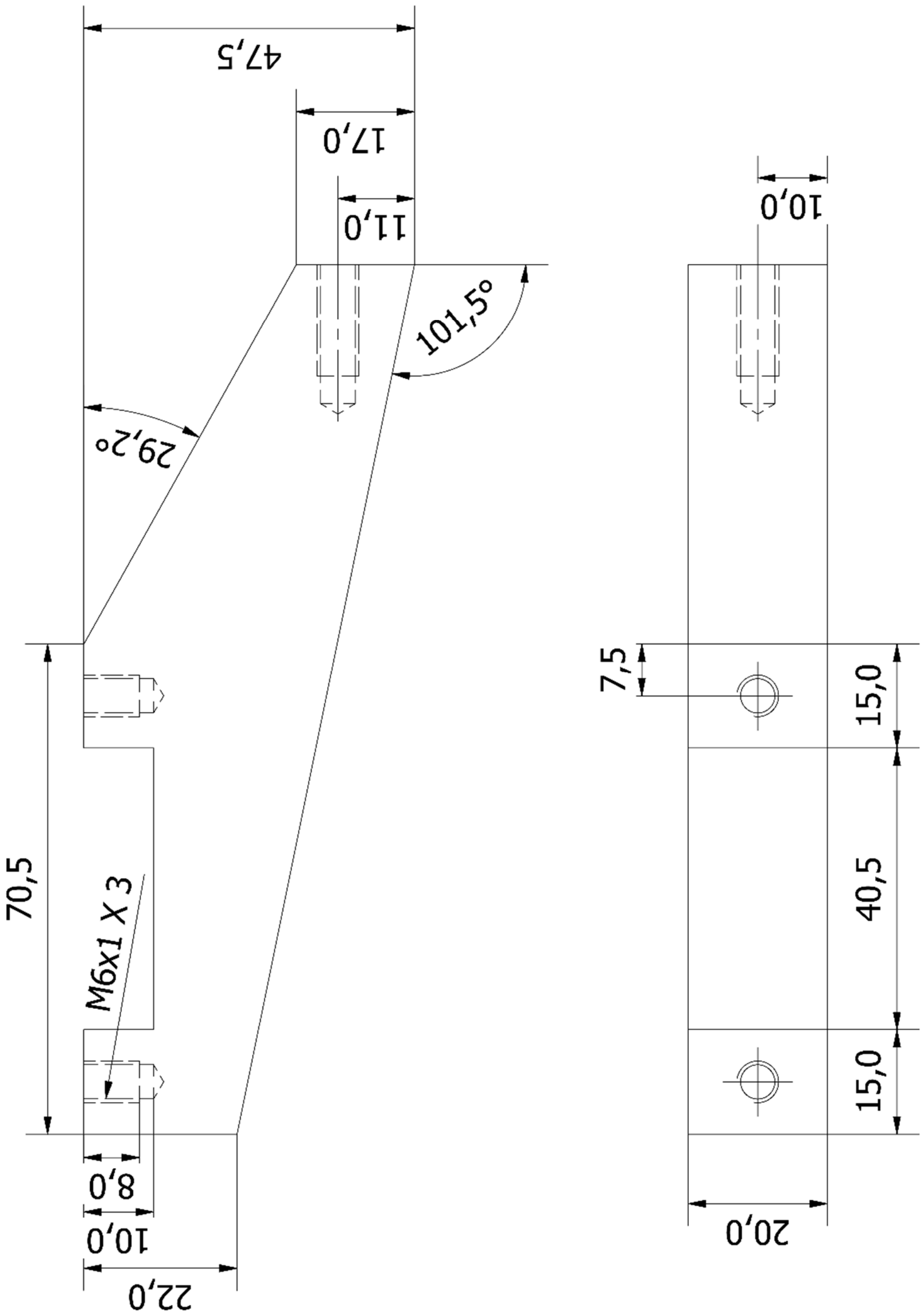

Aluminum arm, **d2** in Figure 6.2.

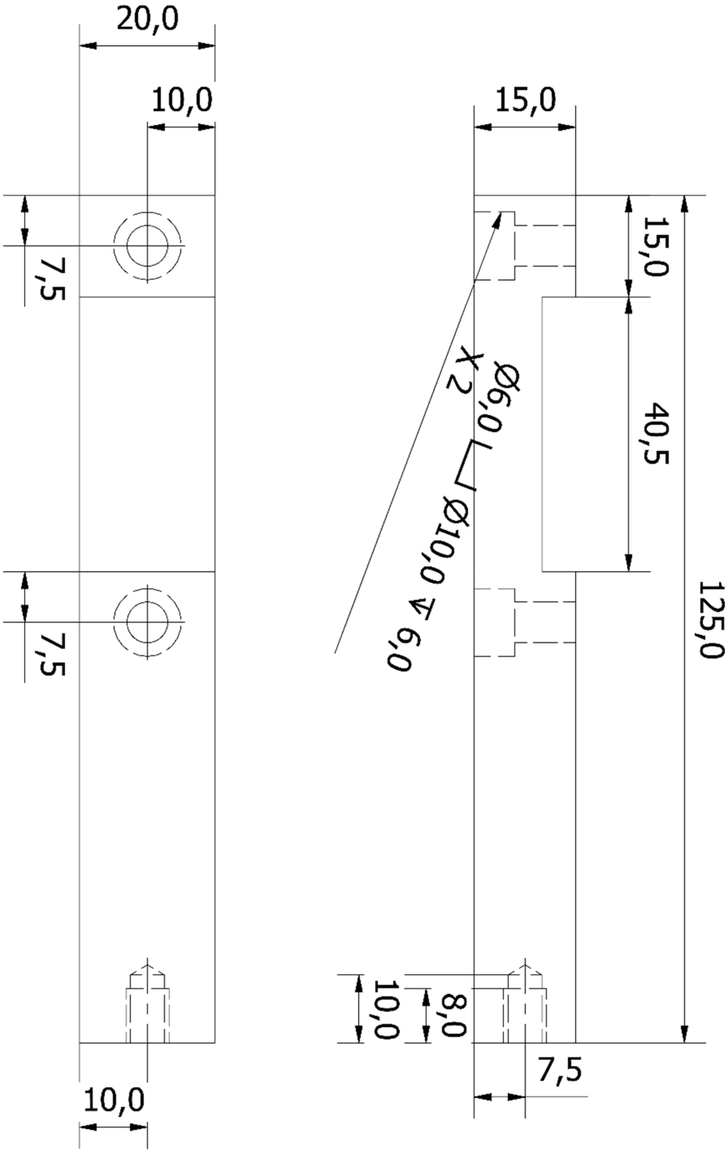

Aluminum arm, **d3** in Figure 6.2.

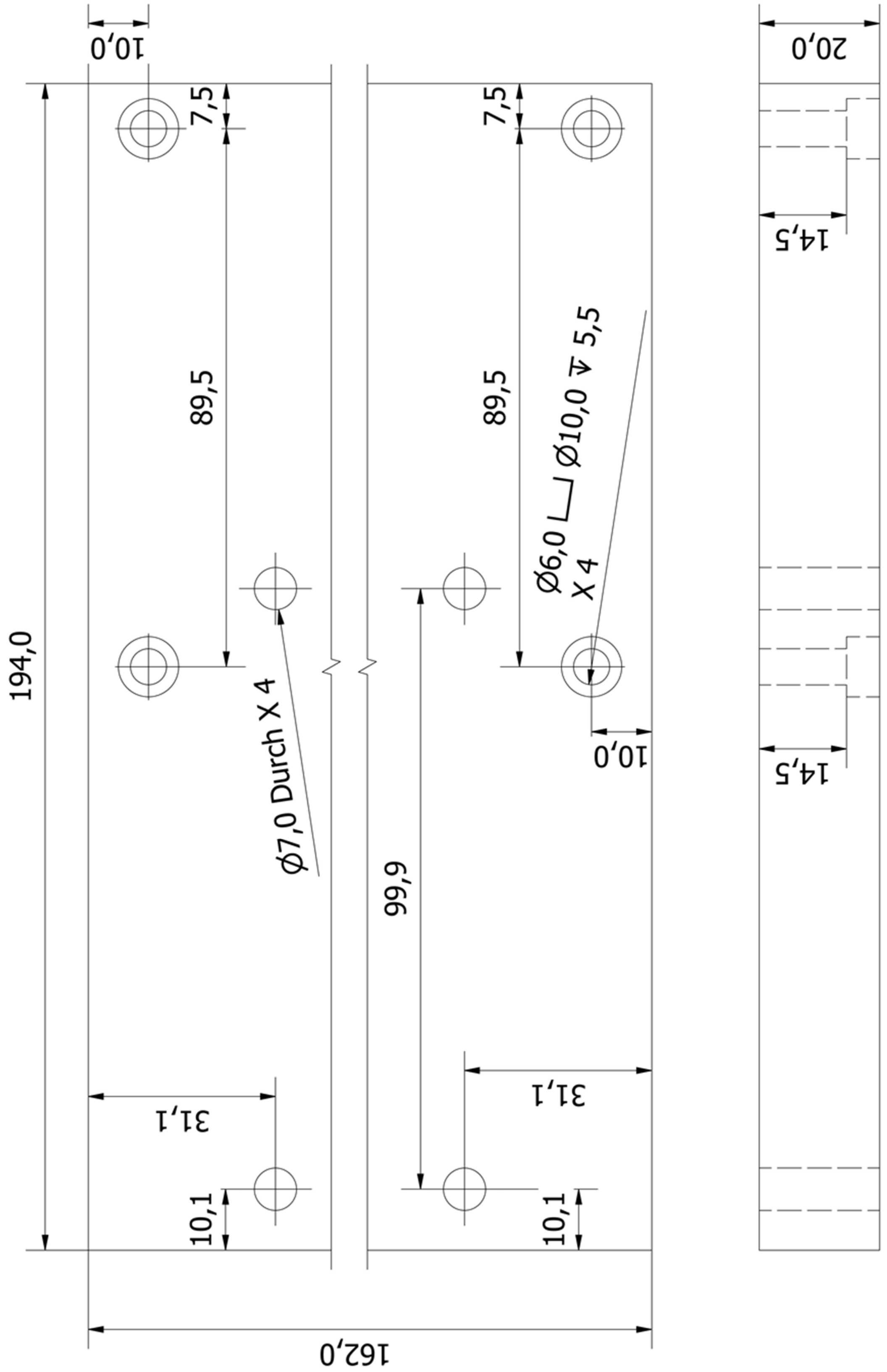

Aluminum base piece, **d1** in Figure 6.2.

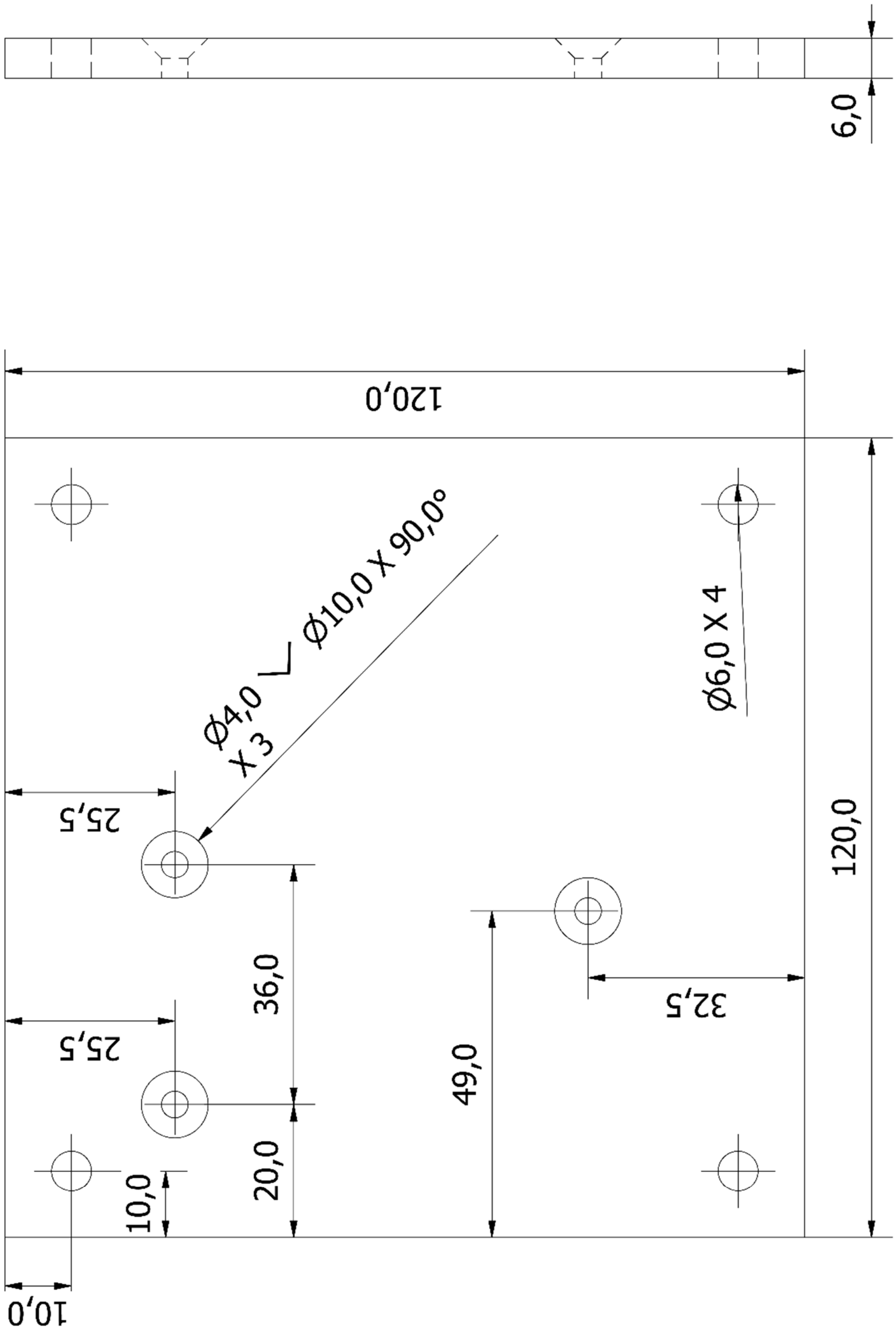

Aluminum adapter, **d4** in Figure 6.2.

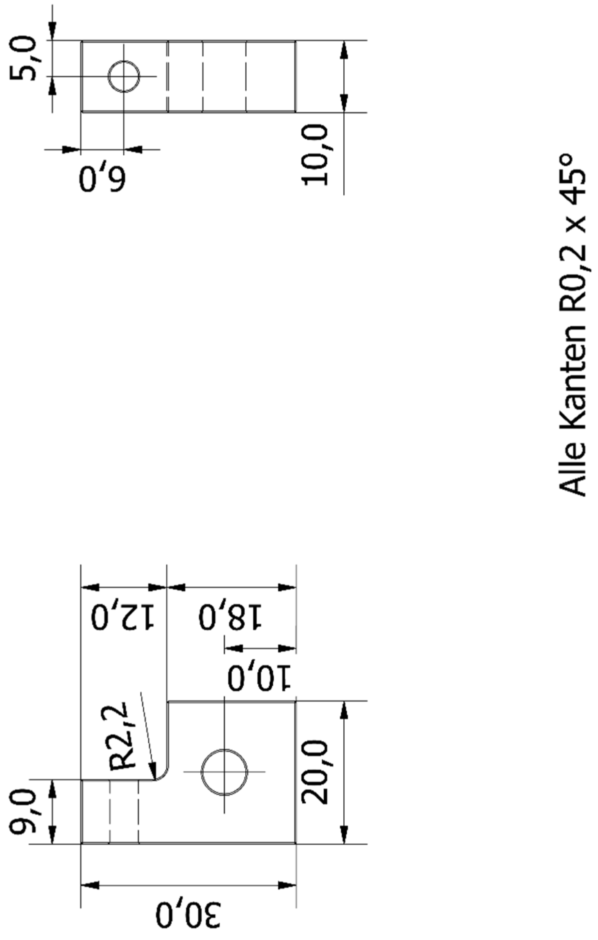

Aluminum adapter, **d5** in Figure 6.2.

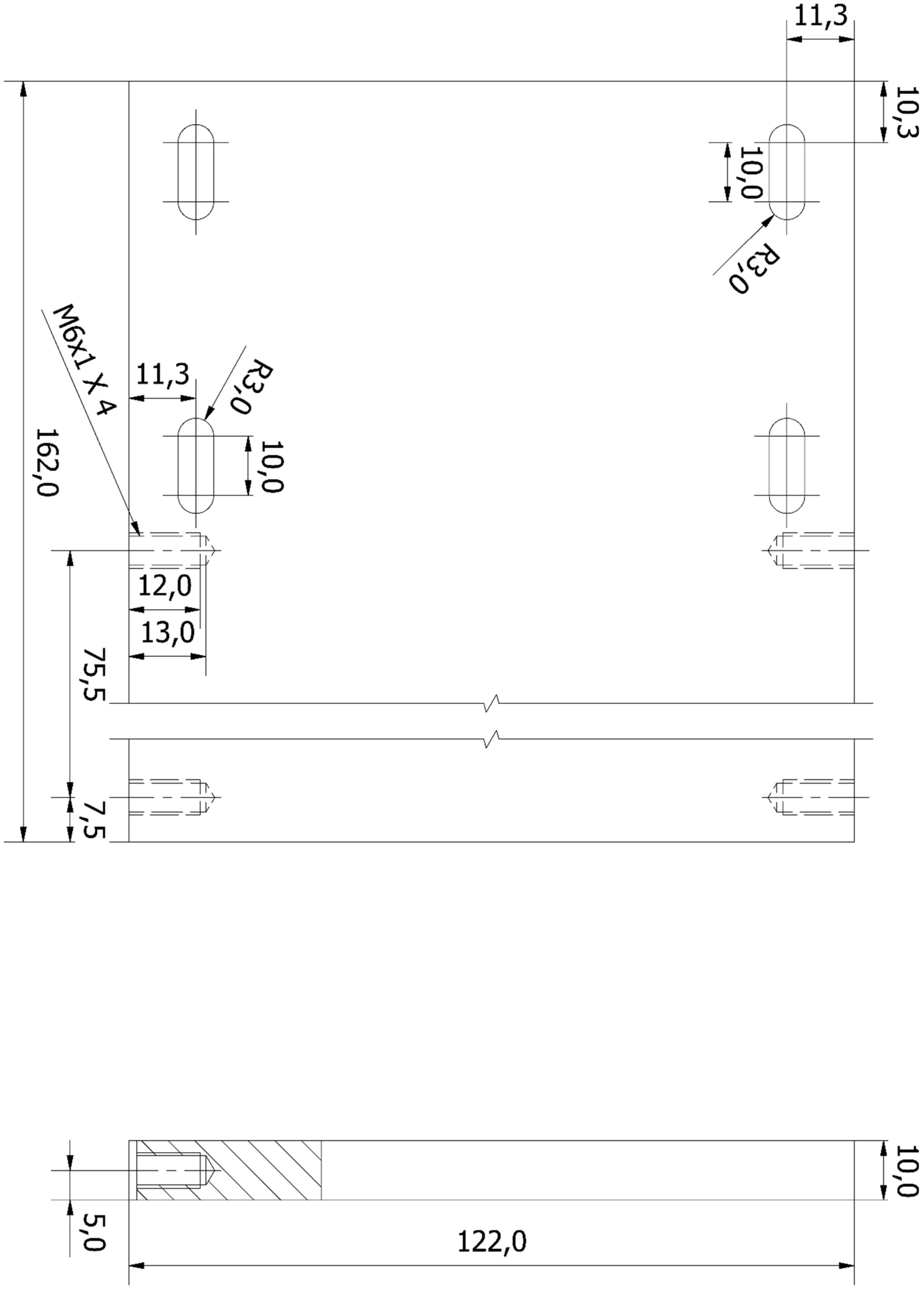

Aluminum base piece, **f1** in Figure 6.3.

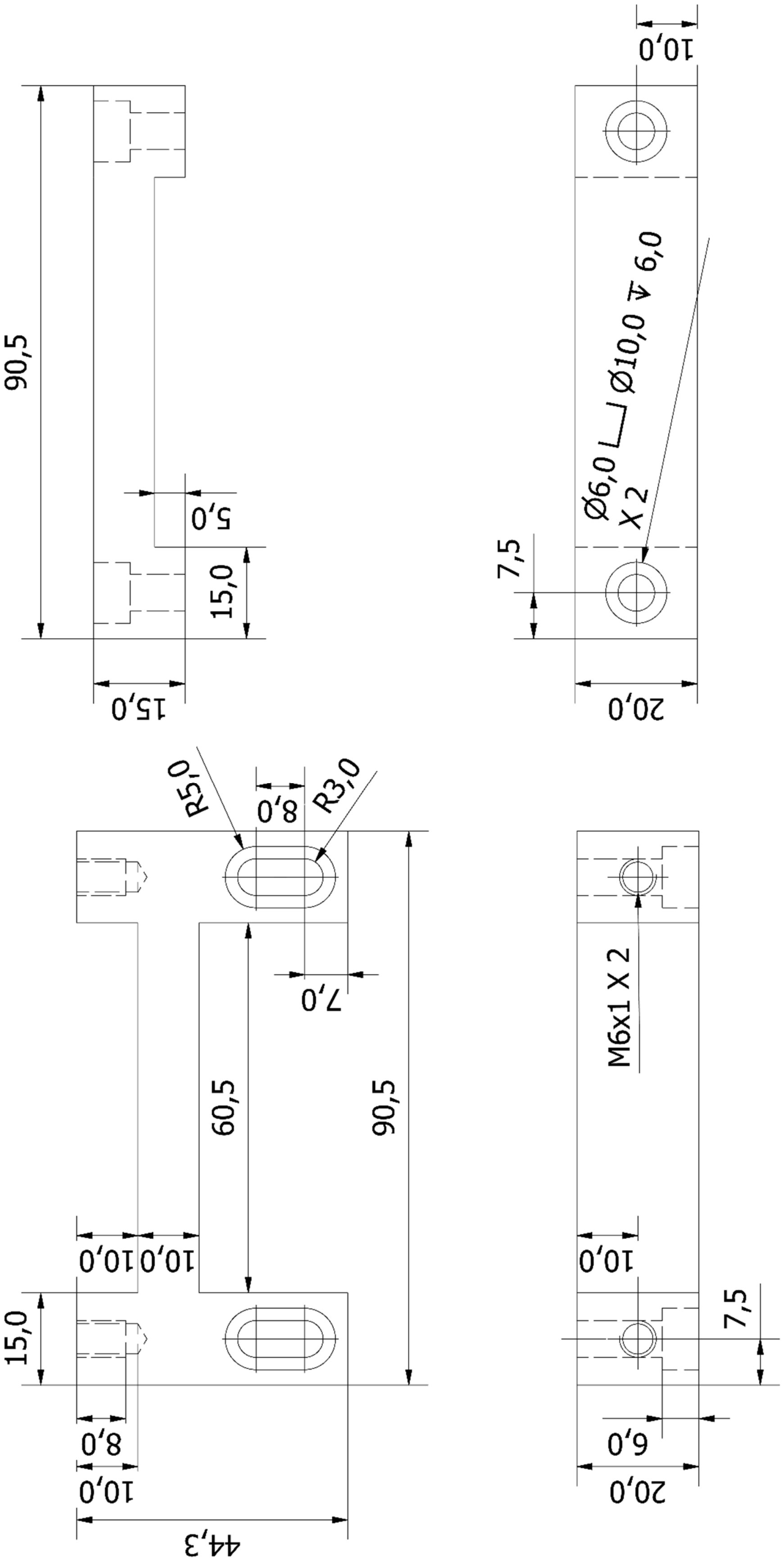

Aluminum arms, **f3** and **f2** in Figure 6.3.

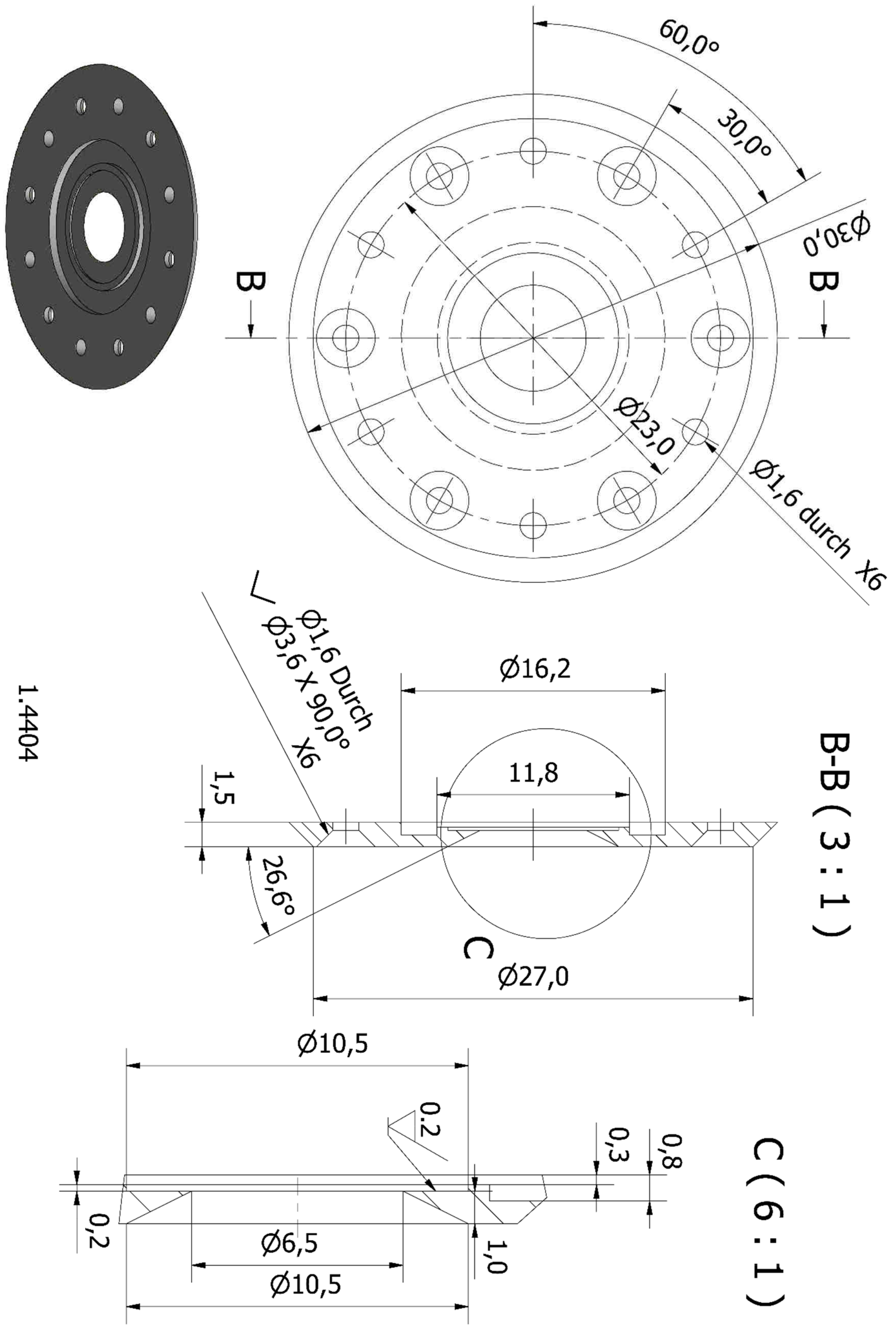

Stainless steel cap, **a** in Figure 6.5.

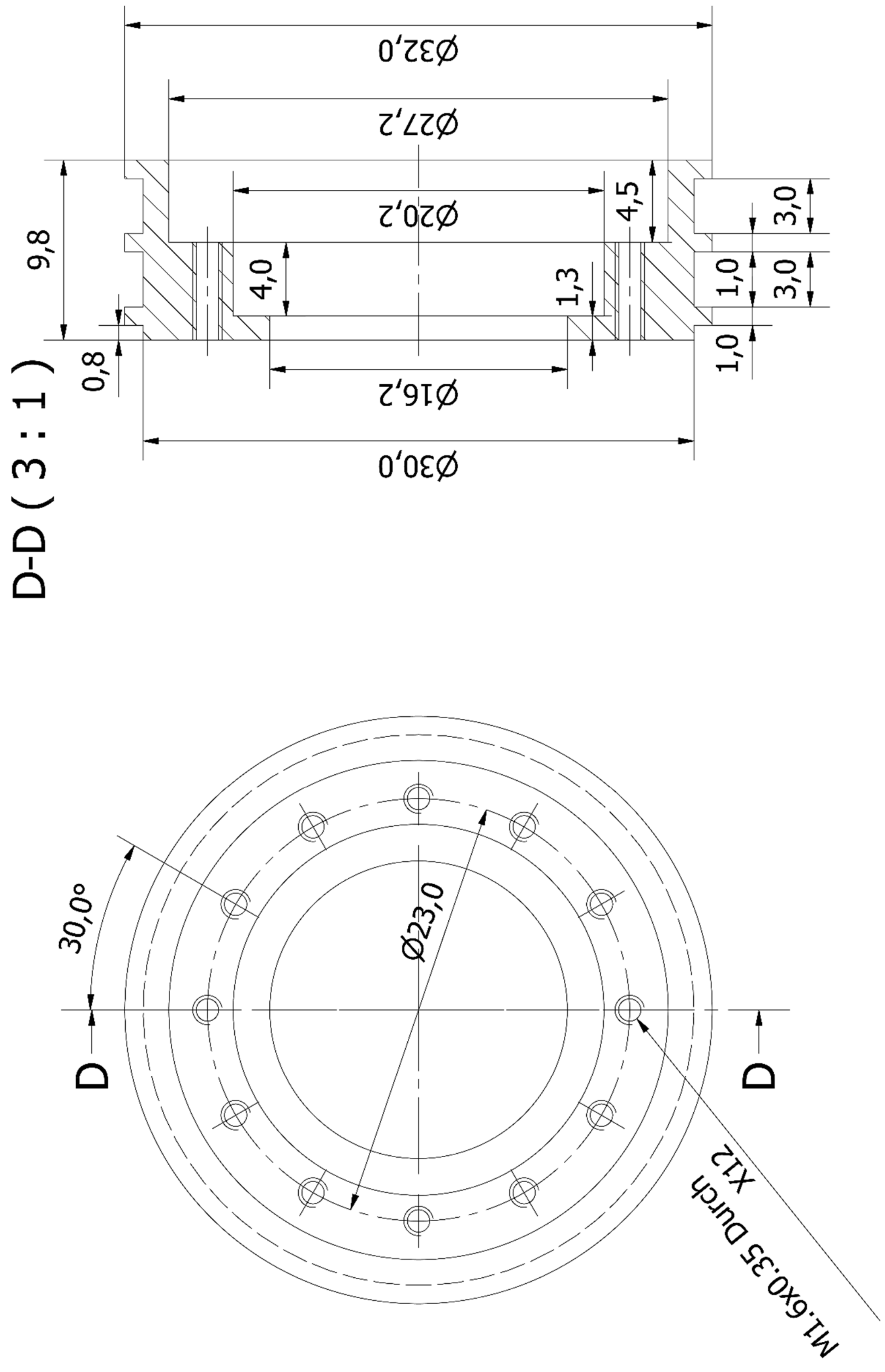

Aluminum frame, **h** in Figure 6.5.

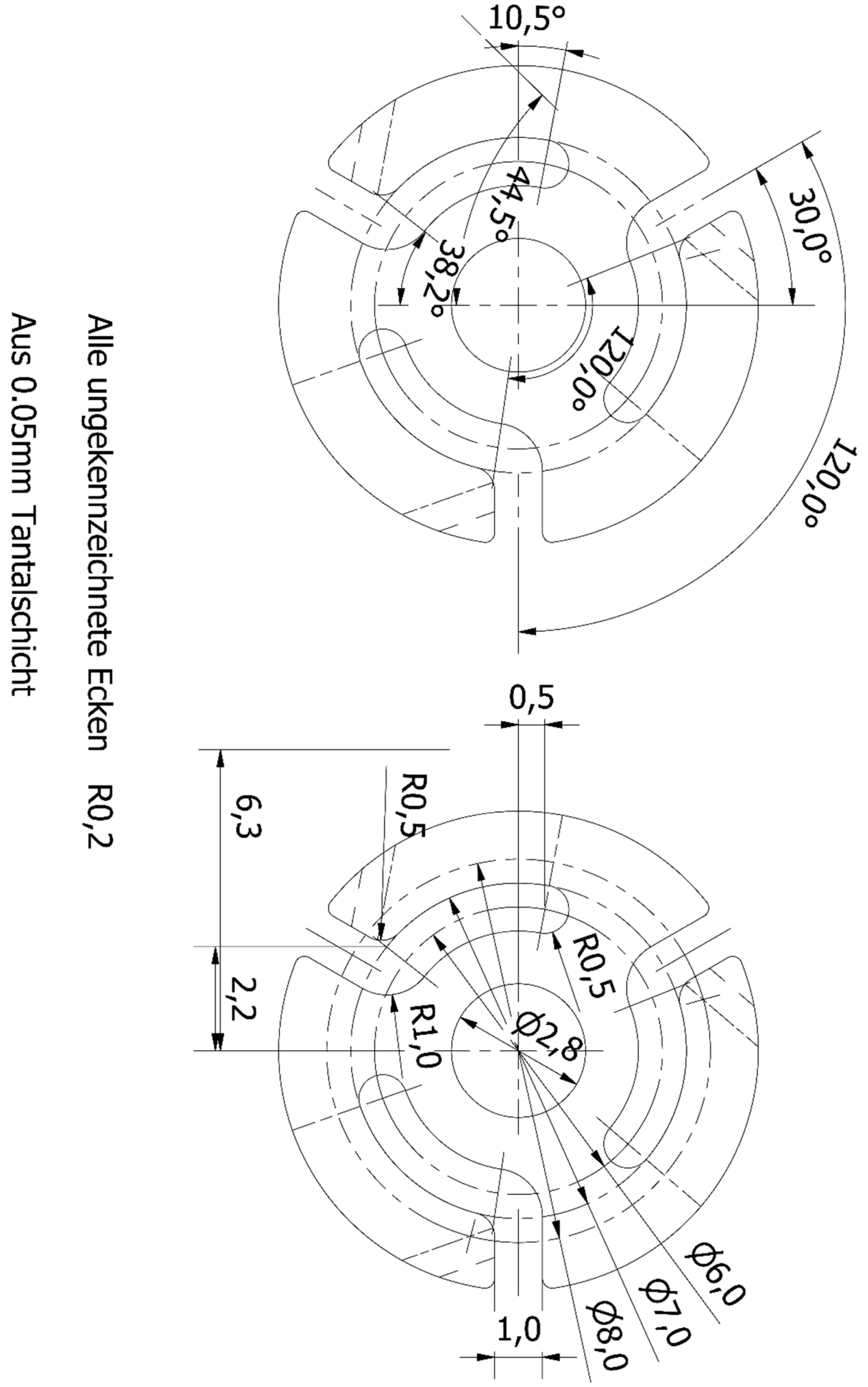

0.05mm Tantalum sheet, **c** in Figure 6.5.

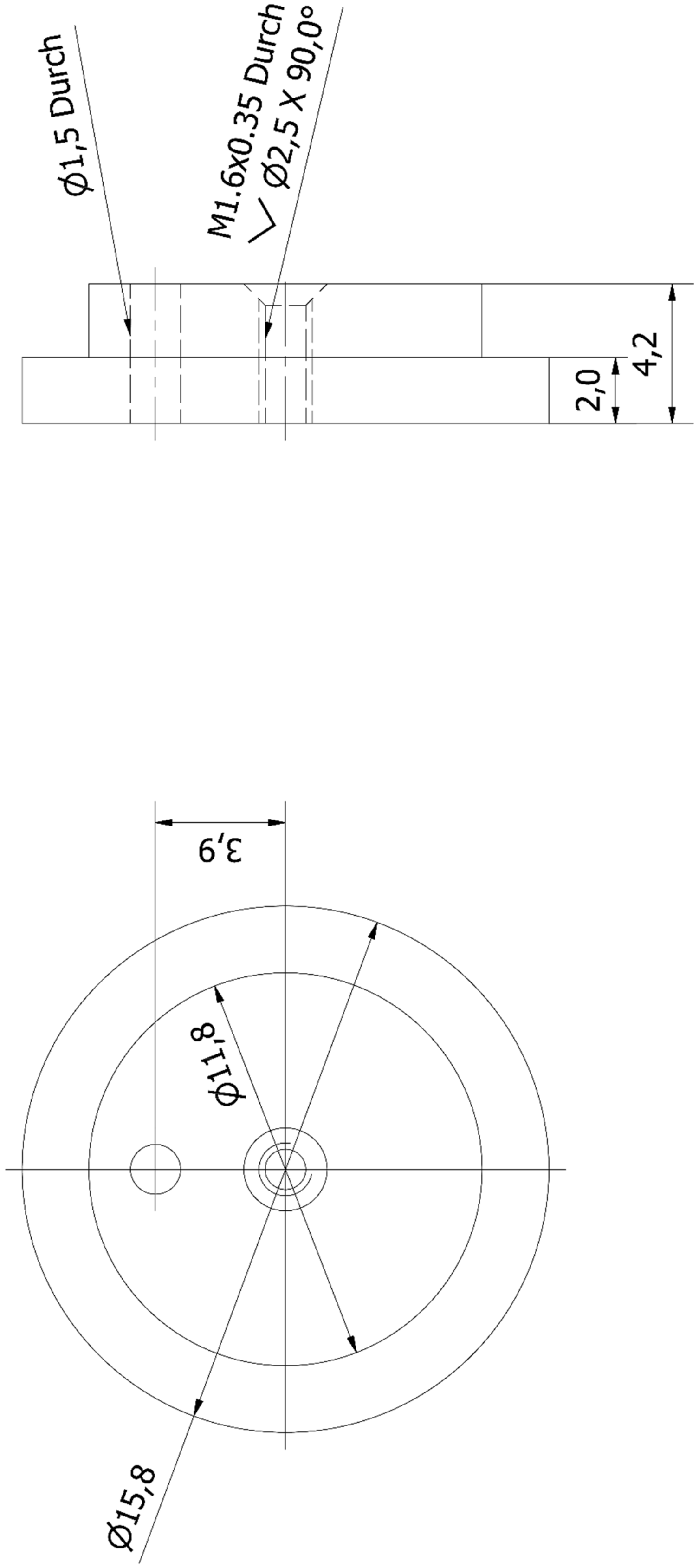

Aluminum back electrode mount, **e** in Figure 6.5.

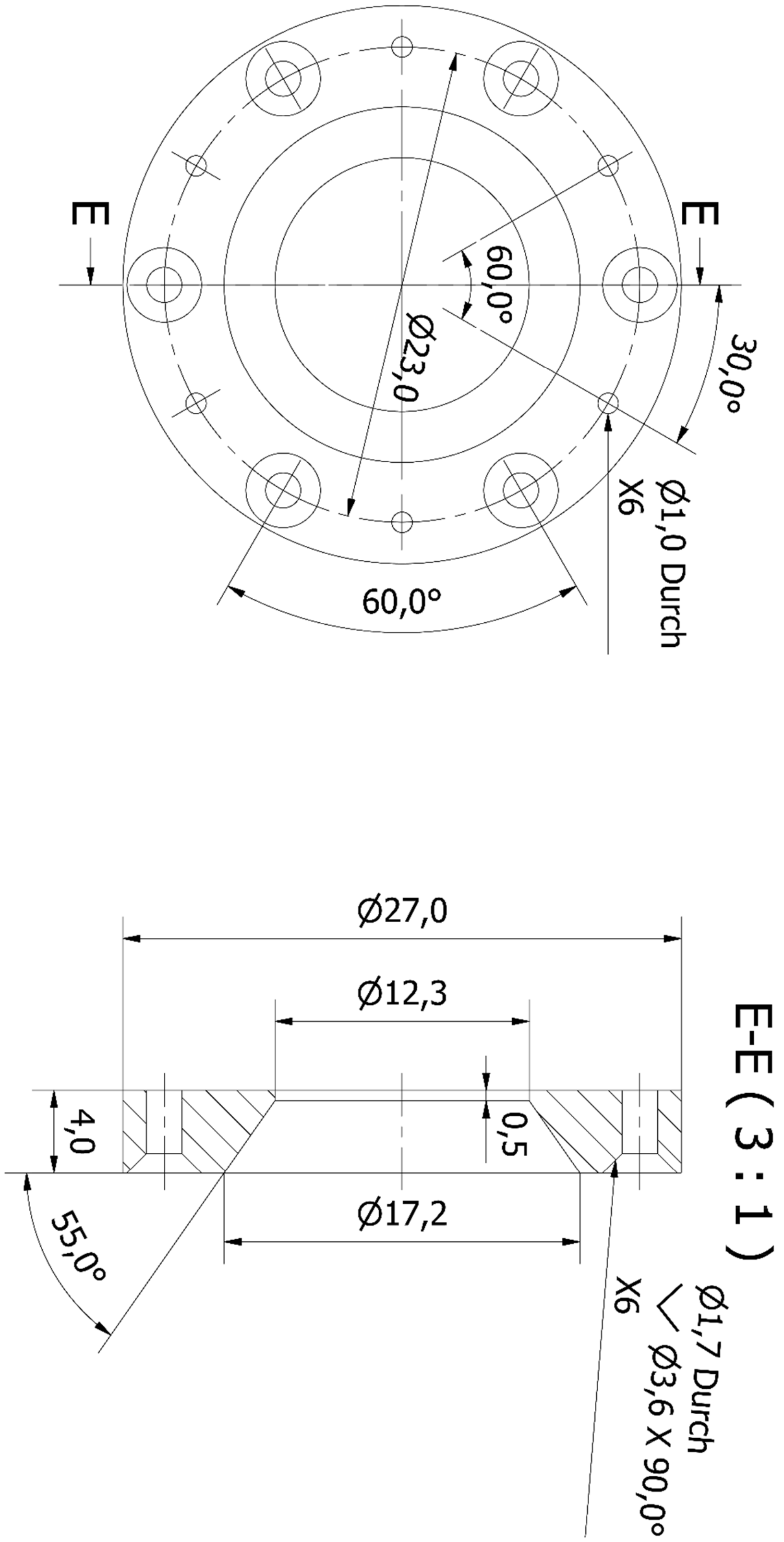

Aluminum back pressing piece, **g** in Figure 6.5.

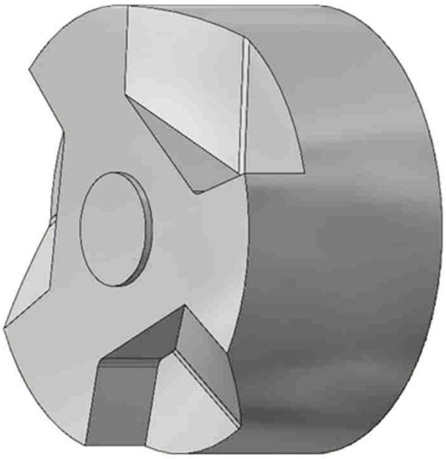

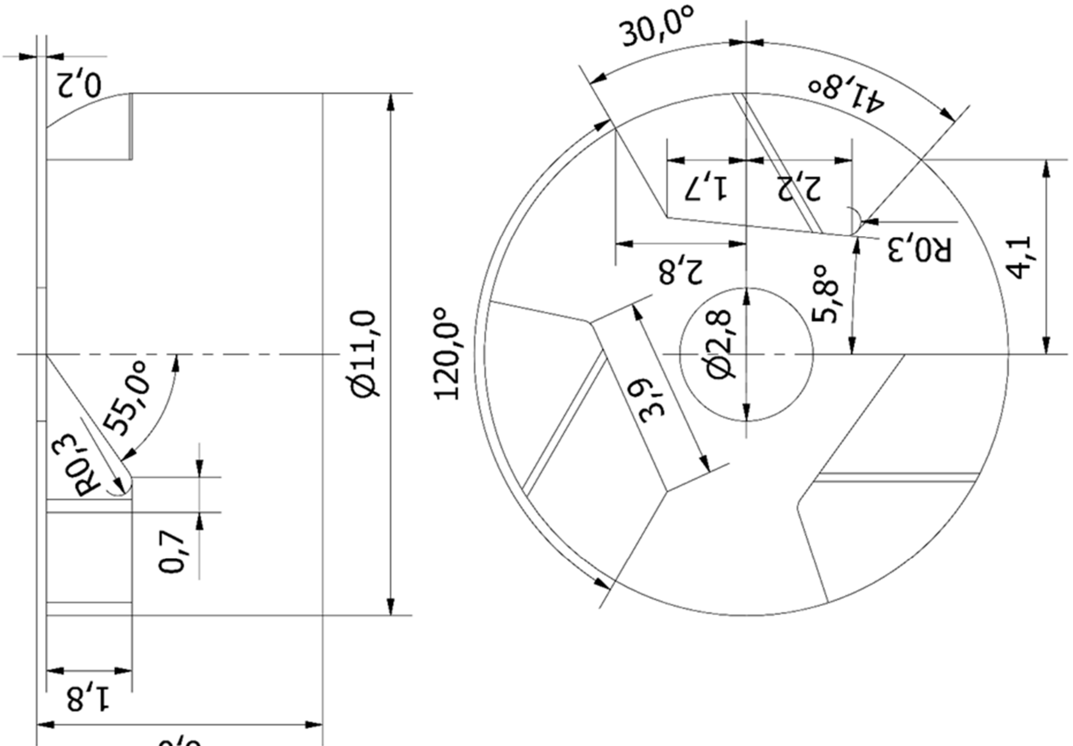

Aluminum female mold, **a2** in Figure 6.6.

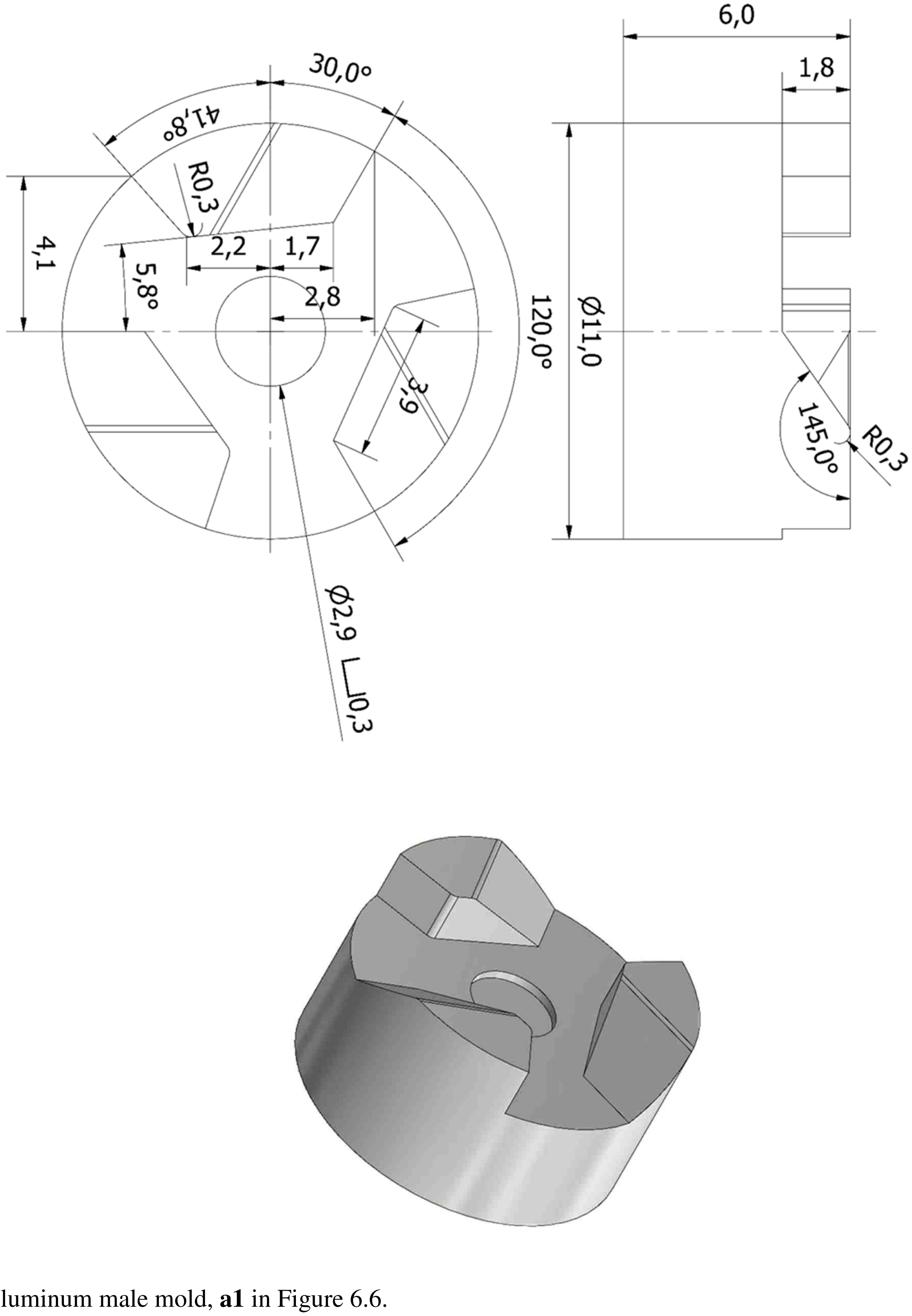

Aluminum male mold, **a1** in Figure 6.6.

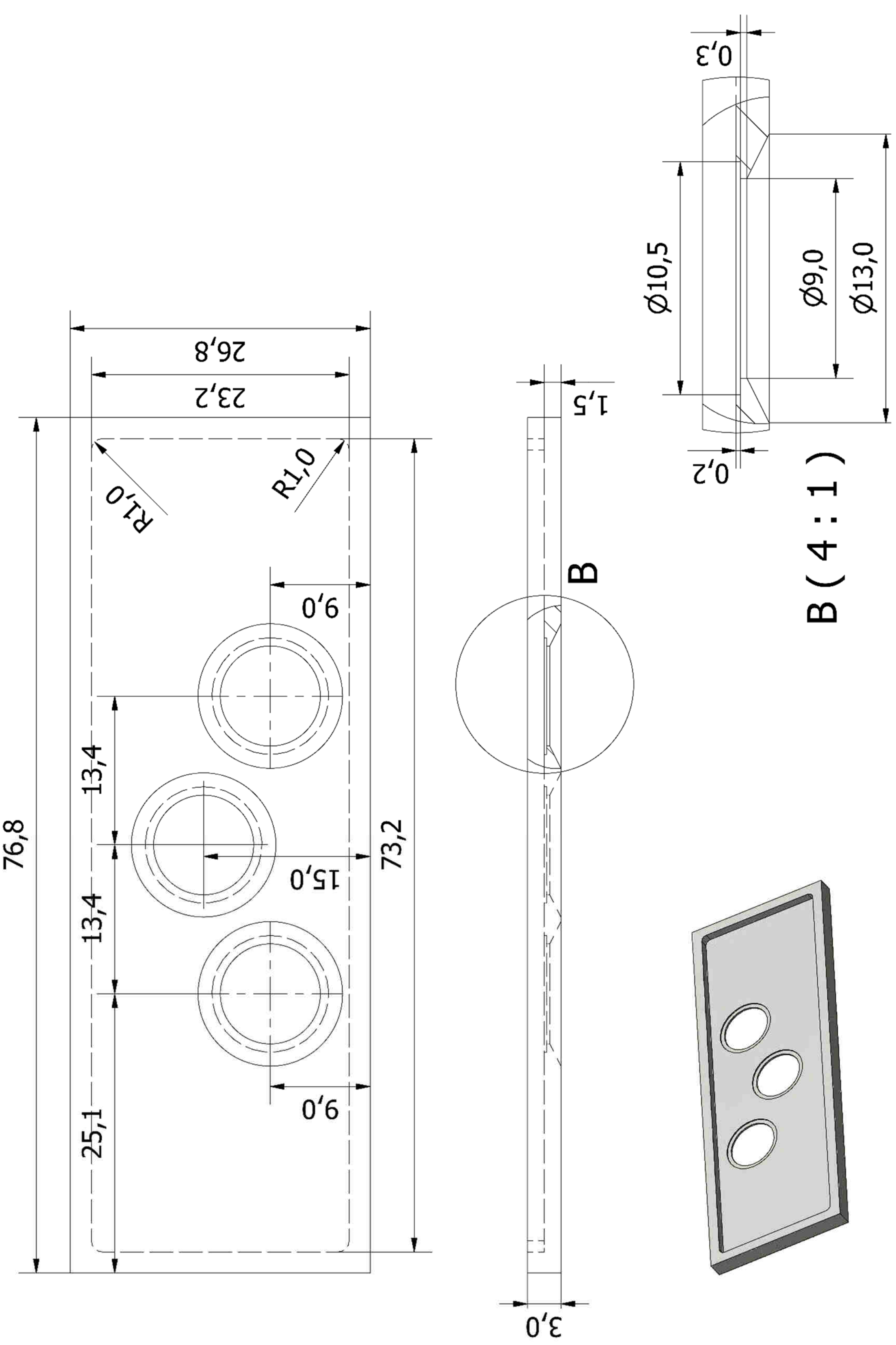

Stainless steel mask (1.4404). Scaled by 85%

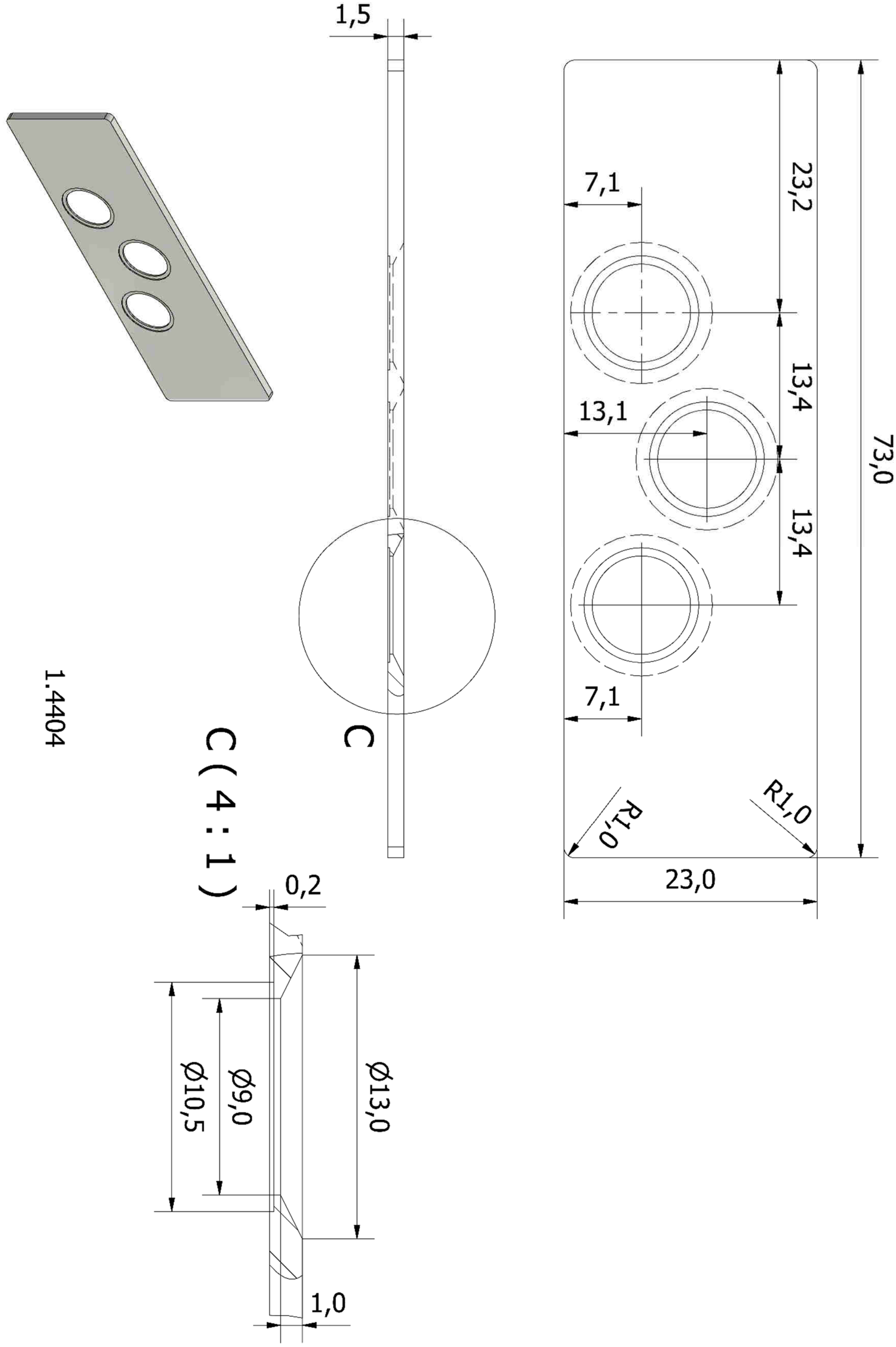

Stainless steel mask (1.4404).

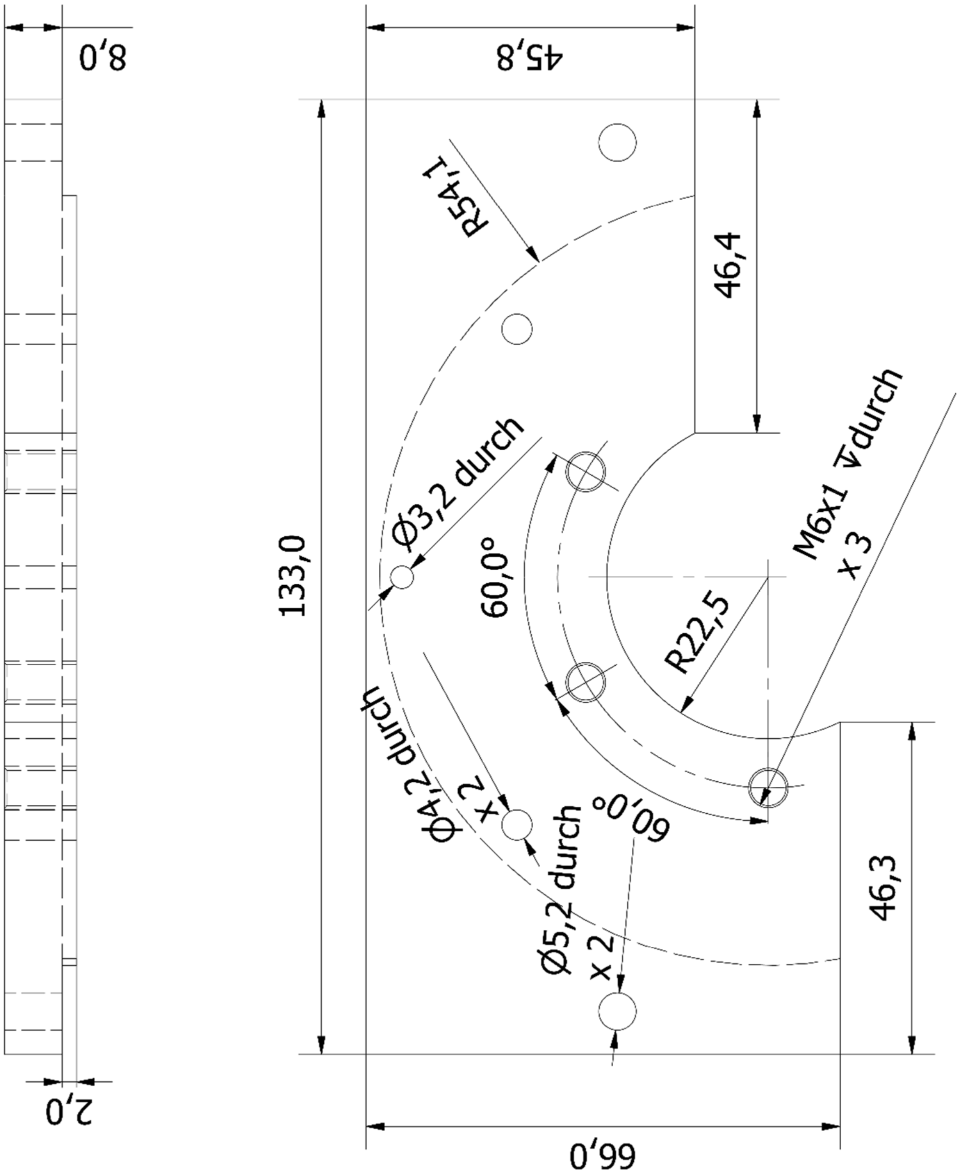

Stainless steel plate, **e1** and **e2** in Figure 6.8.

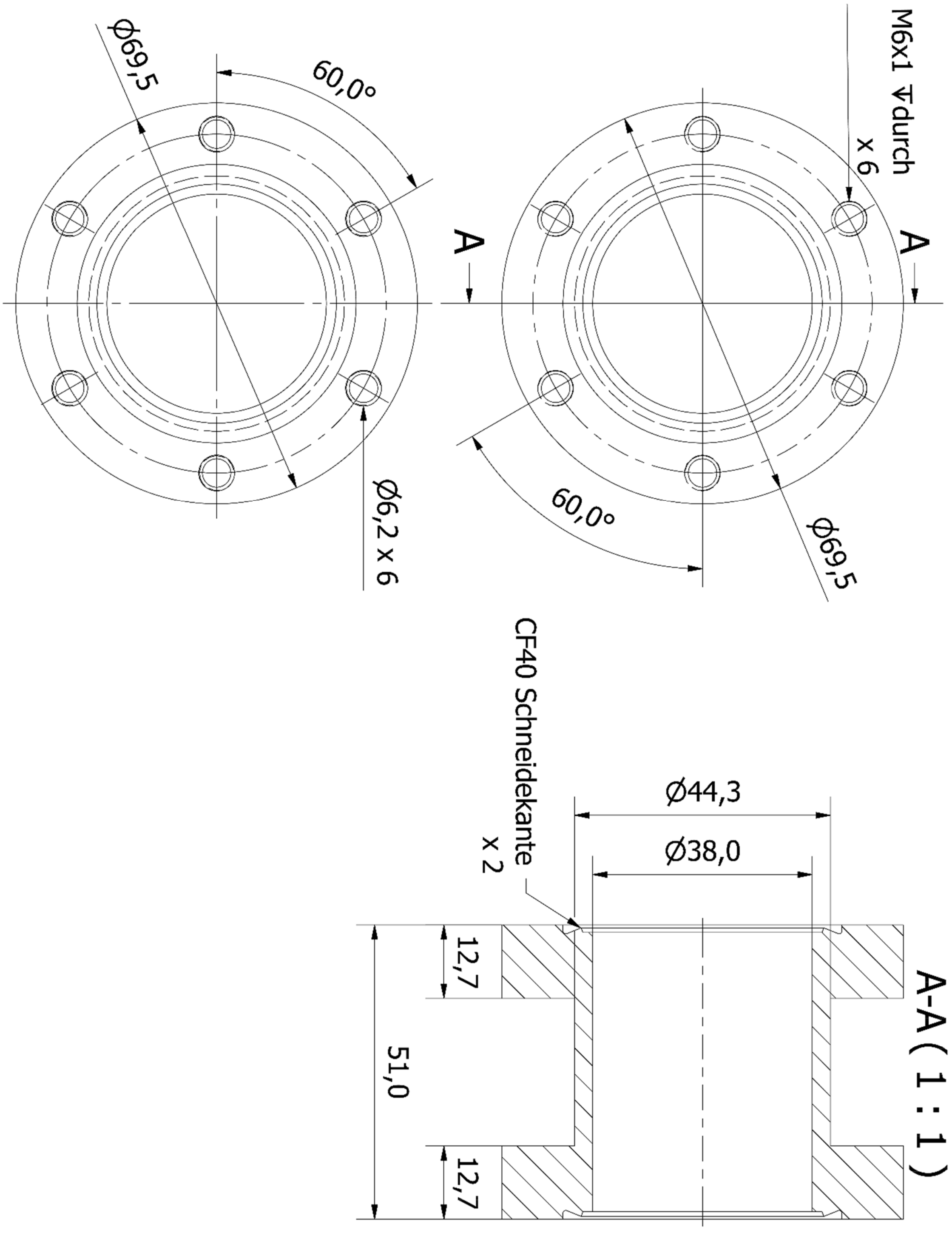

Stainless steel tube (1.4404), **b** in Figure 6.8.

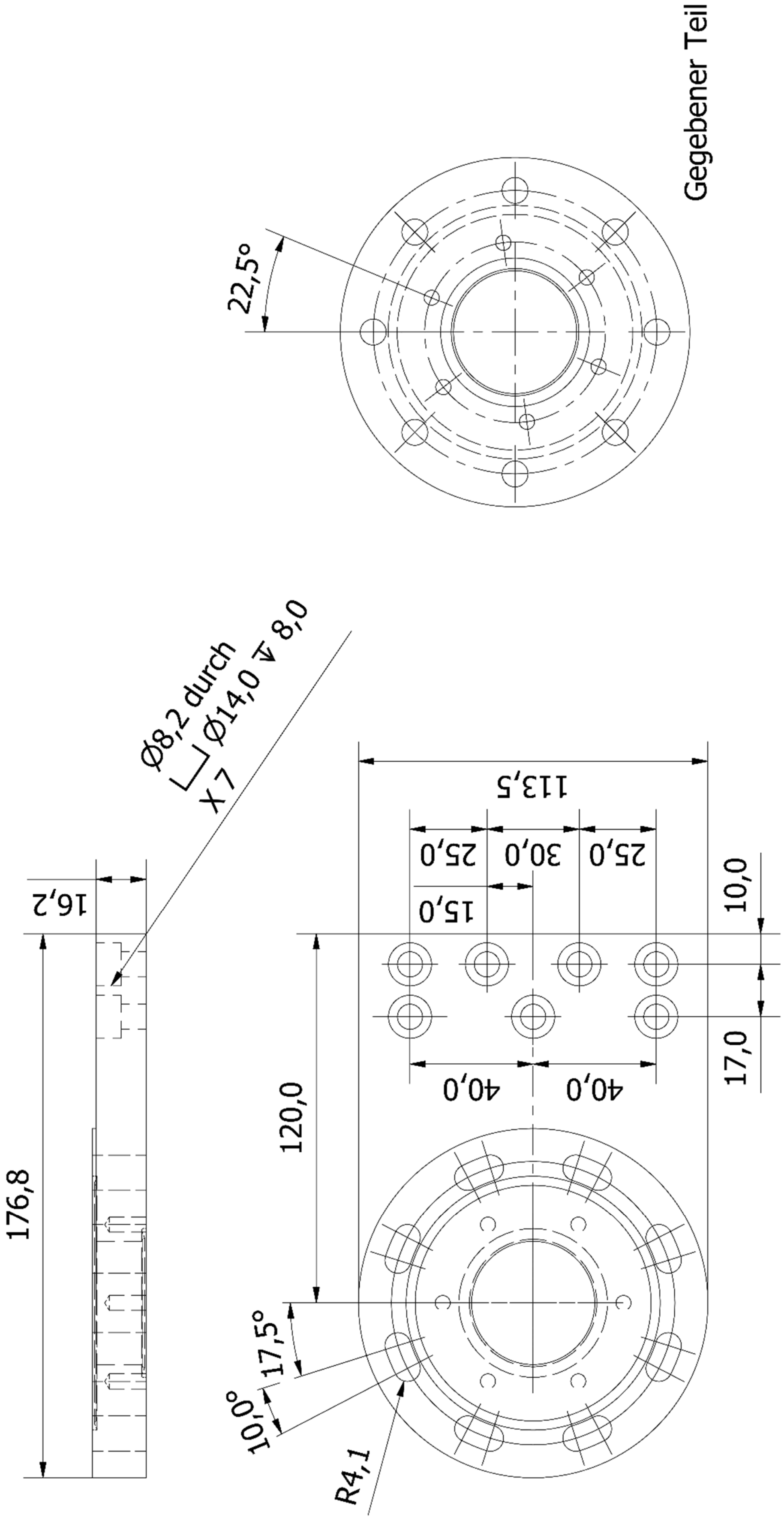

Modified stainless steel flange, **a** in Figure 6.8.

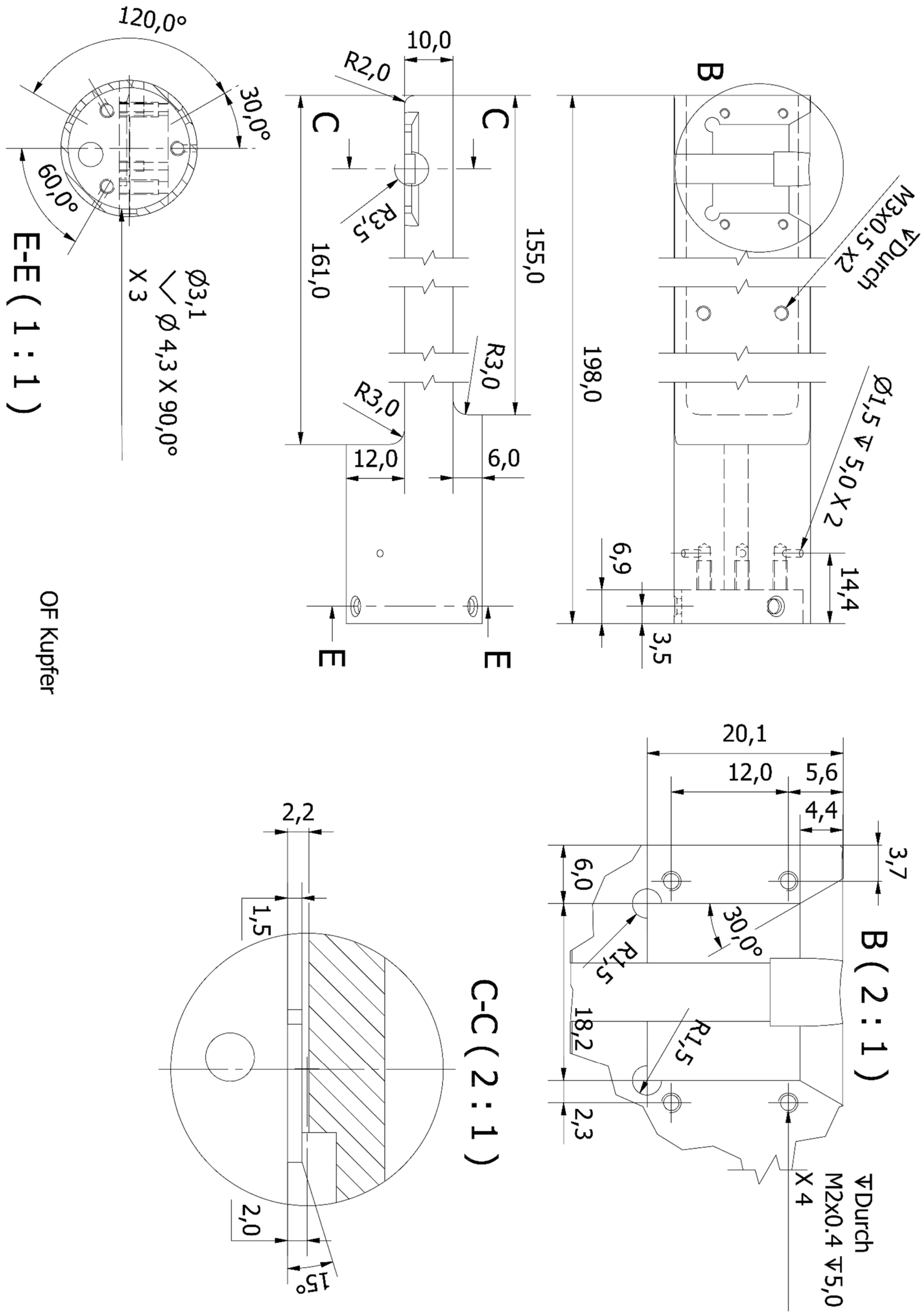

Copper reservoir, **f** in Figure 6.8. Drawing 2-1.

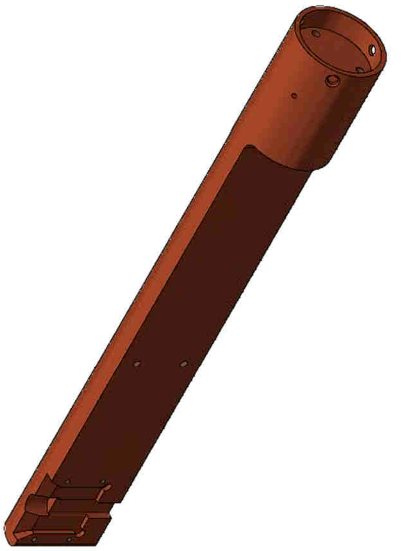

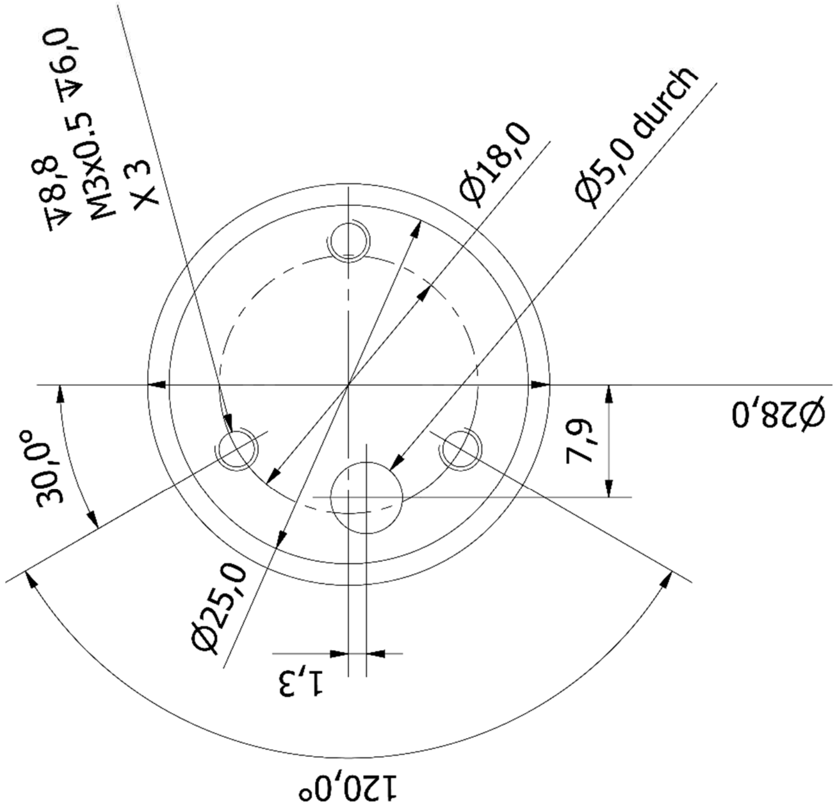

Copper reservoir, **f** in Figure 6.8. Drawing 2-2.

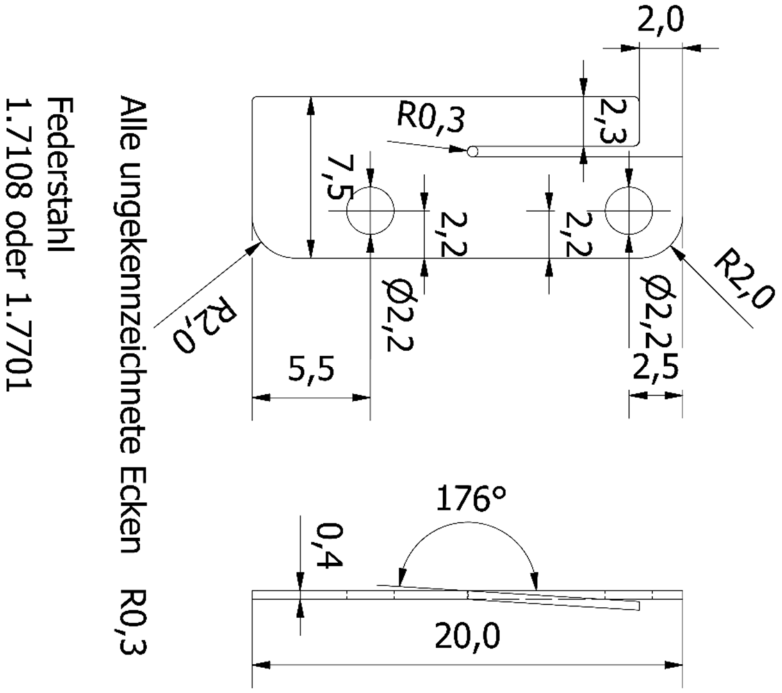

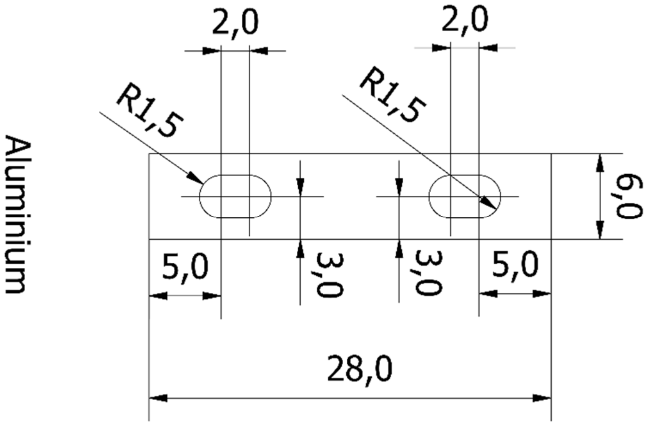

Spring steel pressing sheet, **f1** in Figure 6.9.

Aluminum strip, **f3** in Figure 6.9.